

SAINT PETERSBURG STATE UNIVERSITY
Department of Nuclear Physics Research Methods

13th International Youth School-Conference

MAGNETIC RESONANCE AND ITS APPLICATIONS

Abstracts

an AMPERE event

November 20-26, 2016
Saint Petersburg, Russia

Schola Spinus



13th International Youth School-Conference
MAGNETIC RESONANCE AND ITS APPLICATIONS
SPINUS-2016

ORGANIZING COMMITTEE

Chairman	Denis Markelov, associate professor, SPSU
Vice-chairman	Alexander Ievlev, researcher, SPSU
Committee members	Andrey Egorov, associate professor, SPSU Andrey Komolkin, associate professor, SPSU Pavel Kupriyanov, engineer, SPSU Sergey Bystrov, graduate student, SPSU Sevastyan Rabdano, trainee researcher, SPSU Konstantine Tutukin, senior researcher, SPSU Timofey Popov, SPSU
Layout of Abstracts Book	Aleksandr Levantovskii

CONTACTS

1, Ulyanovskay st., Peterhof, 198504, St. Petersburg, Russia
Department of Nuclear Physics Research Methods
St. Petersburg State University

Tel.	(812) 428-99-48
Fax	(812) 428-72-40
E-mail	spinus@nmr.phys.spbu.ru
Website	http://nmr.phys.spbu.ru/spinus

PROGRAM COMMEETEE

SCIENTIFIC ADVISER OF THE SCHOOL-CONFERENCE

Vladimir Chizhik Honored scientist of Russia,
Professor, SPSU

ADVISORY BOARD

E. B. Aleksandrov	Acad., Prof., St. Petersburg, Russia
V. Balevicius	Prof., Vilnius, Lithuania
Yu. M. Bunkov	Prof., Grenoble, France
V. I. Chizhik	Prof., St. Petersburg, Russia
D. Fruchart	Prof., Grenoble, France
L. Yu. Grunin	PhD, Director of Resonance Systems, Ltd.
E. Lähderanta	Prof., Lappeentanta, Finland
D. Michel	Prof., Leipzig, Germany
V. I. Minkin	Acad., Prof., Rostov-on-Don, Russia
N. R. Skrynnikov	Prof., St. Petersburg, Russia, Purdue, USA
M. S. Tagirov	Prof., Kazan, Russia
S. Vasiliev	Prof., Turku, Finland

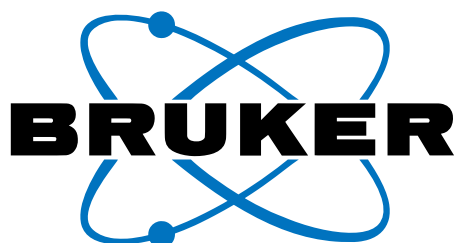


Spinus

SPONSORS



Saint Petersburg
State University
spbu.ru



Bruker Corporation
bruker.com



**RESONANCE
SYSTEMS**

Resonance Systems Ltd.
nmr-design.com



APG Eastern Europe
preforma.ru



Magicplot Systems, LLC
magicplot.com

Contents

SCHEDULE	19
WELCOME TO THE SCHOOL-CONFERENCE "SPINUS" OF SAINT PETERSBURG STATE UNIVERSITY.....	29
LECTURES.....	31
<i>E. B. Aleksandrov</i> Natural Science and the Spirit World	32
<i>N. K. Andreev</i> How to receive more information in NMR using possibilities of pulse sequences.....	33
<i>Yuriy Bunkov</i> Supermagnonics	36
<i>E. V. Charnaya, A. O. Antonenko, D. Yu. Nefedov, D. Yu. Podorozhkin, A. V. Uskov, J. Haase, D. Michel, Yu. A. Kumzerov</i> NMR studies of nanocomposites with metal and alloy particles.....	38
<i>V. I. Chizhik</i> [NMR] echoes of sad news... (in memory of Erwin Hahn).....	39
<i>U. Eichhoff</i> Preclinical Magnetic Resonance Imaging	40
<i>M. E. Elyashberg</i> Computer methods for structure elucidation of <i>new</i> organic compounds from NMR spectra	43
<i>Vyatcheslav Frolov</i> Visualization by NMR. Physical principles.....	46
<i>Leonid Y. Grunin, Innokenty A. Nikolaev</i> Time-Domain NMR Characterization of Solids Structure	48
<i>K. Kaempf, S. O. Rabdano, A. Groves, I. S. Podkorytov and N. R. Skrynnikov</i> Local and global dynamics of intrinsically disordered proteins: a case study of H4 histone tail.....	49
<i>Kirill Kavokin</i> Deep cooling of the nuclear spin system in semiconductor structures	51

<i>Andrei V. Komolkin</i> Earth's magnetic field fluctuations and uncertainty of site finding using the geomagnetic map.....	52
<i>Vilius Kurauskas, Sergei A. Izmailov, Olga N. Rogacheva, Audrey Hessel, Isabel Ayala, Anastasya Shilova, Joyce Woodhouse, Yi Xue, Tairan Yuwen, Oleg Mikhailovskii, Manfred Burghammer, Nicolas Coquelle, Jacques-Philippe Colletier, Nikolai R. Skrynnikov, Paul Schanda</i> Dynamics in protein crystal: insights from MD simulations.....	53
<i>M. S. Kuznetsova, R. V. Cherbunin, I. Ya. Gerlovin, I. V. Ignatiev, M. Yu. Petrov, S. Yu. Verbin, D. R. Yakovlev, and M. Bayer</i> Electron-nuclear spin dynamics in semiconductor QDs	55
<i>Vladimir V. Matveev</i> NMR Applications to Ionic Liquids: Current Status.....	58
<i>Dieter Michel, Dieter Freude and Jürgen Haase</i> MAS NMR studies in combination with pulsed field gradient techniques.....	60
<i>Yuriy I. Neronov</i> Determination of the spin-spin coupling in the molecule HD and possible manifestations of axion-like particles	61
<i>N. M. Sergeyev</i> The NMR time scale	64
<i>N. M. Sergeyev</i> Water mythology.....	65
<i>Peter M. Tolstoy, Benjamin Koeppe, Ilja G. Shenderovich, Gleb S. Denisov, Hans-Heinrich Limbach</i> Cooperativity of Strong Hydrogen Bonds Studied by Liquid State NMR Spectroscopy.....	66
<i>Sergey Vasiliev, Otto Vainio, Lauri Lehtonen, Janne Ahokas, Sergey Sheludiakov, Jarno Järvinen</i> Spin Exchange and Magnons in Cold Atomic Hydrogen Gas.....	68
<i>Valerii S. Zapasskii</i> Advances in Optical Detection of Magnetization	69
ORAL REPORTS	71
<i>Ekaterina S. Babicheva, Nataliia S. Shubina, Alexander M. Perepukhov, Alexander V. Maximychev, Vladimir M. Negrimovsky</i> NMR study of Phthalocyanine solubility in Pluronic solutions.....	72

<i>Yu. V. Bogachev, A. V. Nikitina, S. M. Sukharzhevskii</i> Determination of T1 and T2 relaxation times from stationary saturation of inhomogeneously broadened EPR lines	75
<i>A. A. Bogdan, G. V. Kataeva, Yu. G. Khomenko, A. G. Il'ves, L. N. Prakhova</i> Diagnostic value of in vivo 1H-MRS with short and long Echo Time for patients with Multiple Sclerosis	78
<i>Sergei S. Bystrov, Vladimir I. Chizhik</i> Molecular mobility and translational diffusion analysis of ionic liquid (methyl-octyl imidazolium chloride) in mixture "water – glycerol" by NMR	81
<i>A. V. Chudin, A. V. Ievlev</i> Magnetic resonance spectroscopy as a tool for magnetometry of Earth magnetic field	83
<i>Laurynas Dagys, Vytautas Klimavičius, Vytautas Balevičius</i> Advanced processing of CPMAS kinetics in Ammonium Dihydrogen Phosphate.....	84
<i>S. V. Diachenko, A. I. Zhernovoy</i> Method measurement of temperature in conditions magnetic resonance.....	87
<i>Maxim Dolgushev and Denis A. Markelov</i> NMR Relaxation in Semiflexible Dendrimers	89
<i>A. A. Drozdov, V. M. Cheremisin, I. G. Kamishanskaya, A. A. Yakovlev, V. B. Musatov, I. P. Fedunyak, O. I. Fedunyak, M. N. Artem'eva</i> MRI imaging of CNS tuberculosis among patients with AIDS.....	91
<i>Andrey L. Fedorov, Andrey V. Sergeev, Evgenii D. Baglasov, Evgenii M. Milovidov, Evgenii D. Narkhov, Dmitriy V. Saveluev, Aleksey Yu. Denisov, Vladimir A. Sapunov</i> A Gradient Tolerance Measurements of Proton Overhauser Sensor POS-1.....	93
<i>D. V. Fomina, V. A. Glukhova, M. V. Gulyaev, S. S. Batova, N. V. Anisimov</i> Calculation of optimal parameters for MRI of fluorocarbons	95
<i>Sergei Izmailov, Ivan Podkorytov, Nikolai Skrynnikov</i> MD modeling of disulfide bond formation in peptides and proteins.....	98

<i>Yu. G. Khomenko, G. V. Kataeva, E. A. Gromova, I. V. Milyukhina, M. N. Karpenko, A. A. Bogdan, D. S. Susin</i> Comparison of the magnetic resonance spectroscopy findings with cerebral glucose metabolism and immunological data in Parkinson's disease	99
<i>E. I. Kondratyeva, A. V. Klochkov, I. G. Motygullin, K. R. Safiullin, M. S. Tagirov</i> Vacuum heat treatment of wood and study of its properties by magnetic resonance and other methods	102
<i>M. S. Krestina, A. E. Akulov, O. B. Shevelev, I. V. Koptug</i> ^1H NMR spectroscopy <i>in vitro</i> and <i>in vivo</i> of rat tissues and blood after alcohol impact	105
<i>Pavel Kupriyanov</i> High-Resolution NMR-device in the Earth magnetic field in a laboratory environment.....	107
<i>N. V. Luzhetckaia, S. V. Ievleva, K. V. Tyutyukin, V. V. Frolov</i> Magnetic resonance measurements of the fibrous plants diffusion tensor in ultra-low magnetic field	108
<i>S. S. Mariasina, O. A. Petrova, C.-F. Chang, T.-H. Huang, I. A. Osterman, A. B. Mantsyzov, P. V. Sergiev, V. I. Polshakov</i> NMR Study of the Williams Syndrome Related Methyltransferase WBSCR27	111
<i>V. M. Mikushev, E. V. Charnaya</i> Influence of resonance saturation fields on impurity spin-lattice relaxation of nuclear spin systems in solids.....	114
<i>Anton V. Nikulin, Anna A. Hurshkainen, Stanislav B. Glybovski, Irina V. Melchakova, Pavel A. Belov, Benoit Larrat, Elodie Georget, Stefan Enoch and Redha Abdeddaim</i> A novel design of dual-nuclei RF coils for preclinical MRI at 7 Tesla...	115
<i>D. S. Nuzhina, E. M. Alakshin, A. V. Klochkov, S. Kodjikian, E. I. Kondratyeva, S. L. Korableva, I. V. Romanova, M. S. Tagirov</i> Synthesis of ReF_3 (Re = rare earth ions) nanoparticles for NMR research.....	118
<i>I. N. Petrov, V. M. Cheremisin, I. G. Kamyshanskaya, R. L. Kazarov</i> Diffusion-weighted MRI in clinical oncurology	121
<i>D. A. Pomogailo, A. Kh. Vorobiev</i> Determination of relative positions of paramagnetic probes in smectic liquid crystal by analysis of angular dependence of dipole-dipole broadening of EPR spectra	124

<i>Sevastyan O. Rabdano, Sergei A. Izmailov, Dmitry A. Luzik, Adam Groves, Ivan S. Podkorytov, and Nikolai R. Skrynnikov</i> Second RNA-recognition motif RRM2 of TDP-43 protein: oxidative stress leads to structure destabilization, aggregation and increased susceptibility to proteolytic degradation	126
<i>Olga N. Rogacheva, Sergei A. Izmailov, Nikolai R. Skrynnikov</i> Molecular dynamics studies and <i>in silico</i> mutational analysis as applied to dynamics in ubiquitin crystals	127
<i>T. R. Safin, A. V. Klochkov, I. G. Motygullin, K. R. Safiullin, M. S. Tagirov</i> Evidence of coherent magnon state in easy-plane antiferromagnet and yttrium iron garnet films	128
<i>Aleksey V. Shestakov, Ilshat I. Fazlizhanov, Ivan V. Yatsyk, Mariyam I. Ibragimova, Vladimir A. Shustov, Rushana M. Eremina</i> The oscillations in ESR spectra of Hg _{0.76} Cd _{0.24} Te:Ag	131
<i>Nataliia S. Shubina, Ekaterina S. Babicheva, Alexander M. Perepukhov, Alexander V. Maximychev, Sheyda R. Frolova, Konstantin I. Agladze</i> NMR study of AzoTAB and CTAB photoisomerization when interacting with the lipid bilayer	134
<i>P. I. Simeschenko, V. M. Cheremisin, I. G. Kamyshanskaya</i> Comparison of low-field and high-field MR for the diagnosis of brain metastases	137
<i>Alexey P. Slobozhanyuk, Alena V. Shchelokova, Irina V. Melchakova, Pavel A. Belov</i> Application of metasurfaces for magnetic resonance imaging	139
<i>A. A. Stanislavovas, E. M. Alakshin, A. V. Klochkov, V. V. Kuzmin, T. R. Safin, K. R. Safiullin and M. S. Tagirov</i> Spin kinetics of ³ He in contact with ordered Al ₂ O ₃ aerogel	142
<i>L. Surova, E. Krylova, A. F. Privalov, M. G. Shelyapina</i> Impact of copper on water diffusion in sodium mordenite	145
<i>Irina I. Tyuryaeva, Olga G. Lyublinskaya, Ivan S. Podkorytov, Nikolai R. Skrynnikov</i> Mechanism of cytotoxicity of GO peptides and some other cysteine-containing peptides	148
<i>A. V. Uskov, D. Yu. Nefedov, E. V. Charnaya, J. Haase, D. Michel, Yu. A. Kumzerov, A. V. Fokin, A. S. Bugaev</i> NMR investigations of atomic mobility of sodium embedded in porous glass with pore size 3.5 nm	149

<i>Bing Wu, Mingwen Tian, Jianjun Xu, Junyu Li, Dermot Brougham, Victor Litvinov</i> Spectroscopic Analyses of Nanometer Scale Heterogeneity in PEG-based Polyacrylate Gel	152
<i>Yuriy O. Zgadzay, Sergey V. Efimov, Vladimir V. Klochkov</i> Structure investigation of bovine insulin by two-dimensional NMR spectroscopy	155
POSTER SESSION	159
<i>V. Y. Adelson, V. V. Frolov, V. M. Cheremisin</i> Magnetic Resonance Imaging of the blood and its derivatives.....	161
<i>A. O. Antonenko, E. V. Charnaya, V. V. Marchenkov, S. V. Naumov</i> NMR ^{125}Te in the topological insulator Bi_2Te_3	163
<i>A. G. Badalyan, E. V. Edinach, Yu. A. Uspenskaya, N. G. Romanov, H. R. Asatryan, G. V. Mamin, S. B. Orlinskii, P. G. Baranov</i> Investigation of Ce^{3+} emitters in scintillating garnets by pulsed EPR and ENDOR	165
<i>Yu. V. Bogachev, A. V. Nikitina, A. A. Kostina, V. A. Sabitova, V. V. Pankov, V. O. Natarov, E. G. Petrova, D. A. Kotikov, T. G. Shutova</i> NMR proton's relaxation efficiency research in aqueous solutions of composite magnetic nanoparticles	168
<i>Alexander Dmitriev, Anton Vershovskii</i> Microscale vector magnetic field sensor based on NV centers in diamond for biology and medicine applications.....	171
<i>A. V. Drozdovskii, A. B. Ustinov, B. A. Kalinikos</i> Observation of spin-wave self-modulation instability in a perpendicularly magnetized magnonic crystal	175
<i>V. V. Frolov, V. I. Chizhik, P. A. Kupriyanov</i> Concomittent gradients in low fields	178
<i>Anna A. Hurshkainen, Stanislav B. Glybovski, Ingmar J. Voogt, Irina V. Melchakova, Pavel A. Belov, Cornelis A. T. van den Berg and Alexander J. E. Raaijmakers</i> On the decoupling of dipole transceive antennas for 7 Tesla with mushroom metasurface structures	180
<i>S. V. Ievleva, N. V. Luzhetckaia, K. V. Tyutyukin, V. V. Frolov</i> NMR-visualization of spatial distribution of the self-diffusion coefficient in ultra-low magnetic field.....	183

<i>Roman A. Illarionov, Marina A. Parr, Lyudmila Yu. Yakovleva, Yaroslav Yu. Marchenko, Boris P. Nikolaev and Maxim A. Shevtsov</i> Magnetic nanoparticles SPION-cmHsp70.1 for diagnosis of the orthotopic C6 glioma	186
<i>Aleksey A. Kazarinov, Andrei V. Komolkin</i> Research of ionic liquid in mixture of glycerol and water by algorithm for detecting clusters	189
<i>Aydar I. Khamzin, Radik R. Zaynullin</i> EPR study of $[\text{Co}^{2+} - \text{F}_{\text{int}}^-]$ associative defects formed in the $\text{BaF}_2:\text{Co}$ crystals: reasons of their stability	192
<i>Alexandra A. Kolodina, Eugeny A. Gusakov, Yury A. Sayapin, Anastasia A. Burtseva, Gennady S. Borodkin, Igor V. Dorogan, Valery V. Tkachev, Sergey M. Aldoshin, Vladimir I. Minkin</i> Structural studies of spirocyclic derivative of cyclohepta[e]pyrimido[1,6-a]indole-11-one by heteronuclear, two-dimensional, and dynamic NMR spectroscopy	194
<i>O. A. Kolosova, K. S. Usachev, V. V. Klochkov</i> Structural studies of the antimicrobial peptide protegrin-5 in membrane mimicking environment by high-resolution NMR spectroscopy.....	197
<i>A. V. Koroleva, A. M. Shikin, A. A. Rybkina, I. I. Klimovskikh, O. E. Tereshchenko, A. S. Bogomyakov, K. A. Kokh</i> Investigation of magnetically doped topological insulators and 2D Rashba system by EPR	200
<i>A. V. Koryukin, A. V. Kondrashov, A. B. Ustinov</i> Investigation of parametric excitation of the spin-wave pulses in magnetic films.....	203
<i>Maria Lukyanova, Boris Lukyanov, Ilya Ozhogin, Gennadiy Borodkin, Oksana Komissarova, Artem Pugachev, Vasiliy Malay, Anastasia Kozlenko and Eugene Mukhanov</i> Study of the novel cationic spiropyran structure by NMR spectroscopy	205
<i>D. S. Mazing, A. V. Nikiforova, A. S. Osinin, V. A. Moshnikov, Yu. V. Bogachev, S. M. Sukharzhevskii</i> Electron paramagnetic resonance investigations of ZnSe:Mn nanocrystals.....	207
<i>K. K. Metelkina, A. V. Kondrashov, A. B. Ustinov</i> Investigation of stationary and chaotic regimes of microwave signal generation in the spin-wave microwave photonic oscillator.....	210

<i>M. S. Muravyeva, E. A. Kluev, N. B. Koroleva, M. A. Katkova, I. V. Mukhina</i> Development of contrast complexes based on manganese for high field MRI	212
<i>Ilya Ozhogin, Eugene Mukhanov, Boris Lukyanov, Maria Lukyanova, Oksana Komissarova, Artem Pugachev, Yulia Schekina, Vasiliy Malay, Anastasia Kozlenko</i> The study of nonsymmetrical bis-spiropyrans of 1,3-benzoxazin-4-one series using two-dimensional ¹ H NMR spectroscopy	214
<i>Anastasia V. Penkova, Anna I. Kuzminova, Maria E. Dmitrenko</i> Structure analysis of mixed matrix membranes based on polysulfone and polyvinyl alcohol.....	217
<i>V. I. Petrov, R. K. Speranskiy, E. N. Popov</i> Non-magnetic heat controller in scheme of quantum magnetometer and the angular velocity sensor.....	218
<i>Ansar Safin, Alexey Ustinov</i> Investigation of the nonlinear oscillations in ferromagnetic films taking into account a nonlinear frequency shift and nonlinear damping.....	221
<i>Ali Shaban, Sevastyan Rabdano</i> The Matlab toolbox for fitting the two-dimensional NMR spectra	223
<i>Alexey V. Shestakov, Rushana M. Eremina, Tatiana P. Gavrilova, Ivan V. Yatsyk, Andrey A. Sukhanov, Yuri D. Zavartsev, Alexandr I. Zagumennyi, Sergey A. Kutovoi</i> Investigations of Y ₂ SiO ₅ :Nd ¹⁴³ by ESR method [☆]	224
<i>Alexey N. Shumsky, Tatyana M. Ilyasova, Peter V. Dubovskii</i> Cis/trans isomerism of peptide bonds: the case of cardiotoxins from cobra venom.....	227
<i>N. A. Shvets, A. S. Mazur, T. I. Vinogradova, V. D. Semenov, O. M. Osmolovskaya, M. G. Osmolovsky</i> Application of modified Fe ₃ O ₄ nanoparticles as MRI contrast agents: in vitro and in vivo study	230
<i>S. V. Sokratilin, Yu. S. Chernyshev, V. I. Chizhik, A. V. Ievlev, A. A. Shogina, M. V. Suyasova, V. P. Sedov, V. T. Lebedev</i> Study of the relaxation efficiency of Gd and Fe ions inside fullerenols and they complexes with PVP and Dextrine in aqueous solutions	232

<i>Anton Trofimenko, Sergei Zhurenko, Kirill Okhotnikov, Valeriy Verchenko, Andrei Shevelkov and Andrei Gippius</i> NQR spectroscopy of intermetallic compounds CrGa ₄ and MnGa ₄	235
<i>D. E. Troshkin, A. V. Kondrashov, M. A. Cherkasskii, A. B. Ustinov</i> Investigation of double-frequency excitation of spin-wave chaotic solitons in magnetic films	237
<i>Irina Ustinova, Andrey A. Nikitin, Alexey B. Ustinov</i> Logic gate based on microwave ferrite-ferroelectric interferometer ...	240
<i>E. V. Varzer, D. Ju. Podorozhkin, A. O. Antonenko, D. Ju. Nefedov, E. V. Charnaya, Ju. A. Kumzerov, A. V. Fokin</i> Atomic mobility in triple eutectic alloy Ga-In-Sn	243
<i>Aleksandr S. Voronin, Andrei V. Komolkin</i> Investigation of hydroxylation path of fullerenols C ₆₀ (OH) _n , n=2, 4, 6, 12, 40	244
<i>Denis A. Vinnik, Liubov S. Mashkovtseva, Dimitry A. Zherebtsov, Sandra Nemrava, Nikolay S. Perov, Anna S. Semisalova, Lyudmila I. Isaenko, Rainer Niewa</i> Ti-Substituted BaFe ₁₂ O ₁₉ Single Crystal Growth Magnetic Properties	247
<i>Sergei Zhurenko, Kirill Okhotnikov, Valentin Popov, Valeriy Verchenko, Andrei Shevelkov and Andrei Gippius</i> Crystal structure, ab-initio calculations and NQR spectroscopy of novel superconductor Mo ₈ Ga ₄₁	249
POEMS ABOUT SCHOOL	253
AUTHOR INDEX.....	257

Schedule of Spinus-2016

	20.11.16 Sunday	21.11.16 Monday	22.11.16 Tuesday	23.11.16 Wednesday	24.11.16 Thursday	25.11.16 Friday	26.11.16 Saturday
08:45 – 09:15		BREAKFAST				9:10-10:00 BREAKFAST	BREAKFAST
09:30 – 11:30		Opening Chizhik 40 Bunkov 50 GROUP PHOTO	Elyashberg 60 Zapasskii 60	Excursion in Kronstadt and MR Resource Center of SPbSU	Grunin 45 Bystrov 15 Sergeyev(1)60	Vasiliev 50 Dolgushev 20 Kupriyanov 20	Departure
11:30 – 12:00		COFFEE BREAK			COFFEE BREAK		
12:00 – 14:00		Michel 50 Pomogailo 20 Nikitina 20 Lähteranta 30	Kuznetsova 40 Kavokin 40 Tolstoy 40		Skrynnikov 40 Izmailov 20 Rabdano 20 Tyuryaeva 20 Rogacheva 20	Chudin 20 Surova 20 Safin 20 Nuzhina 20 Kondratyeva 20 Stanislavovas 20	
14:00 – 15:30		LUNCH					
15:30 – 17:00	Registration of participants	Shestakov 20 Dagys 20 Shubina 20 Babicheva 15 Baglasov 15	Charnaya 40 Mikushev 20 Uskov 20 POSTER SESSION	Frolov 30 Belov 15 Glybovski 15 Hurshkainen 15 Khomenko 15	Kaempff 30 Zgadzay 20 Wu 20 Mariasina 20	Neronov 30 Andreev 30 Matveev 30	
17:00 – 17:30		COFFEE BREAK					
17:30 – 19:00		Komolkin 45 Aleksandrov 45	POSTER SESSION	Simeschenko 15 Petrov 15 Drozdov 15 Fomina 15 Bogdan 15	Krestina 20 Diachenko 15 Luzhetckaia 15 Sergeyev(2)40	Awarding Closing	
19:00 – 20:00		DINNER				DINNER	
20.00	Welcome	Cultural and sporting activities			CONFERENCE DINNER		

Schedule

SUNDAY – 20 November 2016	
14:00 – 15:30	LUNCH
15:30 – 19:00	REGISTRATION OF PARTICIPANTS
19:00 –	WELCOME PARTY «EVENING IN KARELIA»

Monday – 21 November 2016	
08:45 – 09:15	BREAKFAST
09:30 – 09:40	OPENING
09:40 – 10:20	V. I. Chizhik [NMR] echoes of sad news... (in memory of Erwin Hahn)
10:20 – 11:10	Y. Bunkov Supermagnonics
11:10 – 11:30	GROUP PHOTO
11:30 – 12:00	COFFEE BREAK
12:00 – 12:50	D. Michel MAS NMR studies in combination with pulsed field gradient techniques
12:50 – 13:10	D. A. Pomogailo Determination of relative positions of paramagnetic probes in smectic liquid crystal by analysis of angular dependence of dipole-dipole broadening of EPR spectra
13:10 – 13:30	A.V. Nikitina Determination of T_1 And T_2 Relaxation Times from Stationary Saturation of Inhomogeneously Broadened EPR Lines
13:30 – 14:00	E. Lähderanta Double Master Program of St. Petersburg State University and the Lappeenranta University of Technology
14:00 – 15:30	LUNCH

15:30 – 15:50	A.V. Shestakov The oscillations in ESR spectra of $\text{Hg}_{0.76}\text{Cd}_{0.24}\text{Te:Ag}$
15:50 – 16:10	L. Dagys Advanced processing of CPMAS kinetics in Ammonium Dihydrogen Phosphate
16:10– 16:30	N. S. Shubina NMR study of AzoTAB and CTAB photoisomerization when interacting with the lipid bilayer
16:30– 16:45	E. S. Babicheva NMR study of Phthalocyanine solubility in Pluronic solutions
16:45– 17:00	E.D. Baglasov A Gradient Tolerance Measurements of Proton Overhauser
17:00 – 17:30	COFFEE BREAK
17:30 – 18:15	A. V. Komolkin Earth's magnetic field fluctuations and uncertainty of site finding using the geomagnetic map
18:15 – 19:00	E. B. Aleksandrov Natural Science and the Spirit World
19:00 – 20:00	DINNER
20:00 –	CULTURAL AND SPORTING ACTIVITIES

TUESDAY – 22 November 2016	
08:45 – 09:15	BREAKFAST
09:30 – 10:10	M.E. Elyashberg Computer methods for structure elucidation of new organic compounds from NMR spectra
10:10 – 10:50	V.S. Zapasskii Advances in Optical Detection of Magnetization
11:30 – 12:00	COFFEE BREAK
12:00 – 12:40	M. S. Kuznetsova Electron-nuclear spin dynamics in semiconductor QDs
12:40 – 13:20	K. Kavokin Deep cooling of the nuclear spin system in semiconductor structures
13:20 – 14:00	P.M. Tolstoy Cooperativity of Strong Hydrogen Bonds Studied by Liquid State NMR Spectroscopy
14:00 – 15:30	LUNCH
15:30 – 16:10	E.V. Charnaya NMR studies of nanocomposites with metal and alloy particles
16:10 – 16:30	V.M. Mikushev Influence of resonance saturation fields on impurity spin-lattice relaxation of nuclear spin systems in solids
16:30– 16:50	A.V. Uskov NMR investigations of atomic mobility of sodium embedded in porous glass with pore size 3.5 nm
16:50–17:00	POSTER SESSION
17:00 – 17:30	COFFEE BREAK
17:30 – 19:00	POSTER SESSION
19:00 – 20:00	DINNER
20:00 –	CULTURAL AND SPORTING ACTIVITIES

WEDNESDAY – 23 November 2016	
08:45 – 09:15	BREAKFAST
09:30 – 14:00	Excursion in Kronstadt and Resource Centers of SPbSU (Petergoff)
14:00 – 15:30	LUNCH
15:30 – 16:00	V.V. Frolov Visualization by NMR. Physical principles
16:00 – 16:15	P.A. Belov Application of metasurfaces for magnetic resonance imaging
16:15 – 16:30	S.B. Glybovski A novel design of dual-nuclei RF coils for preclinical MRI at 7 Tesla
16:30 – 16:45	A.A. Hurshkainen On the decoupling of dipole transeive antennas for 7 Tesla with mushroom metasurface structures
16:45 – 17:00	Yu.G. Khomenko Comparison of the magnetic resonance spectroscopy findings with cerebral glucose metabolism and immunological data in Parkinson's disease
17:00 – 17:30	COFFEE BREAK
17:30 – 17:45	P.I. Simeschenko Comparison of low-field and high-field MR for the diagnosis of brain metastases
17:45 – 18:00	I. N. Petrov Diffusion-Weighted MRI in Clinical Oncourology
18:00 – 18:15	A.A. Drozdov MRI imaging of CNS tuberculosis among patients with AIDS
18:15– 18:30	D.V. Fomina Calculation of Optimal Parameters for MRI of Fluorocarbons
18:30– 18:45	A.A. Bogdan Diagnostic value of in vivo 1H-MRS with short and long Echo Time for patients with Multiple Sclerosis
19:00 – 20:00	DINNER
20:00 –	CULTURAL AND SPORTING ACTIVITIES

THURSDAY – 24 November 2016	
08:45 – 09:15	BREAKFAST
09:30 – 10:15	L.Y. Grunin Time-Domain NMR Characterization of Solids Structure
10:15 – 10:30	S. Bystrov Molecular mobility and translational diffusion analysis of ionic liquid (methyl-octyl imidazolium chloride) in mixture “water – glycerol” by NMR
10:30 – 11:30	N. M. Sergeyev Water mythology
11:30 – 12:00	COFFEE BREAK
12:00 – 12:40	N. R. Skrynnikov Dynamics in protein crystal: insights from MD simulations
12:40 – 13:00	S.A. Izmailov Simple MD model of disulfide bond formation in peptides and proteins
13:00 – 13:20	S.O. Rabdano Second RNA-recognition motif RRM2 of TDP-43 protein: oxidative stress leads to structure destabilization, aggregation and increased susceptibility to proteolytic degradation
13:20 – 13:40	I.I. Tyuryaeva Mechanism of cytotoxicity of GO peptides and some other cysteine-containing peptides
13:40 – 14:00	O.N. Rogacheva Molecular dynamics studies and in silico mutational analysis as applied to dynamics in ubiquitin crystals
14:00 – 15:30	LUNCH
15:30 – 16:00	K. Kaempf Local and global dynamics of intrinsically disordered proteins: a case study of H4 histone tail
16:00 – 16:20	Yu. O. Zgadzay Structure investigation of bovine insulin by two-dimensional NMR spectroscopy
16:20 – 16:40	B. Wu Spectroscopic Analyses of Nanometer Scale Heterogeneity in PEG-based Polyacrylate Gel

16:40 - 17:00	S.S. Mariasina NMR Study of the Williams Syndrome Related Methyltransferase WBSCR27
17:00 - 17:30	COFFEE BREAK
17:30 - 17:50	M.S. Krestina ^1H NMR spectroscopy in vitro and in vivo of rat tissues and blood after alcohol impact
17:50 - 18:10	S.V. Diachenko Method measurement of temperature in conditions magnetic resonance
18:10 - 18:25	N.V. Luzhetckaia Magnetic resonance measurements of the fibrous plants diffusion tensor in ultra-low magnetic field
18:25 - 19:05	N. M. Sergeyev The NMR time scale
20:00 -	CONFERENCE DINNER

FRIDAY – 25 November 2016	
09:10 – 10:00	BREAKFAST
10:00 – 10:50	S. Vasiliev Spin Exchange and Magnons in Cold Atomic Hydrogen Gas
10:50 – 11:10	M. Dolgushev NMR Relaxation in Semiflexible Dendrimers
11:10 – 11:30	P. Kupriyanov High-Resolution NMR-device in the Earth magnetic field in a laboratory environment
11:30 – 12:00	COFFEE BREAK
12:00 – 12:20	A.V. Chudin Magnetic resonance spectroscopy as a tool for magnetometry of Earth magnetic field
12:20 – 12:40	L. Surova Impact of copper on water diffusion in sodium mordenite
12:40 – 13:00	T.R. Safin Evidence of coherent magnon state in easy-plane antiferromagnet and yttrium iron garnet films
13:00 – 13:20	D.S. Nuzhina Synthesis of ReF ₃ (Re= rare earth ions) nanoparticles for NMR research
13:20 – 13:40	E.I. Kondratyeva Vacuum heat treatment of wood and study of its properties by magnetic resonance and other methods
13:40 – 14:00	A.A. Stanislavovas Spin Kinetics of ³ He in Contact With Ordered Al ₂ O ₃ Aerogel
14:00 – 15:30	LUNCH
15:30 – 16:00	Yu. I. Neronov Determination of the spin-spin coupling in the molecule HD and possible manifestations of axion-like particles
16:00 – 16:30	N.K. Andreev How to receive more information in NMR using possibilities of pulse sequences
16:30 – 17:00	V.V. Matveev NMR Applications to Ionic Liquids: Current Status
17:00 – 17:30	COFFEE BREAK

17:30 - 18:00	AWARDING AND CLOSING
18:00 - 19:00	FREE TIME
19:00 - 20:00	DINNER

	SATURDAY - 26 November 2016
08:45 - 09:15	BREAKFAST
11:00 -	DEPARTURE



Spinus

Welcome to the School-Conference “Spinus” of Saint Petersburg State University

The Winter School-Conference “Magnetic resonance and its application” will be held at the St. Petersburg State University in the 13th time. It is organized in accordance with the subjects of researches and master's degree programs, which are developed and implemented in the educational process. In modern physics, the term “magnetic resonance” refers to a set of phenomena accompanied with the emission or absorption of electromagnetic waves of the radiofrequency diapason by quantum systems (nuclei, electrons, atoms, molecules, etc.). These phenomena, the physical nature of which is of independent interest, provided the basis of radiospectroscopic methods for studying the structure of matter and physico-chemical processes in it. They are also used for the creation of quantum generators, amplifiers, and magnetometers. For the development of ideas and applications of magnetic resonance six Nobel Prizes were awarded in the areas of physics, chemistry, biology, physiology and medicine (the latter was in 2003).

Primarily, magnetic resonance methods are:

- Nuclear Magnetic Resonance (NMR)
- Electron Paramagnetic Resonance (EPR)
- Nuclear Quadrupole Resonance (NQR)

These methods, being contactless, do not destroy an object under a study, that makes them unique and in demand not only in physics and chemistry, but also in medicine, geology, biology, archeology. Now, any medical center with high reputation has a magnetic resonance imaging (MRI). In Russia, NMR is used in oil well logging, laboratory analysis of the productivity of oil-bearing reservoirs, analysis of oil content and moisture of seeds; EPR technique is used for geological research, non-destructive control of precious stones; there are NQR applications for remote detection of solid explosives and narcotics. Magnetometry methods based on magnetic resonance are indispensable for carrying out archaeological researches.

The designation “school-conference” means that, on the one hand, the organizers will include in the program the lectures, which reflect the basics of magnetic resonance and current state of knowledge and experience in this field, and, on the other hand, as well as at any conference it is expected to discuss new results, obtained by young scientists, using magnetic resonance techniques. It should be emphasized that our school-conference aims not only to researchers specializing in the field of magnetic resonance, but also to representatives of other sciences, where these methods can be successfully applied.

Earlier the school organizers worked at the Department of quantum magnetic phenomena (KMYA) of the St. Petersburg State University, which was founded in 1993 on the initiative of Professor V.I. Chizhik on the basis of the laboratory, created in the 50s of the last century by F.I. Skripov at the Department of Radio Physics (the branch “Quantum Radiophysics”). On January 1, 2014, the Department of KMYA joined the united Department of nuclear-physics research methods (Head of the Department is Corresponding Member of the Russian Academy of Sciences, Professor Mikhail Kovalchuk). The collective KMYA has a number of priority works in the field of nuclear magnetic resonance. One of the most significant achievements is the first in the world implementation (in 1958) of the Fourier transform of a free induction signal in order to obtain a NMR spectrum. Concurrently with the research activity, the staff of the department are actively involved in the development of practical applications of magnetic resonance. The department graduates work not only in Russia and the CIS, but also in Sweden, USA, New Zealand, England, Germany, France,

Italy, occupying positions from a highly advanced operator of radiospectrometers to professor.

The main research areas developing in the Department of quantum magnetic phenomena:

- Nuclear magnetic relaxation in liquids;
- Nuclear magnetic resonance in solids, including magnetically ordered materials;
- NMR in liquid crystals;
- NMR in heterogeneous systems;
- MRI in weak magnetic fields;
- Electron paramagnetic resonance;
- Nuclear magnetic resonance in the magnetic field of the Earth;
- The quantum magnetometry in archeology.

It is evident from the above that the scope of our research interests is quite wide. We always open for the collaboration with researchers from various science fields.

Our team has published a series of monographs, textbooks and training manuals on Magnetic Resonance. For example:

1. Vladimir I. Chizhik, Yuri S. Chernyshev, Alexey V. Donets, Viatcheslav Frolov, Andrei Komolkin, Marina G. Shelyapina. *Magnetic Resonance and Its Applications*. 2014, Springer-Verlag. 782 pp. (Now more than 17 000 downloads)
2. Квантовая радиофизика: магнитный резонанс и его приложения. Учеб. пособие. 2-е изд., перераб. Под ред. В. И. Чижики. – СПб.: Изд-во С.-Петербур. ун-та, 2009. 700 с.
3. В. И. Чижик. Ядерная магнитная релаксация. Учеб. пособие. 3-е изд. – СПб.: Изд-во С.-Петербур. ун-та, 2004. 388 с.
4. Практикум по магнитному резонансу. Учебное пособие. Под ред. В. И. Чижики. – СПб.: Изд-во С.-Петербур. ун-та, 2003. 184 с.

*The Organizing committee
of the 13th Winter School Youth conference
“Magnetic resonance and its applications” Spinus-2016*

Lectures

Natural Science and the Spirit World

E. B. Aleksandrov

Ioffe Institute, 26 Politekhnicheskaya, St. Petersburg, 194021, Russian Federation

In this talk, I will review the evolution of “esoteric” concepts, penetrating again and again into public consciousness, into politics, and even into scientific community of Russia. Detrimental role of mass media in dissemination of esoteric myths will be emphasized. Absurdity of the widespread myths about reality of the “esoteric” phenomena like telepathy, clairvoyance, telekinesis, and so on, will be justified. Their existence, on the one hand, has never been any reliably confirmed (better to say – has been many times reliably refuted) and, on the other, is incompatible with the totality of all accumulated rational knowledge. The myths about “esoteric” phenomena are harmful not only because of their antiscientific essence, but also because they are exploited for malicious purposes in organized or non-organized criminal groups [1].

Представлен обзор истории развития «эзотерических» воззрений, постоянно проникающих в общественное сознание, политику и даже в научное сообщество России за последние три десятилетия. Отмечена вредоносная роль СМИ в распространении «эзотерических» мифов. Обосновывается утверждение о полной вздорности широко распространенных мифов о существовании «эзотерических» явлений, таких как телепатия, ясновидение, телекинез и т.п. Их существование, во-первых, никогда сколько-нибудь надёжно не подтверждалось – напротив того, многократно надёжно опровергалось, а во-вторых, несовместимо со всей совокупностью накопленного рационального знания. Мифы об «эзотерических» явлениях весьма вредны не только своей антинаучной сущностью, но и тем обстоятельством, что они эксплуатируются в криминальных целях в организованных и неорганизованных преступных сообществах.

References

1. Е. Б. Александров, «Естествознание в мире духов», бюллетень «В защиту науки» №16, стр. 14-29, 2015, Москва.

How to receive more information in NMR using possibilities of pulse sequences

N. K. Andreev

*Faculty of electricity and electronics, Kazan State Power Engineering University
Krasnoselskaya, 51, Kazan, 420066, Russian Federation*

E-mail: ngeikandreev@gmail.com

Introduction

The principles of use of the instrument sensitivity theory (or method of measurement) to receive more information in a pulsed NMR experiment.

What is the problem

Currently, the pulsed NMR method is widely used in physics, chemistry, biology and medical imaging, as well as to control technological processes [1-2]. Pulsed NMR method provides a maximum flux of information. However, experimental results do not always meet researchers. So, not all possibilities of the method are still used. By carefully design of an experiment the researcher can try to get more information using all the possibilities of an instrument and regulating parameters of pulse sequences. First, in pulsed methods, it is necessary to take into account the dependence of a measured amplitude of a signal on the relaxation times, physical-chemical processes occurring in the object of measurement, chemical structure and composition of substances and their dependencies on temperature and concentration of impurities. Let us explain the statement by an example. Sometimes during the growth of crystals with the same chemical formula two modifications of a crystal, differing by the structure of the molecules and their packing in the crystal cell can grow at the same time. More complicated is the case where non-equivalent molecules are within the same cell of the crystal. Such a case was described in our paper [1]. In the study of spin-lattice relaxation in the crystal sample of hydrochloride monohydrate of L-valine was found that the study of NMR in polycrystals is not enough to ascertain the presence of nonequivalent molecules. However, measurements of the temperature and orientation dependences of the spin-lattice relaxation time T_1 revealed the presence of these non-equivalent molecules by comparison with theoretically predicted results calculated according to X-analysis of the structure of this amino acid. The relaxation times T_1 at high-temperature minimum stipulated by the reorientation of amino groups NH_3^+ - around a fixed axis in one of the nonequivalent molecules were two times higher than the calculated values. X-ray diffraction analysis revealed the presence of nonequivalent molecules. But spin diffusion between protons of the two neighboring molecules in the cell have been effective enough to establish a uniform spin temperature. The other protons of the molecule move to the equilibrium using the fast relaxing protons of the amino group of the first molecule. As a result, the whole number of protons of the united spin system is doubled. Then the relaxation time is doubled. The more accurate calculation of the orientation dependence of the relaxation time further confirmed this model.

Taking into account the sensitivity of a measured NMR quantity to physical-chemical characteristics of a sample

If a physical quantity S under study (e.g. signal amplitude) depends on several quantities such as T_1, T_2, T, D, ν , the sensitivity is calculated by the formula:

$$dS = \frac{dS}{dT_1} dT_1 + \frac{dS}{dT_2} dT_2 + \frac{dS}{dT} dT + \frac{dS}{dD} dD + \frac{dS}{d\nu} d\nu, \quad (1)$$

where T_1 , T_2 are the spin-lattice and spin-spin relaxation times, T is a measurement temperature, D is a diffusion coefficient, v is a flow velocity. The derivatives of these values are values of the desired sensitivities of the value under study to them. Very often, these parameters and sensitivities of signal amplitude are temperature dependent. In this case the terms in Eq. (1) take the form:

$$dS = \frac{dS}{dT_1} \frac{dT_1}{dT} dT + \frac{dS}{dT_2} \frac{dT_2}{dT} dT + \frac{dS}{dT} dT + \frac{dS}{dD} \frac{dD}{dT} dT + \frac{dS}{dv} \frac{dv}{dT} dT . \quad (2)$$

Therefore, it is necessary to measure the dependence of parameters of a substance on temperature, to calculate their sensitivity at the measurement temperature, and then to consider their contributions into the measured quantity. Similarly, one must make measurements and analyze contributions to a measured physical quantity on the concentration of components of a substance and its impurities. Interpretation of the results of the experiment will depend on how accurate the major and minor measurements were performed. This is one of reasons in MRI that often it is impossible to diagnose a disease using only magnetic resonance images if there are no differences between the image of an organ in a normal state and damaged one. However, the measurement of relaxation times, local spectra of tissues of the human body helps to make the diagnosis, if we have already studied the regularities of their changes in case of pathologies.

The transfer function of a pulse sequence

To find out what information still lies in the data of NMR measurements, helps the analysis of the Hamiltonians of interactions of a spin system and transfer functions of pulse sequences in NMR techniques, again, in context of the sensitivity of pulse sequences to the relaxation times, chemical shifts, internal and cross-interactions of nuclei spins to molecular movements. This analysis is widely used in all the physical methods of measurement, and, consequently, in the instrument design. The concept of a transfer function means the dependence of a complex amplitude of the signal or measured parameter on characteristic frequencies (time constants): a resonant frequency of nuclei, velocities of molecular motions, frequencies of interactions between the spins under study.

Here the pulse NMR method gives us a wide set of pulse sequences with the possibility of choosing intrinsic interactions (dipole-dipole, scalar, etc.), through which a sensitivity to certain physical and chemical properties can be revealed (or suppressed). This sensitivity will be maximal when the corresponding time intervals in a chosen pulse sequence are equal to the characteristic time constants of interactions.

Let us consider as an example the results of the study of the spin-lattice relaxation $T_{1\rho}$ in a rotating coordinate system in the solid sample [1]. This dependence (transfer function) can be described by:

$$T_{1\rho} = C\tau_c \left[\frac{5}{1+(\omega_0\tau_c)^2} + \frac{2}{1+(2\omega_0\tau_c)^2} + \frac{3}{1+(2\omega_1\tau_c)^2} \right], \quad (3)$$

where ω_0 and ω_1 are the resonant frequency of nuclei and their frequency in the rotating frame, τ_c is the correlation time of molecular motion, C is a constant dependent on the distance between the spins, describing the strength of the dipole-dipole interaction between spins. Measurements in the rotating frame were produced by the registration a signal amplitude after the pulse sequence $(\pi/2)_0 \tau_{90}$. Here τ is the length of a spin-locking pulse with a sufficiently high and regulated amplitude. Since the sample is solid, the requirements for technical characteristics of the pulses, and, through them, to equipment are severe enough: the duration of the 90° pulse needs to be of the order of $1 \mu\text{s}$, the amplitude of the RF field

needs to reach tens of gauss, and adjustable length of the latter must be of the order of several milliseconds. Temperature of the sample must vary in the range of -200 to $+200^{\circ}\text{C}$.

Hardware requirements for NMR spectrometers with a sample size of 1 cm differ dramatically from those of MR-imaging instruments with a sample size of 0.5 m. Biological tissues contain a lot of water, a human body contains fluid flows and periodic motions of organs. To improve the sensitivity, MRI uses high magnetic fields and frequencies. The need for the magnetic encoding puts stringent requirements on the system for the generation pulsed magnetic field gradients.

The geometry of the experiment

During the experiment, especially in MRI, it is necessary to think carefully about the geometry of the experiment. For example, if you want to exclude the influence of blood flow, the corresponding blood vessel should lie within the plane of the slice (image), and the pulse sequence must not be sensitive to fluid flow. At the time period of obtaining the image of the slice, an operator has to exclude any changes of experimental conditions. Images of the beating heart have to be received by the synchronization with phases of the heartbeat and choosing orientation of the slice.

References

1. Andreev N.K. Methods and devices for low-frequency relaxation NMR imaging: Scientific publication. (Metody i pribory nizkochastotnoy relaksatsionnoy YaMR-introskopii). Kazan: Kazan State Power Engineering University Press. 2003 (In Russian).
2. Andreev N.K. NMR flow measurement in modern technology: Scientific publication. (YaMR-raskhodomeria v sovremennykh tekhnologiakh). Kazan: Kazan State Power Engineering University Press. 2004 (In Russian).

Supermagnonics

Yuriy Bunkov

Institute Neel, Grenoble, France

Kazan Federal University, Kazan, Russia

E-mail: Yury.bunkov@neel.cnrs.fr

It is well known that deviations of spins from the magnetic order in magnetic materials (ferromagnets, antiferromagnets and ferrites) have a collective character and are described in terms of spin waves (magnons). Magnons are quasiparticles which represent very useful and universal theoretical concept and a tool to describe various dynamic and thermodynamic processes in magnets. For example, analyzing thermodynamics of magnon gas, we obtain complete picture of the thermodynamic properties of the magnetic system. Since magnons have a magnetic moment, one can create extra magnons by the external pumping, alternating magnetic field, and increase the disorder in the magnetic system. However, in certain conditions, the increase of magnons density can lead to entirely new states called magnon condensates, i.e. macroscopic number of magnons in coherent quantum states (see, [1]) These macroscopic quantum states significantly change the properties of the magnetic system, its dynamics and transport. For example, a single-particle long-range coherency occurs in a quasi-equilibrium as the phenomenon of Bose-Einstein condensation of magnons on the bottom of their spectrum. And it leads to the phenomenon of spin superfluidity.

The spin superfluidity is an extremely interesting and promising phenomenon both for fundamental and applied studies. The main feature of spin superfluidity is the dissipationless transfer of magnetization in magnetic materials for long distances. The real superfluidity means a long distance correlation of non-diagonal terms of the matrix of density, which does not, in general, take place in magnetically ordered materials. The short distance correlation of non-diagonal terms appears due to spin waves or magnons.

For the first time, spin superfluidity was demonstrated in 1984 [2] in the antiferromagnetic liquid crystal of superfluid ^3He where the magnetic part of energy is not directly related to mass superfluidity. In subsequent works there were observed and interpreted a bunch of quantum phenomena, related to the spin superfluidity and so-called Homogeneously Precession Domain. Distinct from the conventional Larmor precession of nuclear spins, the phase coherent precession of magnetization in $^3\text{He-B}$ has all the properties of the coherent Bose condensate of magnons [3]. This is a state with the coherent precession of magnetization described by a single wave function. The phase of precession appears spontaneously after a condensation of non-coherent magnons and radiates a coherent signal of induction even in a very inhomogeneous magnetic field. This spontaneously emerging steady state preserves the phase coherence across the whole sample and exhibits all the superfluid properties which follow from the off-diagonal long-range order for magnons. The BEC state can radiate the signal 100 – 10 000 longer than expected from the inhomogeneity of the magnetic field. In other words, the BEC state very effectively suppresses the local field inhomogeneity.

The particular interest is related to the formation of magnon BEC in superfluid $^3\text{He-A}$, a typical two sublattices antiferromagnet. At bulk conditions the formation of BEC is not possible due to attractive interaction between magnons. The Suhl instability of homogeneous precession was observed. Indeed, in the aerogel, stressed along the magnetic field, the magnons' interaction changes to repulsive. Consequently, the magnon BEC forms and corresponding long living induction signal is observed [4].

The Electronics is the field of science which describes the non-linear behavior of electric current. It has been developed for a century. Later there has been observed the

phenomenon of supercurrent – the coherent transport of electrons without friction. This effect forms the basis of new types of electronics – Superelectronics. The main element of Superelectronics is the Josephson connection – the interference between the coherent wave function of electrons on two sides of a weak connection. This effect leads to a construction of SQUID, the supersensitive device which can measure a quant of magnetic field. The circuits with SQUID may be used as an element of a quantum memory.

Later the new types of non-linear phenomena have been developed – Spintronics and Magnonics. In the first case the magnetic moment of electrons is taken into account. Indeed, the Superspintronics does not exist because the electron Cooper pairs has a zero magnetic moment. The Magnonics case refers to information transport and processing by spin waves. A magnon current has advantages as compared to a conventional spin-polarized electron current. It does not involve the motion of electrons and, thus, it is free of the Joule heat dissipation. In low-damping magnetic dielectrics (for example, yttrium-iron-garnet, YIG) magnons can propagate over millimeter distances whereas an electron-carried spin current is limited by the spin diffusing length, which does not exceed one micrometers.

Indeed the coherent magnon transport was observed about 30 years ago in Kapitza Institute. In different with a simple magnonics, the magnetization transport by Supermagnonics described by a coherent state of magnons – the magnons Bose Condensate. Its gradient leads to a Spin Supercurrent. There was observed the Josephson Effect, the main nonlinear effect of Supermagnonics. The Supermagnonics was observed in superfluid $^3\text{He-B}$. Indeed, the magnetic properties of superfluid $^3\text{He-B}$ are described as a 3 sublattices antiferromagnetic. The other examples, where the magnons BEC was observed, are superfluid $^3\text{He-A}$, Nuclear-electron precession in antiferromagnets (MnCO_3 , CsMnF_3) [5] and yttrium-iron-garnet, YIG. In the last case the Supermagnonics and Josephson Effect may be observed at room temperature. These phenomena are under investigations. We are working on the problem of Supermagnonics in YIG and have first very promising results.

This work was financially supported by the Russian Science Foundation (grant RSF 16-12-10359).

References

1. Yu. M. Bunkov, G. E. Volovik, J. Phys.: Condens. Matter **22** 164210 (2010).
2. A. S. Borovik-Romanov, Yu. M. Bunkov, V. V. Dmitriev, Yu. M. Mukharskiy, JETP Lett., **40**, 1033 (1984).
3. S. Autti, Yu. M. Bunkov, V. B. Eltsov, et al. Phys. Rev. Lett. **108**, 145303 (2012).
4. A.S. Borovik-Romanov, Yu.M. Bunkov, V.V. Dmitriev, Yu.M. Mukharskiy, JETP Letters v.39, p.469, (1984); *P. Hunger, Y. M. Bunkov, E. Collin and H. Godfrin*, J. of Low Temp. Phys **158**, 129–134 (2010).
5. Yu.M. Bunkov, Physics Uspekhi, **53**, 848 (2010); Yu. M. Bunkov, et al., Phys. Rev. Lett., **108**, 177002 (2012).

NMR studies of nanocomposites with metal and alloy particles

*E. V. Charnaya¹, A. O. Antonenko¹, D. Yu. Nefedov¹, D. Yu. Podorozhkin¹, A. V. Uskov¹,
J. Haase², D. Michel², Yu. A. Kumzerov³*

¹*St. Petersburg State University, St. Petersburg, 198504 Russia*

²*Faculty of Physics and Geosciences, Leipzig University, 04103 Germany*

³*A. F. Ioffe Physico-technical Institute RAS, St. Petersburg, 194021 Russia*

E-mail: charnaya@mail.ru

Introduction

We discuss the results of recent NMR studies of properties of metal and metallic alloy nanoparticles embedded into silica mesoporous matrices. The impact of nanoconfinement on the formation of various crystalline phases, changes in atomic mobility and electron-nuclear coupling which manifested in the alterations of the Knight shift, and on nanoparticle melting processes was revealed.

Samples and experiment

The nanocomposites under study were porous glasses and opal matrices with small particles of fusible metals and metallic alloys embedded into pores. Measurements were carried out using Bruker NMR pulse spectrometers at magnetic fields of 9.4, 11.75, and 17.6 T in a large temperature range.

Results

Crystalline structure

Crystalline structure can be modified under nanoconfinement. It was shown that different metastable gallium phases became stable within nanopores. The polymorph phase transition in sodium nanoparticles occurred at higher temperatures compared to bulk which was evidenced by the emergence of an additional NMR line from solid sodium.

Atomic mobility

Self-diffusion in liquid confined metals and alloys slows down noticeably which leads to the remarkable increase of the quadrupole contribution to nuclear spin-lattice relaxation and to reduction of the total relaxation time. While the diffusion processes in solid crystalline nanoparticles of metals and alloys accelerate that also leads to a decrease in the spin-lattice relaxation time. In particular, for confined crystalline nanoparticles of sodium and sodium-potassium alloy the quadrupole contribution to relaxation became comparable to the dipole contribution.

Knight shift

The Knight shift for liquid and solid nanoparticles of metals and alloys near the melting temperature decreases gradually with decreasing the pore size. The temperature dependence of the Knight shift also changes under nanoconfinement up to the change of the temperature coefficient sign.

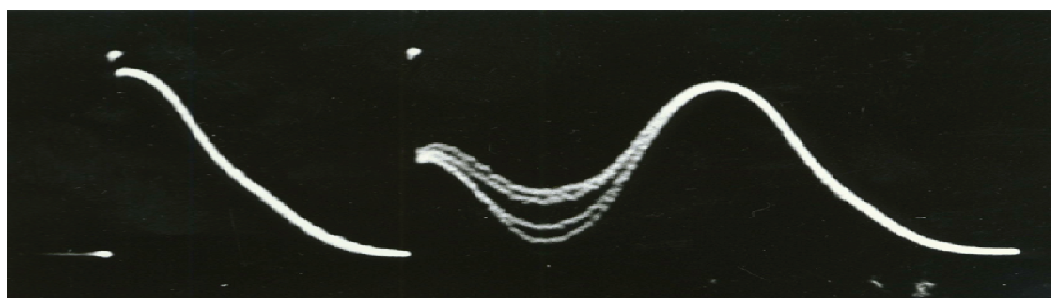
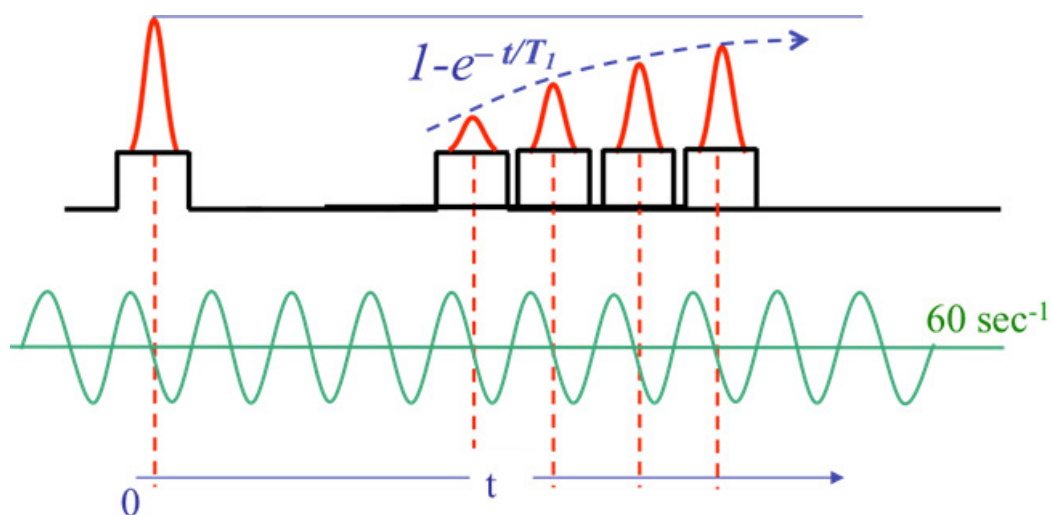
Melting and freezing transition

Melting of nanoparticles within pore can lead to the formation of an intermediate state which could exist in a large temperature interval as, for instance, melting of nanoparticles of the potassium-sodium alloy.

[NMR] echoes of sad news... (in memory of Erwin Hahn)*V. I. Chizhik**Sankt Petersburg State University, St. Petersburg, Russia**E-mail: v.chizhik@spbu.ru**http://nmr.phys.spbu.ru/*

Erwin Louis Hahn (June 9, 1921 – September 20, 2016) was an American physicist, best known for his work on nuclear magnetic resonance.

In 1950 E. L. Hahn discovered the spin echo.



Preclinical Magnetic Resonance Imaging

U. Eichhoff

*Bruker Biospin GmbH (retired), D76275 Ettlingen, Germany
E-mail: barbara.uwe@t-online.de*

Introduction

Magnetic Resonance since more than 60 years is the most powerful method for structural investigation physics, chemistry, biology and has been extended to medical applications. Today NMR together with X-ray-diffraction is the most powerful method for structure determination of proteins. Magnetic Resonance Imaging (MRI) added another dimension to NMR and is now well established as the most informative medical imaging method. MRI is *the* ideal method for preclinical imaging, the non-invasive biomedical and pharmaceutical research on animals [1]. Pathological processes can be followed over a long time period on one single animal. This gives much more reliable results and saves laboratory animals and costs.

Instrumentation

Many universities and research institutions already use analytical NMR spectrometers for biochemical and biomedical investigations on bodyfluids, cell suspensions and tissues. Adding an imaging accessory (gradient unit and probehead) they can extend their research to investigations in living animals. Today special instruments with horizontal magnet bores offer excellent capabilities for developing new imaging methods and strategies. The adaption to (much more expensive) whole body medical imagers is straightforward. In fact most of the current imaging methods have been developed on such small bore systems. Mice can be investigated in a normal wide bore magnet (89 mm) and rats in superwide bore magnets (150 mm). For larger animals systems with horizontal magnets like the permanent magnet system ICON 1T and the superconducting BioSpec and Pharmascan must be used, covering a field range from 1.0 to 17.6 Tesla. The horizontal magnets are much more convenient for anesthesia and handling of the animals. They have been carefully designed for maximal field homogeneity and stability and excellent cryogenic performance. Active shielding reduces the strayfield to a minimum and makes siting easier. Cold transportation results in short installation times

In vivo MRI and MRS

MRI allows to obtain detailed morphological information even in small animals due to its high spatial resolution ($<100\mu\text{m}$) almost comparable to optical microscopy. MR images of the living animal are three-dimensional and any cross section under any angle can be reconstructed. For optical microscopy the animal must be sacrificed to obtain a microtome preparation for each single section.

Fast imaging methods [6-9] extended the temporal resolution into the msec-range allow to follow heart motion in real time and to perform functional imaging in the brain using the fastest available imaging sequences. Blood vessels can be imaged selectively without and with contrast agents and the blood flow parameters can be studied. Additionally chemical information can be obtained with localized spectroscopy and spectroscopic imaging. Endogenous tissue metabolites can be identified at millimolar concentrations and metabolic processes can be monitored.

Organ Function

The excellent time resolution of MRI in the millisecond range allows real time cardiac imaging in animals like mice and rats with an almost 10 times higher heartbeat rate than in

humans. Cardiac wall motion can be displayed in real time and infarcted regions can be recognized. The regeneration of partially resected organs can be followed their volume increase and the function of transplanted kidneys can be evaluated from the transition time of a contrast agent.

Oncology

Already the first publications on MRI concentrated on the ability to distinguish various types of neoplastic tissue [2]. Human tumors can be injected into laboratory animals and the tumor growth can be followed. Preclinical applications of MRI in oncology focus on the assessment of tumor volume, perfusion, neovascularization, metabolism and the influence of antitumor drugs on all these parameters.

Transgenic animals and disease models

The latest developments in molecular biology and genome research allow to exclude (knockout) or to modify the genome of animals and to create transgenic animals, which can serve as excellent models for various human diseases. Molecular imaging and rapid phenotyping of transgenic animals have significantly extended the role of MRI/MRS in pharmacology. For instance mice can be genetically modified to overexpress the corticotropin-releasing factor (CRF). CRF is a neurotransmitter and core mediator of endocrine behavioural responses to stress. The mouse model is allocated to psychiatric disorders in humans. When compared to the wild type the adrenals were significantly enlarged and the thymus volume reduced at the same time. This is also true for humans. These in vivo data of the adrenals correlated perfectly with the post mortem weight of the organs.

Diffusion Tensor Imaging (DTI) and Structural Connectivity

If in diffusion weighted imaging direct the diffusion gradient is directed in three perpendicular directions, slightly different images are obtained, because diffusion is observed along the gradient direction [3]. Mathematically the diffusion must be described as a tensor with three main axes with the main axis. The diffusion information can be displayed in different ways. In brain the white matter shows a high anisotropy, because diffusion is almost free along the fiber direction and limited perpendicular to it. In a very simplified view we can follow the arrows of the diffusion direction and obtain a selective image of the neuronal fibers connecting various brain areas (MR tractography). Since fibers may be kissing and crossing, this is a very complicated mathematical procedure. The resolution may be well in the submillimeter range.

Functional MRI

MRI offers the unique possibility to map brain function without injecting a contrast agent. In activated brain areas oxygen is consumed and therefore blood diamagnetic oxyhemoglobin is converted into paramagnetic deoxyhemoglobin leading to a signal decrease. This effect is immediately overcompensated by supply of oxygenated blood leading to a final increase in oxyhemoglobin resulting in an increase of signal intensity [4, 5]. In rats electric stimulation of the forepaw shows the activated areas in the motor cortex, photic stimulation allows investigation of the visual cortex. Epilepsy has been studied in a rat model by injecting pentylentetrazol (PTZ) and observing brain activation changes between the normal state, pre-seizure putative kindling and fully blown seizure and the effect of treatment.

Resting state fMRI (rs-fMRI)

Functional MRI does not need necessarily a stimulus. If MR images are recorded extremely fast (>500msec) time-dependent fluctuations of the signal intensity can be observed. If these fluctuations are analyzed for frequency, phase and amplitude in all voxels, a synchrony of these variations can be observed in certain brain areas, even if these areas far

apart from each other. In contrary to the *structural connectivity revealed by DTI* this connectivity is called *functional connectivity* [6, 7]. There are two ways of statistical analysis. Independent Component Analysis **ICA** without any assumptions correlates the signal time course in all voxels and finds areas with high synchrony [8]. **Seed based analysis** selects one area and compares its signal time course with all other to find selectively the connectivity to the selected area [9]. Since the evaluation of the very small fluctuations of the signals needs extreme speed and sensitivity, high field MRI systems with extremely strong and fast gradients are a prerequisite.

Rs-fMRI in humans has established three most important brain networks (fig. 1). *Central Executive Network (CEN)* is active during task performance. *Saliency Network (SN)* plays a crucial role in identifying the most biologically and cognitively relevant events for adaptively guiding attention and behavior. *Default Mode Network (DMN)* is active during rest than during task-performance. It is typically deactivated during stimulus-driven cognitive processing [10, 11].

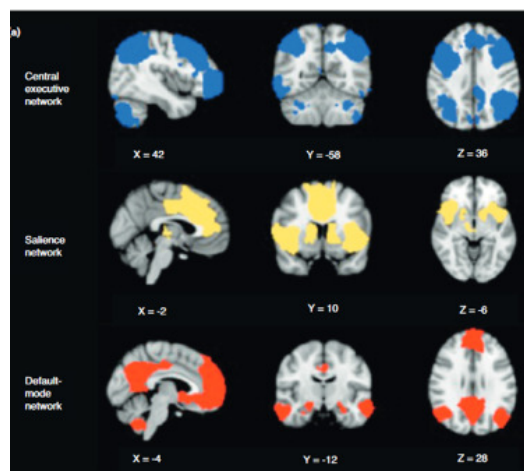


Figure 1. The three most important networks in human brain, established by ICA from rs-fMRI central executive (blue), saliency (yellow) and default mode (red)

The interplay of these three networks guide reaction to external stimuli, creation of emotions and activity based on both and are therefore most important for understanding of mental diseases [12-14].

References

1. M.Rudin, N.Beckmann, R.Porszasz, T.Reese, D.Bochelen, A.Sauter. NMR Biomed. 12(1999)69
2. R. Damadian. Science 171(1971)1151
3. E.A.H. von dem Hagen, R.M.Henkelman. Mag.Reson.Med. 48(2002)454
4. S.Ogawa, T.M.Lee, A.S.Nayak, P.Glynn. Magn.Reson.Med. 14(1990)68
5. Ch.Preibisch, A.Haase. J.Mag.Reson. 140(1999)162
6. B.B. Biswal, [Review]. Neuroimage, 62(2), p. 938(2012)
7. B.B. Biswal. Biological Psychiatry, 69(9), 200(2011)
8. C.F. Beckmann, M.de Luca, J.T. Devlin, S.M.Smith, (2005). Philosophical Transactions of the Royal Society B-Biological Sciences, 360(1457), (2005)
9. D.S. Margulis, A.M.C. Kelly, L.Q. Uddin, B.B. Biswal, F.X. Castellanos, M.P. Milham. Neuroimage, 37(2), 579-588.(2007)
10. M.D.Fox, A.Z. Snyder, J.L.Vincent, M. Corbetta, D.C.Van Essen, M.E. Raichle. Proceeding National Academy of Sciences of the United States of America, 102 (27), 9673 (2005)
11. R.L. Buckner. Neuroimage, 62(2), 1137-1145 (2012)
12. V. Menon, Q. Uddin. Brain Struct.Function DOI 10.1007/s00429-010-0262-0 (2010)
13. Lena Palanipiyappan, P,F.Little. J.Psychiatry Neurosci.1: 17-27(2012)
14. V. Menon. Trends in cognitive Sciences (2011) 1-14

Computer methods for structure elucidation of *new organic compounds* from NMR spectra

M. E. Elyashberg

Moscow Department of Advanced Chemistry Development (ACD/Labs)

117513, Moscow, 6, Akademika Bakuleva street

E-mail: elyas@acdlabs.ru

<http://www.acdlabs.com>

Introduction

The structure elucidation of new organic compounds is one of the most important tasks of the organic chemistry and molecular spectroscopy. The process of structure elucidation reduces to the structural hypotheses forming and their subsequent verification. Each structural hypothesis is based on the complex logical-combinatorial processing of spectral data taking into account the knowledge about the interconnection between spectra and structure. That is the reason why, in the second half of the 60-ies of the last century, simultaneously and independently from each other the four groups of scientists (in USA, Japan and USSR) posed an ambitious task: to develop the computer methods that would allow mimicking spectroscopist's reasoning during determining structures of new organic compounds. The statement of this problem has served as a powerful stimulus for the development of the theory and methods of artificial intelligence. During the last 50 years a long way has been passed from formulation of the general principles to the development of commercial expert systems (ES) which allow structure elucidation of newly synthesized or isolated from natural objects compounds using combination of one-dimensional and two-dimensional NMR spectra.

Methodology

The analysis of the structure elucidation procedure from NMR spectra shows [1] that it is based on the solution of two inverse problems: 1) detection, if possible, of all spin couplings between nuclei in the molecule; 2) construction of all structures satisfying the 1D NMR spectra and detected couplings. The inverse problems usually have ambiguous solutions. A unique solution is found by the introducing additional constraints. It is very important to take this into account for proper interpretation of structural problem solutions.

Another important element of the structure elucidation philosophy is the logic on which the mimicking of the expert's reasoning process is based. It was found [2] that all suppositions for the structure inferring can be regarded as a set of "axioms" (assumptions that we consider true). On the base of these "axioms", an axiomatic theory that is applicable to each specific task is created.

All axioms can be divided into three groups: 1) The axioms reflecting characteristic spectral features in NMR, IR, and other spectra; 2) The axioms of two-dimensional NMR spectroscopy; 3) The axioms used for assembling structures from atoms and fragments (structure generation). The structure elucidation of an unknown compound boils down to inferring all logical corollaries from the set of axioms and hypotheses suggested as a result of experimental spectra and a priory information analysis. In doing so it is assumed that all of the axioms are true and consistent. However, the analysis of information extracted from two-dimensional NMR spectra shows [2] that, in general, it is very often *fuzzy*, *incomplete*, *contradictory* and *uncertain*. Obviously, it is very difficult for a human expert to consider all axioms *explicitly*, and derive all logically consistent structural hypothesis based on the complete set of axioms. This is often caused a wrong solution to the problem. An expert system will be able to adequately mimic the process of structural formulae inference from the spectroscopic data only if the specified properties of the initial information and features of

inverse problems will be considered during its elaboration. ACD/Structure Elucidator [3, 4] is an example of such a system.

Expert System ACD/Structure Elucidator

The system database includes *factual* and *axiomatic* knowledge. The system can also use information reflecting the knowledge and experience of the researcher. The axiomatic knowledge is the information about the characteristic features in the NMR spectra. The factual knowledge includes the libraries containing hundreds of thousands of structural formulae of organic compounds supplied with their ^1H and ^{13}C NMR spectra; the structure databases with the chemical shifts of the nuclei ^{15}N , ^{19}F , ^{31}P ; as well as the library of fragments (> 1.7 million) with their ^1H and ^{13}C sub-spectra. The friendly interface provides a dialog mode of user interaction. The program operates as a machine of logical inference providing all structures that are logical corollaries from experimental data and knowledge of the system.

The program uses data obtained from one-dimensional and two-dimensional NMR experiments. A typical set of input experimental data includes the molecular formula, determined from the high-resolution MS, and the following spectra: ^{13}C , ^1H , HSQC (HMQC), COSY and HMBC. The program analyzes the spectra and builds a molecular connectivity diagram (MCD), on which all connectivities between skeleton atoms are drawn. The atoms and XH_n groups are shown with their chemical shifts and properties (valence, hybridization, etc.). Obviously, the use of MCD makes the system of axioms observable. By default, it is assumed that COSY-connectivities have a length equal to one C-C bond ($^{2-3}\text{J}_{\text{HH}}$); and the length of the HMBC connectivities varies from 1 to 2 bonds ($^{2-3}\text{J}_{\text{CH}}$). Such lengths of connectivities we will call *standard*. In the next step, the program carries out logical analysis of MCD to check data for contradictions (verify the possible presence of connectivities with the *nonstandard* length corresponding to the presence of $^{4-5}\text{J}_{\text{HH,XH}}$ correlations). If contradictions are not found, a *strict* structure generation is performed. It is accompanied by spectral and structural filtering. If the program detects the presence of non-standard connectivities, it switches to the *fuzzy* structure generation mode. This mode allows performing the generation in the presence of unknown number of nonstandard connectivities of unknown length.

If information obtained from 2D NMR is insufficient to solve the problem within a reasonable time (molecules with a deficit of hydrogen atoms, etc.), fragments are "imbedded" into MCD. They are found by ^{13}C search against the fragment library and / or postulated by the spectroscopist. The researcher is allowed to automatically create a *user base* of fragments which are specific for the compounds of a given class. The choice of the most probable structure is based on predicting ^{13}C (and ^1H if necessary) chemical shifts using three empirical methods - incremental, neural network and HOSE code [2,4]. For example, the calculation of carbon chemical shifts by the incremental approach is performed with a speed of up to 30 thousand shifts per second with an average error 1.5-1.8 ppm. The structures are ranked by the deviation increase of the calculated spectra from experimental ones. To determine relative stereochemistry of the most probable structure the NOESY/ROESY spectra are used in the system.

Application examples

The advantages of an expert system in comparison with traditional approaches become most evident as a result of analysis of the reasons for the incorrect structures were deduced and published by spectroscopists. Considering the properties of the initial information and the complexity of its analysis, it is not surprising that different groups of researchers often come to different structures on the basis of logical analysis of the same spectral data. As a result there is a quite large number of works devoted to the revision of previously published

structures. For example, in the period from 1990 to 2004 nearly 1000 such works were published. In the report, the causes leading to the inference of incorrect structures are analyzed. A number of examples [5] demonstrate that the use of ES allows to detect and revise an incorrect structure, and that is especially important - to prevent deducing incorrect structures. Examples of the ES application to elucidate structures, deciphering of which by traditional methods of the two-dimensional NMR spectra analysis was considered as impossible by highly qualified spectroscopists [6]. It is also shown [7] that the use of atomic force microscopy (AFM) in combination with the ES and quantum-chemical DFT-calculation of geometries and ^{13}C chemical shifts allows to determine the structure of molecules in cases where the sample quantity is very small, and therefore it is impossible to perform X-ray analysis. Examples are also given which obviously demonstrate that the synergistic combination of empirical and DFT methods of NMR spectra prediction is a powerful tool for selection of the preferable structure between very similar ones if they proposed by the expert system as equiprobable [8].

The efficiency of ACD/Structure Elucidator is confirmed by the structure elucidation of many hundreds of complex natural compounds. It is expected that in the nearest decade the ES such as ACD/Structure Elucidator will be widely applied in laboratories dealing with the structure elucidation of complex organic molecules by NMR spectra.

Literature

1. Elyashberg M.E. Trends in Anal. Chem., 2015, Vol. 69, Spec. Iss., p. 88-97.
2. Elyashberg M.E., Williams A.J., Blinov K.A. *Contemporary Computer-Assisted Approaches to Molecular Structure Elucidation*, Cambridge: RSC Publishing, 2012.
3. Elyashberg, M. E., Blinov, K. A., Molodtsov, S. G., Williams, A. J., Martin G. E. J. *Chem. Inf. Comput. Sci.*, 2004, Vol. 44, p. 771-792.
4. Elyashberg M.E., Williams A.J., Martin G.E. *Prog. NMR Spectrosc.*, 2008, Vol. 53, p. 1-104
5. Elyashberg M., Williams A., Blinov K. *Nat. Prod. Rep.*, 2010, Vol. 27, 1296-1328.
6. Elyashberg M.E., Blinov K.A., Molodtsov S.G., Williams A.J. *Magn. Reson. Chem.*, 2012, Vol. 50, p. 22-27.
7. Hanssen K. Ø., Schuler B., Williams A.J., Demissie T. B., Hansen E., Andersen J. H., Svenson J., Blinov K., Repisky M., Mohn F., Meyer G., Svendsen J.-S., Ruud K., Elyashberg M., Gross L, Jaspars M., Isaksson J. *Angew. Chem. Int. Ed.*, 2012, Vol. 51, p. 12238-12241.
8. Buevich A., Elyashberg M. Synergistic combination of CASE algorithms and DFT chemical shift predictions: a new powerful approach for structure elucidation, verification and revision. SMASH-2016, September 11-14, 2016, La Jolla, USA.

Visualization by NMR. Physical principles

Vyatcheslav Frolov

Faculty of Physics, Sankt Petersburg State University, St. Petersburg, Russia

E-mail: vfrolovv@bk.ru

Introduction

NMR is well-known among physicists and chemists as an analytical method and method of research of molecular structure and dynamics of matter. However in 1960 there was an idea to use NMR quite in other aspect: to get a signal NMR from determined spatial areas. In 1973 experiments, confirming such possibility and putting began the new method of visualization, were executed. This method got the term magnetic resonance tomography (MRT) or magnetic resonance imaging (MRI). Domains of its application appeared very various (spatial structure of porous objects both natural and in-use as build materials, visualization of processes in chemical reactors, structure of lamellar and turbulent hydrodynamic flows, effects of cavitation, determination of age of trees in the natural state et cetera. however on the clear applications in diagnostic medicine went out reasons into first place (MRI and local spectroscopy). The presented lecture is devoted to physical and mathematical principles of reconstruction of magnetic resonance images and methods of enhancement of their informing.

Specific signs of magnetic resonance images

Popularity of method of MRI is conditioned its specific as compared to other methods, because magnetic resonance images contain an important information for diagnostic medicine. Such characteristic features it is been

1. Selectivity in relation to the sort of nuclei (reflection of concentration of certain isotope, or, that almost equivalently, certain chemical element); a tomography uses most widespread the protons.
2. Sensitivity to the small local changes of structure and dynamics of molecular surroundings and intermolecular interactios;
3. Possibility of reflection of the spatial distributing of rate and direction of maximum rate of self-diffusion;
4. Possibility of visualizatou of the spatial distributing of separate chemical component of object.
5. Sensitivity to a speed and a character of macroscopic motion of media.

Among modern diagnostic methods in medicine, based on high-tech, the method of MRI is distinguished due to great informing and high degree of safety for a man, because no ionizing radiations are used in him. Distinctive signs of MRI as a diagnostic method are ability, unlike X-ray methods, to visualize soft, absence of screening of the probed area surrounding tissues and organs (for example, by the bones of skull), possibility to manipulate purposefully the mode of reception and processing of data depending on character of the required information. By the proper organization of process of reception and processing of data, the got information can be related to different molecular and macroscopic properties of matter. Thus during the inspection of patient by MRT on him the weakest action of physical factors appears as compared to methods, using a X-ray or nuclear radiation, that, certainly, has a primary value for medical applications. A MRI is used not not only in medicine but also in psychology, physiology of plants and animals, biophysics etc.

Contrasting of magnetic resonance images

In a lecture is described the constructing of radio frequency and gradient pulses allowing to enhance a contrast of magnetic resonance tomograms due to the different ways of reflection of areas of object with different NMR-characteristics. Such characteristic may be spin-spin or spin-lattice relaxation times. The reception of images weighted on these parameters, or visualizing on these parameters is examined, with the examples of diagnostic applications. Sensitivity to the change of magnetic properties blood in the process of return of oxygen by haemoglobin to the cells of brain resulted in appearance of functional tomography. Particular interest from the of principle and practical points of view is presented by methods, representing the spatial distributing of tensor of self-diffusion. Directions of most speed diffusion represent the orientation of the nervous conducting ductings, that allows to get the maps of nervous ways (“traktograms”). Important aspect is the use of sensitivity MRI to macroscopic motion of liquid. This allows us to get the image of blood vessels (“magnetic resonance angiography”).

Reduction of inspection time

An inspection by MRI expenes more time what in other methods. Therefore large attention spared the acceleration of process of output of information. Various variants of pulse sequences on the base of series of Carr – Pursell allow us to get as the increased contrast on spin-spin relaxation, so to decrease the expenses of time on the reception of information due to a multi-layered tomography, or to realize implementation of the so-called “phase encoding” for one cycle of measurings (“speed-up” impulsive sequences). Other direction in development of methods of rapid data logging is the use of radio frequency pulses deviating magnetization vector on on a small angle.

References

1. Chizhik V. I., Chernyshev Yu. S., Donets A. V., Frolov V., Komolkin A., Shelyapina M. G. Magnetic Resonance and Its Applications. - Springer. Cham, Heidelberg, New York, Dordrecht, London. 2014, XX, 782 p. 234 illus.— ISBN 978-3-319-05298-4, DOI 10.1007/978-3-319-05299-1. (Section 2.10).
2. Rinck P. A. Magnetic Resonance in Medicine. - Blackwell Science, Berlin, Vienna.- 2001. 245 p.
3. Perrin Vincent. MRI Techniques. - Wiley-ISTE, 2013. ISBN: 9781848215030, Online ISBN: 9781118761281. DOI: 10.1002/9781118761281.
4. C. Westbrook, C. Kaut Roth, J. Talbot. MRI in Practice.- Blackwell Publ., 2005. 448 p.

Time-Domain NMR Characterization of Solids Structure

Leonid Y. Grunin, Innokenty A. Nikolaev

Resonance Systems GmbH, Nabern, Germany

E-mail: mobilenmr@hotmail.com

www.nmr-desing.com

Lecture Content

Well observed in the last decade ongoing rise of Time-Domain NMR (TD-NMR) popularity for scientific and industrial applications is easily explained both by the improvements in devices performance and relatively low instruments price comparing to standard high-resolution NMR (HR-NMR) machines and even other methods like FT-IR or GC and LC. The TD-NMR has got real advantage for the investigation of solids structures because it exploits residual magnetic dipolar interactions that are normally artefacts for conventional HR-NMR. The lecture is devoted to explanation of main features of NMR relaxation together with measurements techniques and is structurized in the following way:

- Overview of up-to-date technical capabilities of TD-NMR equipment: basic hardware diagrams, ringing time and signal-to-noise ratio, sequence resolution, processing software for best fit of relaxation decays and spectral lines.
- Standardized routine applications for different industries: Solid Fat Content, Oil and Moisture in Seeds, Hydrogen Content in Fuels, Spin Finish on artificial fibres, Protein in Milk products.
- Conventional NMR spin-spin and spin-lattice relaxation experiments: Free Induction Decay and Magic Sandwich Echo, CPMG, Saturation- and Inversion-Recovery sequences; Estimation of polymer cross-linking, crystallinity, characterization of porous systems and adsorption processes.
- Background theory of Residual Dipolar Coupling Constant (RDC) usage for structural analysis: Dipolar Hamiltonian, Density Operator and semi-classical Liouville equation, dipolar averaging, correlation function.
- RDC distribution from transverse relaxation.
- RDC distribution from Double Quantum (DQ) NMR experiments: build-up curve theory, DQ relaxation, higher orders of nuclear spins transitions.
- Polarization transfer for measurement of linear structural dimensions: Goldman-Shen experiment, DQ excitation, spin diffusion curve and spin diffusion coefficients.
- Key notes on how to build a TD-NMR experiment for specific tasks in structural chemistry.

All these topics are accompanied with real experimental data and detailed explanation of the pulse sequences and post-measure data processing.

Local and global dynamics of intrinsically disordered proteins: a case study of H4 histone tail

K. Kaempff¹, S. O. Rabdano¹, A. Groves², I. S. Podkorytov¹ and N. R. Skrynnikov^{1,2}

¹Laboratory of Biomolecular NMR, St. Petersburg State University, 7/9 Universitetskaya nab., St. Petersburg 199034, Russia.

²Department of Chemistry, Purdue University, West Lafayette IN 47907 USA.
E-mail: nikolai@purdue.edu, kerstin.kaempff@gmx.de

Intrinsically disordered proteins (IDPs) are proteins without well-defined secondary and tertiary structure and thus possess a high flexibility [1, 2]. They constitute about 25% of human proteome. Their flexibility allows them to bind to multiple targets and to fold upon binding [3]. The multitude of possible conformations of IDPs in some cases includes a pathogenic form. IDPs are major contributors to the pathogenic plaques in Alzheimer, Parkinson and other neurodegenerative diseases [4, 5].

Comparison of Molecular Dynamics simulations of IDPs with various experimental data has shown that commonly used force fields and water models tend to overestimate intramolecular protein interactions, leading to conformational ensembles that are too compact. Significant efforts have been recently undertaken to remedy this problem [6-8]. In order to better characterize the current situation in this important area we have chosen to investigate the temperature-dependent ¹⁵N relaxation in the intrinsically disordered 26-amino-acid long N-terminal segment of the histone protein H4.

Experimentally, we have measured ¹⁵N R₁ and transverse cross-correlation rates η in a range of temperatures from 5 to 55°C. MD simulations were performed using the simulation package AMBER14 with ff14SB force field and SPC/E, TIP3P, TIP4P-EW or TIP4P-D water models. The more traditional TIP3P, SPC/E and TIP4P-EW models showed evidence of systematic bias (cf. Fig. 1 A, B). We have found that the TIP4P-D model, which has been designed specifically for use with disordered proteins [7], produced consistently good agreement with the experimental data (cf. Fig. 1 C, D).

In the literature the dynamics of IDPs has been described to consist from two temperature dependent motional modes that contribute to relaxation [9, 10]. Using the simulation data of the peptide H4 we have validated the model involving a combination of two modes, the origin of which will be discussed in the talk.

We conclude that a combination of temperature-dependent spin relaxation data and the recently developed specialized MD models provides a powerful insight into conformational dynamics of intrinsically disordered proteins.

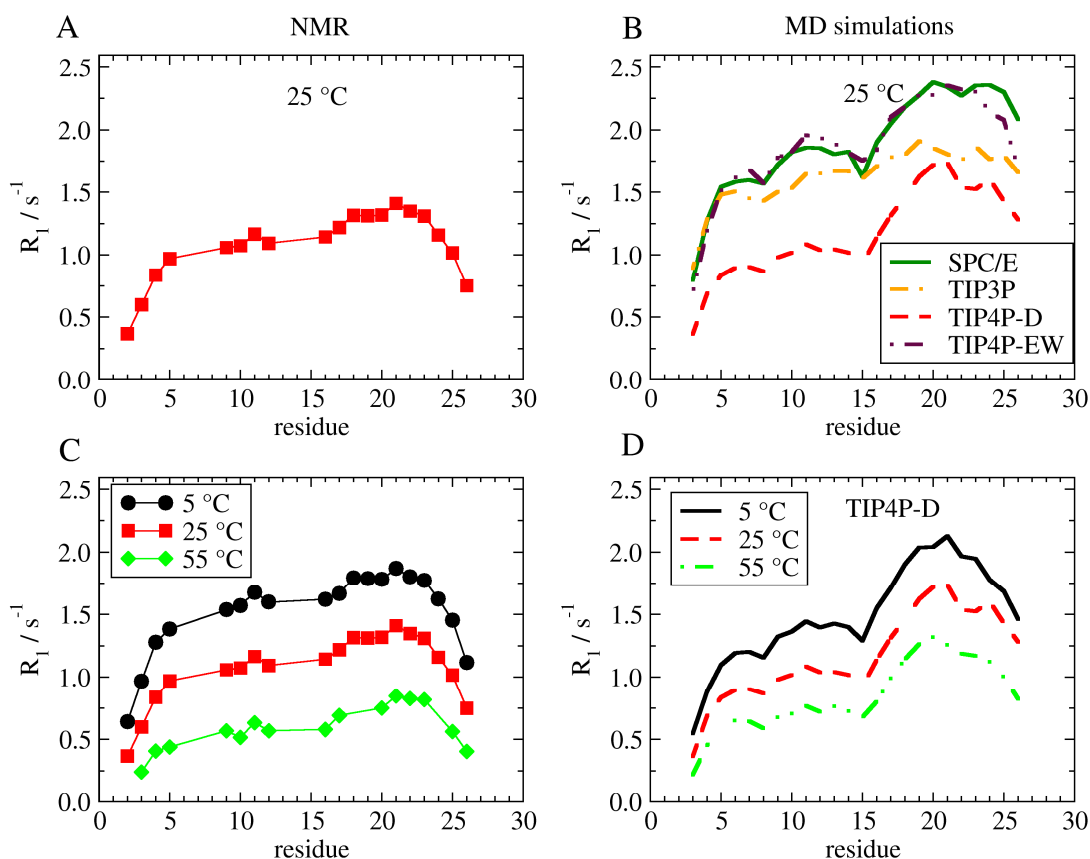


Figure 1. comparison of (A, C) measured and (B, D) simulated longitudinal relaxation rate R_1 in H4 peptide. Measurement / simulation temperatures and water models employed are listed in the legends

This work was supported by the Russian Science Foundation (RSF) (project No. 15-14-20038). All NMR measurements were performed at the Center for Magnetic Resonance in the Research Park of St. Petersburg State University.

References

1. K. Dunker, I. Silman, V. Uversky, and J. Sussman, *Curr. Opin. Struct. Biol.*, 18, 756 (2008).
2. J. Ward, J. Sodhi, L. McGuffin, B. Buxton, and D. Jones, *J. Mol. Biol.*, 337, 635 (2004).
3. N. Rezaei-Ghaleh, M. Blackledge, and M. Zweckstetter, *ChemBioChem*, 13, 930 (2012).
4. N. Rezaei-Ghaleh, K. Giller, S. Becker, and M. Zweckstetter, *Biophys. J.*, 101, 1202 (2011).
5. E. Norris, B. Giasson, and V. Lee, in *Current topics in developmental biology*, 60, 17 (2004).
6. R. Best, W. Zheng, and J. Mittal, *J. Chem. Theory. Comput.*, 10, 11, 5113 (2014).
7. S. Piana, A. Donchev, P. Robustelli, and D. Shaw, *J. Phys. Chem. B*, 119, 5113 (2015).
8. D. Nettels et al., *Proc. Natl. Acad. Sci.*, 106, 20740 (2009).
9. Y. Xue and N. Skrynnikov, *J. Am. Chem. Soc.*, 133, 14614 (2011).
10. A. Abyzov et al., *J. Am. Chem. Soc.*, 138, 6240 (2016).

Deep cooling of the nuclear spin system in semiconductor structures

Kirill Kavokin^{1,2}

¹*Spin Optics Laboratory, St.Petersburg State University*

²*Ioffe Institute of RAS*

E-mail: kkavokin@gmail.com

<http://solab.spbu.ru/index.php/ru/home-ru-3/12-people/21-kirillkavokin.html>

The spin temperature approach is one of the most powerful and beautiful methods of the spin physics and magnetic resonance, especially in the solid state where nuclear spins are energetically well isolated from the crystal lattice. It has been known since 1970s that optical orientation of electron spins in semiconductors allows one to cool nuclear spins via dynamic polarization down to the microkelvins [1]. Recent development of non-destructive techniques of optical control [2, 3] gives a possibility to visualize classical properties of cooled spin systems, such as the Curie law at external fields weaker than local fields of dipole-dipole interaction, to trace changing the nuclear spin temperature during adiabatic demagnetisation, to study in real time the nuclear spin relaxation. Spin noise spectroscopy allows us to determine absolute values of nuclear magnetization and temperature in weak magnetic fields of the order of 1 Gauss. The spin temperatures of about 1 microKelvin, experimentally reached in GaAs structures, give hope for realization of nuclear ferromagnetic ordering via the formation of nuclear spin polarons [4].

References

1. B.Zakharchenya and F.Meier, eds. Optical Orientation. – North Holland, Amsterdam, 1984.
2. R. Giri, S. Cronenberger, M. M. Glazov, K. V. Kavokin, A. Lemaître, J. Bloch, M. Vladimirova, D. Scalbert, “*Nondestructive Measurement of Nuclear Magnetization by Off-Resonant Faraday Rotation*”, Phys. Rev. Letters 111, 087603 (2013).
3. I.I. Ryzhov, S.V. Poltavtsev, K.V. Kavokin, M.M. Glazov, G.G. Kozlov, M. Vladimirova, D. Scalbert, S. Cronenberger, A.V. Kavokin, A. Lemaître, J. Bloch, V.S. Zapasski, “Measurements of nuclear spin dynamics by spin-noise spectroscopy” Applied Phys. Lett. 106, 242405 (2015).
4. V.K.Kalevich, K.V.Kavokin, I.A.Merkulov and M.R.Vladimirova, “Dynamic nuclear polarization and nuclear fields”, Chapter 12 in Spin physics in semiconductors ed. by M.I.Dyakonov, Springer (2nd edition) – to be published

Earth's magnetic field fluctuations and uncertainty of site finding using the geomagnetic map

Andrei V. Komolkin

Faculty of Physics, Saint Petersburg State University, 199034, Saint Petersburg, Russia

E-mail: a.komolkin@spbu.ru

http://nmr.phys.spbu.ru/~komolkin

Introduction

Geomagnetic field is long time used for navigation by mankind [1]. Migrating animals, including Pacific salmon (Fig. 1), can use geomagnetic field to return to natal sites after migrations [2].



Figure 1. Chinook Salmon (Oncorhynchus tshawytscha), one of the six Pacific salmon

Precision and stability of magnetic map

In this report, the analysis of yearly changes and short-time fluctuations of geomagnetic field is presented. An uncertainty of positions finding (at least one of two coordinates) by migrating animals using the total induction of magnetic field of the Earth is discussed.

The source of magnetic data is geomagnetic observatory in Nurmijärvi, Finland, which provides data via the INTERMAGNET project [3].

It is shown, that total magnetic field has at least two components: (1) practically linear increasing in time during each year in the period of 1991-2015, and (2) fluctuations during day. The amplitude of fluctuations depends on local time (sunrise, noon, sunset, midnight), i. e. on position of the Sun with respect to the horizon. Probability density of fluctuations is not Gaussian.

Changes of the induction of the geomagnetic field correspond to shift the isoline on the ground. Both yearly change and fluctuations of the geomagnetic field influence on the precision of “magnetic map”, i. e. on the possibility for migrating animals to find the desired position on the ground using the only intensity of the magnetic field.

Acknowledgements

This work was supported by Saint Petersburg State University (grant No. 1.37.149.2014). We thank observatory at Nurmijärvi (Finnish Meteorological Institute) and INTERMAGNET for promoting high standards of magnetic observatory practice.

References

1. J. Needham, C. A. Ronan. The shorter Science and Civilisation in China. – Cambridge Univ. Press, Cambridge, 1986. Vol. 3. 312 pages. ISBN 978-0-521-31560-9.
2. T. P. Quinn. Models of Pacific salmon orientation and navigation on the open ocean. *J. Theor. Biol.*, 1991, v. 150, p. 539–545
3. J. J. Love, A. Chulliat. An International Network of Magnetic Observatories. *Eos*, 2013, Vol. 94, No. 42, p. 373-384. DOI: 10.1002/2013EO420001

Dynamics in protein crystal: insights from MD simulations

Vilius Kurauskas^{1,2,3,*}, Sergei A. Izmailov^{6,*}, Olga N. Rogacheva^{6,*}, Audrey Hessel^{1,2,3},
 Isabel Ayala^{1,2,3}, Anastasya Shilova⁴, Joyce Woodhouse^{1,2,3}, Yi Xue⁵, Tairan Yuwen⁵,
 Oleg Mikhailovskii⁵, Manfred Burghammer⁴, Nicolas Coquelle^{1,2,3},
 Jacques-Philippe Colletier^{1,2,3,#}, Nikolai R. Skrynnikov^{5,6,#}, Paul Schanda^{1,2,3,#}

¹Université Grenoble Alpes, IBS, F-38044 Grenoble, France.

²CEA, Institut de Biologie Structurale, F-38044 Grenoble, France.

³CNRS, Institut de Biologie Structurale, F-38044 Grenoble, France.

⁴European Synchrotron Radiation Facility, Grenoble, France

⁵Department of Chemistry, Purdue University, West Lafayette, Indiana 47907, USA.

⁶Laboratory of Biomolecular NMR, St. Petersburg State University, St. Petersburg 199034, Russia.

E-mail: nikolai@purdue.edu

*These authors contributed equally to this work.

We have investigated dynamics in three different crystal forms of ubiquitin, as well as ubiquitin in solution, with particular emphasis on (i) conformational exchange between β turn type I and II in the region 51-54 and (ii) rocking dynamics whereby protein molecule as a whole undergoes subtle reorientational motion within the confines of the crystal lattice [1]. Experimentally, both motional processes have been probed using relaxation dispersion techniques, including recently developed near-rotary-resonance dipolar relaxation dispersion experiments. It has been determined that rocking motion in one of the crystal forms (PDB ID 3N30) occurs on the time scale of tens to hundreds of microseconds, same as β I \leftrightarrow β II conformational exchange. Using Molecular Dynamics simulations, we have shown that the commonality of the motional time scales is not accidental: conformational exchange and rocking motion appear to be coupled. We have investigated the mechanisms of this coupling and predicted a number of point mutations that are expected to abrogate (or enhance) rocking. The crystals of ubiquitin containing these mutations have been modeled *in silico*. We have also investigated the interactions (in particular, crystal contacts) that control the balance between β I and β II conformations in different crystal forms. Finally, we have used MD simulations as a basis for chemical shift calculations and illustrated how relaxation dispersion effects can emerge as a function of β I \leftrightarrow β II exchange in conjunction with the rocking motion.

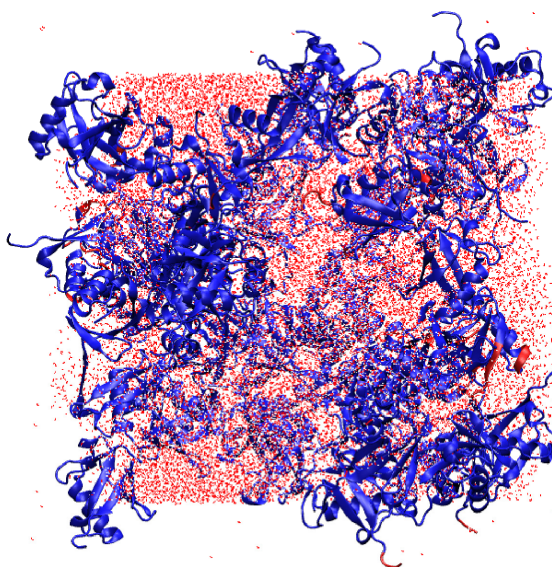


Figure 1. The simulated unit cell from 3N30 crystal

Acknowledgments

This work was supported by the RSF grant 15-14-20038. We also acknowledge the T-Platforms cluster of St. Petersburg State University for providing CPU time for the MD simulations.

References

1. P. Ma, Y. Xue, N. Coquelle, J.D. Haller, T. Yuwen, I. Ayala, O. Mikhailovskii, D. Willbold, J.P. Colletier, N.R. Skrynnikov and P. Schanda, Nature Communications, 6, 8361 (2015).

Electron-nuclear spin dynamics in semiconductor QDs

*M. S. Kuznetsova¹, R. V. Cherbunin¹, I. Ya. Gerlovin², I. V. Ignatiev^{1,2}, M. Yu. Petrov²,
S. Yu. Verbin¹, D. R. Yakovlev^{3,4}, and M. Bayer^{3,4}*

¹*Physics Department, Saint Petersburg State University, 199034 St. Petersburg, Russia*

²*Spin Optics Laboratory, Saint Petersburg State University, 199034 St. Petersburg, Russia*

³*Experimentelle Physik 2, Technische Universität Dortmund, D-44221 Dortmund, Germany*

⁴*Ioffe Institute, Russian Academy of Sciences, 194021 St. Petersburg, Russia*

E-mail: mashakuznecova@bk.ru

Optical orientation of electron spin in semiconductors is followed by the dynamic nuclear spin polarization (DNSP) due to contact Fermi interaction. The DNSP causes back effect on the electron spin polarization [1].

This work presents original results of investigation of nuclear spin dynamics in nanostructure with negatively charged InGaAs/GaAs quantum dots characterized by strong quadrupole splitting of nuclear spin sublevels [2]. The main method of the investigation is the experimental measurement and theoretical analysis of the photoluminescence polarization as the function of the transverse magnetic field (effect Hanle).

The dependence of the Hanle curve on temporal protocol of excitation is examined. Experimental data are analyzed by using an original approach to separate behavior of the longitudinal and transverse components of nuclear polarization. The rise and decay times of each component of nuclear polarization and their dependence on transverse magnetic field strength are determined.

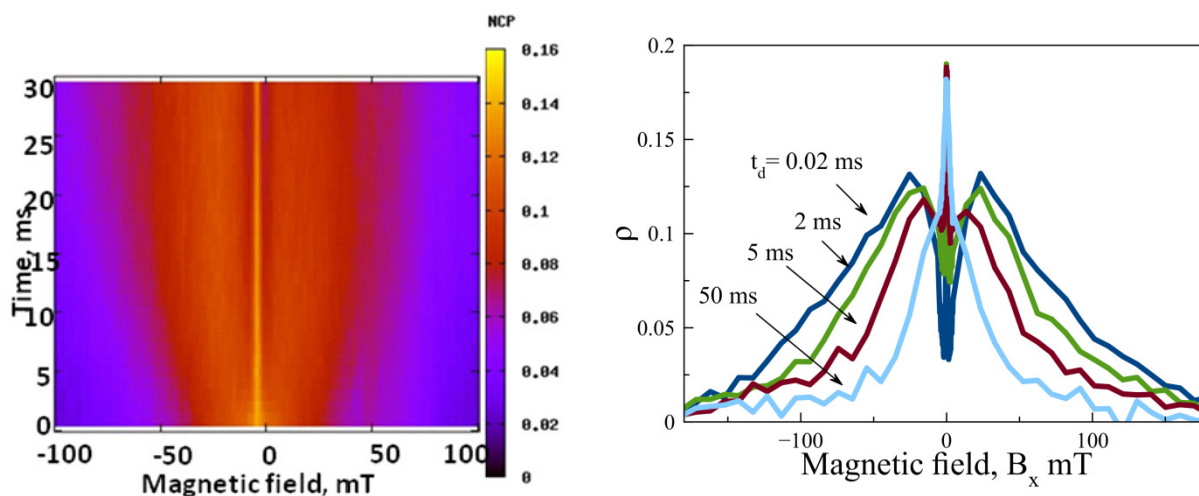


Figure 1. Rise and decay dynamics of nuclear spin polarization

We study the role of effective field created by hyperfine electron-nuclear spin interaction (the Knight field) in the dynamic of nuclear polarization using a weak additional magnetic field parallel to the optical axis. The field controls the efficiency of nuclear spin cooling and the sign of nuclear spin temperature [3]. The standard nuclear spin cooling theory fails to describe the experimental Hanle curves in a certain range of control fields. This controversy is resolved by taking into account the nuclear spin fluctuations. This allows us to accurately describe the measured Hanle curves and to evaluate the parameters of the electron-nuclear spin system of the studied quantum dots.

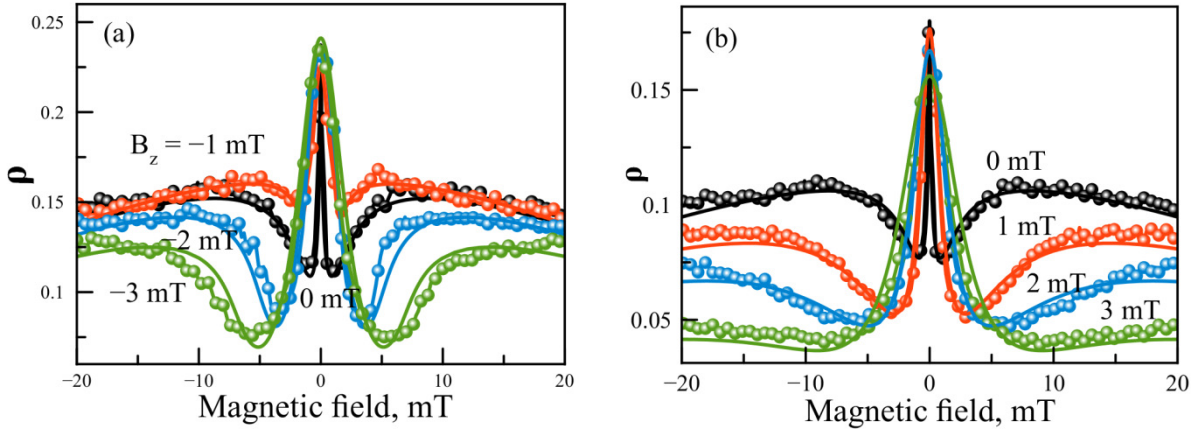


Figure 2. Results of calculations taking into account the NSF (smooth solid lines) in comparison with experimental data (noisy lines) for negative (panel a) and positive (panel b) longitudinal external fields, B_z . Values of B_z are given near each curve

New effect of resonant optical pumping of nuclear spin polarization in an ensemble of singly charged (In,Ga)As/GaAs quantum dots subject to a transverse magnetic field is observed. Electron spin orientation by circularly polarized light with the polarization modulated at the nuclear spin transition frequency is found to create a significant nuclear spin polarization, precessing about the magnetic field. Nuclear spin resonances for all isotopes in the quantum dots are found in that way. In particular, transitions between states splitted off from the $|\pm 1/2\rangle$ doublets by the nuclear quadrupole interaction are identified.

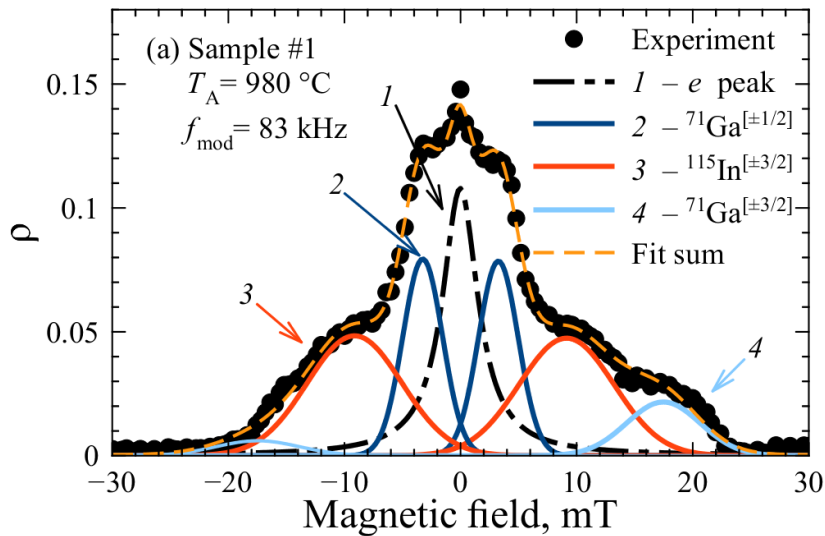


Figure 3. Gaussian decomposition of the Hanle curve (symbols) for $f_{PM}=83$ kHz

To study temporal evolution of nuclear spins we have measured the electron-spin Hanle depolarization curves for the InGaAs/GaAs quantum dots at different modulation frequencies of polarization of the optical pumping. Examples of such dependencies are shown in the Figure 4. Experimental data are analyzed by using an original approach to separate behavior of the dipole and quadrupole components of nuclear field. Our modeling shows that both the nuclear fields decrease with the decreasing the modulation period. The suppression of nuclear polarization occurs when the modulation frequency exceeds the inverse nuclear-spin relaxation time. The modeling allowed us to evaluate the relaxation times for each component of nuclear polarization. It is remarkable that the modulation suppresses not only the well-ordered dynamical nuclear polarization but also the randomized nuclear fluctuations.

The mechanism of frequency dependence of the nuclear spin fluctuations requires further study.

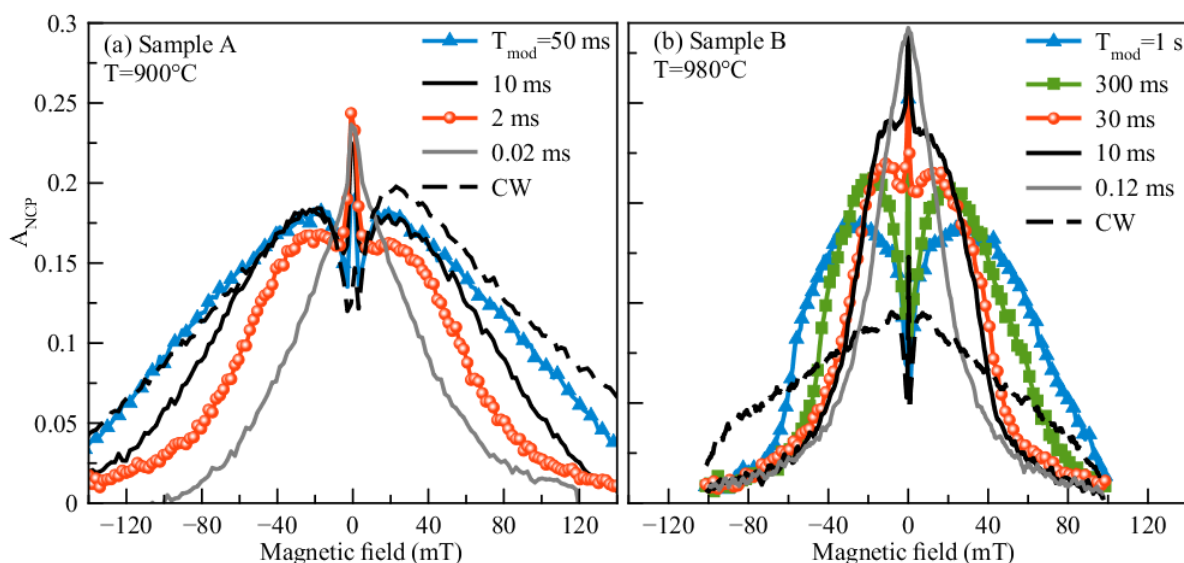


Figure 4. Hanle curves for sample A (left panel) and sample B (right panel) measured at the optical excitation of one circular polarization (CW) as well as with modulated polarization with periods given in the legends

References

1. *Optical Orientation*. Eds. F. Meier and B. P. Zakharchenya (North Holland, Amsterdam 1984).
2. P. S. Sokolov, M. Yu. Petrov, T. Mehrrens, K. Müller-Caspary, and A. Rosenauer, D. Reuter, A. D. Wieck, *Phys. Rev. B* **93**, 045301 (2016)
3. D. Paget, G. Lampel, B. Sapoval, and V. I. Safarov, *Phys. Rev. B* **15**, 5780 (1977).

NMR Applications to Ionic Liquids: Current Status

Vladimir V. Matveev

Faculty of Physics, St. Petersburg University, Universitetskaya nab. 7/9, 199034,
Saint Petersburg, Russia
E-mail: v.matveev@spbu.ru

Introduction

NMR technique (spectra, T_1 & T_2 -relaxation, diffusion, paramagnetic effects, NOE, and combined experiments) has been used successfully during many decades to study a variety of fluid systems, including both pure liquids and various solutions. During 2 or 3 last decades a new class of liquid systems drew much attention and it is known as "Ionic Liquids" (ILs, RTILs). And the appearance of these systems opens up a wide scope for the application of well-known and proven techniques of NMR experiments to obtain information on the local structure and physicochemical characteristics of ILs. The aim of this work is to describe and analyze the main directions of NMR applications to ILs of different kinds, to try to summarize some results obtained and to discuss possible new NMR experiments in the field of pure ILs as well as of IL-other compound mixtures. A special accent is made at T_1 -relaxation and its usefulness for characterization of ILs structure and properties.

At the beginning we describe main IL types namely, imidazolium-based ILs, proton ILs (PILs), so-called "inorganic" ILs i.e. inorganic salt solution in PILs, paramagnetic ILs etc. In the same part of the work we describe the most important area of ILs applications such as green chemistry, dissolving cellulose, uptake of carbon dioxide, novel electrolytes for nonaqueous supercapacitors, ion batteries, and fuel cells. And in all these areas NMR can be useful for understanding these processes at the molecular level.

^{13}C and ^1H NMR Relaxation

Many of pure ILs, especially the imidazolium-based ones, are very suitable for testing by NMR relaxation due to their much higher viscosity comparing to conventional pure liquids and electrolyte solutions. As the result a lot of investigations were made using ^{13}C and ^1H NMR. Here we analyze and compare the results obtained to now with the accent to temperature dependences of $1/T_1$ for ^{13}C nuclei in $[\text{amim}]^+$ cations and to difficulties appeared in procedure of transformation of $1/T_1$ magnitudes to the (τ_c) values. Our analysis showed that ^{13}C T_1 relaxation data themselves were enough for direct calculation of the reorientation times (τ_c) for each group in the investigated ILs, and no additional NOE experiments are required [1].

Next we present a comparison of ^1H and ^{13}C relaxation data for three ILs. We have found that the proton data for a number of functional groups are similar to ^{13}C ones at higher temperatures while at lower temperatures ^1H relaxation is controlled by spin-diffusion interaction and the $1/T_{1\text{H}}$ magnitudes do not practically depend on temperature, see Fig. 1b. At the same time $1/T_{1\text{H}}$ magnitudes are still suitable for calculation of the τ_c numerical value for some groups of $[\text{emim}]\text{OAc}$ (Fig. 1a), [2].

Further, we have found that ^1H relaxation curves in some cases allowed one to detect motions, unobservable in the carbon relaxation and, thereby, to extract more information concerning details of a dynamics of the $[\text{amim}]^+$ cations. In particular, different temperature behavior of ^1H relaxation of C(2) hydrogen for $[\text{emim}]\text{CH}_3\text{COO}$ from one side and for $[\text{bmim}]\text{BF}_4$ or $[\text{bmim}]\text{PF}_6$, from another side (see Fig. 2) allowed to hypothesize different ways of the cations packing in these systems. And it turned out that this assumption correlates well with the literature data on computer simulation of the same ionic liquids.

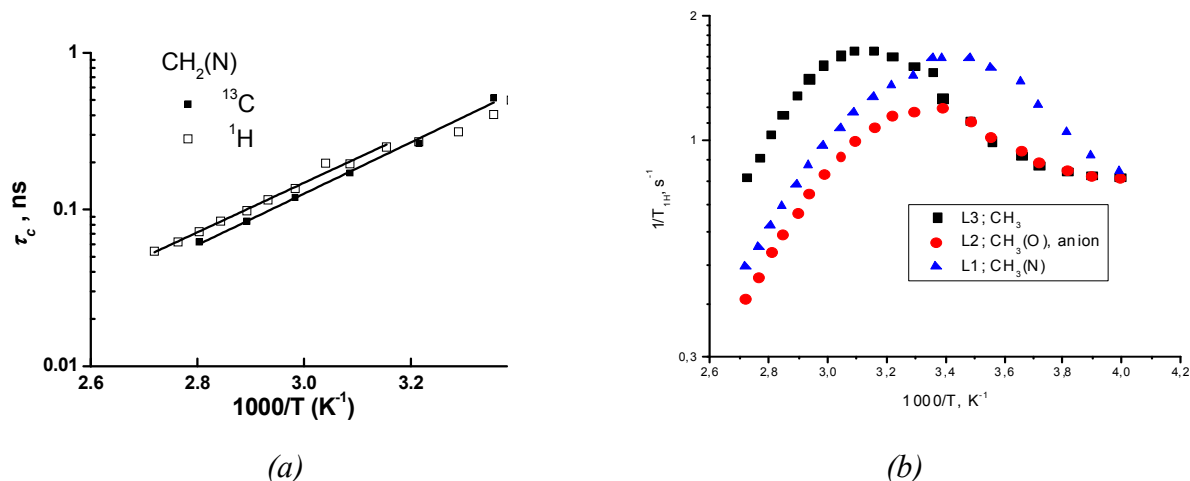


Figure 1. Correlation times calculated from 1H and ^{13}C relaxation data (a) and $1/T_{1H}$ temperature dependences (b) for $[emim]CH_3COO$ ionic liquid

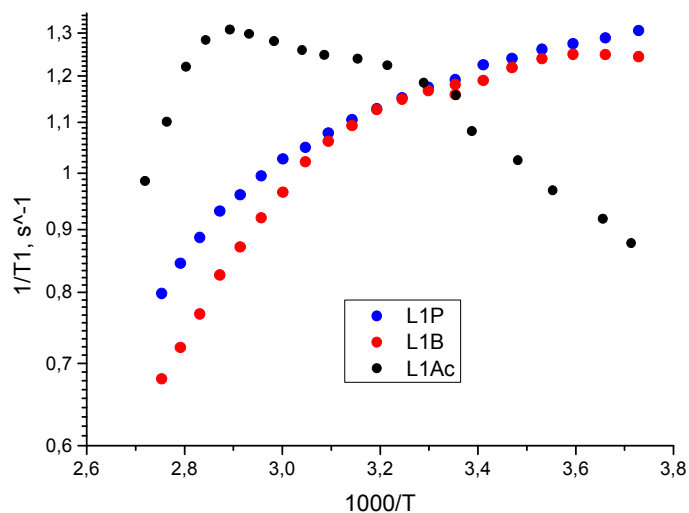


Figure 2. $1/T_{1H}$ temperature dependences of $C(2)H$ group for three pure ionic liquids: $[emim]CH_3COO$, $[bmim]BF_4$, and $[bmim]PF_6$

Other

In the final section of the lecture we present some examples of NMR application to so-called “inorganic” ionic liquids. In particular, we analyzed some solutions of inorganic salts in ethylammonium nitrate (EAN), using well-known model of the formation of aqua-acido complexes.

Acknowledgements

The NMR measurements have been partially carried out in the Center for Magnetic Resonance of Research Park of St. Petersburg State University. The work was suggested by SPbGU Research program, grant #11.57.121.2016.

References

1. V.V. Matveev *et al.*, Phys. Chem. Chem. Phys. **16**, 10480–10484 (2014).
2. V.V. Matveev *et al.*, Russ. Chem. Bull. **62** (9), 1985–1990 (2013).

MAS NMR studies in combination with pulsed field gradient techniques

Dieter Michel, Dieter Freude and Jürgen Haase

Leipzig University, Faculty of Physics and Earth Sciences, Institute for Experimental Physics II, Linné-Strasse 5, 04103 Leipzig, Germany

E-mail: michel@physik.uni-leipzig.de; Phone: +49 341 97 32683

Structure and mobility of molecules adsorbed in restricted geometry has been widely investigated by means of NMR spectroscopy. Very often nuclear spins were used (e.g. ^{13}C and ^{15}N), where a sufficient spectral resolution can be achieved because of large chemical shifts and J coupling constants. In case of proton NMR spectroscopy, however, the applicability of NMR spectroscopy to molecules adsorbed on surfaces is often limited due to the poor resolution. A notable enhancement in resolution of the spectra may be achieved by the application of MAS techniques. It will be shown that the main reason of this successful application is that the susceptibility broadening can be (partially) averaged out.

The aim of the lecture is:

- to introduce into the fundamentals of MAS NMR in nanosized porous systems and to treat the influence of thermal motions of molecules in these systems in competition to coherent averaging due to magic angle spinning: We describe advantages and shortcoming of these techniques. It will be shown that the studies may be broadly applied if a well-defined preparation *under conditions of vacuo* may be achieved for samples suitable for MAS.
- to show that MAS NMR techniques may be combined with measurements by means of NMR pulsed field gradient techniques to study self-diffusion processes in spectra with resolved lines. Special experimental requirements will be discussed. Thus, selective measurements of self-diffusion coefficients may be possible by using the various resonance lines in the MAS NMR spectra.
- to mention briefly two special applications: It will be discussed how the information on thermal mobility derived from the side-band analysis in ^1H MAS NMR experiments for these systems may be combined with the study of proton spin relaxation over a wider temperature range. Furthermore, the applicability of two-dimensional NMR of adsorbed molecules is discussed when the spectral resolution is enlarged by means of MAS NMR studies

Determination of the spin-spin coupling in the molecule HD and possible manifestations of axion-like particles

Yuriy I. Neronov

*Mendeleev Institute for Metrology, St. Petersburg, Moskovsky pr. 19, Russia
E-mail: yineronov@mail.ru*

Introduction

A light pseudoscalar particle, called the axion, was proposed to solve the problem of conservation of CP parity in the strong interaction. Stable or nearly stable axion-like particles are also attractive candidates for the sought carriers of dark matter. Several research groups conduct a search for these particles both among the particles coming from outer space, and with the help of special experiments.

In the article [1] it has been informed of a precision experiment on determining the energy of the spin-spin interaction between the proton and deuteron in the molecule HD. It has been found [1] that there is a discrepancy between the experimental and calculated data [2] for this constant J_{pd} . In the work [1], it was suggested to use the evaluation of the work [3] and to explain the discrepancy as a manifestation of the effect of axion-like particles. This assumption is interesting enough to perform a more thorough check of the existence of such discrepancies.

One of the possible reasons for the discrepancy of the experimental and calculated data for the J_{pd} can be as follows. Theoretical data for J_{pd} were calculated for the isolated single molecule HD [2]. However, the technique for determining J_{pd} requires the use of ampoules, in which hydrogen gas is at a pressure of about 60 atmospheres or higher. Under such pressures, relaxation processes allow excite long time NMR signals of the free precession of spin magnetization from protons (or deuterons) and, respectively, to receive (after the Fourier transform) signals with a width of spectral lines of a few hertz. In this connection, the aim of this study was a comparative experimental determination J_{pd} at consecutive study of two samples with pressure 95 and 155 atmospheres.

Samples preparation

As in the works [4-7], deuterated hydrogen HD was obtained by the chemical reaction: $\text{H}_2\text{O} + \text{LiD} \rightarrow \text{HD} + \text{LiOH}$. The chemical reaction was carried out in ampoules after sealing on a gas burner. Ampoules with hydrogen HD were made of glass tubes having an outer diameter 5 mm and a wall thickness of 1 mm. The sequence of filling the samples was as follows. On a bottom, the ampoule was placed water, the amount of which has been previously calculated from the need to have a pressure in the ampoule 95 and 155 atmospheres. Above the water, it was placed a cotton swab, which sprinkled crystals LiD. Weight of crystals, placed in an ampoule, was calculated so that the water has been completely used and ampoules were free of water vapor.

In addition, before the sealed ampoule, it was frozen in liquid nitrogen and was evacuated. This eliminates the broadening of spectral lines due to the influence of the paramagnetic oxygen. Evaluation of pressure in the ampoules so prepared contains the error associated with the estimation error of the internal volume of the sample and with a weighing error of the initial reagents. Accuracy assessment of our pressure in the ampoule is less than 5%.

NMR spectrometer

In this work, we could not use any commercial NMR spectrometer because of its possible damage to break the samples. Note that J_{pd} value is independent of the magnetic

induction field NMR spectrometer. In this case, superconducting magnets with high field have no advantage.

Constant J_{pd} can be determined with minimal error when it is possible to provide high uniformity of magnetic field, when the broadening of the spectral line is $\approx 90\%$ due to its own process of spin relaxation of the nuclear magnetization vector. In this case, the shape of the NMR signal line will fit quite well the theoretically grounded form of Lorentz. In this paper, the spectrometer used was the basis of which the author has described earlier in [8]. The spectrometer used an electromagnet, manufactured by «Bruker», having a magnetic field $B \approx 2.14$ T.

Stabilization of resonance conditions was performed by proton NMR signal at frequency $f_p \approx 91.2$ MHz. NMR signal to stabilize the resonance conditions of the magnetic field formed protons rubber tube. The rubber tube tightly covered resonant inductance with its outer side. The resonant inductance was common to receive a proton and deuteron NMR signal. The number of turns of the resonance inductor was chosen taking into account to provide maximum sensitivity to resonance of deuterium nuclei at a frequency of $f_d \approx 14$ MHz.

Before registering basic samples, we minimize the magnetic field gradients. For this purpose we used a sample with deuterated acetone $(CD_3)_2CO$. This substance allows the operator to reduce due to the magnetic field inhomogeneity broadening of the NMR signal to ≈ 0.2 Hz. Then, two samples with HD alternately were placed in the NMR spectrometer and spectra recorded under identical conditions.

The results of the experiment

Deuteron resonance signals from HD were recorded in the form of a doublet. We carried out a numerical treatment of the spectral array by the method, which was described earlier [7, 8].

The numerical results are shown in Table 1, where shows the signals of width from HD and D_2 , and given to the frequency intervals between the pair of signals of molecules HD, which are J_{pd} .

Table 1. Results of the study of two samples with deuterated hydrogen HD

Nambe ampule	The first sample	A second sample
P/atmospheres	95(+/- 5)	155(+/- 5)
$\Delta\nu(DH)/\text{Hz}$	2.73(+/- 0.03)	2.45(+/- 0.02)
$\Delta\nu(D_2)/\text{Hz}$	2.23(+/- 0.03)	2.04(+/- 0.02)
J_{pd}/Hz	43.112(+/- 0.005)	43.112(+/- 0.004)

The discussion of the results

With increasing pressure change relaxation processes and allow us to register NMR signals with a smaller width. However, the energy of the spin-spin interaction J_{pd} not changed. As we can see (Table 1) result for J_{pd} is independent of pressure changes in the sample.

The theoretical result for J_{pd} was calculated [2] ten times less precise than the experimental new our result (Table 1). The authors note [2] that the greatest contribution to their computing error brings uncertainty associated with the estimate of the equilibrium value of the distance between the nuclei of the molecule HD: $\delta_1 \approx 0.02 - 0.03$ Hz. Contribution to the uncertainty associated with taking into account the relativistic correction authors estimate at $\delta_2 \approx 0.01$ Hz. Other contributions to the overall uncertainty, according to the authors of, are at level $\delta_3 \approx 0.01$ Hz or less. In general, the authors [2] believe that their results and error, estimated at a maximum, equal: $J_{pd} = 43.31(+/- 0.05)$ Hz.

Ledbetter et al. [3] using the earlier data for J_{pd} and estimated the maximum difference between the theoretical calculation and experiment:

$$\Delta J_{pd} \approx 0.24 \text{ Hz.} \quad (1)$$

In addition, they showed that difference (1) produces more severe constraints on the existence of an anomalous spin-dependent potential between nucleons (two orders of magnitude lower than the estimates obtained previously in other works). In particular, Ledbetter et al. [3] deduced from Eq. (1) the following upper limit for the mass of axion-like particles:

$$m_a \leq 1000 \text{ eV}/c^2. \quad (2)$$

Now, a more accurate comparison of the calculated and experimental data for J_{pd} can perform. The difference between the theoretical calculations [2] and the experimental data (Table 1) will be equal to:

$$\Delta J_{pd} = 43.31(5) - 43.112(5) = 0.20(+/- 0.05) \text{ Hz.} \quad (3)$$

We can assume that (for the optimal variant), the difference (3) associated with the manifestation of non-electromagnetic interactions, and is the result of the spin-spin interaction with the axion-like particles. Then, similar to the estimates of (1) and (2) the difference $\Delta J_{pd} = 0.20 +/- 0.05$ Hz may be explained by the influence of the axion-like particles with mass:

$$m_a \approx (800 +/- 200) \text{ eV}/c^2 \quad (4)$$

Another way to estimate the mass m_a (based on (3)) can be obtained by comparing the de Broglie wavelength: $\lambda_i = \pi\hbar/(2m_i E_i)^{1/2}$, where m_i - mass of the particle and E_i - its kinetic energy. We apply this equation for the electron and the axion-like particles. The ratio λ_e/λ_a gives an estimate:

$$m_a \approx m_e(T_e/T_a)(J_a/J_e)^2 \approx (1070 +/- 350) \text{ eV}/c^2 \quad (5)$$

In this case is taken into account: 1) the kinetic energy is proportional to the temperature ($E_i \approx kT_i$); 2) the ratio of the de Broglie waves is inversely proportional to the spin-spin coupling ($\lambda_a/\lambda_e \approx J_e/J_a$). It is assumed that electrons and axion-like particles provide spin-spin coupling in HD independently. For estimates was used: $m_e \approx 0.5 \text{ MeV}/c^2$; $T_e \approx 300 \text{ }^\circ\text{K}$; $T_a \approx 3 \text{ }^\circ\text{K}$; $J_a \approx (0.2 \pm 0.05) \text{ Hz}$; $J_e \approx 43.3 \text{ Hz}$. Two estimates (4) and (5) agree.

References

1. Yu. I. Neronov and N. N. Seregin, JETP Letters, **100**, 609–612. (2014).
2. T. Helgaker, M. Jaszunski, P. Garbacz, and K. Jackowski, Mol. Phys. **110**, 2611 (2012).
3. M. P. Ledbetter, M. V. Romalis, D. F. Jackson Kimball, Phys. Rev. Lett. **110**, 040402 (2013).
4. Yu. I. Neronov and A. E. Barsach, Soviet Physics JETP **42**, 950-958 (1975).
5. M.V. Gorshkov, Yu.I. Neronov, E.N. Nikolaev, Yu.V. Tarbeev, V.L. Talroze, Soviet Physics Doklady the Academy of Sciences of the USSR, **34**, 362-363 (1989).
6. N. N. Aruev and Yu. I. Neronov, Technical Physics, **57**, 1579-1584 (2012).
7. Yu. I. Neronov and N. N. Seregin, Metrologia **51**, 54-60 (2014).
8. Yu. I. Neronov and A. N. Seregin, Measurement Techniques, **53**, 926-935 (2010).

The NMR time scale

N. M. Sergeev

*Department of Chemistry, Moscow state University, Moscow
E-mail: sergeev2010@yandex.ru*

In the literature, it has been proposed various types of time constants for the study of molecular dynamics and chemical kinetics. In numerous textbooks (see, for example [1-3]) argues that the characteristic times of the various physical and chemical methods are available using the uncertainty principle. Thus, the characteristic time of the method can be defined as a value inversely proportional to the frequency ν (Hz) of the quantum transitions for the systems that can be tested with a specific physical method. Nevertheless, based on the uncertainty principle, we can find only an upper limit for the the measured rate constants. Thus, the uncertainty principle limits the range of measured rate constants from one side only. For NMR, this means that when using the spectrometer with operating frequency which is around 10^8 Hz, we can examine only processes with frequencies faster than 10^7 Hz. But this conclusion is usually not very interesting as these rates are found only in particular conditions (at very high temperatures, and for certain types of processes). In addition, the uncertainty principle does not answer the main question - what is the characteristic time of NMR. Uncertainty principle shows that we can not study the processes at speeds prohibited according to this principle, however, we are interested in another question - what can we study using this method. It is a misunderstanding that led Bryant to the conclusion that "any blanket statements about the "NMR time scale" imprecise at best and more often than not completely meaningless". For the method of NMR time scale it can be determined by the introduction of an operational definition of the characteristic time. For all measurements there is always a constant characteristic that shows the most accurate value for this type of measurement, since any real measurement is a statistical procedure that leads to the measured value of θ with the statistical error ($\pm \Delta\theta$). The results of dynamic analysis using NMR line shape indicate that the magnitude of the time scales of NMR various modifications (including ^1H , ^{13}C , ^{19}F -NMR spectra) are different. It is shown that in a series of ^1H , ^{13}C , ^{19}F NMR spectra the limit shifts toward higher speeds from the values of the order of 10^{-1} to 10^{-3} sec for nuclei ^1H to the times of the order of 10^{-3} - 10^{-5} s for ^{19}F nuclei.

References

1. H. Gunther, NMR Spectroscopy. John Wiley & Sons., New York, 1985.
2. L. V Vilkov, Yu. A. Pentin, Physical methods in chemistry, Mir Publishing House, 2006 (In Russian).
3. E. V. Anslyn, D. A. Dougherty, Modern Physical Organic Chemistry, University Science Books 2006s.
4. R. Bryant, J. Chem. Education, 1983, 60, 933-935.

Water mythology

N. M. Sergeev

Department of Chemistry, Moscow state University, Moscow

E-mail: sergeev2010@yandex.ru

Water is of great importance for the life on the Earth, because people almost half consist of water. This explains constant interest of researchers from different fields of science to study the properties and anomalies of water.

Water is famous for its numerous anomalies. Although it is unclear what is considered normal and what is abnormal, still plenty of weirdness on the water is amazing. For example, Martin Chaplin on your website Water Structure and Science has 64 anomalies of water including phase anomalies, anomalies of density, material science anomalies, thermodynamic anomalies, anomalies of physical properties. Water is also a very favorite subject for different myths including declustering water (Penta-water, Nevada), Hayashi microwater (including Lorentz water). Also there are many pseudoscientific legends (the memory of water (Zenin theory, saint water, melting water, magnetic water etc).

Science, too, has not been without the creation of myths and legends. As a member of the Academy of Sciences of the USSR B.V.Deryagin led a group for studying the properties of the so-called anomalous water (60-70 years of the last century) what turned later to be a myth. There are many activities and discussions on magnetic water treatment, when in some papers magnetic water treatment as to detect significant effects on water purification from impurities

In 2007-2012, we participated in an international project to study the properties of spin isomers of water. A group from the Institute of General Physics (Volkov and Tikhonov) was able to separate water using chromatography into two spin isomers (para and ortho isomers). However the further investigations showed that at room temperature to separate water into two spin isomers is not possible due to the rapid proton exchange. However, the astronomical studies have shown that it is possible to determine the ratio of the ortho and para isomers of water for some space objects and these measurements were used to determine the temperature of some comets. Thus the existence of water spin isomers is a reality though separation of water into to isomers at room temperature is a myth.

Cooperativity of Strong Hydrogen Bonds Studied by Liquid State NMR Spectroscopy

*Peter M. Tolstoy*¹, *Benjamin Koeppe*², *Ilja G. Shenderovich*³, *Gleb S. Denisov*⁴,
*Hans-Heinrich Limbach*⁵

¹*Center for Magnetic Resonance, St. Petersburg State University, Russia*

²*Department of Chemistry, Humboldt-Universität zu Berlin, Germany*

³*Institute of Chemistry, University of Regensburg, Germany*

⁴*Department of Physics, St. Petersburg State University, Russia*

⁵*Institute of Chemistry and Biochemistry, Freie Universität Berlin, Germany*

E-mail: peter.tolstoy@spbu.ru

<http://cmr.spbu.ru>

Introduction

It is a common knowledge that hydrogen bonding interaction plays an important role in biochemistry. From the structure of DNA double helix, to the secondary and tertiary structure of proteins, to the structure of water itself – hydrogen bonds (H-bonds) are ubiquitous. Short strong H-bonds with the bridging proton delocalized between two heavy atoms can be considered an extreme manifestation of the phenomenon. Assumptions of the crucial role of strong H-bonds in the enzymatic catalysis – for example in the active site of trypsin, see Fig. 1 – were first made in 1994 [1] and since then this topic has attracted a great attention [2] (not without some criticism [3]).

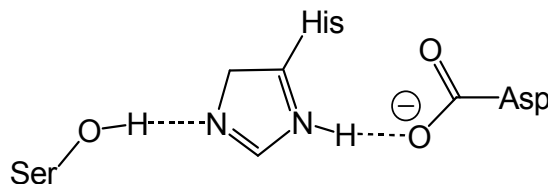


Figure 1. The schematic structure of the catalytic triad in active site of trypsin

According to some authors, short strong H-bond formed in the transition state of the catalytic cycle can reduce the activation energy by 10-20 kcal/mol, which increases the rate of reaction by several orders of magnitude. Other authors explain that the role of short H-bonds is in inducing of considerable atomic charges facilitating nucleophilic reactions without the thermodynamically disadvantageous stage of proton transfer to the substrate. In both cases the geometry of the H-bond, *i.e.* the bridging proton position is at the heart of the question. The issue is further complicated by the mutual influence of several H-bonds often present in the active centers of enzymes. Such cooperative interactions can strengthen (or weaken) neighboring H-bonds. Investigation of the cooperative interactions in complexes with several coupled strong hydrogen bonds is an intensively discussed and fast developing part of the physics of condensed matter.

Methods and objects

One of the most informative methods to study hydrogen bonded complexes is NMR spectroscopy. A number of NMR parameters (f.e. isotropic chemical shifts and spin-spin coupling constants in liquid-state NMR) correlate with the bridging proton position [4, 5]. To measure these parameters often low-temperature NMR is used in order to increase the lifetime of the complexes and to reach the slow proton and molecular exchange regime. Obtained correlational dependencies might then be used to interpret NMR spectra in terms of hydrogen bond geometry and to study the cooperativity effects. The latter can be studied by using H/D isotope effects on geometry as a weak perturbation of the system [6]. Geometric effects translate into H/D isotope effects on NMR chemical shifts and can be indicative to the

cooperative/anticooperative coupling schemes for complexes with several hydrogen bonds [7]. Most of the work reported here was done using small intermolecular H-bonded complexes as model systems. The main types of the studied systems are listed in Fig. 2.

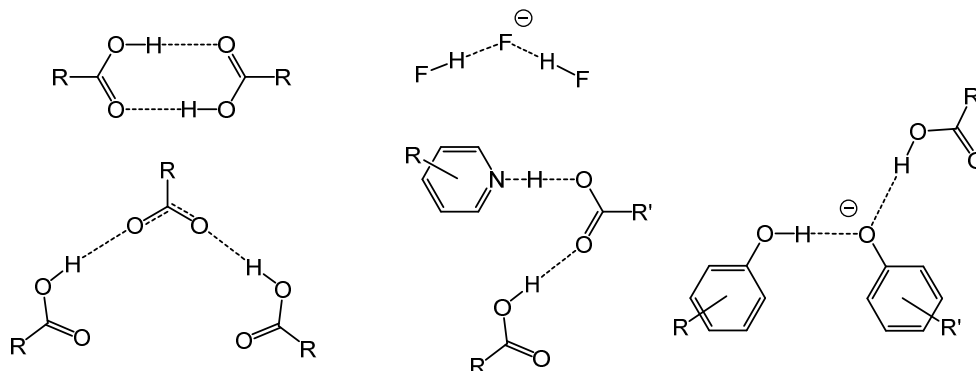


Figure 2. The main types of systems with coupled H-bonds, discussed in this work

Scope of the presentation

Firstly, we will discuss the principle of hydrogen bond correlations, linking NMR observables to the interatomic distances with the hydrogen bridge. Several examples will be given for ^1H , ^{15}N , ^{19}F and ^{13}C NMR chemical shifts. Secondly, the origins of H/D isotope effects on hydrogen bond geometry will be outlined. The spectral manifestations of geometric isotope effects can be rationalized using the previously established hydrogen bond correlations. One of the advantages of studying isotope effects is that in this differential quantity all contributions to the chemical shifts specific for a particular molecule are cancelled. Thirdly, we will illustrate on examples the cooperative and anticooperative coupling schemes in systems with several interacting hydrogen bonds. Cooperativity means mutual strengthening (shortening) of H-bonds, as in the carboxylic acid cyclic dimer (Fig. 2 top left). Anticooperativity means mutual weakening (lengthening) of hydrogen bonds, as in dihydrogen trisacetate (Fig. 2 bottom left). Finally, H/D isotope effects will be employed to reveal the coupling schemes in model systems.

Acknowledgements

This work was partially supported by RFBR grants 14-03-00111 (systems with CH bonds and proton transfer) and 14-03-00716 (systems with coupled OHOHO and OHOHN hydrogen bonds).

References

1. Cleland, W. W.; Kreevoy, M. M., *Science* 1994, 264, 1887; Frey, P. A.; Whitt, S. A.; Tobin, J. B., *Science* 1994, 264, 1927.
2. Northrop, D. B., *Acc. Chem. Res.* 2001, 34, 790.
3. Warshel, A.; Papazyan, A.; Kollman, P. A., *Science* 1995, 269, 102.
4. P.M. Tolstoy, P. Schah-Mohammedi, S.N. Smirnov, N.S. Golubev, G.S. Denisov, H.-H. Limbach, *J. Am. Chem. Soc.* 2004, 126, 5621.
5. H.-H. Limbach, P.M. Tolstoy, N. Perez-Hernandez, J. Guo, I.G. Shenderovich, G.S. Denisov, *Israel J. Chem.* 2009, 49, 199.
6. P. Schah-Mohammedi, I.G. Shenderovich, C. Detering, H.-H. Limbach, P.M. Tolstoy, S.N. Smirnov, G.S. Denisov, N.S. Golubev, *J. Am. Chem. Soc.* 2000, 122, 12878.
7. C. Detering, P.M. Tolstoy, N.S. Golubev, G.S. Denisov, H.-H. Limbach, *Doklady Phys. Chem.* 2001, 379, 1.

Spin Exchange and Magnons in Cold Atomic Hydrogen Gas

Sergey Vasiliev, Otto Vainio, Lauri Lehtonen, Janne Ahokas, Sergey Sheludiakov, Jarno Järvinen

*Department of Physics and Astronomy University of Turku, 20500 Turku, Finland
servas@utu.fi*

We report on an experimental study of electron spin waves (magnons) in the gas of atomic hydrogen. H atoms are stabilized with respect to their recombination by polarizing their electron spins in strong magnetic fields of 4.6 T and temperatures below 0.5 K. Using special hydraulic compression by a piston of superfluid helium we compress the gas to very high densities of the order of $5 \cdot 10^{18} \text{ cm}^{-3}$. At these conditions, the gas is fully in a quantum regime when the thermal de-Broglie wavelength is much larger than the scattering length of atoms in binary collisions. The quantum effects related with indistinguishability of atoms start to play important role and lead to strong spin-exchange. As a result, in such spin changing collisions the spins of the atoms slightly rotate around their sum, exhibiting a phenomenon known as an Identical Spin Rotation (ISR) effect [1]. Accumulating in multiple collisions the ISR leads to a coherent macroscopic oscillations of the transversal component of the spin of the atoms and its propagation through the gas volume in the form of spin waves.

Electron Spin Resonance (ESR) at 130 GHz is used for detection of the atoms, and for manipulation of their electron spins. At high enough densities of the gas, the ESR lines of the H atoms split to several distinct peaks, which are the signatures of the electron spin waves [2]. We found that the quantized electron spin waves (magnons) can be trapped in the maximum of the magnetic field in a similar way as it can be done with real atoms. We show that at high hydrogen gas densities the magnons accumulate in their ground state in the trap and exhibit long-term coherence, profoundly changing the electron spin resonance spectra of the atomic hydrogen gas (fig. 1a). In the decomposition of the free induction decay signal recorded by pulsed ESR, we see the spontaneous emergence of a coherent component (fig. 1b). Such behavior is explained in terms of a Bose-Einstein condensation of trapped magnons [3].

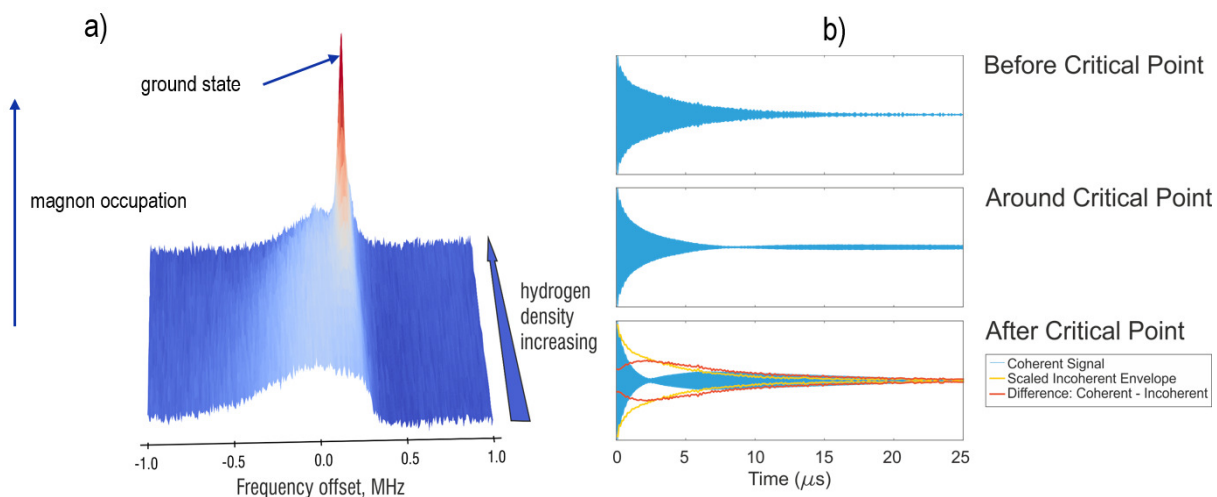


Figure 1

References

1. C. Lhuillier and F. Laloe, *J. Phys (Paris)* **43**, 197 (1982),
2. O. Vainio et. al., *Phys. Rev. Lett.* **108**, 185304 (2012)
3. O. Vainio et. al., *Phys. Rev. Lett.* **114**, 125304 (2015).

Advances in Optical Detection of Magnetization

Valerii S. Zapasskii

Saint-Petersburg State University, Spin Optics Laboratory, Saint-Petersburg, 195504 Russia

Connection between magnetization of a medium and its optical properties was first noticed in 1845 by Michael Faraday who has found that polarization plane of the light transmitted through a magnetized medium is rotated. Since then, a lot of water has flowed under the bridge: now we better understand what happens with light propagating through a magnetized medium and can better measure changes in the state of the light. We have learnt much about how magnetic field affects appearance of the medium, and it became clear that magnetized and non-magnetized bodies look differently – they differently refract light and differently absorb light; they are differently colored in different polarizations and at different angles of observation. Of course, this difference is usually rather small, and the question about whether one can detect it or not depends on sensitivity of the measurements. This is why the advances in optical methods of magnetization detection were largely controlled by increasing sensitivity of the measurements. In particular, a dramatic impact upon development of optical detection of magnetization had the advent of lasers. With the use of laser sources the sensitivity of polarimetric measurements has been increased by several orders of magnitude [1], and optical technique has turned into a standard method of measuring magnetic resonance, magnetic relaxation, and magnetic susceptibility [2, 3]. High spatial resolution and total decoupling of the channels of microwave excitation and optical detection made optical EPR spectroscopy unique for many measurements in the fundamental and applied science. The laser-polarimetric technique could be universally used for EPR detection practically in all transparent paramagnets without matching the wavelength of the probe laser beam to optical spectrum of the particular paramagnet. Further increase in sensitivity of the measurements, based on achievements of the up-to-date electronics, has allowed us to develop a fundamentally new approach to detection of magnetic resonance and spin dynamics – the so-called spin noise spectroscopy or spectroscopy of spontaneous magnetic resonance [4, 5]. This fascinating technique, which allowed us to detect magnetic resonance without its excitation, has substantially enriched arsenal of experimental tools for studying spin dynamics in atomic and semiconductor systems.

In this talk, we will briefly consider basics of optical detection of magnetization and advances in this field of physics for the last several decades.

References

1. V. S. Zapasskii, *J. Appl. Spectrosc.* 37, 857–869 (1982).
2. V. S. Zapasskii “Optical detection of spin-system magnetization in rare-earth-activated crystals and glasses” in *Spectroscopy of Solids Containing Rare Earth Ions*, A. A. Kaplyanskii and M. F. Macfarlane, eds. (Elsevier, 1987), pp. 674–711.
3. E. B. Aleksandrov and V. S. Zapasskii, *J. Sov. Laser Res.* 6, 291–296 (1985).
4. E. B. Aleksandrov and V. S. Zapasskii, *J. Exp. Theor. Phys.* 54, 64–67 (1981).
5. V.S.Zapasskii, *Adv. in Opt. Phot.*, vol. 5, 131-168 (2013)

Oral Reports

NMR study of Phthalocyanine solubility in Pluronic solutions

*Ekaterina S. Babicheva*¹, *Nataliia S. Shubina*¹, *Alexander M. Perepukhov*¹,
*Alexander V. Maximychev*¹, *Vladimir M. Negrimovsky*²

¹Moscow Institute of Physics and Technology (State University)

²GNTS RF "NIOPIK"

E-mail: babicheva.es@mipt.ru

Introduction

Phthalocyanines is a class of organic compounds widely used in light industry and medicine as dyes and photosensitizers in photodynamic therapy [1]. The majority of these substances are highly-hydrophobic, so it becomes difficult to use them in aqueous media. We studied the solubilization of model phthalocyanine in water solution of Pluronic F68 (Fig.1a) with NMR spectroscopy. Octasense (Fig. 1b) was used as a model phthalocyanine.

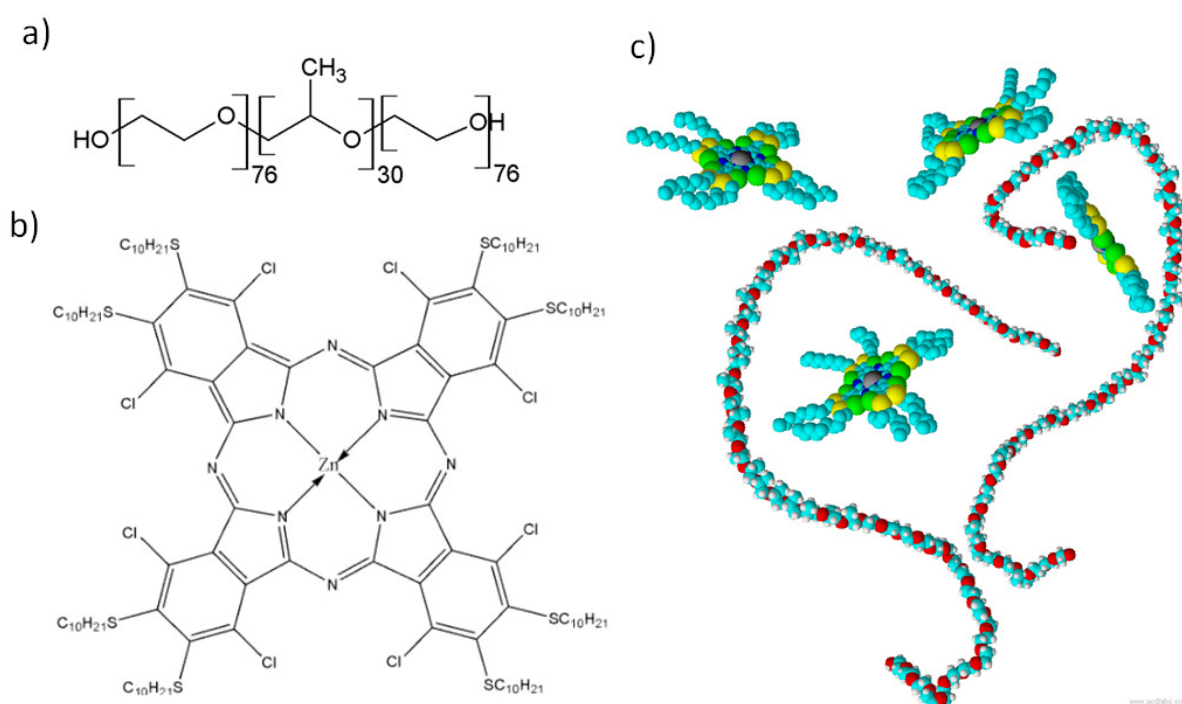


Figure 1. Structures of octasense (a) and pluronic F68 (b) and 3D image of pluronic and phthalocyanine system (c)

Experiments and results

NMR spectra were acquired on Varian Unity Inova 500 spectrometer with Larmor frequency 500 MHz for ¹H. Solutions of pure Pluronic F68 in D₂O were prepared with concentrations 0.1, 0.5, 2.5, 5.0, 10.0, 20.0, 30.0, and 40.0% by weight. The micellization process was studied by the changes of chemical shifts in ¹H NMR spectra which was registered for solutions with different concentrations of F68 at various temperatures. The new proton signal appears at 3.40 ppm both for heated and concentrated solutions (Fig 2). The appearance of such signals is usually attributed to micellization processes. [2, 3]. The concentration dependence of critical micellar temperature (cmt) was obtained and the value of critical micellar concentration (cmc) for room temperature was appraised at 35%.

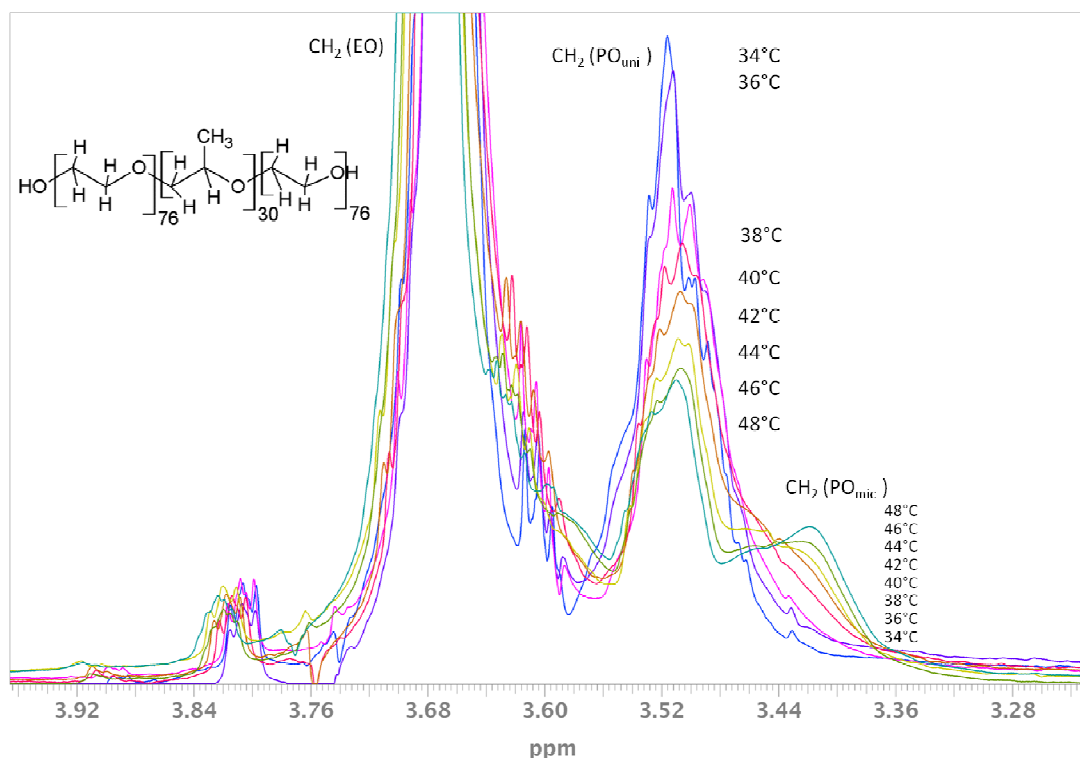


Figure 2. ¹H NMR spectra of F68 at various temperatures

Samples of phthalocyanine in pluronic were prepared by addition of octasense to F68 solution below cmc. The temperature dependence of NMR spectra of these samples shows that the presence of octasense does not affect cmc of pluronic.

If a supramolecule complex of octasense with F68 is formed it will be characterized by a single self-diffusion coefficient (D). However, results of Diffusion Ordered Spectroscopy (DOSY) reveal significant difference between diffusion coefficients (Fig. 3) of octasense and F68 indicating that they do not form a single structure.

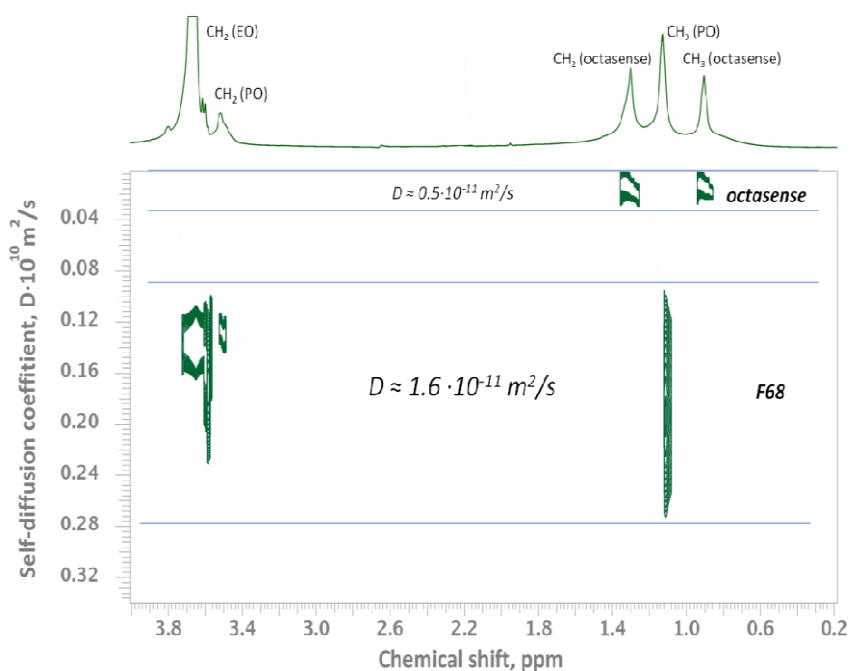


Figure 3. DOSY spectra of 10% F68 + octasense in D₂O

Thus it has been shown that the presense of octasense in pluronic media is not affecting surfactant aggregation. The detailed mechanism of solubilisation of octasense still be a subject of futher investigations.

References

1. Patent RF № 2164136 C2, 09.09.1998. *Lukyanets E.A.* [et al.]. Photosinsebilizer for photodynamic therapy.
2. J. Ma et al. — *J. Colloid Interface Sci.*, 312, 390–396 (2007).
3. J. Ma et al. — *J. Phys. Chem. B*, Vol. 111, No. 47, 13371–13378 (2007).

Determination of T1 and T2 relaxation times from stationary saturation of inhomogeneously broadened EPR lines

Yu. V. Bogachev¹, A. V. Nikitina¹, S. M. Sukharzhevskii²

¹*Department of Physics, Saint-Petersburg Electrotechnical University "LETI", 5, prof. Popov st., Saint-Petersburg, 197376, Russia*

E-mail: Yu.Bogachev@mail.ru

²*Magnetic Resonance Research Center, St. Petersburg State University, St. Petersburg, Russia*

Abstract

The analysis of stationary saturation of inhomogeneously broadened electron paramagnetic resonance (EPR) lines has been carried out under the magnetic field's modulation and adiabatic slow scanning. The dependence between the EPR signal intensity and saturation factor, the number of spin packets and magnetic field's modulation amplitude was also determined. The new method for T_1 and T_2 relaxation times determination of spin systems with inhomogeneously broadened EPR lines has been developed.

Introduction

Recently, extensive attention is attracted to the study of molecular nanomagnets as the fundamental units of quantum information (q-bits) in the development of quantum computers [1]. Quantum states of unpaired electrons in such systems depend on the interaction of electron spins as each other, well as the interaction with the surrounding nuclear spins, and the dynamics of spin systems in time. These effects lead to the decoherence of quantum states of unpaired electrons, which appears in inhomogeneous broadening of EPR lines. The most informative parameters to assess the effects of decoherence are the spin-lattice T_1 and spin-spin T_2 relaxation times.

For the determination of T_1 and T_2 relaxation times in EPR spectroscopy commonly use the method of stationary resonance microwave power saturation [2, 3] and the method of pulsed EPR [4, 5]. Using the method of pulsed EPR is limited by insufficient prevalence of pulsed EPR spectrometers.

Effects of stationary saturation of inhomogeneously broadened EPR lines consisting of spin packets are described by the relations of Bloembergen-Purcell-Pound (BPP) theory [6-8].

The influence of the magnetic field's modulation on the characteristics of stationary saturation of inhomogeneously broadened EPR lines is described in works [9-11].

The results of [7-11] are valid only for the case of weak saturation. Expressions for first harmonics of absorption signal obtained in [9-11] are difficult to use for experimental determination of T_1 and T_2 relaxation times.

Results and discussion

We performed the analysis of stationary saturation of inhomogeneously broadened EPR lines with magnetic field's modulation at a frequency ω_m under adiabatic slow passage ($\omega_m \ll T_2^{-1}, T_1^{-1}$).

We suppose that the inhomogeneously broadened EPR line consists of non-interacting spin packets, each of that is characterized by a Lorentzian absorption line

$$g(\omega - \omega') = \frac{T_2}{\pi} \frac{1}{1 + (\omega - \omega')^2 \cdot T_2^2}$$

Magnetic field modulation is described as $\omega = \omega(t) = \omega + \gamma H_m \cos(\omega_m t)$, where ω_m and γH_m – the frequency and amplitude of modulation.

We obtained the following equation for the first harmonic of the EPR absorption signal:

$$I_1 = \chi_0 \omega_0 \sqrt{\frac{T_2}{T_1}} \frac{s}{\gamma b \sqrt{1+s^2}} \int_0^\infty J_1(\alpha A_m) \sin(y\alpha) \exp\left(-\frac{\alpha^2}{4} - \alpha \cdot \frac{\sqrt{1+s^2}}{b}\right) d\alpha \quad (1)$$

Equation (1) determines the dependence of form and intensity of the first harmonic absorption signal on the saturation factor s , the number of spin-packets b and the normalized amplitude of magnetic field modulation A_m .

We performed the computer simulation of saturation curves of the first harmonic of the EPR absorption signal in dependence on the s^2 and b . We propose a simpler and more accurate (than [9, 11]) method for determining of T_1 and T_2 relaxation times of inhomogeneously broadened EPR lines.

This method uses the normalized saturation curves $I_{1m} / I_{1mm} = f(s^2 / s_m^2)$ where I_{1mm} – maximum value of the function I_{1m} at $s = s_m$. Graphs of the dependence $I_{1m} / I_{1mm} = f(s^2 / s_m^2)$ for $A_m = 0.1$ and different values of b are shown in Fig. 1.

Values s_m , H_{1m} and $P_{\omega m}$ correspond to the maximum of saturation curve. P_ω – microwave power incident on the sample in the resonance cavity of the EPR spectrometer.

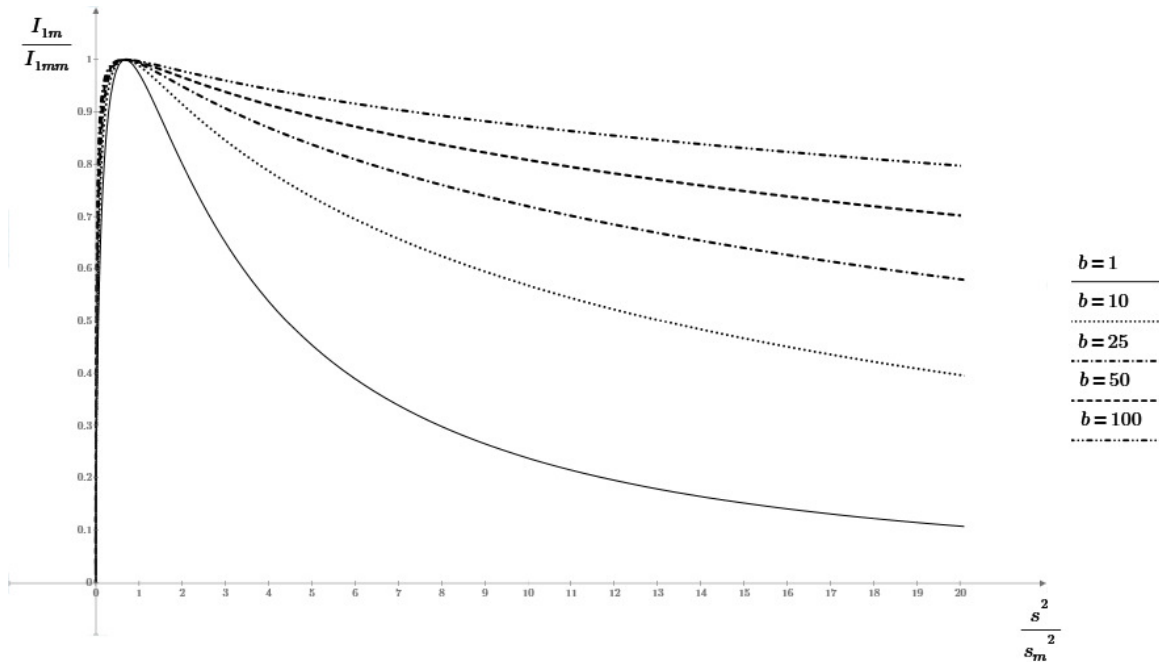


Figure 1

From the graphs in Fig.1 (for certain values of b) it is possible to determine any of the parameters: $q_{0.5} = (s_{0.5as}^2 / s_m^2)$; $q_{0.6} = (s_{0.6as}^2 / s_m^2)$; ...; $q_{0.9} = (s_{0.9as}^2 / s_m^2)$, where $s_{0.5as}$, $s_{0.6as}$, ... , $s_{0.9as}$ – saturation factors values at the levels when $I_{1m} / I_{1mm} = 0.5; 0.6; \dots; 0.9$ respectively. « As » index (after saturation) shows that the saturation factor values are determined from the graph on the right, after the point of maximum of normalized saturation curve. We have constructed the nomograms $q_i(b)$ and $s_m = f(b)$.

Using the most optimal parameter q_i , on that from nomograms $q_i(b)$ it is possible to determine the number of spin-packets b . Then from relation $b = \Delta\omega_2 \cdot T_2$ using the experimental value of $\Delta\omega_2$ (the width of inhomogeneously broadened EPR line) we can find experimental value of T_2 .

From the nomogram of $s_m = f(b)$, using the value of b we can determine a value of s_m relevant to our experiment. On the other hand

$$s_m = \gamma H_{1s}^{1.0} \sqrt{T_1 T_2} . \quad (2)$$

Value $H_{1s}^{1.0}$ corresponding to the maximum of saturation curve is associated with the value of microwave power P_{om} [3]:

$$\left(H_{1s}^{1.0}\right)^2 = 2 \cdot 10^{-3} \cdot P_{om} \cdot Q_L \cdot \eta \cdot \frac{V_\omega}{V_s} , \quad (3)$$

where Q_L – quality factor of a resonance cavity, η – fill factor, V_ω – a volume of the waveguide, V_s – a sample volume.

According to the experimental value of the microwave power P_{om} found from (3) it is possible to determine $H_{1s}^{1.0}$. Then, based on the calculated values of $s_m, T_2, H_{1s}^{1.0}$ we can to determine the value of T_1 from an equation (2).

Conclusion

Thus, we have developed a method of determining of T_1 and T_2 relaxation times for spin systems with inhomogeneously broadened EPR lines in the stationary saturation EPR experiment. A comparison of our method with the method of pulse EPR [4, 5] shows that the last requires the using of a special and more expensive equipment.

References

1. Troiani F., Affronte M. Molecular spins for quantum information technologies. // Chem.Soc.Rev. 2011. Vol.40. P.3119-3129.
2. Lebedev Y.S., Muromtsev V.I. EPR and relaxation of stabilized radicals. - M.: Chemistry, 1972, 256 p.
3. Pool C. EPR spectroscopy technique. - M.: Mir, 1972, 558 p.
4. Salikhov K.M., Semenov A.G., Tsvetkov Y.D. Electronic spin echo and its application. – ‘Science’ Novosibirsk Publishing House, 1976, 344 p.
5. Schweiger A. and Jeschke G. Principles of Pulse Electron Paramagnetic Resonance. - Oxford University Press, Oxford, 2001, 578 pp.
6. Bloembergen N., Purcell E.M., Pound R.V. Relaxation effects in nuclear magnetic resonance absorption // Phys.Rev. 1948. Vol.73. P.420.
7. Portis A.M. Electronic Structure of F- Centers. Saturation of the Electron Spin Resonance. // Phys.Rev. 1953. Vol.91. No.5. P.1071.
8. Castner T.G. Saturation of the Paramagnetic Resonance of a V Center // Phys.Rev. 1959. Vol. 115. No.6. P.1506.
9. Zhidkov O.P., Lebedev Y.S., Mikhailov A.I., Provotorov B.N. Deduction of relaxation parameters from saturation in non-uniformly broadened ESR lines. // Theoretical and Experimental Chemistry. 1969. Vol. 3. Issue 2 . P. 135-139.
10. Khutsishvili G.R. Saturation of the magnetic resonance inhomogeneously broadened line // JETPh. 1966. T.50. No.6. P. 1641.
11. Bowman M.K., Hase H., Kevan L. Saturation Behavior of Inhomogeneous Broadened EPR Lines Detected with Magnetic Field Modulation // J. Magn. Reson. 1976. Vol.22. P.23-32.

Diagnostic value of in vivo 1H-MRS with short and long Echo Time for patients with Multiple Sclerosis

A. A. Bogdan, G. V. Kataeva, Yu. G. Khomenko, A. G. Il'ves, L. N. Prakhova

N.P. Bechtereva Institute of the Human Brain, Russian Academy of Sciences, St.Petersburg
E-mail: andrey.a.bogdan@gmail.com

Introduction

Possibilities of modern neuroimaging methods considerably extended with introduction to clinical practice of the magnetic resonance spectroscopy (MRS). This technique based on the phenomenon of nuclear magnetic resonance (NMR) and so-called "chemical shift" provides independent biochemical information about concentration of several metabolites into the brain and has become an invaluable adjunct to MRI and other imaging modalities. For researches of the central nervous system (CNS) the proton MRS (1H-MRS) which allows to estimate concentration of such metabolites as N-acetylaspartate (NAA) (a marker of neuronal integrity), creatine (Cr) (reflects ATP metabolism), choline and choline-containing compounds (Cho) (considered to be the marker of membrane integrity), and also myoinositol (mI), lactate (Lac), glutamine-glutamate complex (Glx), and even, under certain circumstances, gamma aminobutyric acid (GABA) is used.

However, quality of the signal received from metabolites directly depends on physical parameters of the impulse sequence used, namely on Time of Echo (TE). The less this parameter is (TE 5-70ms), the more metabolites could be assessed. For "long" TE (>100 ms) only NAA, Cr, and Cho are "visible" (and a pathological Lac if it is present in the tissue under investigation). The peak of Lactate has one more feature — it can be partially inverted, and for its calculation we need to use only specified TE (different manufacturers recommend 135 and 270, 144 and 288 ms).

Although short TE is considered more precise in evaluating of main metabolites (NAA, Cr, Cho) concentration, at long TE the attenuation of signals from metabolites with more short time of relaxation improve the signal-to-noise ratio of these three metabolites which are the most often used for clinical purposes.

Table 1. Known advantages and disadvantages of short and long TE

TE	5-70 ms	>100 ms
mI, Glx	Picks are visible	Picks are invisible
Background noise level	high	low
Lactate visibility	Pick is invisible	Visible at 144 or 288 ms

Considering all above-mentioned features, we decided to compare MRS data acquired at two various TE (53 and 144 ms) for patients with the multiple sclerosis (MS) and healthy volunteers, and to evaluate advantages and disadvantages of these two Echo Time in clinical practice.

Methods

Multivoxel H-MRS was performed on Achieva 3T scanner (2D PRESS 1H-MRS (TE= 53 and 144 ms, TR=2000 ms) and included supraventricular white matter (WM) and medial cortex. Anatomical localization: the area of MRS study (8*9 voxels (10*10*15 mm), whole volume 80*90*15 mm) was divided into 9 ROIs: 6 in WM (3 ROIs: anterior, medium and posterior for each hemisphere) and 3 ROIs in medial cortex (See Fig.1). NAA/Cr and Cho/Cr ratios (NAA – N-acetylaspartate, Cr – creatine, Cho – choline,) were analyzed.

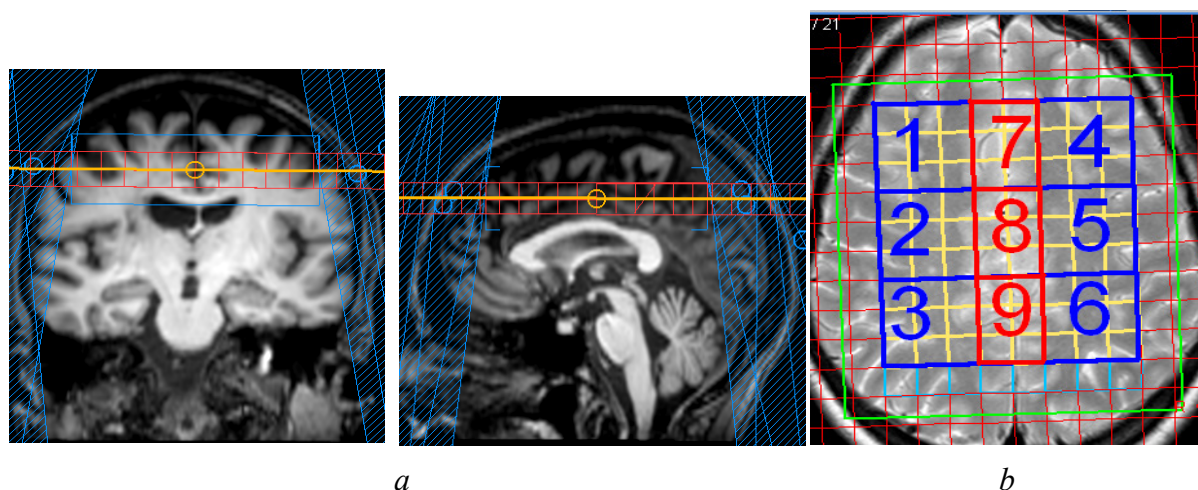


Figure 1. (a) – Anatomical localization of Region of interest
 (b) ROIs 1-6 – white matter, ROIs 7-9 – gray matter (medial cortex)

Table 2. NAA/Cr comparison at TE 144 and 53 ms

Metabolites ratio*	Control group		RRMS		SPRS		p**
	Mean	SD	Mean	SD	Mean	SD	
NAA/Cr_144_1	2.04	0.17	1.94	0.24	1.72	0.14	0.0001
NAA/Cr_144_2	2.18	0.18	1.99	0.23	1.80	0.21	0.0001
NAA/Cr_144_3	2.05	0.18	1.92	0.19	1.78	0.13	0.0001
NAA/Cr_144_4	2.08	0.13	1.91	0.18	1.71	0.11	0.0000
NAA/Cr_144_5	2.26	0.18	2.01	0.26	1.81	0.16	0.0000
NAA/Cr_144_6	2.15	0.18	1.99	0.22	1.80	0.18	0.0000
NAA/Cr_144_7	1.68	0.12	1.55	0.13	1.43	0.11	0.0002
NAA/Cr_144_8	1.68	0.13	1.60	0.15	1.46	0.11	0.0000
NAA/Cr_144_9	1.68	0.12	1.63	0.11	1.49	0.14	0.0001
NAA/Cr_53_1	1.67	0.27	1.58	0.12	1.46	0.12	0.0154
NAA/Cr_53_2	1.73	0.22	1.65	0.14	1.47	0.10	0.0011
NAA/Cr_53_3	1.75	0.27	1.67	0.16	1.53	0.22	0.1419
NAA/Cr_53_4	1.61	0.20	1.58	0.14	1.96	1.34	0.1077
NAA/Cr_53_5	1.82	0.25	1.68	0.19	1.81	0.58	0.0717
NAA/Cr_53_6	1.73	0.19	1.67	0.20	1.62	0.23	0.2499
NAA/Cr_53_7	1.41	0.14	1.35	0.11	1.44	0.25	0.1075
NAA/Cr_53_8	1.38	0.11	1.33	0.11	1.32	0.11	0.1972
NAA/Cr_53_9	1.46	0.12	1.38	0.10	1.40	0.11	0.0731

Notes:

* – NAA/Cr ratio in different ROIs (see Fig.1) with various TE (144 and 53 ms);

** – Kruskal-Wallis test

In total 25 patients with the confirmed diagnosis of relapsing-remitting multiple sclerosis (RRMS), 20 patients with the diagnosis of secondary progressive multiple sclerosis, (SPRS) were examined. The control group consisted of 21 healthy volunteers, comparable on age. For suppression of a signal from bones of a skull 10 strips of a saturation were used, the

research was conducted with use of automatic shimming of PencilBeam-auto (PB-auto) and water suppression (see Fig. 1).

Results

The main results are presented in Table 2: NAA/Cr ratios received at TE=144 ms significantly differed in all 3 groups (according to the Kruskal-Wallis test) while at TE of 53 ms this difference reaches significance only in white matter of the right hemisphere (areas 1 and 2 according to fig. 1).

At the same time the greatest NAA/Cr values were observed in control group, at RRMS they were lower, and reached the minimum values in the SPMS group, that mean that the aggravation of symptoms was accompanied by NAA/Cr depression [1]. At TE=53 ms the same patterns of change of NAA/Cr were observed, however they did not reach the statistical significance.

The difference in Cho/Cr ratio was not significant.

Thus, the received results allow to conclude that TE = 144 ms is better for discriminate MS patients and control group based on NAA/Cr values, due to smaller variability of data.

References

1. Barker P.B. Bizzi A., De Stefano N., Gullapalli R.P., Lin D. M. Clinical MR Spectroscopy: Techniques and Applications. Cambridge University Press, 2009.

Molecular mobility and translational diffusion analysis of ionic liquid (methyl-octyl imidazolium chloride) in mixture "water – glycerol" by NMR

Sergei S. Bystrov, Prof. Dr. Vladimir I. Chizhik

*Department of Nuclear-Physics Research Methods, Faculty of Physics,
Saint-Petersburg State University
E-mail: barigapunk@gmail.com*

Introduction

Ionic liquids (IL) are defined as ionic compounds that are characterized by a melting point below 100°C. Cations determine mainly physical properties of IL (melting point, viscosity, density), whereas anions determine chemical properties. Since the physical and chemical properties of ILs can be adapted to the specific conditions by careful selection of types of cations and anions, IL have become widely used in many scientific and industrial applications [1-3].

Self-aggregation in ionic liquids

It is well known that IL molecules as well as surface-active substances (SAS) due to their amphiphilic nature are capable of forming molecular aggregates also called micelles. Figure 1 represents different types of these aggregates

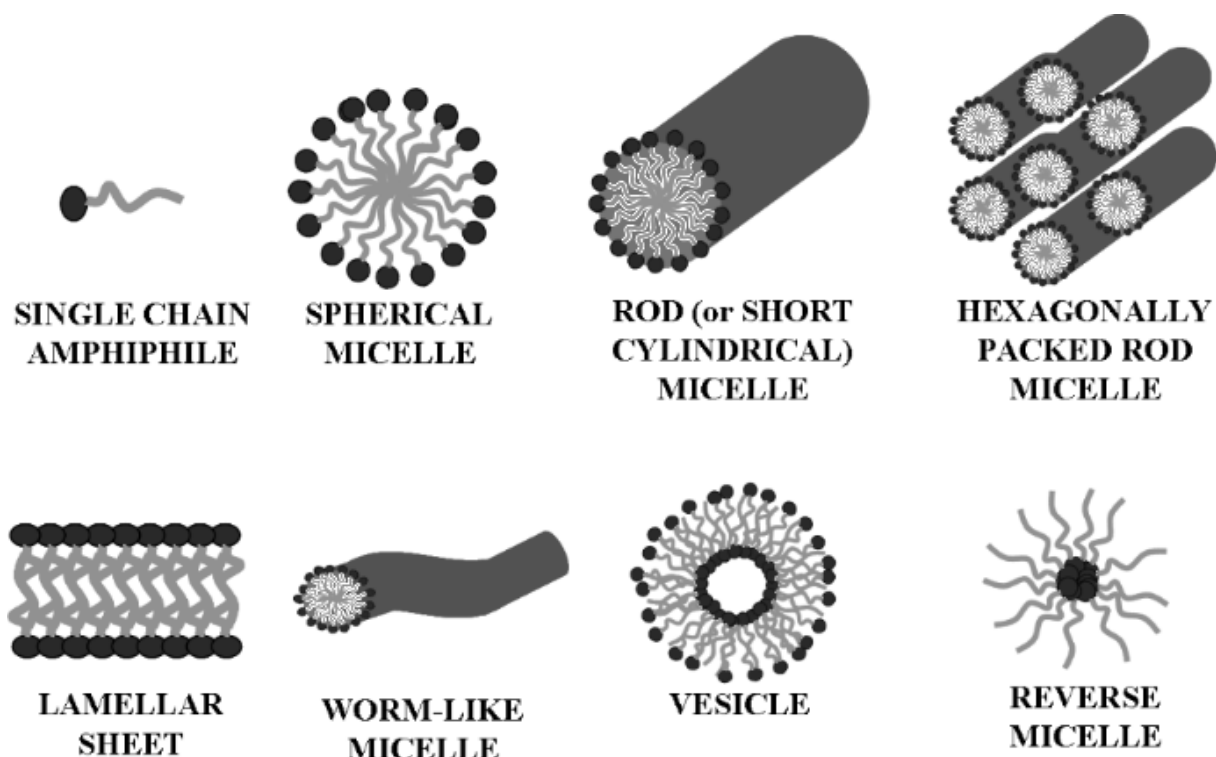


Figure 1. Types of molecular aggregates

Results

Formulation of the problem

This research is devoted to the study of the effects of glycerol media on the micellization of IL in aqueous solutions that is of great interest for cosmetology, pharmaceuticals and other industries. One of most commonly used types of ILs nowadays is based on imidazolium ring due to their unique chemical properties and easiness of variation of

cations and carbon backbones. Up to the present moment there were only a few works related to micellization in glycerol media but they were focusing at systems with SAS. The significant work in this aspect has been undertaken and the latest results are summarized in the present paper.

Theoretical model

There exist two commonly used models for describing micelle formation: model based on law of mass action and phase separation model. In the first model, we consider the equilibrium of complexes of two types: monomeric and micellar. In the second model, which is much more convenient for experimental data interpretation, we consider any experimental quantity as an average of two complemented states: free and bonded into micelle. Thus, from experimental data analysis we can obtain physical and chemical properties related to these states. In our research, we will be focusing only at second model.

Basic results

The research of the system (IL-glycerol-heavy water) was carried out at the Bruker 500 MHz facility by high resolution NMR and stimulated echo technique with bipolar gradient pulse (bpSTE). The existence of molecular aggregates in water-glycerol media was confirmed. Aggregation process is not abrupt and takes place in a wide concentration range from slightly to strongly bound micelles. Isotopic exchange of H \leftrightarrow D was investigated. IL aggregation degree affects the rate of this exchange. Micellization concentration range for this system was obtained: 2 points of interest reveal in concentration range from 0.05 to 1.2 mol/l that may be referred to different formations of micelle. Glycerol molecules, as well as water molecules, form coordination sphere of molecular aggregates and translate as a whole within the micelle.

Acknowledgements

We express our gratitude to the Center for Magnetic Resonance at Saint-Petersburg State University for the assistance provided in this study.

References

1. Ruiz C. C., D.Lopez L., Aguiar J. Micellization of Sodium Dodecyl Sulfate in Glycerol Aqueous Mixtures // Journal of Dispersion Science and Technology. 2008. Vol. 29, no. 2. Pp. 266–273.
2. Wang H., Wang J., Zhang S., Xuan X. Structural Effects of Anions and Cations on the Aggregation Behavior of Ionic Liquids in Aqueous Solutions // J. Phys. Chem. B. 2008. Vol. 112, no. 51. Pp. 16682–16689.
3. Pino V., Yao C., Anderson J. L. Micellization and interfacial behavior of imidazolium-based ionic liquids in organic solvent – water mixtures // Journal of Colloid and Interface Science. 2009. Vol. 333, no. 2. Pp. 548–556.

Magnetic resonance spectroscopy as a tool for magnetometry of Earth magnetic field

A. V. Chudin, A. V. Ievlev

Saint Petersburg University, Department of Nuclear-Physics Research Methods, Nuclear magnetic resonance

E-mail: andrei.chudin@gmail.com

Introduction

Field magnetometry (magnetic survey) - one of the main methods of applied geophysics. It is in use for more than half a century. Many methods of interpretation of magnetometric data have been developed during this period [1].

Many ordinary software tools (math algorithms) for "big data" (to which the data of magnetometric survey it certainly relate) became available to researchers with the increasing computing power of personal computers [2, 3].

More and more of possible instruments has become available with use powerful hardware of Research Park of St. Petersburg State University. With help of applying of these modern instruments the tasks of analysis of magnetic data can reach a qualitatively new level informativeness and reliability.

We use the following tools: kappametry, the SQUID-magnetometry, IRM, TRM and NMR methods, NMR and EPR spectrometers.

Results and Discussion

In this report, we will focus on the application of the above methods in applied geophysics and archeology. Having a great experience in this field, we are engaged in the study of historical and cultural monuments such as the fortress Koporje; ruins of old estates, churches and temples. The study of the physical properties of soil samples in the laboratory will accurately interpret the data obtained in the magnetometric survey of such objects.

More detailed information on the results of our work can be found at the time of presentation of the report.

References

1. Natural science methods in field archaeology, with the case study of Crimea T. N. Smekalova, E. B. Yatsishina, A. S. Garipov, A. E. Pasumanskii, R. S. Ketsko, A. V. Chudin, Crystallography Reports, Volume 61, Issue 4, 1 July 2016, Pages 533-542. DOI 10.1134/S1063774516030251
2. Discovering geo-magnetic anomalies: a clustering-based approach Elena Volzhina ; Andrei Chudin ; Boris Novikov ; Natalia Grafeeva ; Elena Mikhailova. 2016, Page(s):1-7 Intelligence, Social Media and Web (ISMW FRUCT), 2016 International FRUCT Conference
3. The Discovery of an Ancient Greek Vineyard. Smekalova, T.N., Bevan, B.W., Chudin, A.V., Garipov, A.S. ARCHAEOLOGICAL PROSPECTION. Volume 23, Issue 1, 1 January 2016, Pages 15-26. DOI: 10.1002/arp.1517

Advanced processing of CP-MAS kinetics in Ammonium Dihydrogen Phosphate

Laurynas Dagys, Vytautas Klimavičius, Vytautas Balevičius

*Department of General Physics and Spectroscopy, Vilnius University,
Sauletekio 9-3, Vilnius LT-10222, Lithuania*

E-mail: dagys.laurynas@gmail.com

Introduction

Complex solids, such as ammonium dihydrogen phosphate (ADP), are gaining interest because of their unique features. However, characterizing the distribution of various chemical species in such complex materials is an extremely challenging task, where the most traditionally used X-ray (XRD) and neutron diffraction (ND) methods do not provide detailed or enough rigorous information [1]. In this work, $^1\text{H} \rightarrow ^{31}\text{P}$ CP-MAS kinetics in ADP was investigated. Variable temperature and high data point density measurements provided enough information for detailed analysis. Hence, in this work mathematical route of processing CP-MAS data is presented and results are compared with those obtained using XRD and Neutron diffraction ND techniques.

Experimental setup

NMR measurements were carried out on Bruker AVANCE III HD spectrometer operating at resonance frequencies of 400 and 162 MHz for ^1H and ^{31}P , respectively, at different temperatures from -40°C to $+90^\circ\text{C}$, stepping by 10° . MAS measurements for $^1\text{H} \rightarrow ^{31}\text{P}$ CP were performed at 7 and 10 kHz. A rectangular variable contact time pulse shape was used in CP-MAS experiments in order to fulfill one of Hartmann-Hahn matching conditions. The RF fields were 90 kHz and 80/83 kHz (depending on MAS rate) for ^{31}P and ^1H , respectively. The ^1H $\pi/2$ polarizing pulse was $2.5 \mu\text{s}$, the repetition delay was 2 s. A 4 mm 80 μl zirconia rotor was used for all measurements. NMR spectra were processed using Topspin 3.2 software. The signal shapes and CP kinetic curves were processed using *Microcal Origin 9* and *Matchad 15* packages. Commercial ammonium dihydrogen phosphate (powdered), from Reachem Slovakia, 99% purity, was used without additional purification.

Results and analysis

The CP kinetics observed in powdered ADP exhibit the blurred oscillation of intensity in the short- and moderate contact time range (Fig. 1). When the oscillation of CP kinetics was first observed, it was deduced that the frequency of oscillation depends on the orientation of the crystal and it is equal to one-half of the dipolar splitting [2]. The CP kinetics was described by the equation

$$I(t) = I_0 e^{\frac{-t}{T_{1\rho}}} \left[1 - \frac{1}{2} e^{-k_2 t} - \frac{1}{2} e^{-k_1 t} \cos\left(2\pi \frac{b}{2} t\right) \right],$$

where $T_{1\rho}$ is the spin-lattice relaxation time in the rotating frame, k_1 and k_2 are rate constants which describe the decay of the oscillations and b is the dipolar splitting. Equation is valid only for single crystal with only one equivalent spin pair, but authors also provide a way to understand this effect in the powdered samples. If one has such sample where crystallites have random size spin pairs, previous equation has to be averaged over all distances.

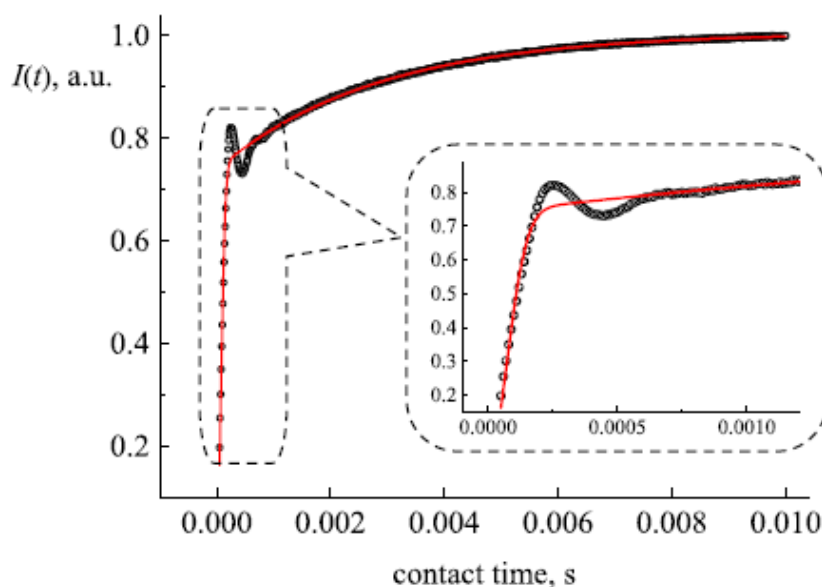


Figure 1. ^1H - ^{31}P CP-MAS kinetics in powdered ADP for $n=1$ Hartmann-Hahn condition. Sample was spun at 7 kHz MAS rate in room temperature. Curve fitting was done using Eq. 2

Then using Fourier series for short delays or weak dipolar interactions, cosine function can become Gauss function. This assumption can be used in different equations. However, in this work different starting point equation was used:

$$I(t) = I_0 \left\{ \left[e^{\frac{-t}{T_{1\rho}}} - e^{-k_1 t} g(t) \right] + \frac{N-1}{N+2} \left[e^{\frac{-t}{T_{1\rho}}} - e^{-k_2 t} \right] \right\},$$

where N is number of equivalent spin pairs, $g(t)$ is a function that describes oscillatory behavior. This model includes MAS motion as well as possible spin pair clustering [3]. Fitting such model gives parameters which can be subtracted from experimental curve. This leaves only oscillatory part I_{osc} which then can be analyzed. In present work, it was derived how this term can be transformed to the dipolar constant distribution $P(D)$ that is completely averaged over all angles and distances.

$$P\left(\frac{D/\sqrt{2}}{2}\right) \approx \int_0^\infty [I_{osc}(t)\sqrt{t}] \cos\left(2\pi \frac{D/\sqrt{2}}{2}\right) dt.$$

The results of this processing of experimental CP-MAS kinetics including the recalculation of $P(D)$ from D -variable to internuclear distances r are presented in Fig. 2. It is seen, that complete averaging gives out more pronounced results which are in a good resemblance with other crystallographic data (Table 1). Despite that, CP-MAS kinetic curves measured at different temperatures shows macroscopic feature of spin dynamics. As it was seen spin diffusion tends to accelerate at higher temperatures. Hence, spin diffusion is easily activated in explored temperature range. This proves that NMR CP-MAS technique can also give an additional results beside complementary ones.

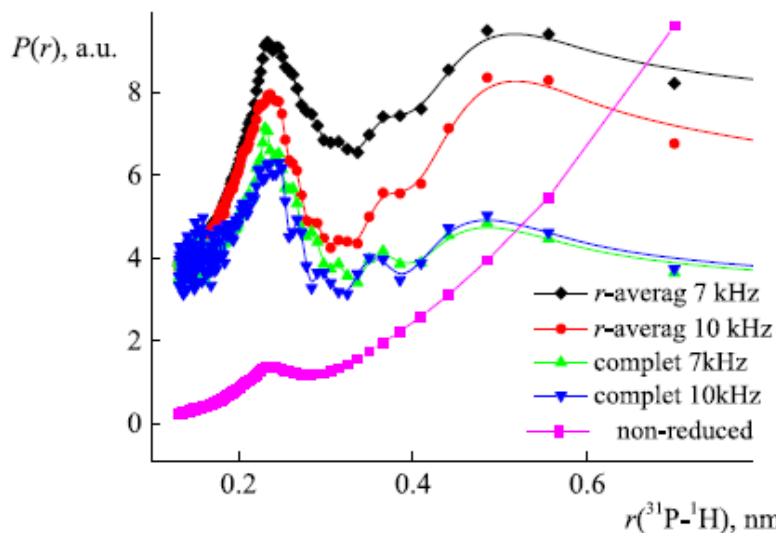


Figure 2. Spatial distributions of protons surrounding ^{31}P nuclei in the powdered ADP at 7 and 10 kHz MAS. For comparison, results of other mathematical approaches is shown

Table 1. Peak position (in nm) of the spatial distribution of protons surrounding ^{31}P nuclei in powdered ADP compared to ND and XRD data (from [4])

Method	Peak 1	Peak 2	Peak 3
7 kHz MAS r-averaging	0.239	0.376	0.507
10 kHz MAS r-averaging	0.237	0.376	0.507
7 kHz MAS complete av.	0.234	0.364	0.476
10 k Hz MAS complete av.	0.236	0.357	0.479
Neutron diffraction	0.219-0.222	0.33-0.344	0.429-0.444
X-ray diffraction	0.235-0.244	0.329-0.335	0.430-0.441

Conclusion

The advanced route of CP-MAS kinetic data processing has been developed. It is based on reducing the incoherent far range order spin couplings and extracting the CP oscillatory term. Obtained peak positions show a good resemblance to the ND and XRD data. Despite that, the variable temperature experiments have revealed that the more pronounced effect that was seen out of the experimental error was the increase of the CP rate constant k_1 upon heating. These results can be considered as a certain step developing NMR crystallography for complex solids in a complementary way through the kinetics of CP transfer.

Acknowledgements

We would like to acknowledge Center of Spectroscopic Characterization of Materials and Electronic/Molecular Processes (Scientific infrastructure „SPECTROVERSUM“) at Lithuanian National Center for Physical Sciences and Technology for the use of spectroscopic equipment. We thank Professor Maria Gdaniec for the help collecting and analyzing crystallographic data.

References

1. E. Davies, M. J. Duer, S. E. Ashbrook, J. M. Griffin – *J. Am. Chem. Soc.*, **134**, 12508 (2012).
2. W. Kolodziejski, J. Klinowski – *Chem. Rev.*, **102**, 613 (2002).
3. G. Mali, N. Rajić, N. Z. Logar, V. Kaučič – *J. Phys. Chem. B*, **107**, 1286 (2003).
4. L. Dagys, V. Klimavičius, V. Balevičius – *J. Chem. Phys.*, **145**, 114202 (2016).

Method measurement of temperature in conditions magnetic resonance

S. V. Diachenko, A. I. Zhernovoy

Saint-Petersburg state institute of technology (technical university)

190013, Saint-Petersburg, Russia

E-mail: samyon2008@yandex.ru

http://technolog.edu.ru

Introduction

At present, the actual task of measuring thermodynamic temperature without the use of reference points of the temperature scale. The magnetic fluid may be used as the thermometric substance for measurement of temperature, as in the initial part of the magnetization curve is fulfilled of the law of Curie [1]: $\chi=C/T$. Convert the Curie law using Langeven equation, we can derive an equation for the temperature T :

$$T = \frac{M_{sat}PB}{3M} \quad (1)$$

The essence of the method

Based on the equation (1) for finding T necessary determine four unknowns. To determine the induction B , the magnetization M and the saturation magnetization M_{sat} of the magnetic fluid are encouraged to use the experimental setup, based on the NMR method [2]. The induction B can be determined by direct measurement of the frequency NMR f_1 of sensor nutation. The magnetization M can be determined from the equation $M=B/\mu_0-H$, corresponding in frequency view as $M=(f_1-f_2)/\beta$, where β – the gyromagnetic ratio of protons, f_1 and f_2 - frequencies NMR in the sensors, f_1 corresponds to the induction B , f_2 – intensity H the magnetic field inside the sample. Also it is possible to determine the saturation magnetization M_{sat} at this device. By varying the strength of the external magnetic field H_0 , can build the dependence M from $1/B$. From it at $(1/B)=0$ by means of extrapolation can find independent on T saturation magnetization M_{sat} .

To determine the magnetic moment P put forward the following idea: in order to determine the average magnetic moment of the nanoparticles in the ferrofluid is necessary to create conditions for magnetic resonance nanoparticles: $2PB=hF_{res}$ (h – Planck's constant). For this purpose, necessary to act of electromagnetic field with frequency F on the magnetic fluid. After configuring at the induction B of the internal field and the resonant frequency F equal to the value of $F=F_{res}$, that is create conditions of magnetic resonance, can find the magnetic moment of the nanoparticles: $P=hF_{res}/2B$. Substituting this equation in (1) we obtain an expression for determining the temperature in Joules:

$$T = \frac{hF_{res}M_{sat}}{6M}$$

For exposure to the electromagnetic field at the sample of magnetic fluid necessary to use the radiation source. The source can be used the CO₂ laser, microwave generator, or IR spectrometer. Under the influence of radiation on the sample of the magnetic fluid, part of the magnetic moments of the particles directed along the external magnetic field will change its orientation and will be decrease of magnetization M . This phenomenon can be register on the existing experimental plant, setting NMR sensor near the sample of magnetic fluid .

Experiment: Receipt of Magnetic Resonance in magnetic fluid

For researches was prepared colloid solution of nanoparticles magnetite with the solvent - kerosene, poorly absorbing IR radiation, and stabilizer based on oleic acid. For prepared the infrared spectrum of absorption was applied spectrometer PERKIN ELMER with

range of wave numbers K from 500 before 5500 cm^{-1} . Figure 1 shows the dependence from of the wave number K of reducing the intensity transmitted through the colloidal solution of the beam of IR radiation at magnetic field with the induction of $0,075 \text{ T}$.

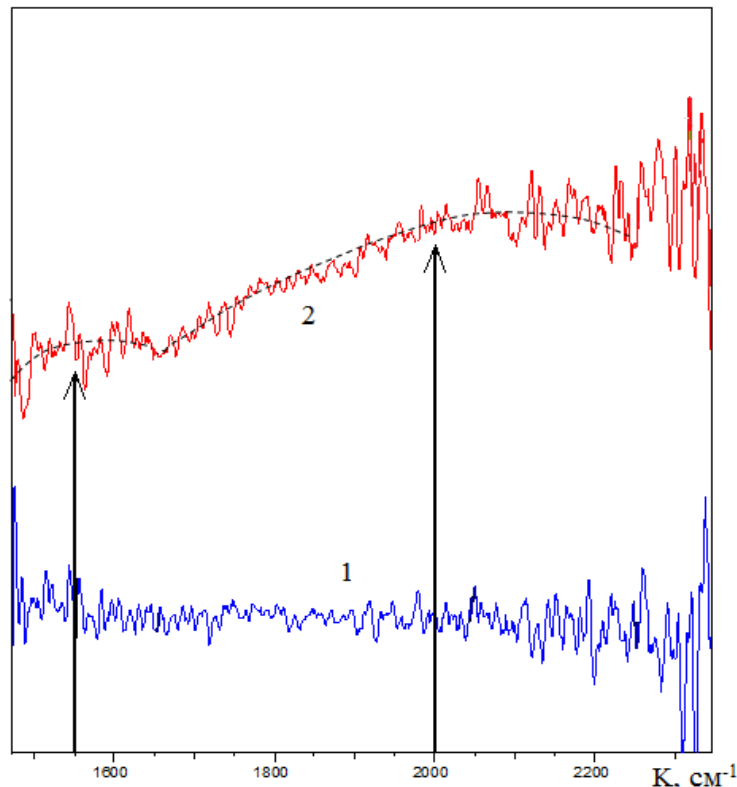


Figure 1. IR-spectrum of absorption the magnetic fluid in magnetic field with induction B .
Curve 1 – $B=0$, curve 2 – $B=0,075 \text{ T}$

At figure 1 have lines resonant absorption of IR radiation with peaks at wave numbers $K_1 \approx 1550 \text{ cm}^{-1}$ и $K_2 \approx 2000 \text{ cm}^{-1}$. Rate the magnetic moments of nanoparticles capable of causing resonance absorption of photons with such wave numbers can be according to the formula: $P = hKc/2B$ (c – velocity light). Substituting $B = 0,075 \text{ T}$ and wave number $K_1 = 1,55 \cdot 10^5 \text{ m}^{-1}$, we obtained $P_1 = 2,0 \cdot 10^{-19} \text{ A} \cdot \text{m}^2$, substituting the wave number $K_2 = 2,0 \cdot 10^5 \text{ m}^{-1}$, we obtained $P_2 = 2,64 \cdot 10^{-19} \text{ A} \cdot \text{m}^2$.

Separately, at experimental device using the method [3] was determined by the medium magnetic moment of the this magnetic fluid $P = 2,60 \cdot 10^{-19} \text{ A} \cdot \text{m}^2$. This confirms the adequacy of the determination of the magnetic moment in conditions magnetic resonance in magnetic fluid. Further research in this field will allow to implement the described method the measurement of temperature.

References

1. Zhernovoy A.I., Diachenko S.V. // Russian Physics Journal. 2015, V. 58, Issue 1, P. 133–137.
2. Zhernovoy A.I., Diachenko S.V. // Technical Physics. The Russian Journal of Applied Physics. 2015. V. 60. Issue 4. C. 595-599.
3. Zhernovoy A.I., Diachenko S.V. // Nauchnoye priborostroyeniye. 2015. V.25, №1. P. 42-48.

NMR Relaxation in Semiflexible Dendrimers

Maxim Dolgushev^{1,2} and Denis A. Markelov³

¹*Theoretical Polymer Physics, University of Freiburg, Hermann-Herder-Str. 3, 79104 Freiburg, Germany*

²*Institut Charles Sadron, Université de Strasbourg & CNRS, 23 rue du Loess, 67034 Strasbourg Cedex, France*

³*St. Petersburg State University, 7/9 Universitetskaya nab., St. Petersburg, 199034, Russia*
E-mail: dolgushev@physik.uni-freiburg.de
<http://top10.physik.uni-freiburg.de/~max/>

Dendrimers are perfectly branched tree-like macromolecules (see Fig. 1). Their local properties are an important topic of recent research, given the possibility of using dendrimers as nanocontainers for catalysts or medical drugs. In this respect, the NMR relaxation technique is of much help. In particular, recent measurements on Fréchet-type dendrimers show that one can distinguish between signals from different shells of the dendrimer [1].

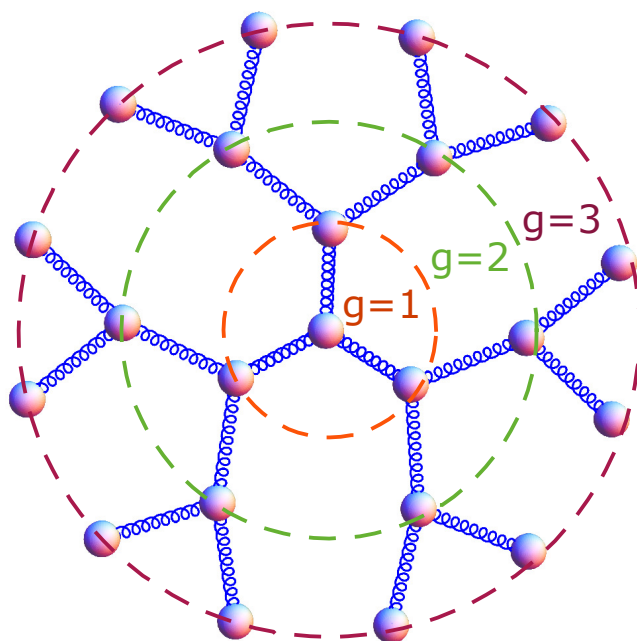


Figure 1. Schematic representation of a dendrimer of generation $G = 3$ (beads and springs). Dashed circles indicate different shells g

We analyze here the relaxation of single segments in semiflexible dendrimers [2]. The dynamics is described by means of Langevin equations, where the dendrimer structure is modeled through a generalized harmonic potential. The semiflexibility is taken into account following Refs. [3, 4], by which the local constraints on the bonds' orientations are readily included. Thus, the correlations between nearest-neighbor bonds are a function of the stiffness parameter q , and those of non-nearest-neighbor bonds correspond to those of the freely-rotating chain [3, 4].

Both for flexible ($q=0$) and for semiflexible ($q=0.45$) dendrimers we find that the orientation autocorrelation function of each segment, $M_1(t)$, is mainly determined by the length of the branch which emanates from that segment. In other words, $M_1(t)$ depends very strongly on $m = (G - g)$, the topological distance of that particular segment from the dendrimer's periphery. However, semiflexibility leads to an increase of the contribution of large-scale motions to $M_1(t)$, so that semiflexible and flexible dendrimers differ strongly in

their behavior. Calculating the spin-lattice relaxation time, $T_1(\omega)$, we find, in contrast to flexible dendrimers [5], that for semiflexible dendrimers the maximum of the $[1/T_1(\omega)]$ -function depends strongly on the topological distance of the particular segment from the core, see Fig. 2 (adapted from [2]). This conclusion is confirmed by a number of NMR experiments [1, 6, 7] and simulations [8]. Finally, we note that the inclusion of hydrodynamic interactions does not change qualitatively the effect of signal splitting for semiflexible dendrimers [9].

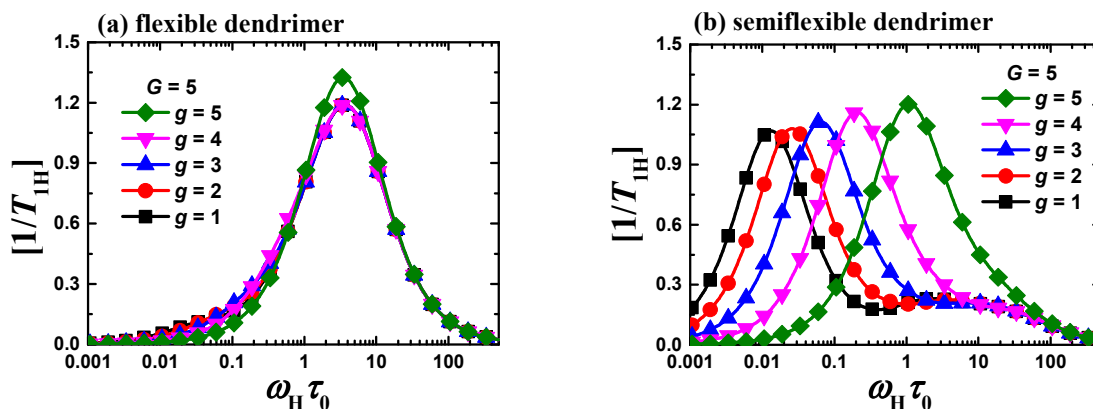


Figure 2. NMR spin-lattice relaxation functions $[1/T_1(\omega)]$ for ^1H nuclei for different topological core-segment distances (labeled by g) of (a) flexible and (b) semiflexible dendrimers of generation $G = 5$. Adapted from [2]

References

1. L. F. Pinto, J. Correa, M. Martin-Pastor, and R. Riguera, *J. Am. Chem. Soc.* **135**, 1972 (2013).
2. D. A. Markelov, M. Dolgushev, Yu. Ya. Gotlib, and A. Blumen, *J. Chem. Phys.* **140**, 244904 (2014).
3. M. Dolgushev and A. Blumen, *J. Chem. Phys.* **131**, 044905 (2009).
4. M. Dolgushev and A. Blumen, *Macromolecules* **42**, 5378 (2009).
5. Yu. Ya. Gotlib and D. A. Markelov, *Polymer Sci. Ser. A* **49**, 1137 (2007).
6. C. Malveau, W. E. Baille, X. X. Zhu, and W. T. Ford, *J. Polym. Sci., Part B: Polym. Phys.* **41**, 2969 (2003).
7. D. A. Markelov, V. V. Matveev, P. Ingman, M. N. Nikolaeva, E. Lähderanta, V. A. Shevelev, and N. I. Boiko, *J. Phys. Chem. B* **114**, 4159 (2010).
8. D. A. Markelov, S. G. Falkovich, I. M. Neelov, M. Y. Ilyash, V. V. Matveev, E. Lähderanta, P. Ingman, and A. A. Darinskii, *Phys. Chem. Chem. Phys.* **17**, 3214 (2015).
9. M. Dolgushev, S. Schnell, and D. A. Markelov, in preparation.

MRI imaging of CNS tuberculosis among patients with AIDS

*A. A. Drozdov¹, V. M. Cheremisin¹, I. G. Kamishanskaya¹, A. A. Yakovlev²,
V. B. Musatov², I. P. Fedunyak², O. I. Fedunyak², M. N. Artem'eva²*

St. Petersburg State University, Faculty of Medicine, 21 line V.O., 8a

¹St. Petersburg State University Mariinsky Hospital, Litejny pr., 56

²St. Petersburg S.P. Botkin Clinical Infectious Diseases Hospital, Mirgorodskaya ul, 3.

Introduction

Tuberculosis usually is classified as pulmonary or extrapulmonary with extrapulmonary form accounted about 22% of all incident cases in countries with extensive chemotherapy available. But HIV epidemics plays a dramatic role by increasing number of all tuberculosis forms spread, being the most important risk factor globally, increasing the risk of reactivating of latent forms of TB (threefold compared to HIV-negative people) and incising the percent of extrapulmonary forms (fivefold compared to HIV-negative people).

Clinical symptoms often are nonspecific with a neurological deficit and headache that could be associated with a series of HIV associated conditions. MRI with contrast is the radiologic investigation of choice in both excluding other causes as well as confirming clinical and laboratory tests results.

Goal

To determine the ability of contrast enhanced MRI imaging to evaluate the CNS for tuberculosis associated changes; to describe forms of tuberculosis associated CNS lesions;

Methods and Materials

In our retrospective study we enrolled 46 patients with both AIDS and tuberculosis diagnoses made by St. Petersburg S.P. Botkin Clinical Infectious Diseases Hospital. All of the patients had neurological symptoms and CD4+ count less than 100/ml. Brain MRI with Gd-DTPA (0.2 mmol/kg body weight) was performed at Mariinski Hospital at Siemens Magnetom Avanto 1.5T.

Results:

Tuberculosis associated CNS lesions were determined in 27 patients out of 46 (58,6%). Several tuberculosis associated CNS lesions have been identified:

Intracranial tuberculous granuloma (tuberculoma): the most common tuberculosis associated finding of CNS. Typically present as a ring-enhancing round lesion 3-10mm in a diameter, surrounded by vasogenic edema. MR signal is usually hypointense on T1WI, hyperintense on T2WI +/- hypointense rim. These lesions might be single or multiple.

Spinal cord tuberculous granuloma (tuberculoma): radiologically present similar to intracranial tuberculomas. More common in thoracic and lumbar regions. May be associated with intracranial tuberculomas and/or meningeal enhancement.

Tuberculous vasculitis: middle cerebral arteries and their branches are most commonly affected. MRI angiography (MRA) is helpful by detection vascular occlusions, areas of arterial walls irregularities, regions of intermittent stenosis and dilatations. T1WI with contrast might demonstrate perivascular enhancement with irregular borders. Acute ischemia might appear as a consequence of the process.

Tuberculous focal cerebritis: is a rare condition associated with *M. tuberculosis*. The only case in our practice was associated with tuberculosis vasculitis. T2 FLAIR, T2WI and T1WI have demonstrated changes similar to ischemic stroke, but T1WI with contrast demonstrated focal granular and annular enhancement, that looks different from enhancement pattern, associated with ischemic stroke.

Tuberculous pachymeningitis: presents as thickening of the dura matter, that is hypo intense on T2WI, isointense to gray matter with intense enhancement at T1WI C+. Subdural effusion might also be present as a complication of pachymeningitis. Dural matter thickening and enhancement might also spread to spinal area.

Epidural abscess: is a rare form of intracranial tuberculosis. Present as an encapsulated proteinaceous fluid collection (central low intensity (hyperintense to CSF) on T1WI; central high intensity (hypointense to CSF) on T2WI, that does not fully attenuate on T2 FLAIR). Central area demonstrates high signal on DWI (b 1000). Capsule enhances on T1WI C+.

Tuberculous leptomeningitis: even mentioned to be the most common form of intracranial tuberculosis, classic tuberculous leptomeningitis with diffuse basal enhancement has not been recognized among our group of patients. That could be associated with profound immunodeficiency (all the patients had CD4+ level below 100/ml) or with the fact that all of the patients had BCG vaccination during childhood (several studies have reported the ability of BCG vaccination to diminish the risk of tuberculous meningitis among children).

Conclusion

MR neuroimaging is critical for patient with both AIDS and tuberculosis due to ability to aid in excluding other causes of neurologic problems, supplementing the diagnosis of neuro tuberculosis, useful in administering proper treatment and monitoring response to treatment.

A Gradient Tolerance Measurements of Proton Overhauser Sensor POS-1

*Andrey L. Fedorov, Andrey V. Sergeev, Evgenii D. Baglasov, Evgenii M. Milovidov,
Evgenii D. Narkhov, Dmitriy V. Saveluev, Aleksey Yu. Denisov, Vladimir A. Sapunov*

*Quantum magnetic laboratory of Ural federal university, Russia
E-mail: vasapunov@urfu.ru*

Introduction

One of the critical parameters of proton magnetometers is gradient tolerance, that characterizes ability to work and parameters of accepted signals while working in fields with high values of magnetic gradients. In the report method and results of QMLab measurements of gradient tolerance of the POS-1 magnetometer [1], crafted by quantum magnetic laboratory of Ural Federal University and having wide spectra of appliance in different spheres, are presented.

Short description

The short description of the POS-1 magnetometer developed by QMLab and its general characteristics are presented in the report: sensitivity 0.01-0.05 nT with cycles of measurements 3 and 1 sec respectively and gradient tolerance up to 30 000 nT/m. Working size of Overhauser sensor is 69*120 mm.

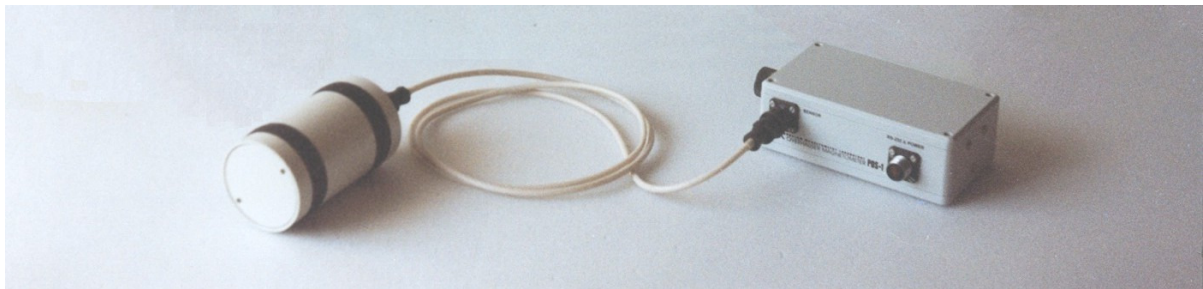


Figure 1. Magnetometer POS-1

Gradient tolerance

The special attention is given to gradient tolerance parameter, which was defined as border of sharp decrease in sensitivity of measurements.

The gradient tolerance measurements were conducted in a laboratory magnetic field standard has geomagnetic range. The standard of magnetic field is based on a four-layers permalloy shielding and an internal solenoid coil.

Method of measurements

The measurement technique is based on continuous measurement of the magnetic field and calculation of its root mean square deviations (RMS) along the axis of standard magnetic field of inhomogeneous area and distribution of this field along the axis. Previously such research has been done for LOM-2 borehole magnetometer [2]. Measurements were done in different cycles and for sensors, adapted for work in various cycles. For each case maximum values of gradient tolerance of POS sensor were calculated. Overhauser magnetometer POS has the record gradient tolerance up to 30000 nT/m due to special algorithms of signal treating and small dimensions of sensors (30*70 working volume).

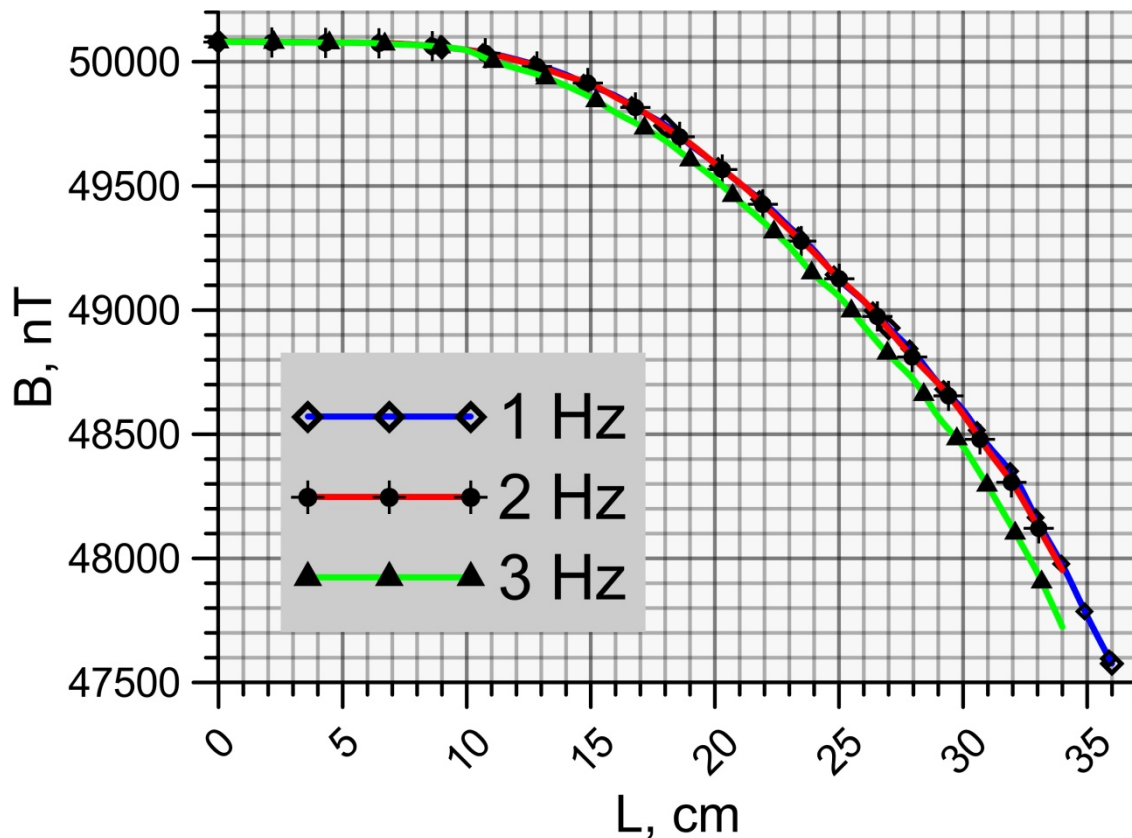


Figure 2. Measurements of the magnetic field in laboratory field standard run on three cycles

References

1. V. A. Sapunov, E. D. Narkhov, A. L. Fedorov, A. Sergeev, A. Y. Denisov, Ground Overhauser DNP geophysical devices, 15th International Multidisciplinary Scientific GeoConference SGEM 2015. Science and Technologies in Geology, Exploration and Mining: Proceedings, V.1, 2015, P.215-222
2. V. Sapunov, E. Narkhov, A. Denisov, T. Wu, X. Cao, A gradient tolerance measurement method of borehole Overhauser magnetometer LOM-2 in laboratory conditions, 15th International Multidisciplinary Scientific GeoConference SGEM 2015. Science and Technologies in Geology, Exploration and Mining: Proceedings, V.1, 2015, P.29-36

Calculation of optimal parameters for MRI of fluorocarbons

D. V. Fomina¹, V. A. Glukhova¹, M. V. Gulyaev², S. S. Batova¹, N. V. Anisimov²

¹*Faculty of Physics,*

²*Faculty of Fundamental Medicine*

M.V. Lomonosov Moscow State University

E-mail: dv.fomina@physics.msu.ru

This paper presents a method for optimizing the parameters of the scanning pulse sequences for MRI in relation to objects with a wide spectrum of NMR. The method is especially urgent for ^{19}F NMR spectra of fluorocarbons which are characterized by large chemical shifts and constants of the spin-spin interaction [1, 2]. In this case, a broadband excitation of the spin system is difficult because of hardware limitations.

The idea of the method is to calculate the signal of nuclear induction for different variants of frequency-selective excitation of the spin system (excitation frequency, the width of the excited spectrum Δ) and to select the optimal one. Sorting out of versions is realized by specialized software that makes calculations in batch mode and gives the excitation parameters in which the maximal signal is realized. Fig. 1 shows a scheme of the method. High resolution NMR spectrum $F(\omega)$ is multiplied by a Gaussian function $G(\omega)$. The result is undergone to inverse Fourier transform, and its magnitude $M(t)$ is calculated from the resulting time function.

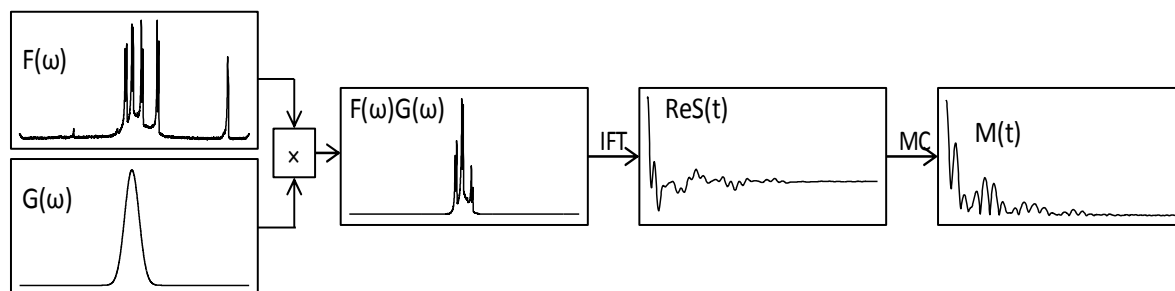


Figure 1. The scheme of calculating the NMR signal by the selective excitation

It is assumed that $M(t)$ determines the brightness of the pixels on the MRI image. Therefore, the extreme values of the function $M(t)$ serve as a guide for setting the TE value of scanning pulse sequence (PS) gradient echo (GE). The value of $M(0)$ determines the signal for spin echo PS (SE). The method most successfully works at small flip angles ($\leq 30^\circ$), which is typical for GE technique. However, the results of calculations can be demanded for the SE technique where the angles are 90° and 180° . To clarify the optimal parameters SE it additionally requires the experimentally measured dependence of $S = S(TE)$ to take into account the effects of transverse relaxation and J-modulation.

The range of variable parameters of frequency-selective excitation is defined with considering hardware limitations. Power of the gradient system determines the minimal values of TE (TE_{\min}), the transmitter power and the permissible radiofrequency load on the transmitting coil determine maximal value Δ , as it is inversely proportional to the pulse duration.

The method has been tested for fluorocarbon drug Perftoranum® [3]. Fig. 2 shows its ^{19}F NMR spectra which were obtained in the fields of 0.5 and 7 Tesla using the Bruker's scanners – Tomikon S50 and BioSpec 70/30, and dependence of S on frequency offset with fixed parameters TE and Δ .

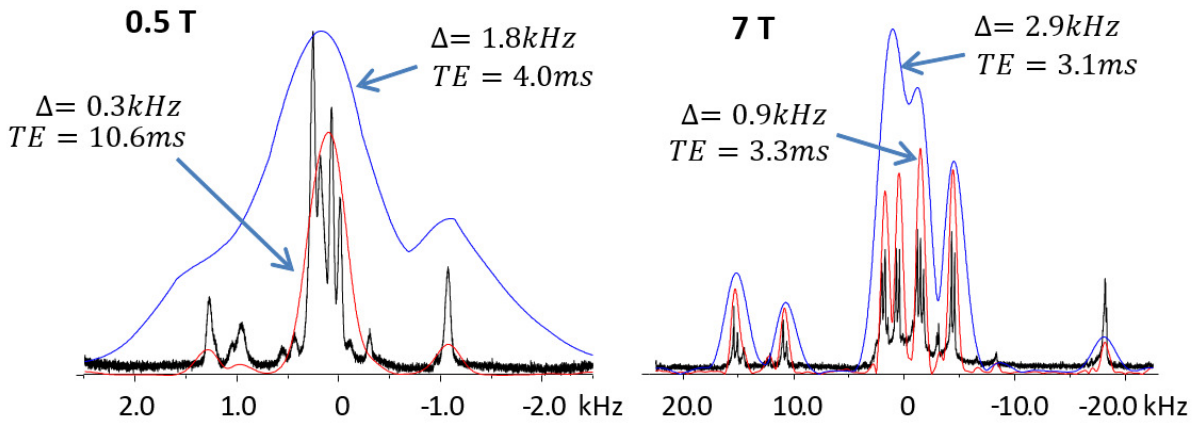


Figure 2. Dependence of S on the frequency offset with fixed Δ and TE

It may be noted that the position of the curve maximum depends in complex manner on Δ . But at the optimal choice of selective excitation frequency the signal dependence on Δ $S = S(\Delta)$ is very simple – S increases steadily with increasing Δ . However, on the condition that Δ agreed with the receiver bandwidth, for dependence of the signal-to-noise ratio (S/N) the situation is reversed – fig. 3.

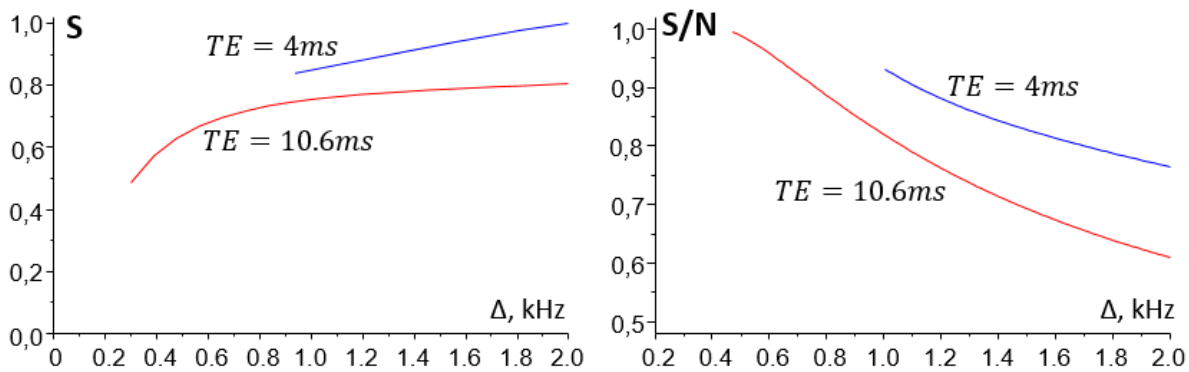


Figure 3. Dependence of S and S/N on Δ at fixed TE (0.5 T) for GE. The precipice of curves in area of small Δ is associated with unrealizable marked TE values because of hardware limitations

NMR spectrum is not usually a bandpass and is represented by a set of narrow lines. Therefore, with the increase of Δ the total induction signal is growing slower than the thermal noise whose spectrum is continuous and its amplitude increases $\sim \Delta^{1/2}$.

In addition to hardware factors the minimal value Δ (maximal TE) is limited by the transverse relaxation rate – $1/T_2$. Since $S(TE) \sim \exp(-TE/T_2)$, then for $TE \sim T_2$ relaxation factor is becoming crucial for the NMR signal, fig. 3.

For ^{19}F NMR spectra obtained in fields of 0.5 and 7 Tesla scan parameters for GE and SE were calculated that ensure the maximal values for S and S/N . The calculations take into account the hardware limitations, in particular, the minimal $TE_{\min} = 3.4$ ms for the 0.5 Tesla and 2.1 ms for the 7 Tesla. These values were comparable to $T_2 = 12$ ms (0.5 T) and 17 ms (7 T). It should be noted for reference that $T_1 = 0.67$ s (0.5 T) and 1 s (7 T). Therefore, for GE the values TE can be recommend only closest to TE_{\min} , and for SE – the minimal possible ones for the hardware implementation, but with considering the J-modulation. Fig. 4 is a plot of dependence of the spin-echo signal on TE for Perftoranum® in the field of 0.5 Tesla. The curve shows an exponential decay due to the transverse relaxation and J-modulation – local

minimal values at $TE = 1/2J$ are due to the multiplet splitting in the NMR spectrum. The Gaussian pulses were used with a duration 1.5 ms that ensure $\Delta = 1827$ Hz.

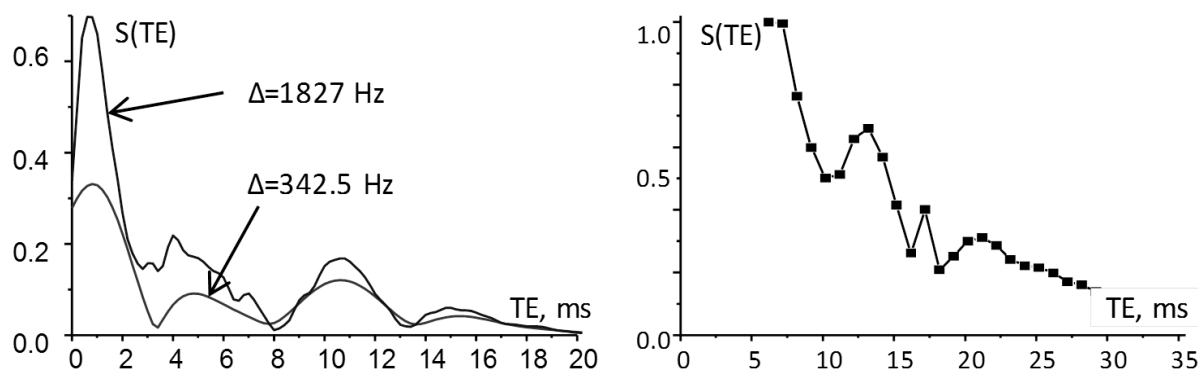


Figure 4. Dependence of $S = S(TE)$ for Perftoranum® in the field 0.5 T for different bands of selective excitation. On the left for GE, on the right for the SE at $\Delta = 1827$ Hz

As a result, for GE TE were the following values as the optimal: 4.0 ms for the field of 0.5 Tesla and 3.2 ms for the field 7 Tesla. For the SE, respectively, 6.2 ms for 0.5 Tesla and 5.5 ms for 7 Tesla.

Overall, the experimental results correspond to the calculations for both of fields 0.5 and 7 Tesla. When analyzing the reasons for the small divergence of experimental and calculated optimal parameters of the selective excitation at 7 Tesla, deviation of programmed and implemented values TE of 0.02 ms was revealed. The reason is unclear – it can be either gradient system imperfections or errors in the firm program. However, this factor can be taken into account when setting TE in the scanning pulse sequence.

The method developed allows in relatively simple manner to calculate the optimal parameters of MRI scanning of objects with complex NMR spectrum with considering hardware resources. The method effectiveness increases with the using the information on the relaxation parameters and constants of spin-spin interaction.

The work is supported by a grant from the Ministry of Education of the Russian Federation №14.604.21.0060 (RFMEFI60414X0060).

References

1. Jesu's Ruiz-Cabelloa, Barnett B.P., Bottomley P.A., Bulte J.W.M. Fluorine (^{19}F) MRS and MRI in biomedicine // *NMR in Biomed.* 2011. V. 24.P. 114-129.
2. Tirotta I., Dichiarante V., Pigliacelli C., Cavallo G., Terraneo G., Bombelli F.B., Metrangolo P., Resnati G. ^{19}F Magnetic Resonance Imaging (MRI): From Design of Materials to Clinical Applications // *Chem. Rev.*2015.115(2). P. 1106–1129.
3. Maevsky E.I., Gervits L.L. // *Supplement of Chimica Oggi / Chemistry Today, Focus on Fluorine Chemistry.* 2008. V. 26, No 3.
4. Gulyaev M.V., Gervits L.L., Ustynyuk Y.A., Anisimov N.V., Pirogov Y.A., Khokhlov A.R. Poluchenie izobrazheniy v magnitno-rezonansnoy tomografii na yadrah ^{19}F s pomoshyu preparata Perftoran® // *Zhurnal radioelektroniki (elektronny zhurnal).* 2013. № 8, (in Russian) <http://jre.cplire.ru/win/aug13/11/text.html>

MD modeling of disulfide bond formation in peptides and proteins

Sergei Izmailov¹, Ivan Podkorytov¹, Nikolai Skrynnikov^{1,2}

¹Laboratory of Biomolecular NMR, St. Petersburg State University, St. Petersburg 199034, Russia

²Department of Chemistry, Purdue University, West Lafayette IN 47907, USA
E-mail: sergei.a.izmailov@gmail.com

Significant strides have been recently made to fold peptides and small proteins *in silico* using regular MD simulations. However, facilities are currently lacking to include disulfide bonding in the MD models of protein folding. To address this problem, we have developed a simple empirical approach where reactive cysteines are modeled as (deprotonated, neutral) thiyl radicals. When two thiyl sulfur atoms move within capture radius of each other during the course of the MD simulation, the procedure is initiated to form a disulfide bond. The developed protocol is perturbation-free and retains the same speed as conventional MD simulations. For almost the entire duration of time the system evolves under the control of the original (unaltered) force field. If desired, the rate of disulfide formation can be easily adjusted by assuming that only a certain fraction of thiyl encounters is productive.

The new protocol has been tested on peptide guanylin containing four cysteine residues. Fifty trajectories of guanylin with the net duration of 16.6 μ s have been recorded under Amber ff14SB force field. The resulting isomer distribution is in good agreement with experiment, suggesting that oxidative folding of guanylin *in vitro* occurs under kinetic control. One of the obtained low-energy conformers provides a high-quality structural model, comparable to the NMR structure of guanylin. Oxidative folding of guanylin within the 94-aminoacid prohormone proguanylin has also been simulated. Likewise, a successfully folded structure has been obtained in close agreement with the NMR coordinates. The proposed modeling strategy can help to explore certain fundamental aspects of protein folding and is potentially relevant for manufacturing of synthetic peptides and recombinant proteins.

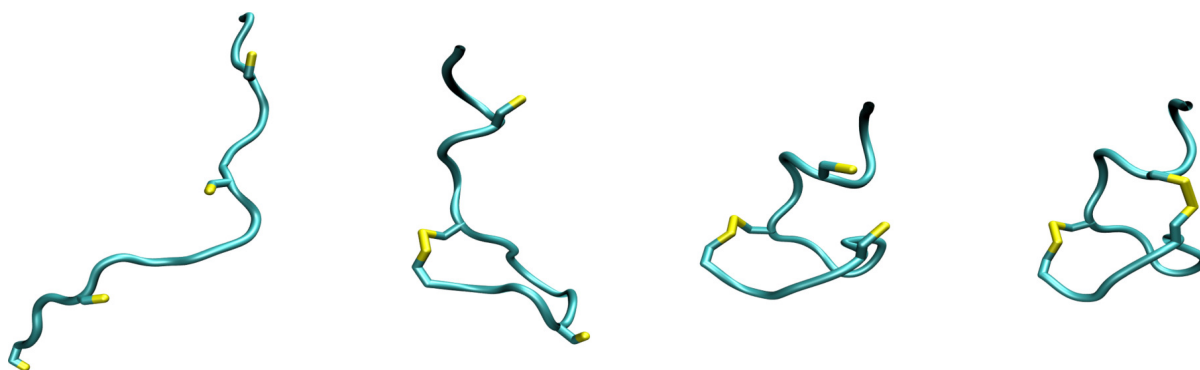


*Figure 1. The process of disulfide bonds formation in guanylin.
Snapshots are taken from MD simulation*

This work has been supported by RSF grant 15-14-20038.

Comparison of the magnetic resonance spectroscopy findings with cerebral glucose metabolism and immunological data in Parkinson's disease

Yu. G. Khomenko¹, G. V. Kataeva¹, E. A. Gromova¹, I. V. Milyukhina², M. N. Karpenko²,
A. A. Bogdan¹, D. S. Susin¹

¹N.P. Bechtereva Institute of the Human Brain RAS, St.Petersburg

²Institute of the Experimental Medicine RAMS, St.Petersburg

E-mail: julkhom@rambler.ru

Introduction

Magnetic resonance spectroscopy (MRS) allows to receive data on different metabolites concentration in brain tissue in vivo, that is of great interest for the study of pathogenesis of neurodegenerative diseases. Besides that, MRS in addition with another imaging methods may have the diagnostic value.

The purpose of this research was to analyze MRS data of patients suffered from Parkinson's disease and match them with positron emission tomography (PET), immunological and clinical data.

Methods

26 patients suffered from PD (age 62,8±9,6; 14 males; 1,0-3,0 stages by Hoehn and Yahr scale) were examined. Standard neurological examination, MRS, PET and cerebrospinal fluid immunoassay with the evaluation of interleukine (IL) 2, 4, 10, 17, beta and tumor necrosis factor alpha (TNF-alpha) were performed.

Multivoxel H-MRS in supraventricular region was performed on Achieva 3T scanner, Philips (2D PRESS, TE/TR=53/1500 ms). Anatomical localization is presented on Figure 1. The area of MRS study - 8*9 voxels (10*10*15 mm), whole volume 80*90*15 mm was divided into 9 regions of interest (ROI): 6 in white matter (WM) of semioval centers (3 ROIs: anterior, medium and posterior for each hemisphere) and 3 ROIs in gray matter (GM) of medial cortex. NAA/Cr, NAA/Cho, Cho/Cr and Glx/Cr ratios (NAA – N-acethyl aspartate, Cr – creatine, Cho – choline, Glx – glutamin + glutamate) were analyzed separately for each ROI.

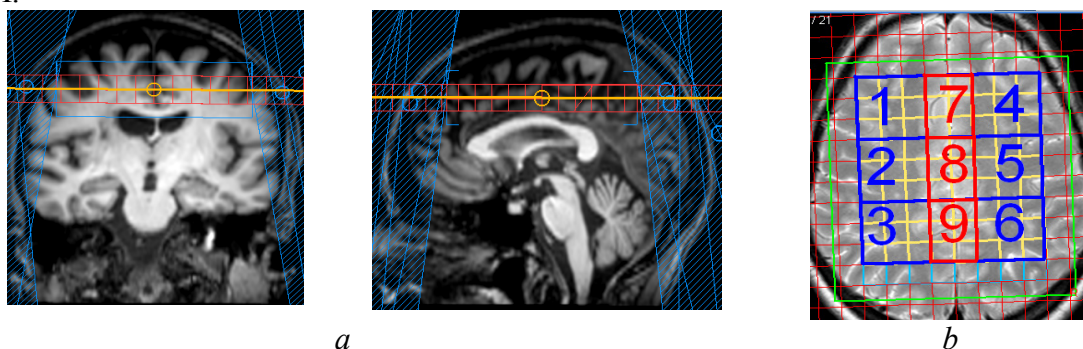


Fig.1(a) — MRS anatomical localization in the supraventricular region;
(b) — localization of regions of interest in white (1-3 and 4-6) and gray matter (7-9).

PET study with 18F-fluorodesoxyglucose (FDG) was performed with GE Discovery-710 PET scanner. PET images were spatially normalized with Statistical Parametric Mapping program (SPM8) [1], cerebral glucose metabolism rate (CMRglu) in Brodmann areas (BA) (Fig.2) were calculated using WFU Pickatlas [2]. The detailed description of the FDG PET study method is given in [3].

Results

Correlations of NAA/Cr and NAA/Cho ratios in supraventricular white matter of left hemisphere with disease stage were revealed ($r=-0,45$, $p<0,05$). However, we did not find correlations of these ratios with the age of patients; only Cho/Cr in the right hemisphere white matter correlated negatively with the age ($r=-0,62$, $p=0,01$).

Besides that, negative correlations of THF-alpha concentration in cerebrospinal fluid and NAA/Cr ($r=-0,53$, $p<0,05$) and NAA/Cho ratios ($r=-0,49$, $p<0,05$) in the right hemisphere white matter were revealed. Glx/Cr ratio showed positive correlation with THF-alpha ($r=0,55$, $p<0,05$), IL-2 ($r=0,54$, $p<0,05$), and IL-17 ($r=0,62$, $p<0,01$).

Metabolite ratios in medial cortex correlated with cytokines similarly: NAA/Cho with IL-2 ($r=-0,63$, $p<0,01$), Glx/Cr with IL-17 ($r=0,52$, $p<0,05$). NAA/Cr and Glx/Cr correlated negatively, that is corresponding to the role of NAA as a marker of neuronal integrity and to the role of glutamate as a mediator of excitotoxicity in neural tissue.

The results of comparison of MRS and PET data showed in Figure 2. Cho/Cr ration in supraventricular white matter (areas 1, 3 and 4 according to Figure 1) negatively correlated with CMRglu in frontal and parieto-occipital cortex - BA 8,9,10,47 and 39 ($r=-0.6-0.8$; $p<0.01$). NAA/Cho ratio both in white and gray matter (areas 1,3,4,7,9) showed positive correlation with CMRglu in cingulate cortex bilaterally ($r=0.6-0.8$; $p<0.01$) and also NAA/Cho ratio in white matter correlated with CMRglu in BA 8,10,46 ($r=-0.6-0.8$; $p<0.01$).

Besides that, Cho/Cr ration in medial cortex (gray matter) negatively correlated with CMRglu in BA 10 and 39 in left hemisphere ($r=-0.7-0.75$; $p<0.01$); NAA/Cr – positively with CMRglu in sensorimotor cortex - BA 1-4 of right hemisphere ($r=0.7$, $p<0.01$) and left parietal cortex - BA 7 ($r=0.8$; $p<0.01$).

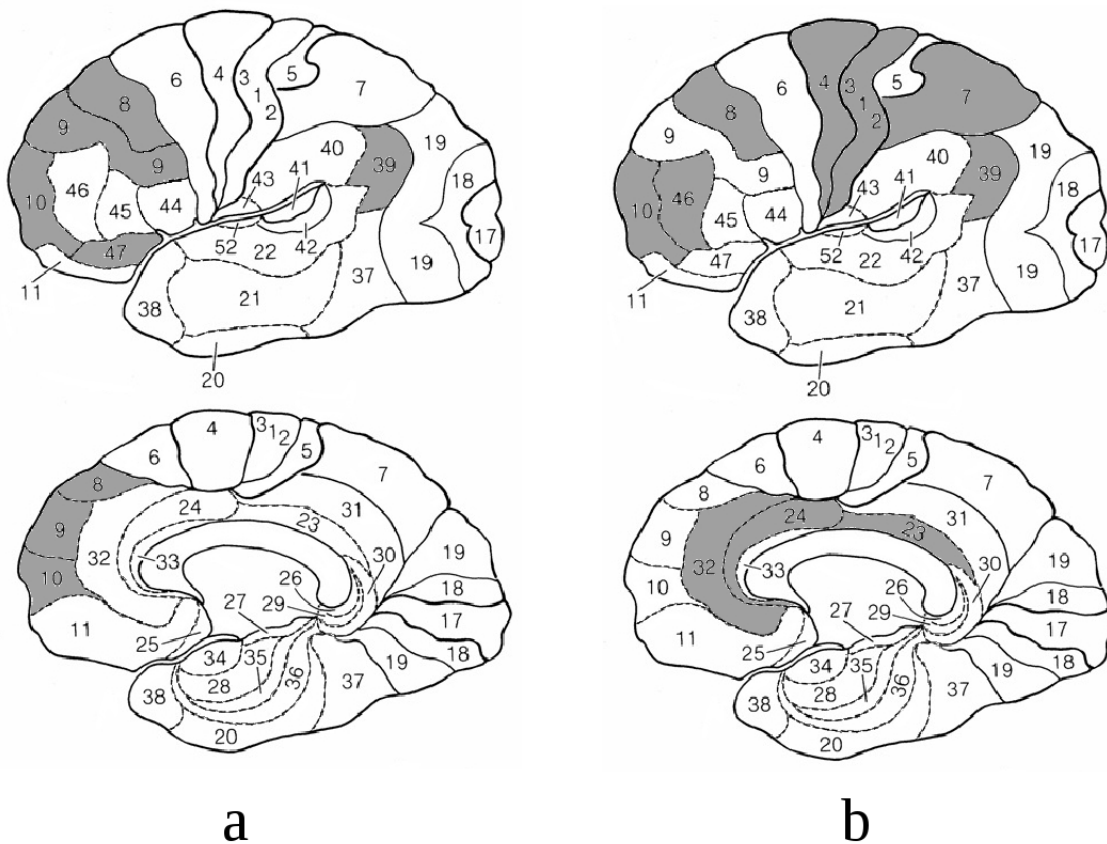


Figure 2. Brodmann areas, in which correlations of CMRglu and MRS data were found: (a) — Cho/Cr (negative correlations), (b) — NAA/Cr and NAA/Cho (positive correlations), detailed description is given in the text

Thus, NAA/Cr and NAA/Cho ratios correlated positively with factors reflected better functional state of brain tissue and negatively — with the disease stage and immunological data as a representatives of the pathological process. These findings are in agreement with the common suggestion that NAA is a marker of neuronal integrity [4].

In our previous research we revealed correlations of NAA/Cr and NAA/Cho in supraventricular white matter with CMRglu in cingulate cortex in HIV-infected patients [3] and in dementia and mild cognitive impairment, that could be the evidence of the existence of common pathogenetic mechanism associated with the limbic system functioning in different types of neurodegenerative pathology.

It is not easy to explain correlations of Cho/Cr and CMRglu in visually intact brain tissue. Different studies showed both its decrease and increase in neurodegenerative pathology. In current research we revealed its correlation with the decrease of cerebral glucose metabolism, that could be associated with the neurodegenerative process beginning (membranes degradation causes Cho concentration increase and glucose metabolism decrease, because the number of viable neurons declines).

Further MRS researches required, including examination of the PD patients with more severe disease stages according to the Hoehn and Yahr scale in order to evaluate the MRS as a method for the study of biochemical processes associated with the PD pathogenesis and neurodegeneration progression.

References

1. Statistical Parametric Mapping. URL: www.fil.ion.ucl.ac.uk/spm/ (27.10.2016).
2. WFU PickAtlas. URL: http://www.nitrc.org/projects/wfu_pickatlas/ (27.10.2016).
3. Gromova E.A., Bogdan A.A., Kataeva G.V., Kotomin I.A., Khomenko Yu.G., Korotkov A.D., Trofimova T.N., Rassokhin V.V., Belyakov N.A. Peculiarities of brain structures functional state in HIV-infected patients // *Luchevaya diagnostica*. 2016. № 1. C. 41-48.
4. Barker P.B., Bizzi A., De Stefano N., Gullapalli R.P., Lin D. M. *Clinical MR Spectroscopy: Techniques and Applications*. Cambridge University Press, 2009.

Vacuum heat treatment of wood and study of its properties by magnetic resonance and other methods

E. I. Kondratyeva^{1,2}, A. V. Klochkov^{1,2}, I. G. Motygullin¹, K. R. Safiullin^{1,2}, M. S. Tagirov^{1,2}

¹*Institute of Physics, Kazan Federal University, Kremlevskaya 18, Kazan*

²*Institute of Perspective Research, Academy of Sciences of the Republic of Tatarstan, L. Bulachnaya 36a, Kazan*

E-mail: katarina.kondratyeva@gmail.com

Vacuum heat treatment of wood is the effective type of drying on the duration and quality that allows to improve some of the properties of wood [1]. Electron paramagnetic resonance (EPR) method is a non-invasive method that allows to provide information about changes in the structure of the wood as well as control or assess the quality of heat treatment wood. This work is devoted to the study of the effect of heat treatment on the properties of wood of different species by electron paramagnetic resonance, pulse nuclear magnetic resonance, optical microscopy methods and measurement of changes of some sample properties as moisture resistance, hardness and color [2, 3].

The wood species such as a birch, larch, lime, pine and spruce were dried by vacuum oven. Thermal treatment of wood pieces was carried out at a temperature of 220⁰C and with pressure values lower than 50 mbar. The duration of this process varied from 40 min to 8 h for all wood species. After the treatment, wood pieces were cooled down to room temperature and stored under conditions of constant air relative humidity in a number of air tight boxes.

We studied parameters of wood samples such as hardness and change in the equilibrium moisture content. The hardness of the wood was measured by indentation of steel ball with a diameter of 10 mm with a force of 100 kgf at the surface of wood and hardness value were found using a standard equation for the Brinell hardness HB[4]. Wood moisture was measured after 60 days of sample storage under different constant relative humidity conditions. The measured equilibrium MC values were then compared to the ones before the storage and to the default equilibrium values.

EPR experiments were carried out on the Varian E-12 X-Band spectrometer at 9.3 GHz frequency and at the room temperature. During the experiments special reference sample were used to qualitatively and quantitatively compare the obtained EPR spectra of different samples. The signal of free radicals of wood near $g = 2.002$ has been observed. The influence of vacuum 220⁰C heat treatment duration on free radicals signal amplitude has been studied. Experimentally obtained dependencies for larch, pine, spruce and linden are shown in fig.1.

The amplitude of the free radical signal in spruce samples increases linearly with the thermal treatment duration. This may indicate a break of chemical bonds in wood polymer chains that leads to the formation of free radicals. The amplitude of the signal of free radicals also increases linearly with the heat treatment duration for other wood species as larch, linden and pine trees. However, after long heat treatment duration the free radicals signal amplitude values decrease. Probably this effect is connected with the severe destructive process in the wood samples.

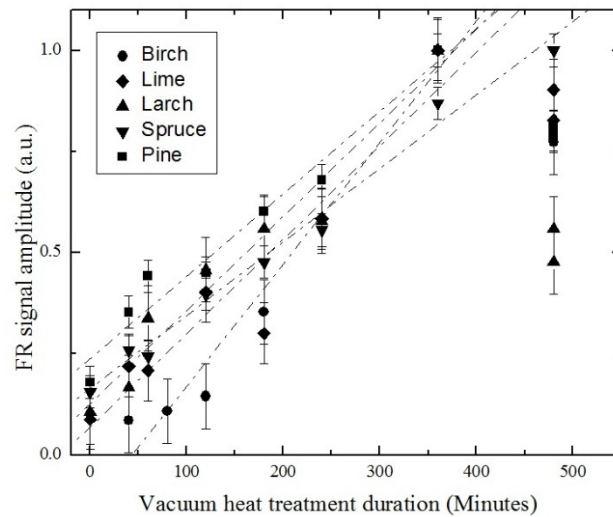


Figure 1. Normalized EPR signal amplitude of spruce, pine, birch, larch and lime samples and its correlation with the vacuum thermal treatment duration at 220⁰C

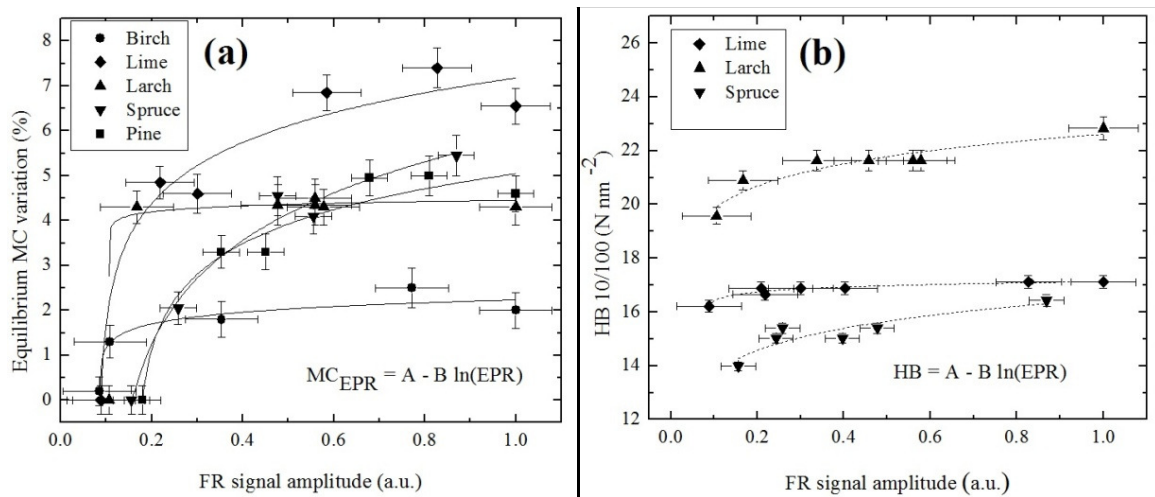


Figure 2. a) Correlation between equilibrium moisture content variation MC_{var} at 50 % relative humidity and room temperature and the normalized EPR signal amplitude of vacuum heat treated at 220⁰C spruce, lime, pine, birch and larch samples.

b) Correlation between the radial Brinell hardness of spruce, lime and larch samples and normalized EPR signal amplitude

A good correlation between equilibrium moisture content and results of EPR experiments (figure 2a) is observed with a logarithmic equation $MC_{var} = a - b \ln(EPR)$. Similar type of regression is reported for thermally treated beech and spruce samples [5]. However, the relationship between the equilibrium MC and the free radicals concentration in wood remains unclear.

Also a correlation between Brinell hardness of larch, spruce and lime and results of EPR experiments is plotted in Figure 2b). The results also fit with a logarithmic equation $HB = a - b \ln(EPR)$ as well as results of equilibrium moisture content measurements. For samples of wood of birch and pine such a correlation is not detected.

Finally, the following conclusions are made that magnetic resonance method is a good method for quality control of thermally modified wood.

References

1. B. Esteves, H. Pereira Wood modification by heat treatment: A review. – *BioResources.*, 4, 370-404 (2008)
2. E.I. Kondratyeva, K.R. Safiullin, I.G. Motygullin, A.V. Klochkov, M.S. Tagirov, V.V. Kuzmin Electron paramagnetic resonance and quantitative color investigations of various vacuum heat treated wood species. – *Magn. Reson. Solids.*, 17, 15202 (2015)
3. E.I. Kondratyeva, K.R. Safiullin, I.G. Motygullin, A.V. Klochkov, M.S. Tagirov, V. Reita Thermal modification of wood and a complex study of its properties by magnetic resonance and other methods. – *Wood Science and Technology.*, 50(№5), 895-916 (2016).
4. H. Holmberg Influence of grain angle on Brinell hardness of Scots pine (*Pinus sylvestris*L.). – *Holz Roh-Werkst.*, 58(1-2), 91–95 (2000).
5. M. Altgen, C. Welzbacher, M. Humar, W. Willems, H. Militz Bestimmung der Behandlungsqualität von Thermoholz mithilfe von Schnellverfahren; Teil 1: Elektronenspin-Resonanz-Spektroskopie (Determination of the treatment quality of thermally modified wood by means of rapid methods; Part 1: ESR-spectroscopy) (In German). – *Holztechnologie.*, 53(6), 44–49 (2012).

¹H NMR spectroscopy *in vitro* and *in vivo* of rat tissues and blood after alcohol impact

M. S. Krestina^{1,3}, *A. E. Akulov*², *O. B. Shevelev*², *I. V. Koptyug*^{1,3}

¹*International Tomography Center, SB RAS, Institutskaya, 3a, 630090, Novosibirsk, Russia*

²*Institute of Cytology and Genetics, SB RAS, prospect Lavrentyeva, 10, 630090, Novosibirsk, Russia*

³*Novosibirsk State University, Pirogova, 2, 630090, Novosibirsk, Russia*

E-mail: mariya.krestina@tomo.nsc.ru

Metabonomics studies the metabolic response of a living organism to pathophysiological effects or genetic modification, and thereby investigates the changes in metabolism. Nowadays this field of research is growing and developing rapidly, because any disease or treatment first of all effects on metabolic reactions, so that metabolism reflects the state of the whole organism at every pathology stage. The aim of this study was the investigation of brain, liver and blood metabolism under alcohol consumption, the possibility of evaluation of liver state with blood metabolic profile and the comparison of *in vivo* and *in vitro* brain studies.

There are two most popular methods for metabolic researches: NMR spectroscopy and mass-spectrometry. Mass-spectrometry is more sensitive than NMR spectroscopy, but NMR spectroscopy allows one to perform *in vivo* studies. Therefore it is useful to use both techniques. In this study we used mass spectrometry (ESI q-TOF MS Bruker Maxis 4G) for metabolites identification, ¹H NMR spectroscopy (Bruker Avance III, 700 MHz) in order to determine metabolites concentrations *in vitro*, and ¹H NMR spectroscopy (Bruker, Biospec 117/16 USR, 500 MHz) for *in vivo* researches (brain cortex metabolism).

As a pathology model, alcohol consumption was considered, total daily alcohol dose was 10-12 g/kg. Reishi is the extract of fungus *G. lucidum* which was used as a hepatoprotective medicine. Forty outbred Spague-Dawley rats were divided into 4 experimental groups. Animals in *group C* received 5 ml of water twice a day intragastrically; for *group R*, the experimental scheme was like in the previous one, but before water Reishi was given once a day; animals in *group A* received 5 ml of alcohol (50% ethanol) twice a day; *group AR* was treated like group R, but alcohol was given instead of water. The pathology modeling continued for 4 weeks. In the middle of the experiment, ¹H NMR spectroscopy *in vivo* was done and blood was taken for ¹H NMR spectroscopy *in vitro*; in the end of the experiment the procedure was repeated and then animals were decapitated, and brain and liver were removed for ¹H NMR spectroscopy *in vitro*.

All samples for *in vitro* studies were prepared using the established protocol comprising homogenization, ethanol extraction, hydrophobic and hydrophilic metabolites separation and vacuum drying. Then ¹H NMR spectra and MS spectra were acquired (the representative ¹H NMR spectra *in vitro* are shown Fig. 1). As a result of MS spectra and NMR spectra processing and the analysis of literature and metabolic NMR databases we determined and quantified 40 liver metabolites, 38 brain metabolites and 28 blood metabolites in the *in vitro* studies and 7 brain metabolites in the *in vivo* studies. The obtained data were handled using statistical approaches: correlation coefficient, LSD-test, PLS-DA, ANOVA.

According to LSD-test, it was found that 18 liver metabolites, 9 brain metabolites, 6 blood metabolites after 2 weeks of pathology modeling and 12 blood metabolites in the end of experiment had reliable changes between experimental groups. Furthermore, PLS analysis confirmed significant differences between the groups under alcohol and Reishi impact and an increase in these differences with time. Comparison of the blood and liver metabolism

showed that 5 metabolites correlate with each other and 4 (alanine, creatine, valine, isoleucine, Table 1.) of them exhibit reliable changes between groups with the same tendency.

According to the LSD-test, in vitro and in vivo spectroscopies gave the same results for some of the metabolites (increase in glutamate level, decrease in NAA level), but individual correlation between animals in the in vivo and in vitro experiments was not found. According to PLS analysis and LSD-test, which were done for in vitro data, the brain influence of alcohol was less significant than blood or liver metabolic changes. In vivo spectra have low spectral resolution and signal-to-noise ratio, making it impossible to reliably identify small effects by in vivo NMR spectroscopy.

To conclude, this work addressed brain, blood and liver metabolism after the impact of alcohol, and reliable metabolic changes were established. Blood metabolic profile provides an opportunity to evaluate liver metabolism using the levels of alanine, creatine, valine and isoleucine. Brain was more resistant to alcohol consumption, so that no significant metabolic differences could be established using ¹H NMR spectroscopy in vivo.

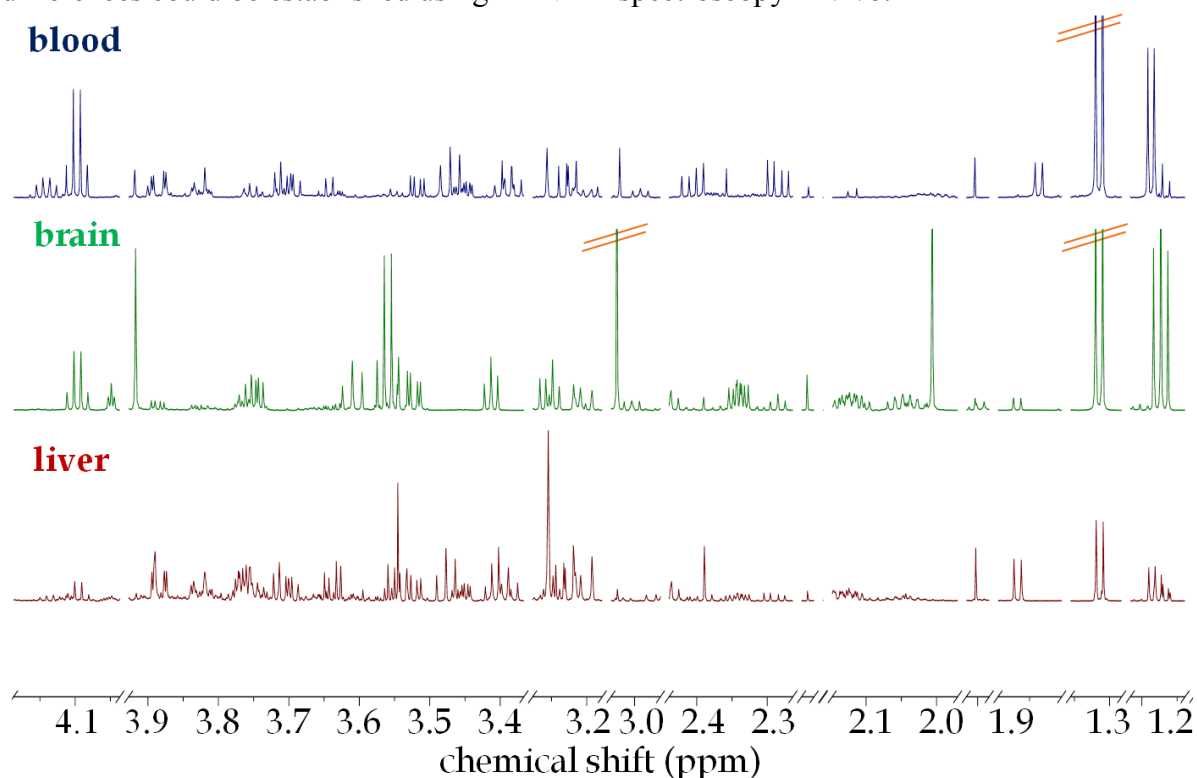


Figure 1. Parts of the ¹H NMR spectra in vitro of blood, brain and liver samples (Bruker Avance III, 700 MHz)

Table 1. Concentration changes of liver and blood metabolites

Metabolite	Blood				Liver			
	group C (N=10)	group R (N=8)	group A (N=10)	group AR (N=5)	group C (N=10)	group R (N=8)	group A (N=10)	group AR (N=5)
Alanine	72.3±8.2 A	62.8±7.1 A,B	46±4.4 B↓	59.3±3.4 A,B	39.2±2.5 A	37.1±2.2 A	30.4±0.8 B↓	29.5±1.8 B↓
Valine	20.5±1.3 A	19.3±1.3 A,B	17.2±0.5 B↓	16.6±0.6 B↓	15.3±1.8 A	14.5±1.6 A,B	11.6±0.6 B↓	12.6±1.2 A,B
Isoleucine	12.4±0.9 A	11±0.8 A,B	9.3±0.4 B↓	9.5±0.6 B↓	4±0.5 A	3.5±0.3 A,B	2.9±0.1 B↓	2.68±0.3 B↓
Creatine	36.2±1.5 A	32.4±1.5 A,B	29±1.6 B↓	31.3±2.5 A,B	3.7±0.8 A	3.2±0.3 A,B	2±0.1 B↓	2.2±0.1 B↓

A, B – statistically significant difference between groups, p<0.05 (LSD-test).

High-Resolution NMR-device in the Earth magnetic field in a laboratory environment

Pavel Kupriyanov

Faculty of Physics, St. Petersburg University, Universitetskaya nab. 7/9, 199034, Saint Petersburg, Russia

E-mail:p.kupriyanov@spbu.ru

The initial homogeneity of the Earth magnetic field is very high and NMR spectral lines should be very narrow since if relaxation times are long. This fact is very tempting for the high-resolution radio-spectroscopy. However, in the laboratory conditions a number of problems arise: (i) local field inhomogeneity due to ferromagnetic things and ferroconcrete of buildings, (ii) high electromagnetic interferences in the laboratory, (iii) natural and artificial fluctuations of the magnetic field that makes it difficult the signal accumulation. Nevertheless, all problems mentioned can be solved.

In the report the existing options for low field NMR-device are examined and the new version of the NMR-spectrometer in the Earth magnetic field is proposed. It includes electromagnetic interference shielding, active shimming system and two-sensor system for neutralization Earth magnetic field fluctuation.

The extremely good shielding was achieved with nonmagnetic cube created from of 3 mm cuprum and 7 mm aluminum sheets. The single scan spectrum from the 130 ml sample of three-methyl-phosphate is shown in Fig.1.

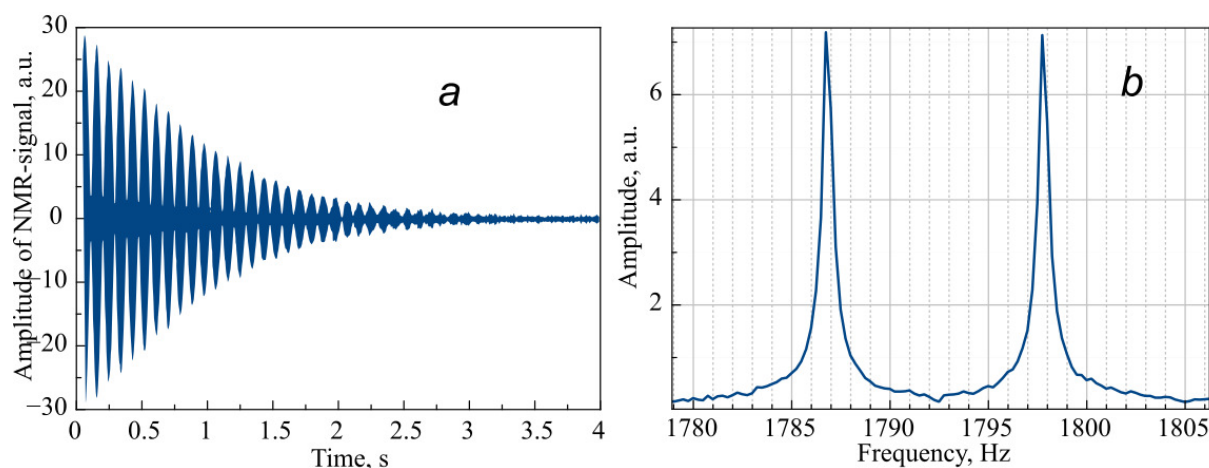


Figure 1. NMR-signal and its spectrum from the 130 ml sample of three-methyl-phosphate in laboratory environment (single scan)

At the same time, Fig.1 demonstrates the high homogeneity of the Earth magnetic field, which achieved with active shimming. Such field uniformity could be obtained by one couple of Maxwell's coils directed along the vector of the Earth's magnetic field.

The “heart” of the device is a microcontroller STM32F103C8, which forms the pulse sequences for two NMR channels. One of them is used for obtaining the spectrum of a studied substance and the second one is used for calculating the exact Larmor frequency. The frequency value is necessary for the neutralization of field fluctuations.

Magnetic resonance measurements of the fibrous plants diffusion tensor in ultra-low magnetic field

N. V. Luzhetckaia, S. V. Ievleva, K. V. Tyutyukin, V. V. Frolov

St. Petersburg State University, 1, Ulyanovskaya str., St. Petersburg, 198504, Russian Federation

E-mail: jennet24@mail.ru

Introduction

By the present day, magnetic resonance imaging (MRI) has become one of the most powerful tools for medical visualization. The technique is still being developed, and new branches of it are becoming more and more useful for medical and scientific purposes. One of them, diffusion tensor imaging, is a subject of our research.

Diffusion tensor imaging (DTI) technique started its development in the end of 20th century [1]. As the majority of others MRI techniques, this one is based on the fact that there is a strong nuclear magnetic resonance signal of hydrogen atoms. The hydrogen atoms are elements of water which is known as the main component of biological tissues. This fact explains the successful use of the method. The technique allows us to quantitatively characterize the variation in diffusion, which occurs for different spatial directions in fibrous tissues. One of the most important applications of the method is reconstruction of nerve fiber passes in a human brain.

Most of DTI experiments are done in high magnetic field (3 T and higher) [2]. However, there are some advantages of the same experiments in low magnetic field, for example, equipment mobility and wide range of possible equipment and software modifications. The low magnetic field techniques can also be used in order to decrease cost of testing new pulse sequences, training operators of MRI machine and working with phantoms. It is especially useful for the DTI techniques because the diffusion coefficient doesn't depend on magnetic field strength.

In this research report we are going to demonstrate the ability of detecting diffusion anisotropy in fibrous plants with our ultra-low magnetic field imager and make a preparation for further experiments.

Measurements of the diffusion coefficient

We used the echo pulse sequence with addition of two strong diffusion gradients for measuring diffusion coefficients of different samples. The figure and the formula are presented below.

$$D = \frac{-\ln(S/S_0)}{(\gamma\delta G)^2(\Delta - \delta/3)}$$

Here γ is a gyromagnetic ratio, S and S_0 are signal intensities respectively with and without diffusion gradients. Other parameters are shown on Fig.1.

First of all, we measured the diffusion coefficient for a jar filled with water to estimate the best parameters of pulse sequence for our further experiments with anisotropic samples. The results were close enough to already known data. The result achieved when using best matching parameters was $D_{water} = (2.7 \pm 0.1) 10^{-5} \text{ cm}^2/\text{s}$.

After that, we measured diffusion coefficients for fibrous plants, a celery and a sansevieria along and perpendicularly to their fibers. One of the results is presented: $D_{sansevieria_lengthwise} = (2.0 \pm 0.2) 10^{-5} \text{ cm}^2/\text{s}$, $D_{sansevieria_crosswise} = (1.6 \pm 0.1) 10^{-5} \text{ cm}^2/\text{s}$. So, we demonstrated the ability to distinguish diffusion coefficients for different spatial directions in fibrous plants.

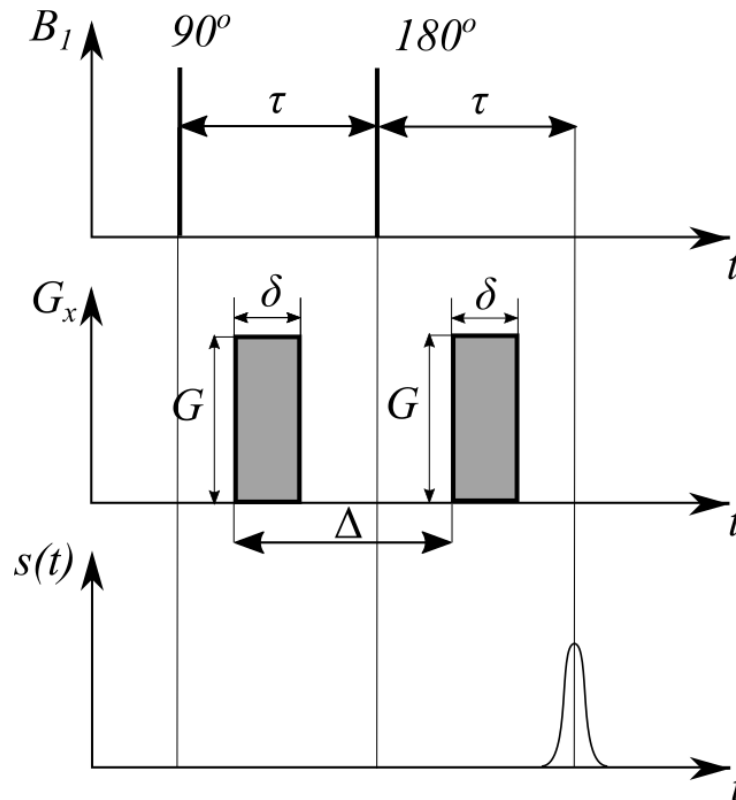


Figure 1. The pulse sequence for diffusion coefficient measurements

DTI study

Diffusion-weighted imaging

Although we were not able to perform the DTI multi-pixel experiment correctly because of some hard- and software problems, we did some steps for further experiments. Firstly, we performed a diffusion-weighted isotropic imaging (DWI) to show our ability of doing multi-pixel experiments. The main feature of this technique is the simultaneous use of encoding gradients and strong diffusion gradients in the selected direction. For more information please read our paper [3].

Adaptation of DTI algorithm

After we demonstrated the ability to carry out diffusion coefficient measurements for anisotropic samples, our next goal becomes finding a way of calculating the diffusion tensor. For this purpose we adapted a simple DTI algorithm. Its main steps are:

1. Determination of diagonal elements of the diffusion tensor.
2. Determination of off-diagonal elements of the diffusion tensor.
3. Presentation of the diffusion tensor in general form.
4. Determination of eigenvalues and eigenvectors.
5. Determination of the angle between main axis of the diffusion ellipse and x-axis.
6. Visualization of the self-diffusion tensor.

The result for a fibrous plant is presented below.

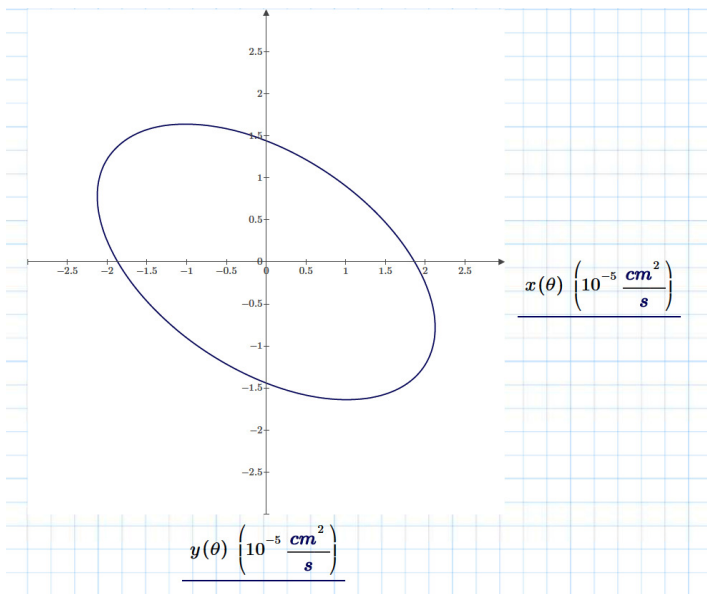


Figure 2. The diffusion tensor visualization of a fibrous plant “sansevieria”

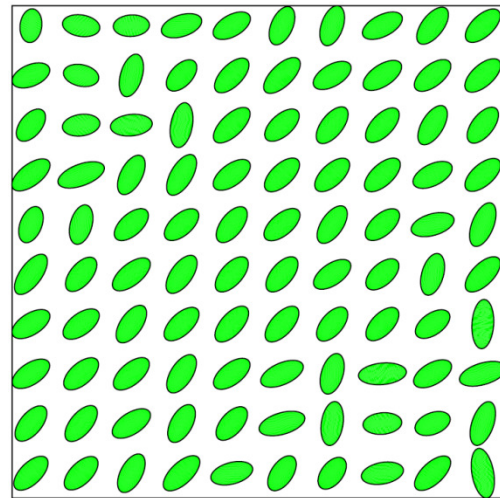


Figure 3. The diffusion tensor visualization of pseudorandom data with main direction of diffusion - 45°

We also generalized this algorithm for multi-pixel measurements and tested it for computer model data. The result is presented on Fig. 3.

Summary

In a conclusion we would like to summarise our main results. In this research we carried out our experiments in low magnetic field using homebuilt ultra-low magnetic field imager 7 mT. We showed the ability to obtain proofs of diffusion anisotropy in diffusion coefficient measurements experiments. We demonstrated the ability to conduct multi-pixels experiments with diffusion gradients with a DWI research. And finally, we adapted the DTI algorithm to our measurements and tested it for real and pseudorandom data.

As a practical demonstration, we presented the measurements and visualization of the diffusion tensor for fibrous plants in ultra-low magnetic field.

References

1. B. Stieltjes, R.M. Brunner, K.H. Fritzsche, F.B. Laun Diffusion Tensor Imaging. Springer Berlin Heidelberg, 2013. 380 p.
2. S. Mori, J-Donald Tournier Introduction to Diffusion Tensor Imaging: And Higher Order Models. Academic Press, 2013.140 p.
3. С. В. Иевлева, Н. В. Лужецкая, К. В. Тютюкин, В. В. Фролов. Диффузионно-взвешенные изображения в очень слабом магнитном поле // Вестник СПбГУ, 2016. Сер.4 Т.3(61). с. 76-81.

NMR Study of the Williams Syndrome Related Methyltransferase WBSCR27

*S. S. Mariasina¹, O. A. Petrova¹, C.-F. Chang², T.-H. Huang³, I. A. Osterman¹,
A. B. Mantsyzov¹, P. V. Sergiev¹, V. I. Polshakov¹*

¹*M. V. Lomonosov Moscow State University, Russia*

²*Genomics Research Center, Academia Sinica, Taiwan*

³*Institute of Biomedical Sciences, Academia Sinica, Taiwan*

E-mail: sm1024sm@yandex.ru

Introduction

The Williams syndrome is a rare genetic disorder characterized by a distinctive, "elfin" facial appearance, developmental delay, and cardiovascular problems. It is caused by a deletion of 26 genes from the chromosome 7. One of these genes encodes WBSCR27 protein. Its product has been recently discovered in human proteom, and bioinformatically showed to be an RNA methyltransferase – specialized enzyme, that plays regulatory role by altering the secondary and/or tertiary structure of the RNA molecule.

To understand function and an exact physiological role of biologically active macromolecules, information on its three-dimensional structure and dynamical properties is very desired. Such information helps to design the methods aimed to control its physiological activity. As no structural information on the WBSCR27 is available, we aimed to determine the solution structure of this protein using the methods of heteronuclear multidimensional NMR spectroscopy.

Features of protein behavior in solution

Protein WBSCR27 is quite difficult object for NMR studies. First of all, its molecular weight is sufficiently high ~ 27 kDa. As a result, there is overlap of signals in 2D and even in 3D spectra. In addition, large molecules exhibit slower tumbling, which results by the increased linewidths, even on spectra obtained using high-field NMR instruments. This leads the need to use higher temperature (up to 35°C) to collect NMR experiments and complicates the analysis of the spectra. However, high dispersion of ¹H-chemical shifts of WBSCR27 indicates that this protein is structured (fig. 1).

Performing procedure of backbone assignment, we discovered that some of the signals are doubled. This indicates that WBSCR27 exists in solution as the mixture of two conformers, complicating spectral analysis (fig. 2).

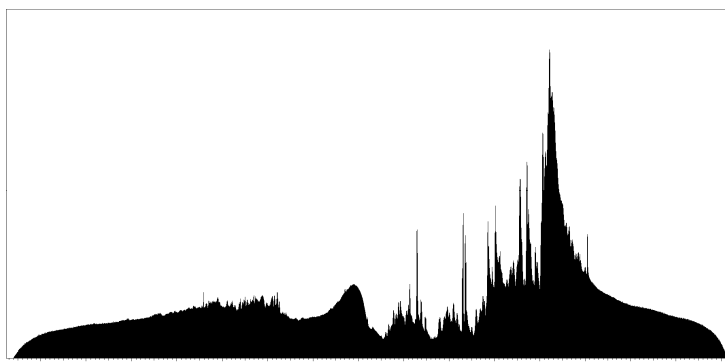


Figure 1. ¹H NMR spectra of WBSCR27

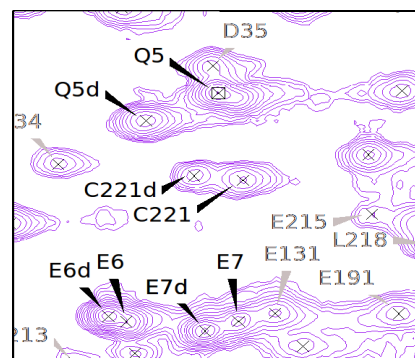


Figure 2. Fragment of ¹⁵N HSQC of WBSCR27

Binding of cofactor changes protein conformation

Another problem related to this protein is its challenging cofactor-binding behavior. It was bioinformatically shown that WBSR27 has S-adenosylmethionine (SAM) binding site. Therefore, as most of known methyltransferases, it uses SAM as a cofactor in enzymatic methylation reaction. Because of considerable intracellular level of SAM (about 30 μM) and low value of K_d (less than 0.1 μM for the most of known methyltransferases), purified WBSR27 can still contain cofactor molecule. However, SAM is not stable molecule, and it easily degrades by different ways (fig. 3).

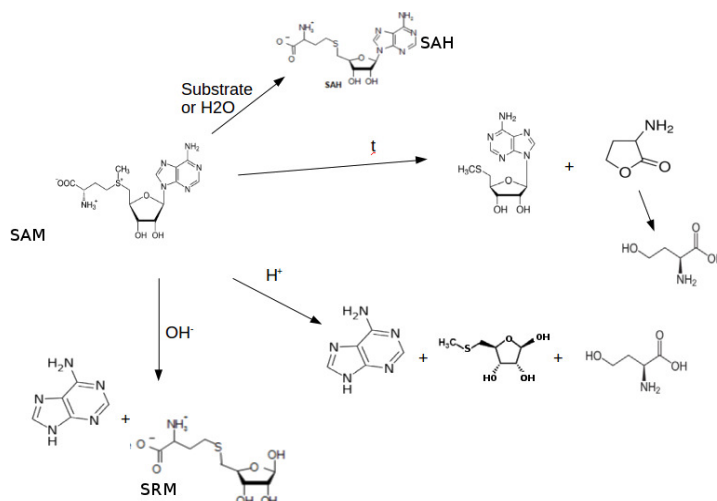


Figure 3. Degradation of S-adenosylmethionine.

Depending on the minor changes in purification and storage conditions, and, probably, during the spectra measurements, SAM molecule can be degraded, resulting in apo-form of the protein. This process is accompanied by conformational transformation of protein, which can be visualized by shifting of some of the resonances on the spectra (fig. 4 and 5).

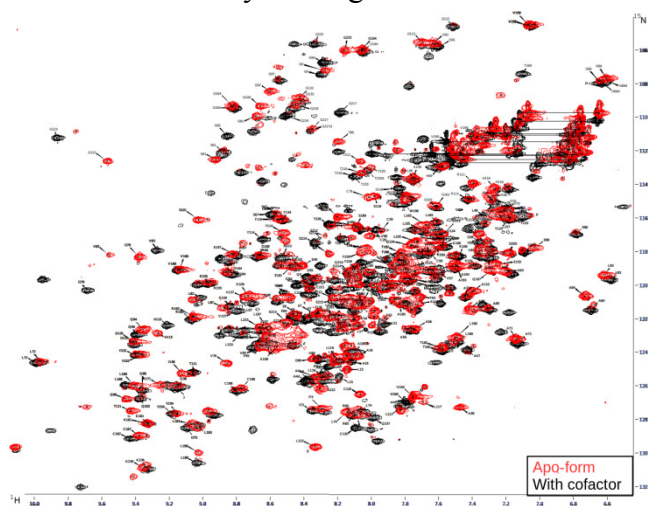


Figure 4. ^{15}N HSQC of apo-form (grey) and cofactor bounded WBSR27 (black)

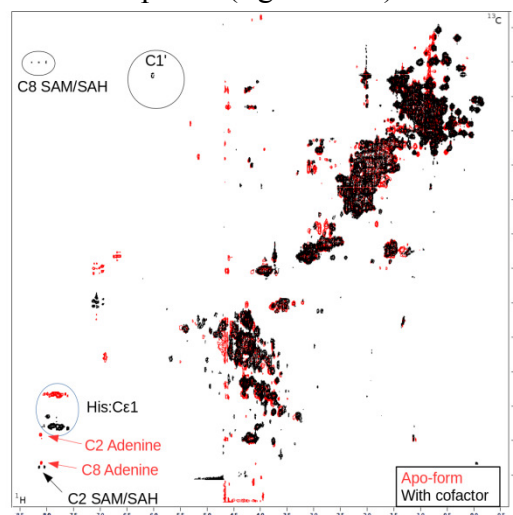


Figure 5. ^{13}C HSQC of apo-form (grey) and cofactor bounded WBSR27 (black)

Degradation of SAM molecule can be detected in ^{13}C -HSQC: peaks of ^{13}C -SAM appear in spectra of the protein bound to cofactor, and signals of ^{13}C -adenine moiety, which is the product of SAM decomposition, could be observed in the ^{13}C -HSQC spectra of the apo-form (fig. 5).

Assessment of protein backbone mobility

Chemical shifts of apo-form of WBSCR27 and protein bound to the cofactor were used to assess protein backbone mobility, using the Random Coil Index (RCI S^2). This parameter is calculated by analysis of the observed chemical shifts against chemical shift statistics for unstructured (random coil) proteins. Low RCI S^2 at the N-terminal part of the protein and within 210-230 a.a. region indicate high flexibility of these protein fragments (fig. 6).

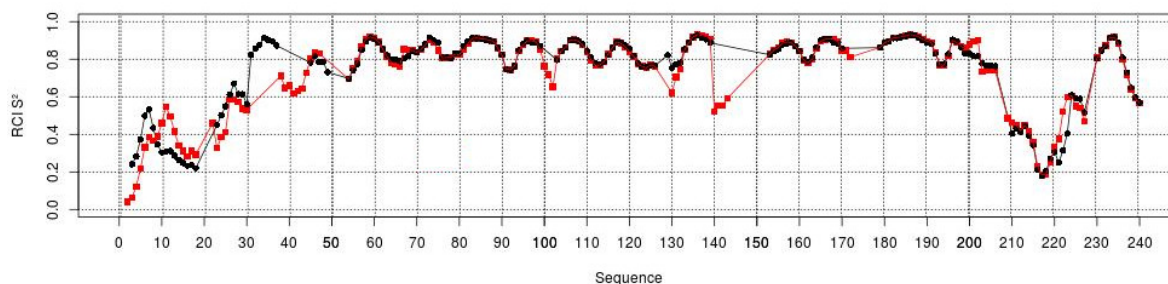


Figure 6. Predicted protein chain mobility for apo-form (grey) and cofactor bounded WBSCR27 (black)

It is interesting to note that Random Coil Indexes for apo-form and for protein complex with cofactor are almost identical even for the fragments that exhibit high mobility.

Secondary structure prediction

For the fragments of WBSCR27 with low backbone mobility secondary structure was predicted by the analysis of chemical shift changes of backbone atoms from their random coil values ($\delta_{\text{observed}} - \delta_{\text{random coil}}$) (fig. 7).

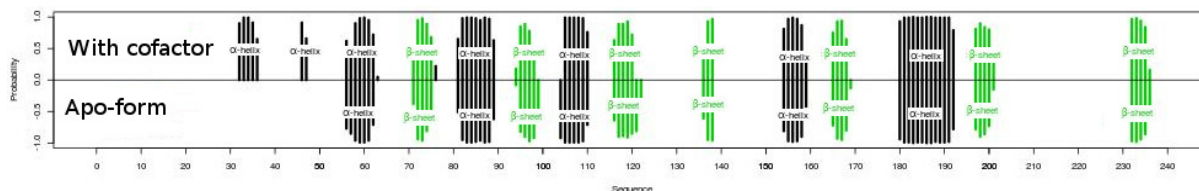


Figure 7. Predicted secondary structure for apo-form (lower) and cofactor bounded WBSCR27 (upper)

It can be seen that secondary structure of the WBSCR27 does not depend on cofactor binding.

The reported results will be used to determine 3D structure of WBSCR27 in solution which facilitates understanding the mechanism of its action and its role in the related genetic disease.

Acknowledgements

This research is supported by the Russian Science Foundation (grant 14-14-00598).

Influence of resonance saturation fields on impurity spin-lattice relaxation of nuclear spin systems in solids

V. M. Mikushev, E. V. Charnaya

St. Petersburg State University, St. Petersburg, 198504 Russia

E-mail: vicedean@rambler.ru

Introduction

The impact of various point defects on nuclear spin-lattice relaxation in crystalline solids is discussed. The so-called “defect” mechanism of local heating of nuclear spin systems through paramagnetic centers (impurities, electron centers and others) is suggested.

Samples and experiment

Single crystals of Al_2O_3 , NaCl , NaF , CsI , and GaAs , doped and undoped, were used. The time of longitudinal magnetization recovery after 90-degree and 180-degree pulses were measured at the presence of strong continuous resonance magnetic, acoustic, and electric fields. Experiments were carried out using a home-made spectrometer within the temperature range from 80 to 295 K and a Bruker Avance 400 pulse spectrometer at room temperature.

Results

The impurity relaxation via spin diffusion is effective when the local inverse spin temperature near defects, α_{loc} , is closer to the equilibrium value equal to the inverse lattice temperature, α_l , than the average value over the sample, $\langle\alpha\rangle$. If the spin-lattice relaxation time is measured using the conventional saturation recovery procedure, the impurity relaxation proceeds under the condition $\alpha_{\text{loc}} > \langle\alpha\rangle$. A rather strong additional magnetic (as well as acoustic or electric) steady saturation produces local heating of the nuclear spin-system, corresponding to $\alpha_{\text{loc}} = 0$ while $\langle\alpha\rangle$ is equal to a steady-state value $\langle\alpha\rangle_{\text{st}} > 0$. This means that the regions near impurities become warmer than the spin-system in the main crystal volume. In this case, the impurity relaxation should be turned off and the restoration of the magnetization in the sample should be caused by the lattice mechanism only.

The contributions of different mechanisms of nuclear spin-lattice relaxation are experimentally separated for ^{69}Ga and ^{71}Ga nuclei in GaAs crystals (nominally pure and doped with copper and chromium), ^{23}Na nuclei in a nominally pure NaCl crystal, and ^{27}Al nuclei in nominally pure and lightly chromium-doped Al_2O_3 crystals in the temperature range 80–300 K. The contribution of impurities to spin-lattice relaxation is separated under the condition of additional stationary saturation of NMR line in magnetic, electric and acoustic resonance fields. It is demonstrated that, upon suppression of the impurity mechanism of spin-lattice relaxation, the temperature dependence of the spin-lattice relaxation time T_1 for GaAs and NaCl crystals is described within the model of two-phonon Raman processes in the Debye approximation, whereas the temperature dependence of T_1 for corundum crystals deviates from the theoretical curve for relaxation due to the spin-phonon interaction. Possibility of direct separating and measuring the impurity and lattice contributions to nuclear spin-lattice relaxation under the condition of a steady-state magnetic saturation is demonstrated in the particular case of ^{27}Al nuclei in a γ -irradiated ruby crystal. Contributions from trivalent and charge-exchanged chromium ions to impurity nuclear relaxation were separated. The number of charge-exchanged chromium ions was found. The spin-relaxation time of Cr^{4+} centers was estimated. Contributions of F-centers and impurities to spin-lattice relaxation of ^{23}Na nuclei in a γ -irradiated NaCl crystal were clearly separated under the condition of a steady-state magnetic and acoustic saturation. The spin relaxation time of F-centers at 77 K was estimated. The change in impurity contribution to ^{23}Na relaxation as a result of irradiation was studied.

A novel design of dual-nuclei RF coils for preclinical MRI at 7 Tesla

*Anton V. Nikulin¹, Anna A. Hurshkainen¹, Stanislav B. Glybovski¹, Irina V. Melchakova¹,
Pavel A. Belov¹, Benoit Larrat², Elodie Georget², Stefan Enoch³ and Redha Abdeddaim³*

¹*ITMO University, 187101 St. Petersburg, Russia*

²*CEA-Saclay, DRF/I2BM/Neurospin/UNIRS, 91191 Gif-sur-Yvette Cedex, France*

³*Aix-Marseille Université, Institut Fresnel, 13397 Marseille Cedex, France*

E-mail: a.v.nikulin@live.ru

Introduction

Metamaterials are artificial periodic structures with subwavelength periodicity imitating continuous materials with unique electromagnetic properties. The constituents of metamaterials, the unit cells of a periodic structure, having engineered microstructure determine the macroscopic material properties. Among different types of metamaterials there are so-called wire media composed of periodically arranged thin metallic wires. A resonating slab of a wire medium is capable of lensing with subwavelength resolution and local magnetic field enhancement. Both of these properties were shown to be applicable in MRI [1-2]. Conventional radio-frequency (RF) coils for preclinical MRI contain lumped capacitive circuits for tuning and matching small loop antennas to Larmor frequencies [3]. Such circuits may be especially complex in the case of two or more operational frequencies, i.e. in multi-nuclei MRI.

In this work we use periodic resonant structures of metal wires to construct novel RF coils for preclinical dual-nuclei MRI at 7 Tesla. The proposed design operating with the nuclei ^1H and ^{19}F simultaneously has been studied numerically and experimentally using Bruker Pharmascan MRI system.

Design and study

In the considered application RF coils have to be tuned to and matched at two frequencies (282.2 and 300.1 MHz) simultaneously. The first frequency is the Larmor frequency of Fluorine ^{19}F , while the second one is the Larmor frequency of Hydrogen ^1H at the magnetic field of 7 Tesla. In this case two images for different nuclei can be obtained independently using the same RF coil and superposed in post-processing.

It was previously shown that a periodic structure composed of near-half-wavelength metal wires and/or electrically short wires loaded by capacitive patches may operate as a resonator with multiple hybridized eigenmodes due to coupling between the wires [2, 4, 5]. These eigenmodes can be excited in the same resonators in order to achieve multi-band operation, which is required in multi-nuclei MRI. In the considered coil (see Fig. 1) two mutually orthogonal periodic structures of resonant metal wires are used as resonators having high quality factors at the desired Larmor frequencies. The coil is fed with a small loop inductively coupled to a RF cable. The loop position is carefully chosen to match the impedance of the coil to 50 Ohm.

In the proposed coil the feeding loop as well as two orthogonal periodic structures of wires were realized using the printed-circuit board (PCB) technology. Each wire of the coil was a copper strip with the thickness 1 mm over Rogers 4003 substrate. Such arrays of printed wires, when being half-wavelength, support multiple resonances of hybridized eigenmodes. Recently it was shown that coupling of an electrically-small loop feed to these eigenmodes improves the near-field homogeneity and the signal-to-noise ratio in preclinical MRI [4] at 7 Tesla. Here we use two quasi-independent periodic structures: one (the upper PCB) with six wires parallel to B_0 axis and another (the lower PCB) with six wires perpendicular to B_0 as shown in Fig. 1. The wires of the upper PCB have nearly half wave

lengths at 282.2 MHz, while the lower PCB operating at 300.1 MHz due to the lack of space inside the bore supports electrically short wires loaded by grounded capacitive patches. From both the periodic structures a lowest-frequency eigenmode is used and excited by the same loop feed.

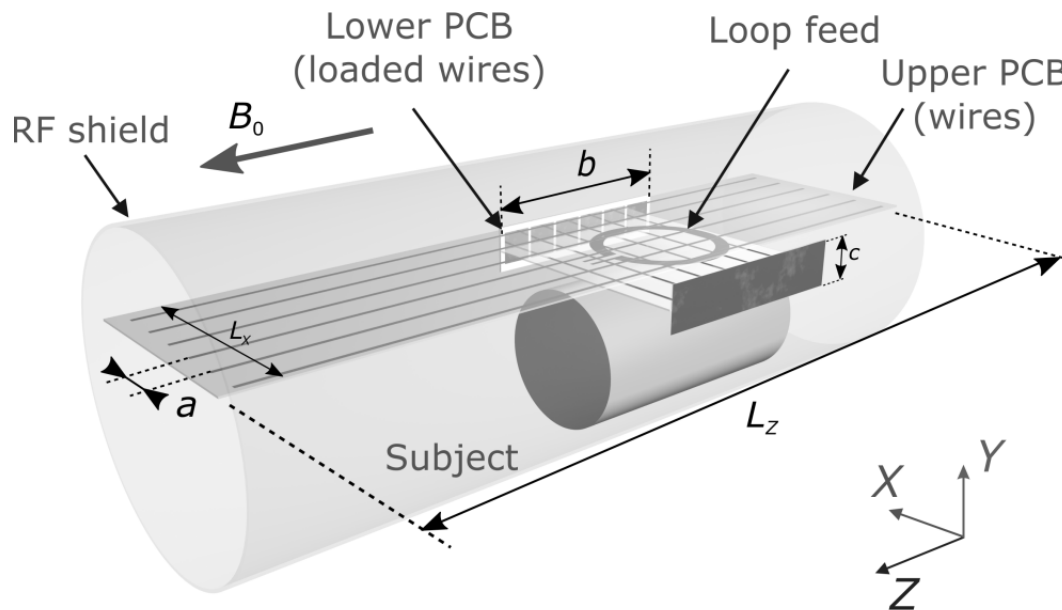


Figure 1. Geometry of the proposed coil

We have conducted numerical simulations using CST Microwave Studio (the Frequency-domain solver). The numerical optimization of geometric parameters allowed to tune and match the coil at the two desired Larmor frequencies simultaneously with the reflection coefficient lower than -10 dB. The subject was simulated as a homogeneous phantom with the relative permittivity of $39+1.5i$. The coil was manufactured and measured using a vector network analyser (VNA). Also it was tested using the research 7 Tesla preclinical system Bruker Pharmascan 7 Tesla with a phantom based on the mixture containing both ^1H and ^{19}F nuclei. The results demonstrate matching of better than -10 dB at the corresponding frequencies, which is in good agreement with the simulation results. The coil was capable of imaging at the two nuclei with the SNR level sufficient for purposes of functional preclinical MRI.

Conclusion

In conclusion, a novel dual-frequency RF-coil design has been proposed, which is based on resonant excitation of hybridized eigenmodes of periodic wire structures. In this work based on this design we optimized and experimentally realized an RF coil for dual-nuclei MRI for Fluorine and Hydrogen imaging at 7 Tesla. Importantly, the new coil requires no expensive variable non-magnetic capacitors for tuning and matching, which makes the coil much cheaper.

Acknowledgements

This work was supported by the Russian Science Foundation (Project No. 15-19-20054).

References

1. A.P. Slobozhanyuk, I.V. Melchakova, A.V. Kozachenko, P.A. Belov, C.R. Simovski. Wire metamaterial for the improvement of magnetic resonance imaging – *Microwave and Optoelectronics Conference (IMOC)*, 1-3 (2013).

2. A. P. Slobozhanyuk, A. N. Poddubny, A. J. E. Raaijmakers, C. A. T. van den Berg, A. V. Kozachenko, I. A. Dubrovina, I. V. Melchakova, Y. S. Kivshar and P. A. Belov. Enhancement of Magnetic Resonance Imaging with Metasurfaces – *Advanced Materials*, **28**, 18321838 (2016).
3. F. D. Doty, G. Entzminger, J. Kulkarni, K. Pamarthy and J. P. Staab. Radio frequency coil technology for small-animal MRI – *NMR in Biomedicine*, **20**, 304325 (2007).
4. C. Jouvaud, R. Abdeddaim, B. Larrat and J. de Rosny. Volume coil based on hybridized resonators for magnetic resonance imaging – *Applied Physics Letters*, **108**, 023503 (2016).
5. S. B. Glybovski, A. V. Shchelokova, A. V. Kozachenko, A. P. Slobozhanyuk, I. V. Melchakova, P. A. Belov, A. V. Sokolov, A. Y. Efimtsev and V. A. Fokin. Capacitively-loaded metasurfaces and their application in magnetic resonance imaging – *Radio and Antenna Days of the Indian Ocean (RADIO)*, Belle Mare, 1-2 (2015).

Synthesis of ReF_3 (Re = rare earth ions) nanoparticles for NMR research

*D. S. Nuzhina*¹, *E. M. Alakshin*^{1,2}, *A. V. Klochkov*^{1,2}, *S. Kodjikian*³, *E. I. Kondratyeva*^{1,2},
*S. L. Korableva*¹, *I. V. Romanova*¹, *M. S. Tagirov*^{1,2,3}

¹*Institute of Physics, Kazan Federal University, 420008, Kremlevskaya 18, Kazan, Russia*

²*Institute of Perspective Research, TAS, 420111, L. Bulachnaya 36a Kazan, Russia*

³*Institut NEEL CNRS, 38042, 25 rue des Martyrs BP 166, Grenoble, France*

e-mail: nuzh.darya@gmail.com

Studying the properties of the nanopowder DyF_3 is one of the most interesting subject in connection with the fact that DyF_3 improves the characteristics of Nd-Fe-B magnets [1-4]. The ferromagnetic phase transition in a single crystal was observed at $T_c=2.55$ K [5]. Investigation of Curie temperature dependence versus the size of DyF_3 nanoparticles by ^3He NMR is a fundamental problem. The results of the hydrothermal synthesis DyF_3 is published only in a few works [6-8] in despite of the large number of articles on the synthesis rare earths trifluorides. Therefore the synthesis of such nanoparticles is also an actual task.

In this work synthesis series of DyF_3 nanosized samples was prepared for investigation of Curie temperature dependence versus the size of DyF_3 nanoparticles by ^3He NMR.

The samples of DyF_3 were synthesized using following technology [9, 10] with different microwave-assisted hydrothermal treatment time (0, 30, 420 min). The chemical reactions can be expressed as follows:



Transmission electron microscope (TEM) images were taken with Philips CM300 operated at 300 kV (Neel Institute, Grenoble, France). Figure 1 shows the TEM image with the corresponding electron diffraction pattern in the insert and size distribution diagram for sample #3. On sharp diffraction rings can judge of the good crystallinity of samples (rings radii: 0.36 nm, 0.32 nm, 0.20 nm). The synthesized nanoparticles have average size of about 16 - 18 nm (sample #1 – 16.9 nm, sample #2 – 16.9 nm, sample #3 – 18.2 nm).

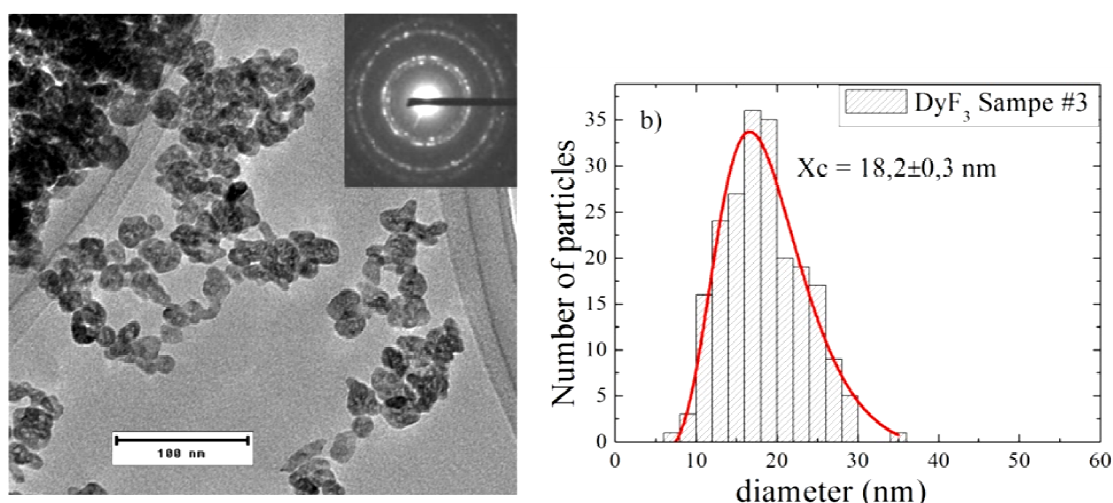


Figure 1. a) TEM image of DyF_3 nanoparticles with corresponding electron diffraction pattern in the insert (sample #3). b) The size distribution diagrams for sample #3. Solid line is the log-normal distribution fitting, X_c is the center

Crystal structure of DyF_3 nanoparticles was characterized by X-ray diffraction (XRD). The XRD patterns of three DyF_3 nanosized samples are shown on Figure 2. They were recorded using a Bruker D8 Advance X-ray diffractometer with use of copper $\text{K}\alpha$

($\lambda = 1.5418 \text{ \AA}$) radiation at a scanning rate of 5° min^{-1} in 2θ range of $20\text{--}60^\circ$ by step 0.015° . Diffraction peaks could be indexed from the simulated pattern calculated by PowderCell [11] software (space group $Pnma$ ($\text{No}62$), lattice constants $a = 0.6460 \text{ nm}$, $b = 0.6906 \text{ nm}$, $c = 0.4376 \text{ nm}$ [12]). Obviously, that peaks on XRD pattern for samples #1-3 become narrower with increasing microwave-assisted hydrothermal treatment time (Figure 2a-2c).

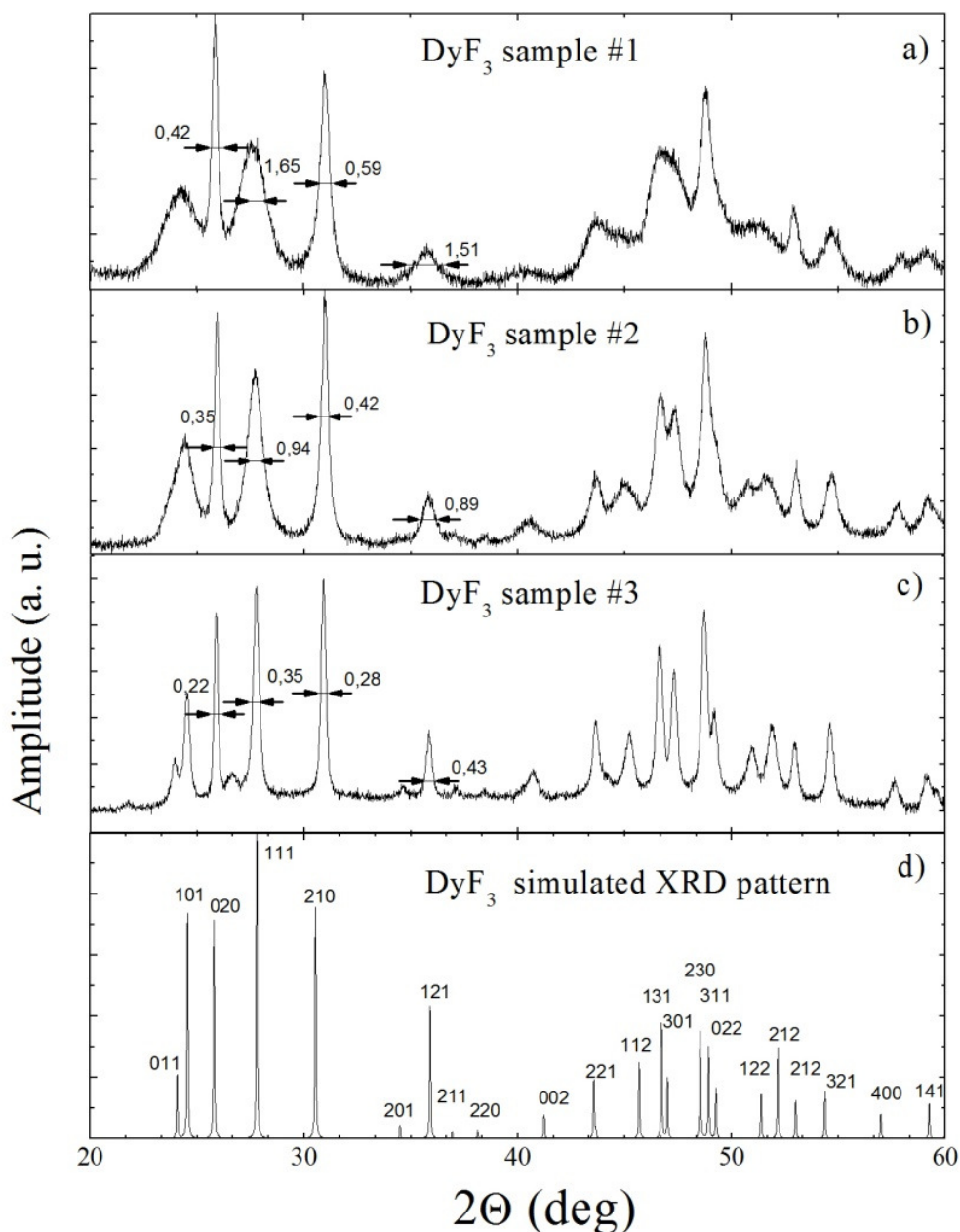


Figure 2. a) - c) experimental XRD patterns of synthesized DyF₃ nanosized samples #1-3. d) simulated XRD patterns in PowderCell software

Thus, for the first time using a microwave hydrothermal method the series of nanoparticles DyF₃ were synthesized with average size about 16-18 nm. Influence of microwave radiation has been found on the particle size distribution and XRD peaks width.

Also the results of the synthesis nanoparticles DyF₃ and TbF₃ will be presented.

Acknowledgments

This work was partially supported by RNF grant №16-12-10359.

References

1. S.-E. Park, T.-H. Kim, S.-R. Lee, S. Namkung et al. – *Journal of applied physics*, 111(7), 07A707 (2012).
2. X.J. Cao, L. Chen, S. Guo et al., - *Journal of Alloys and Compounds*, 63, 315-320 (2015).
3. S. Sawatzki, I. Dirba, L. Schultz, O. Gutfleisch. – *Journal of applied physics*, 114, 133902-133905 (2013).
4. R. Sueptitz, S. Sawatzki, M. Moore, M. Uhlemann et al., – *Materials and Corrosion*, 66(2), 152-157, (2015).
5. A. V. Savinkov, S.L. Korableva, A.A. Rodionov et al., – *J. Phys.: Condens. Matter*, 20(48), 485220 (2008).
6. Bhowmik, S., Gorai, T., Maitra, U. - *J. Mater. Chem. C*, 2, 1597-1600 (2014).
7. Li, C., Yang, J., Yang, P., Lian, H., Lin, J. - *Chem. Mater.*, 20, 4317-4326 (2008).
8. Ye, X., Chen, J., Engel, M., Millan, J.A., Li, W., Qi, L., Xing, G., Collins, J.E., Kagan, C.R., Li, J., Glotzer, S.C., Murray, C.B. - *Nature Chemistry*, 5, 466-473 (2013).
9. L. Ma et al., - *Materials Letters*, 61(13), 2765-2768 (2007).
10. E.M. Alakshin, B.M. Gabidullin, A.T. Gubaidullinet. al., – *arXiv:condmat*, 1104, 0208 (2011).
11. W. Kraus, G. Nolze, - *Journal of Applied Crystallography*, 29, 301-303 (1996).
12. DyF₃ crystal structure, Springer Materials (electronic resource)
http://materials.springer.com/isp/crystallographic/docs/sd_1300541 (up to 28.02.2016)

Diffusion-weighted MRI in clinical oncology

I. N. Petrov^{1,2}, V. M. Cheremisin^{1,2}, I. G. Kamyshanskaya^{1,2}, R. L. Kazarov¹

¹*Mariinskaya hospital, St. Petersburg State University,*

²*Medical faculty, oncology department,
St. Petersburg, Russia*

Diffusion-weighted imaging (DWI) has become a part of standard protocols in clinical routine practice. For instance, this sequence is irreplaceable in stroke diagnostic. However the application area of DWI spread widely on the whole human body MR-imaging. Currently it's used to diagnose oncological, inflammatory and other pathology. There is no wonder, because DWI directly presents the rate of free water motion in extra intracellular space, into the vessels lumen. The grade of diffusion restriction in biological tissues correlates with membranes integrity and cellularity of a particular tissue. DWI doesn't depend on relaxation time and independently affects the image contrast.

DWI is based on the application of the gradient pulses on turbo spine echo sequence. As a result we gain images simultaneously weighted by T2 relaxation time and water molecules motion rate. Depending on the amplitude, duration of the pulses, and interval between them, there exist different b-factors, which reflect sensitivity of the DWI. With the increasing of the b-factor, normal tissue signal intensity decreases. At the higher factor levels ($800 > s/mm^2$) the hyperintensive signal remains from zones with restricted diffusion only, for instance, abscesses, malign tumors, cytotoxic edema. To quantify the rate of diffusion in tissues we use an apparent diffusion coefficient (ADC).

In clinical practice DWI is a useful application in different conditions associated with the change of the quantitative composition of cells, damage of their membranes and perfusion changes. The evaluation of the ADC of the patients suffering from malign bladder tumors takes place at the MRI department of Mariinskaya hospital. It's known from literature, that the ADC in a malign tissue is much lower, than in a normal one. And there we have a tendency to decrease ADC with an increase of the grade and T-stage of malign neoplasm. However, according to different localizations, the data from different researchers varies. For instance, Takeuci et al. showed statistically significant results of comparing the ADC with histological grade, T-stage of bladder cancer. On the other hand there are few reports about absence of statistically significant results in comparing of the ADC with the grade in rectal cancer. Moreover, the data gained from different centers in the same diseases varies, which is associated with investigation uncertainty, difference in MR-units and protocols. In general, currently we don't have enough information to use this method as a «gold standard» and as a basement for treatment planning.

According to cancer patients treatment, regardless from treatment regimen, in positive therapy response, there is a tendency toward diffusion improvement and an increase of the ADC. Based upon it, potentially, the ADC quantification can become a good marker of the therapy effectiveness.

As an example of clinical application of this method, there are some MR-studies and histological conclusions from Mariinskaya hospital below.

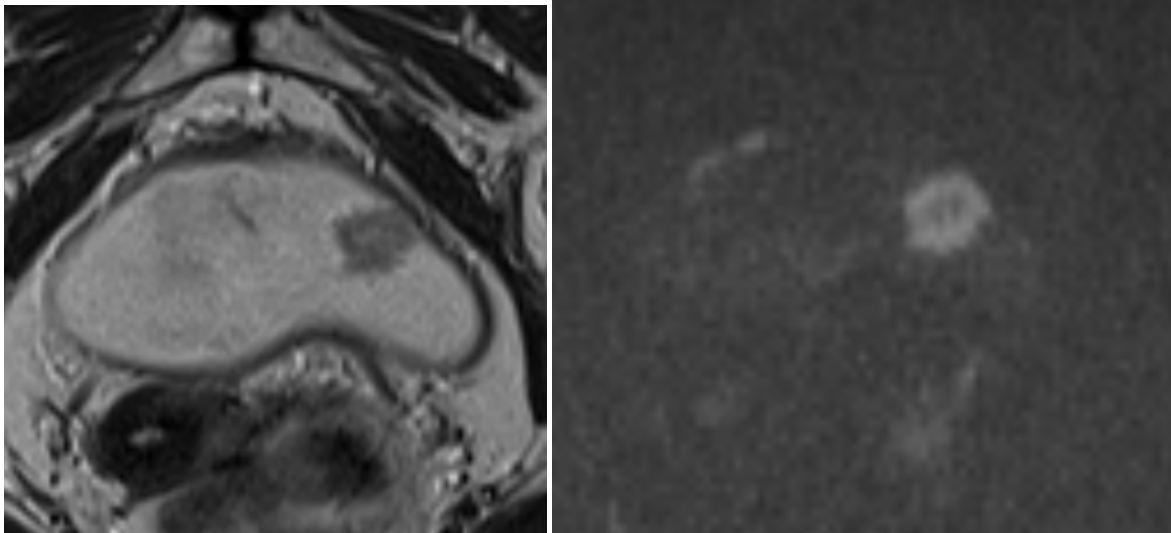


Figure 1. T2 in axial plane (left), DWI b1000 (right). The neoplasm on the left anterior bladder wall has hyperintensive signal on DWI without invasion in muscle layer

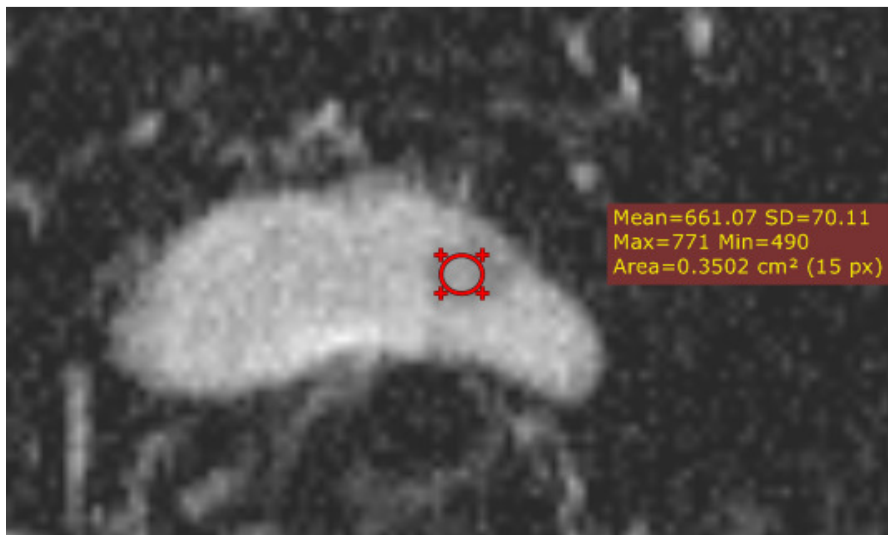


Figure 2. ADC map. Mean ADC in area of interest 661. Histological conclusion: noninvasive transitional cell carcinoma G1

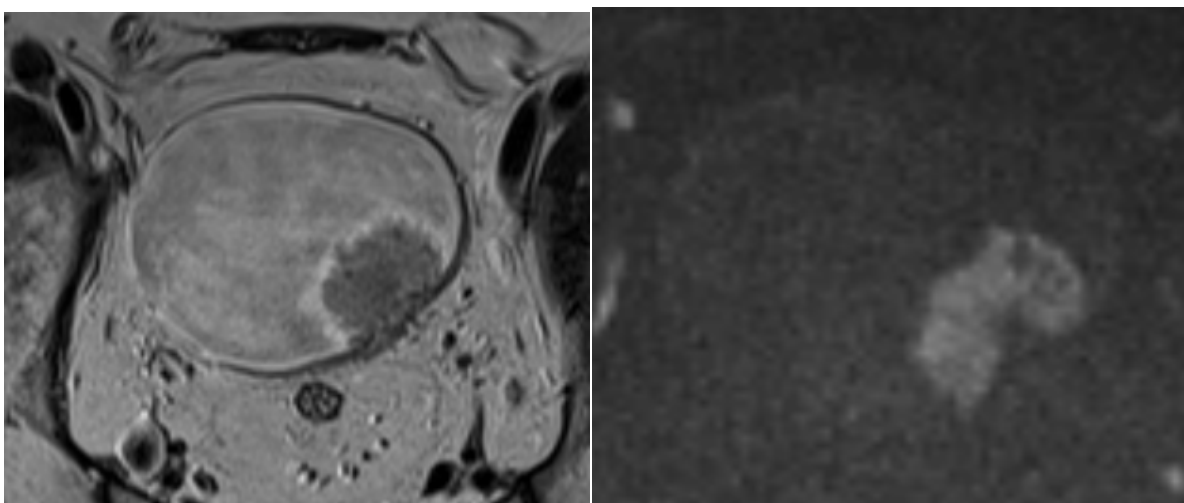


Figure 3. T2 in axial plane (left), DWI b1000 (right). The neoplasm on left posterior bladder wall has a hyperintensive signal on DWI with invasion in muscle layer and adjacent fat

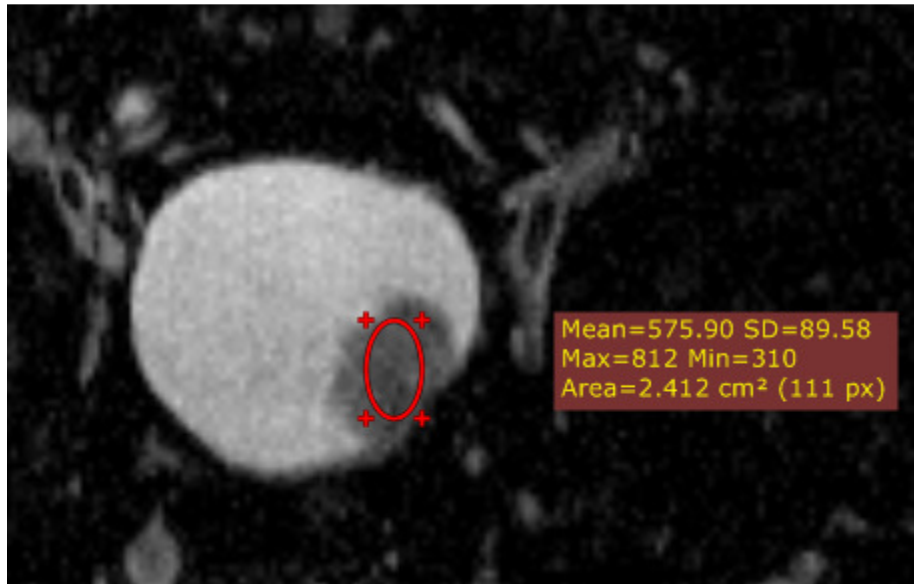


Figure 4. ADC map. Mean ADC in area of interest 576. Histological conclusion: invasive papillary urothelial carcinoma G3

The disadvantage of this method is varying of data when using different units and protocols. To solve this problem, Japanese researchers suggested using the ratio between the tumor ADC and the skeletal muscle ADC.

In our study we are trying to find out if it is correctly to quantify the ratio between the tumor ADC and the normal bladder wall ADC (given that wall edema is absent). It's essential to standardize this ratio for different MR-units and sequence protocols.

Determination of relative positions of paramagnetic probes in smectic liquid crystal by analysis of angular dependence of dipole-dipole broadening of EPR spectra

D. A. Pomogailo, A. Kh. Vorobiev

*Department of Chemistry, M.V. Lomonosov Moscow State University
119991, Moscow, Leninskie Gory, 1-3
texafirin@ya.ru*

Mutual positions of molecules of soft matters determine the properties of the latter. Liquid crystals (LC) are partially disordered materials, therefore it is difficult to determine relative arrangement of the molecules in these materials.

In the present work, the relative positions of paramagnetic molecules in liquid crystals are determined by paramagnetic probe method, which consists in inserting of paramagnetic probe in liquid crystal and recording of EPR spectrum. The information about the structure of LC matrix is extracted from the spectrum.

It is known, that the dipole-dipole broadening of EPR spectrum depends on distance between paramagnetic particles and angle between the magnetic field direction and the line connecting two spins. This fact leads to angular dependence of dipole-dipole broadening of EPR spectra, when paramagnetic particles take certain positions. The method of determination of probe molecules arrangement in the liquid crystalline structure is described in present work. The method is based on analysis of angular dependence of dipole-dipole broadening of EPR spectra.

For this purpose angular dependencies of EPR spectrum for samples with low and high probe concentrations were recorded, the width of central component (the distance between minimum and maximum points for the component recorded as first derivative curve) was measured. The broadening was calculated as difference between these widths at different positions of sample relatively magnetic field.

The liquid crystals 8CB (4-n-octyl-4'-cyanobiphenyl) and HOPDOB (p-hexyloxyphenyl ester of p-decyloxybenzoic acid) were chosen as smectic materials. Radicals C4, TPV, A3, A5 were used as a paramagnetic probes. The structures of used liquid crystals and paramagnetic probes are presented in Fig. 1.

It was found that for liquid crystal 8CB the angular dependence of dipole-dipole broadening is absent. It means that paramagnetic species are randomly distributed in the sample. On the contrary, evident angular dependence of broadening of EPR spectra were found in liquid crystal HOPDOB (Fig. 2a). The presence of the angular dependence means that probes take the certain positions in LC structure.

The line shape of EPR spectrum was calculated by theoretical simulations of angular dependence of dipole-dipole broadening. Experimental and calculated angular dependencies are shown on Fig 2a by points and lines correspondingly. Distance between nitroxide groups of paramagnetic probes R and angle σ were determined as a result of modeling. Relative position of the probe molecules in accordance with these data is shown in Fig. 2b. The position of pairs of liquid crystalline molecules is also shown in Fig. 2b for comparison. Coordinates of this pair were determined from the results of X-ray diffraction for crystalline phase of HOPOOB, which is the closest analog of HOPDOB. The assumptions about probable weak bonding, responsible for this arrangement were discussed.

This work was supported by The Russian Foundation for Basic Research (Grant №14-03-00323).

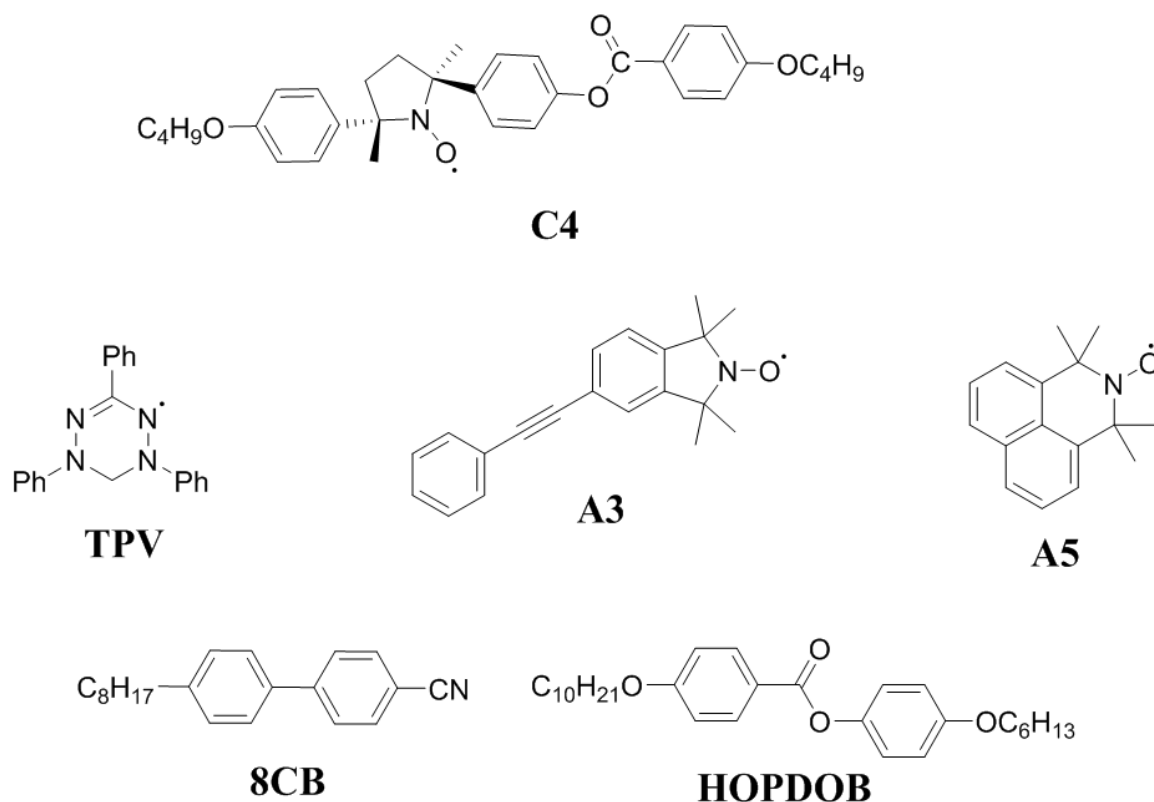


Figure 1. Used paramagnetic probes and liquid crystals

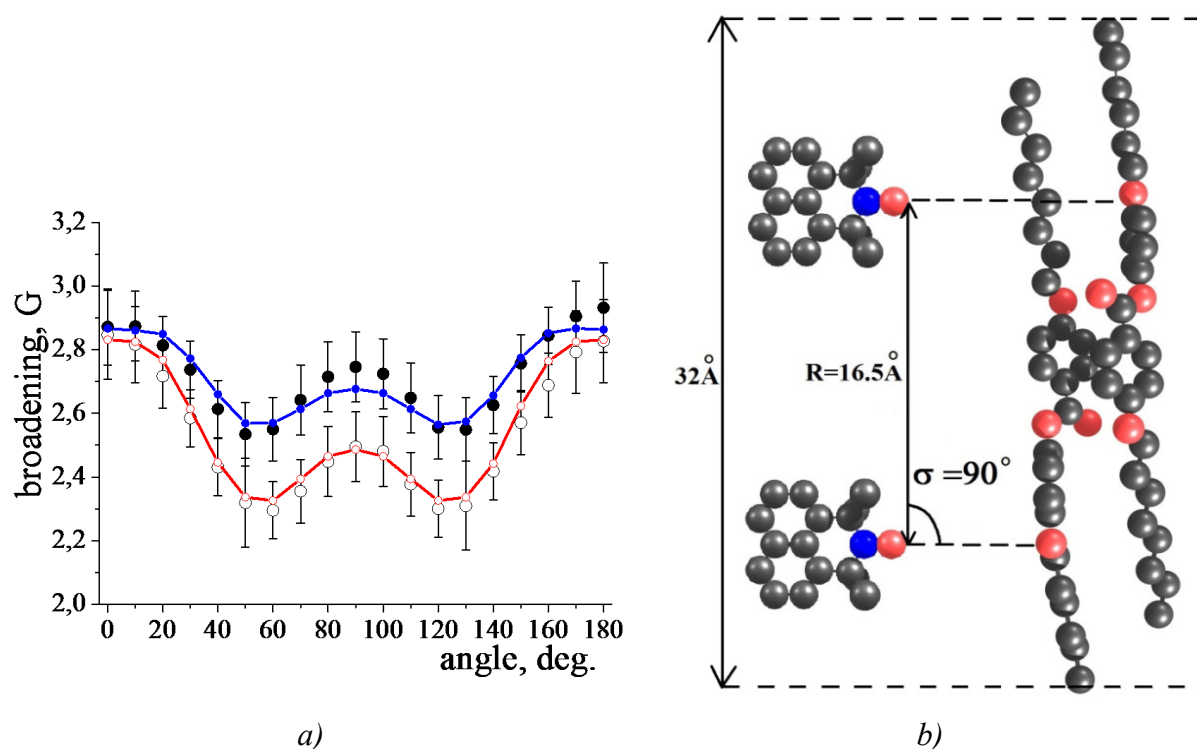


Figure 2. a) Angular dependencies of dipole-dipole broadening in SmA and SmC phases of HOPDOB (points – experiment, lines – result of modeling, empty points – SmC, filled points – SmA), b) relative positions of paramagnetic probe A5 in SmA phase of liquid crystal HOPDOB. Dashed line – rigid part of smectic layer

Second RNA-recognition motif RRM2 of TDP-43 protein: oxidative stress leads to structure destabilization, aggregation and increased susceptibility to proteolytic degradation

*Sevastyan O. Rabdano¹, Sergei A. Izmailov¹, Dmitry A. Luzik¹, Adam Groves²,
Ivan S. Podkorytov¹, and Nikolai R. Skrynnikov^{1,2}*

¹Laboratory of Biomolecular NMR, SPbSU, 199034, 7/9 Universitetskaya nab., St. Petersburg

²Department of Chemistry, Purdue University, 47907, 560, Oval Drive,
West Lafayette IN, USA.

E-mail: sevastyan@rabdano.ru

<http://bio-nmr.spbu.ru>

Cysteine-containing proteins are highly susceptible to oxidative stress. In particular, indiscriminate oxidation of cysteine side-chains and formation of intermolecular disulfide bonds brings into contact protein surfaces, which have not evolved to complement each other. The resulting random pairing of surface residues at the protein-protein interfaces is likely to have an appreciable destabilizing effect on the protein structure.

To test this hypothesis we have investigated the effect of oxidative stress (modeled by hydrogen peroxide treatment) on the second RNA-recognition motif (RRM2) from the neuropathological protein TDP-43. Formation of disulfide-bridged dimers in this system was confirmed by non-reducing SDS-PAGE and ESI mass spectrometry. To assess the effect of intermolecular disulfide linkages on the structural stability of RRM2, we have conducted the HSQC-based H/D exchange experiments. The measurements were more complicated than expected due to the increased propensity of disulfide-bonded dimers to form aggregates. A special experimental protocol has been developed to address this problem, involving peroxide treatment of the sample dissolved in the D₂O solvent followed by dithiothreitol reduction to break the aggregates and recover the signal. The obtained experimental data unequivocally demonstrated loss of structural stability in disulfide-linked dimers of RRM2. The destabilization of RRM2 could lead to proteolytic cleavage of this domain at the sites that normally remain protected in the unperturbed RRM2. The C-terminal fragments of TDP-43 resulting from proteolytic cleavage of the RRM2 domain have been viewed as one of the causative factors in the genesis of the neuronal inclusion bodies [1].

The measurements were performed using multiple facilities of the Research Park at St. Petersburg State University. The study was supported Russian Science Foundation grant #15-14-20038.

References

1. Zhang, Y. J. et al. – *Proc. Natl. Acad. Sci. USA*, **106**, 7607-7612 (2009).

Molecular dynamics studies and *in silico* mutational analysis as applied to dynamics in ubiquitin crystals

Olga N. Rogacheva^{1*}, *Sergei A. Izmailov*^{1,*}, *Nikolai R. Skrynnikov*^{1,2}

¹Laboratory of Biomolecular NMR, St. Petersburg State University, St. Petersburg 199034, Russia.

²Department of Chemistry, Purdue University, West Lafayette, Indiana 47907, USA.

E-mail: nikolai@purdue.edu

*These authors contributed equally to this work.

We have performed molecular dynamics (MD) simulation of different crystal forms of ubiquitin in order to investigate (i) conformational exchange between β turn type I and II in the region 51-54 and (ii) rocking dynamics whereby protein molecule as a whole undergoes subtle reorientational motion within the confines of the crystal lattice. To better understand these motional processes we introduced certain *in silico* point mutations and recorded trajectories of the selected mutants. The mutant trajectories involved from 24 to 48 ubiquitin molecules in explicit solvent and had a length of 2 μ s per trajectory.

β I conformation in ubiquitin represents a “default” state, which is found in solution and in the majority of crystal structures. At the same time β II conformation has also been observed in a number of crystals, such as PDB ID 3ONS. Crystal MD simulations featuring K63A, E64A or E24A point mutations helped us elucidate the role of specific intermolecular contacts and steric factors in the stabilization of the β II conformation. As it turned out, the protonation of the E24 side chain and the steric confinement of this side chain play a key role in the β II propensity found in this crystal form.

Experimental data suggest that rocking motion in the ubiquitin crystal PDB ID 3N30 occurs on the time scale similar to β I \leftrightarrow β II conformational exchange. This raises the question whether these two motional modes are coupled. To elucidate this point we have introduced K11A and G53A mutations. The first one abrogates intermolecular K11-D52 salt bridge, which is potentially responsible for statistical coupling between rocking motion and β I \leftrightarrow β II exchange. The second effectively locks the system in the β I conformation. The resulting trajectories led us to conclude that conformational exchange in the β turn can indeed be coupled to rocking and the coupling is mediated by the K11-D52 salt bridge.

Acknowledgments

This work was supported by the RSF grant 15-14-20038. We also acknowledge the T-Platforms cluster of St. Petersburg State University for providing CPU time for the MD simulations.

Evidence of coherent magnon state in easy-plane antiferromagnet and yttrium iron garnet films

T. R. Safin¹, A. V. Klochkov¹, I. G. Motygullin¹, K. R. Safiullin^{1,2}, M. S. Tagirov^{1,2}

¹*Kazan Federal University, 420008, Kremlevskaya 18, Kazan, Russia*

²*Institute of Perspective Research, TAS, 420111, L. Bulachnaya, 36a, Kazan, Russia*

E-mail: TiRSafin@gmail.com

Bose-Einstein condensation (BEC) corresponds to the accumulation of the macroscopic number of particles at the ground-state level, described by a single wave function. The formation of this state for bosonic particles was predicted by S.N. Bose and A.Einstein in 1925. The “pure” BEC state of ⁸⁷Rb atoms was experimentally observed in 1995 by E.Cornell et al. [1]. The coherent precession of magnetization was observed in superfluid ³He-B in 1984 [2]. It was explained as a formation of coherent quantum state [3] even in very inhomogeneous magnetic field, which is equivalent of magnon BEC [4]. Many magnonic superfluid properties have been observed and investigated for last 30 years like: the Josephson effect [5], quantum spin current vortex [6], Goldstone modes [7], phase slippage [8] and many other coherent quantum phenomena. Later the coherent precession of magnetization have been found in other ³He systems: texture trap in ³He-B [9], that shows the properties of Q-ball [10]; ³He-A immersed in a squeezed aerogel [11,12] ; ³He-B immersed in stretched aerogel [13]; etc. The review of this phenomena one can found in [14-16]. The very similar states of magnon BEC were found in easy-plane antiferromagnets CsMnF₃ and MnCO₃ [17-20].

In case of equilibrium magnon state BEC of magnons cannot be formed due to zero chemical potential of magnons. Magnon BEC can be observed only in presence of non-equilibrium magnons, which density is more than critical. The energy minimum corresponds to the precessing magnetization, deflected on the angle, which is conforms to a chemical potential of non-equilibrium magnons [16]. The different coherent magnon states, similar to charge density waves in metallic wires was also found in yttrium iron garnet films [21].

The question about coherent magnon state under different pumping conditions has been raised in present work. The solid state easy-plane antiferromagnet MnCO₃ has been studied by pulse and continuous wave (CW) nuclear magnetic resonance technique at the temperature of 1.5 K. The ferromagnetic resonance (FMR) spectra investigations of yttrium iron garnet (YIG) Y₃Fe₅O₁₂ single crystal thin and thick films have also investigated. The obtained data on YIG films at a room temperature will be reported later.

In experiments with pulse nuclear magnetic resonance (NMR) the magnetization is created by constant magnetic field. Pulse of radiofrequency field (RF) deflects the magnetization on the β angle, after that the free induction decay (FID) signal is measured. In the incoherent precession state spins almost instantly lose the information about primary phase and frequency after the RF pulse. The observed decay signal is extremely small due to this incoherent. In coherent state all spins precess in phase. That is mean that the whole macroscopic magnetization precesses in volume V of the sample as follows from the experiments in superfluid ³He, its frequency and phase are determined by a density of magnons, not by RF pulse.

We have found the method to test magnetic coherence of the observed state. The spin echo technique was applied. For the case of the incoherent magnon state the echo signal should form. It can be seen after a BEC signal decays. But during the BEC signal the echo does not form, as the deflection angle of magnetization is more than critical angle [22]. Such behavior demonstrates the absence of inhomogeneous broadening during the observation BEC signal, Fig.1.

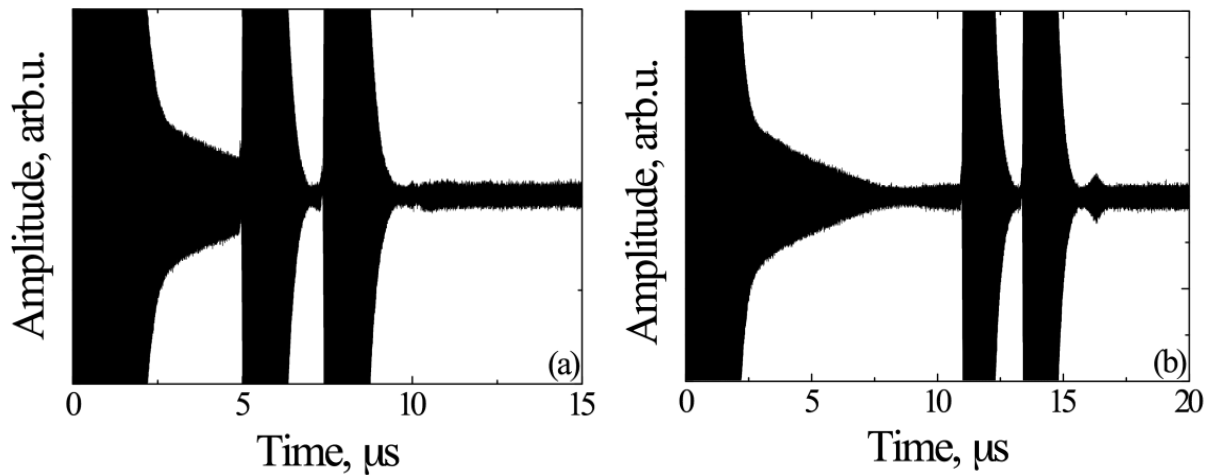


Figure 1. Free induction decay and echo signals. 5 μs (a) and 11 μs (b) delay between 100 ms pulse and echo pulse sequence has been applied

The Goldstone modes of a BEC state in MnCO_3 excited by a low frequency phase modulation of RF field will be reviewed in report.

References

1. M.H.Anderson, J.R.Ensher, M.R.Matthews, C.E.Wieman and E.A.Cornell, *Science.*, **269**, No. 5221, pp. 198-201 (1995).
2. Borovik-Romanov A.S., Bunkov Yu. M., Dmitriev V. V., Mukharskiy Y.M., *JETP Lett.*, **40**, 1033 (1984).
3. Fomin I. A., *JETP Lett.*, **40**, 1037 (1984).
4. Bunkov Yu.M., Volovik G.E., *JETP.*, **76**, 794 (1993).
5. Borovik-Romanov A.S., Bunkov Yu.M., de Waard A., Dmitriev V.V., Makroczyova V., Mukharskiy Yu.M., Sergatskov D.A., *JETP Lett.*, **47**, 478 (1988).
6. Borovik-Romanov A.S., Bunkov Yu.M., Dmitriev V.V., Mukharskiy Yu.M., Sergatskov D.A., *Physica B*, **165**, 649 (1990).
7. Bunkov Yu.M., Dmitriev V.V., Mukharskiy Yu.M., *JETP Lett.* **43**, 168 (1986).
8. Borovik-Romanov A.S., Bunkov Yu.M., Dmitriev V.V., Mukharskiy Yu.M., *JETP Lett.*, **45**, 124 (1987).
9. Bunkov Yu.M., Fisher S.N., Guenault A.M., Pickett G.R., *Phys. Rev. Lett.*, **69**, 3092, (1992).
10. Bunkov Yu.M., Volovik G.E., *Phys. Rev. Lett.*, **98**, 265302 (2007).
11. Bunkov Yu.M., Volovik G.E., *JETP Lett.*, **89**, 356 (2009).
12. Sato T., Kunimatsu T., Izumina K., Matsubara A., Kubota M., Mizusaki T., Bunkov Yu.M. *Phys. Rev. Lett.*, **101**, 055301 (2008).
13. Hunger P., Bunkov Yu.M., Collin E., Godfrin H. *J. Phys.: Conf. Ser.*, **400** 012019 (2012).
14. Bunkov Yu.M. *J. Phys.: Condens. Matter*, **21**, 164201 (2009).
15. Bunkov Yu.M., Volovik G.E. *J. Phys.: Condens. Matter*, **22** 164210 (2010).
16. Bunkov Yu. M., Volovik G. E. "Spin superfluidity and magnon BEC" Chapter IV of the book "Novel Superfluids", eds. K. H. Bennemann and J. B. Ketterson, Oxford University press, (2013).
17. Bunkov Yu. M., Alakshin E. M., Gazizulin R. R., Klochkov A. V., Kuzmin V. V., Safin T. R., Tagirov M. S., *JETP Lett.* **94**, 68 (2011).

18. Bunkov Yu. M., Alakshin E. M., Gazizulin R. R., Klochkov A. V., Kuzmin V. V., L'Vov V. S., Tagirov M. S., *Phys. Rev. Lett.* **108**, 177002 (2012).
19. Tagirov M. S., Alakshin E. M., Bunkov Y. M., Gazizulin R. R., Gazizulina A. M., Isaenko L. I., Klochkov A. V., Safin T. R., Safiullin K. R., Zhurkov S. A., *J. Low Temp. Phys.* **175**, 167 (2014).
20. Alakshin E. M., Bunkov Y. M., Gazizulin R. R., Klochkov A. V., Kuzmin V. V., Rakhmatullin R. M., Sabitova A. M., Safin T. R., Tagirov M. S., *Appl. Magn. Reson.* **44**, 595 (2013).
21. Demokritov S.O., Demidov V.E., Dzyapko O., Melkov G.A., Serga A.A., Hillebrands B., Slavin A.N., *Nature*, **443**, 430 (2006).
22. Gazizulin R.R., Bunkov Yu.M., Safonov V.L., *JETP Lett.*, **102**, 766 (2015).

The oscillations in ESR spectra of $\text{Hg}_{0.76}\text{Cd}_{0.24}\text{Te:Ag}$

*Aleksey V. Shestakov^{1,2}, Ilshat I. Fazlizhanov^{1,2}, Ivan V. Yatsyk^{1,2},
Mariyam I. Ibragimova², Vladimir A. Shustov², Rushana M. Eremina^{1,2}*

¹Physics Institute, Kazan (Volga Region) Federal University, Russian Federation

²Kazan E.K. Zavoisky Physical-Technical Institute, KSC of the RAS, Russian Federation

E-mail: aleksey665@gmail.com

<http://kfti.knc.ru/en/>

Introduction

The mercury chalcogenides HgSe and HgTe in the zinc-blende (ZB) structure belong to a group of unique materials exhibiting the so-called inverted band structure [1] and it are semimagnetic semiconductors n-type ($A^{\text{II}} B^{\text{VI}}$). Compound HgCdTe is the most widely used semiconductor with a variable band gap [2]. Ion implantation modifies the carrier concentrations at the introduction of impurities in the surface layer that greatly affects the skin effect. In these samples an oscillation of the conductivity and magnetization can be observed, at low temperatures in the presence of very intense magnetic fields, known as Shubnikov–de Haas (SdH) and de Haas van Alfen (HvA) effects. The SdH and HvA effects are a macroscopic manifestation of the inherent quantum mechanical nature of matter. The aim of our work is the study of the magnetic and transport properties of implanted silver ions $\text{Hg}_{0.76}\text{Cd}_{0.24}\text{Te}$ by magnetic resonance method.

Samples and experimental

The samples were grown by continuous feeding of the melt. Grown crystal $\text{Hg}_{0.76}\text{Cd}_{0.24}\text{Te}$ had n-type conductivity with concentration of 10^{16} - 10^{17} cm^{-3} , the sample was subjected to ion implantation by ions of Ag^+ ion on ILU-3 accelerator. After implantation the sample was annealed in a sealed quartz tube in a saturated mercury atmosphere at a temperature of 300°C for 20 days. Subsequent annealing of the crystal in the atmosphere of mercury ions the conductivity is inverted to p-type with carrier concentration of $\approx 10^{14}$ cm^{-3} .

Spectra investigations were performed on a spectrometer Varian E12 at X-band frequency (9.36 GHz) at the temperature 4.2 K and at the magnetic field from 0 to 10^4 Oe. The experiments with different orientations of the sample relative direction field and with difference microwave power magnetic field were performed in three planes, perpendicular to the selected axis (0) in the plane of the axis (90), and at an angle of 45 degrees to the selected direction.

Results and discussion

The angular dependencies of spectra of $\text{Hg}_{0.76}\text{Cd}_{0.24}\text{Te:Ag}^+$ single crystal are shown in Figure 1 (a). Strong oscillations were observed in the derivative of microwave absorption ($f = 9.4$ GHz) in the of $\text{Hg}_{0.76}\text{Cd}_{0.24}\text{Te:Ag}^+$ using electron-paramagnetic resonance spectroscopy at low temperatures (4.2–20 K) and in the magnetic field up to 10 kOe.

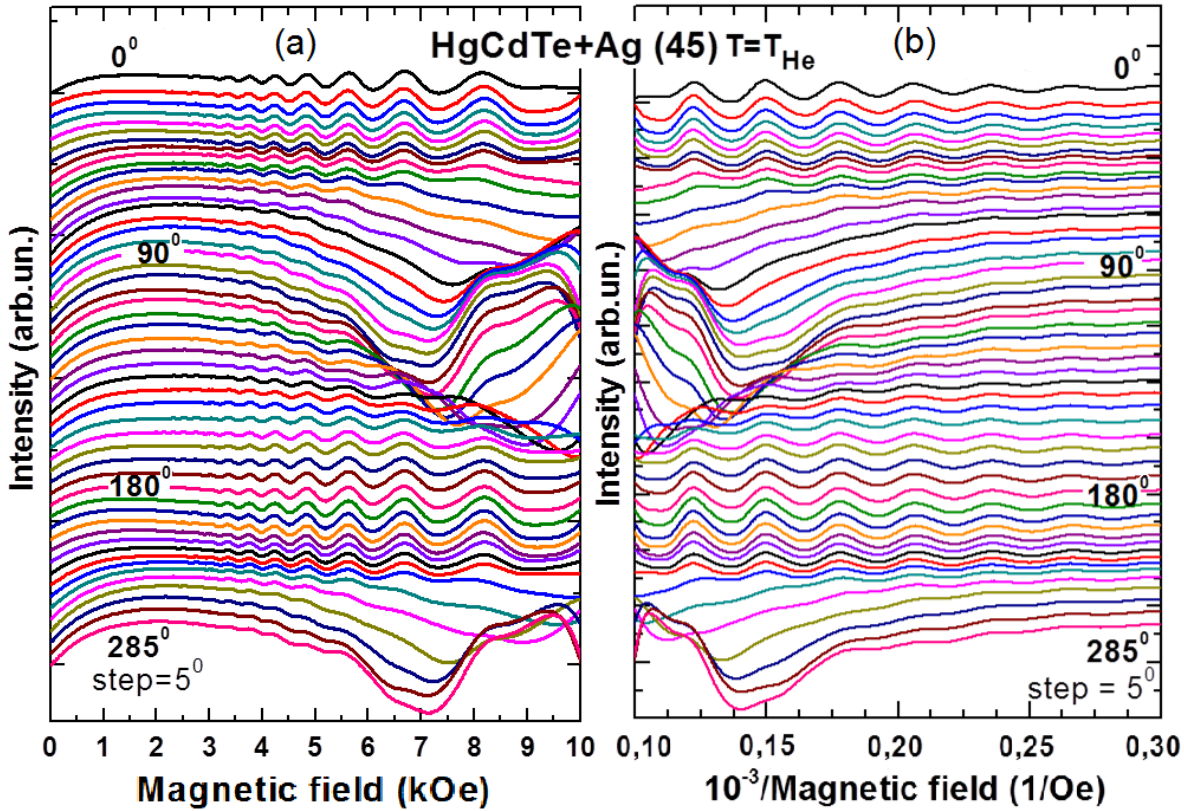


Figure 1. Angular dependencies of EPR spectra in HgCdTe:Ag⁺(a) and angular dependence of ESR spectra in the reverse magnetic field. $T=4.2$ K (b)

The samples of $2 \times 2 \times 2$ mm³ were placed in the cavity and the outside magnetic field was applied. The microwave absorption power derivative (dP/dH) was registered in the experiments. Microwave current induces in the microwave field. Oscillations of the microwave power derivative correspond to the transverse magnetoresistance $\Delta\rho/\rho$ and magnetization $\Delta M/M$ [1]. We fitted period dependence of high-frequency oscillations using the formula:

$$\Delta H = A \cdot H^2 + C, \quad (1)$$

where H – external magnetic field, $A=26,6 \cdot 10^{-6}$, $C=55$ – fitting parameters. Up to experimental error obtained parameters A and C are the same for all directions of the external magnetic field relative to the crystallographic axes of the crystal (see Figure 2). This behaviour was connected with resistivity dependencies from magnetic field, according [1].

Figures 3 and 1(b) shows the microwave absorption power derivative as a function of the inverse applied magnetic field. The oscillation periods $\Delta(H^{-1})$ in the reverse magnetic field are equal $2,8 - 3,23 \cdot 10^{-5} \text{ Oe}^{-1}$, the carrier concentration n_s has been determined by [3]:

$$n_s = \frac{e}{\pi \Delta(H^{-1})} = 4,48 - 5,17 \cdot 10^{21} \text{ cm}^{-2} \quad (2)$$

We investigated the temperature dependencies of quantum oscillation for HgCdTe+Ag, from 6 to 12 K (Figure 3 (a)). The reduction of oscillation amplitude in 2D gas [4] determined by:

$$A(T)/A(T_0) = \frac{T \sinh \alpha T_0}{T_0 \sinh \alpha T} \quad (3)$$

Obtained experimental data is very well fitting by formula (3) at $\alpha=0,38186$ (Figure 3(b)).

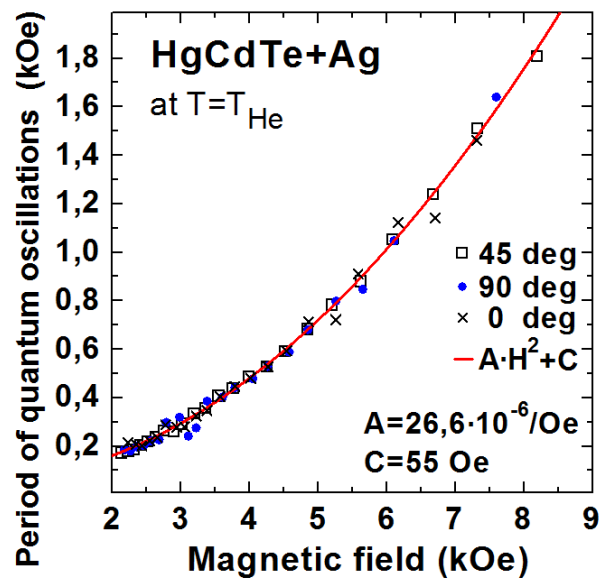


Figure 2. The dependence of the period of quantum oscillations from the applied magnetic field in HgCdTe:Ag^+

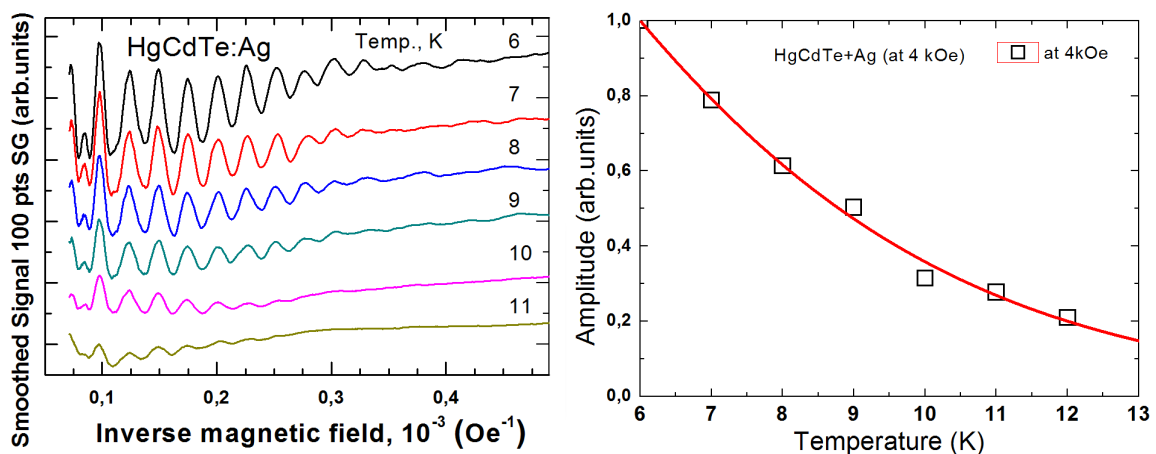


Figure 3. Temperature dependence of the quantum oscillations amplitude in HgCdTe:Ag^+

Conclusions

The implantation of silver ions leads to increase of carrier concentration on surface and observation the quantum oscillations in the spectrum of magnetic resonance.

References

1. A.Veynger, A. Zabrodskii, T. Tisnek, G. Biskupská. – *Phys. and Tech. Semiconductor (FTP)*, **32**, 557-563 (1998).
2. L. Winterfeld, L.A. Agapito, J. Li, N. Kioussis, P. Blaha, Y.P. Chen. – *Phys. Rev. B*, **87**, 075A. 143 (2013).
3. N. Popenko, A. Bakirov, I. Ivanchenko, A. Bludov and V. Pascenco. – *JETF Letters*, **100**, 247-322 (2014).
4. H. J. von Bardeleben, Y. Q. Jia, M. O. Manasreh, and C. E. Stuz. – *Applied Physics Letters* **62**, 90 (1993).

NMR study of AzoTAB and CTAB photoisomerization when interacting with the lipid bilayer

*Nataliia S. Shubina, Ekaterina S. Babicheva, Alexander M. Perepukhov,
Alexander V. Maximychev, Sheyda R. Frolova, Konstantin I. Agladze*

Moscow Institute of Physics and Technology (State University)

E-mail: shubina_natalya93@mail.ru

Introduction

(*E*)-conformations of AzoTAB and CTAB (Fig. 1) interact with the lipid bilayer which can be used in biotechnology [1, 2].

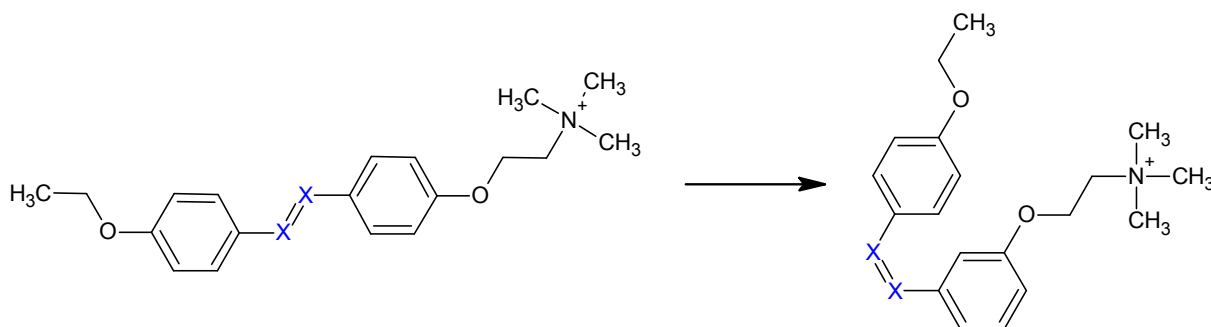


Figure 1. The photochemical isomerization of AzoTAB ($X = N$) and CTAB ($X = C$)

UV irradiation results in formation of (*Z*)-AzoTAB and (*Z*)-CTAB. Photoregulation is resulted by a double bond photoisomerisation azobenzene and stilbene fragments, respectively (Fig. 1). In this paper, photoisomerization and interaction with the lipid bilayer of AzoTAB and CTAB was studied using high-resolution NMR spectroscopy.

Results and discussion

Analysis of ^1H -NMR spectra of AzoTAB shows that photoisomerization of AzoTAB is reversible. ^1H -NMR signals of AzoTAB are extremely broadened in lipid bilayer condition. Directly bounded with molecular mobility the signal width can indicate the interaction of (*E*)-AzoTAB with a lipid bilayer. Also (*Z*)- to (*E*)- transformation in the absence of light appears as a first order reaction ($K=3\times 10^{-5} \text{ c}^{-1}$)

UV (*E*)-(*Z*) isomerization causes a disturbance of the interaction between molecules AzoTAB and lipid bilayer that is observed as a significant narrowing of the signals in the spectrum of the mixture AzoTAB with a lipid bilayer.

Analysis of ^1H NMR spectra of CTAB and CTAB/lipid bilayer mixture shows that the behavior of CTAB molecules differs from the behavior of AzoTAB molecules. It has been found that the reaction of CTAB photoisomerization is irreversible. The interaction of the lipid bilayer with (*E*)-CTAB and (*E*)-AzoTAB cause broadening of signals in the ^1H -NMR spectrum (Fig. 3). The signal width of (*Z*)-CTAB in contrast of (*Z*)-AzoTAB is not decreased in bilayer lipid mixture, that indicating irreversible binding.

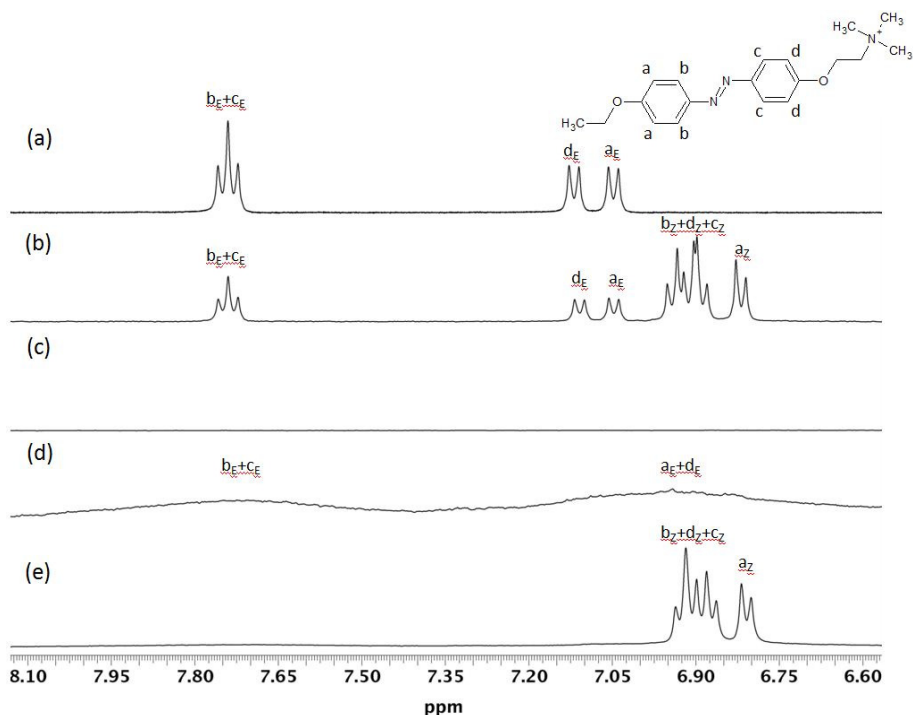


Figure 2. ^1H NMR spectra of AzoTAB, lipid bilayer and AzoTAB/lipid bilayer mixture in D_2O : a) AzoTAB before UV irradiation b) AzoTAB after UV irradiation c) lipid bilayer d) AzoTAB/lipid bilayer mixture before UV irradiation e) AzoTAB/lipid bilayer mixture after UV irradiation. The eight protons of azobenzene groups are shown by letters a-d. The subscripts E and Z denote (E)- and (Z)- isomers, respectively.

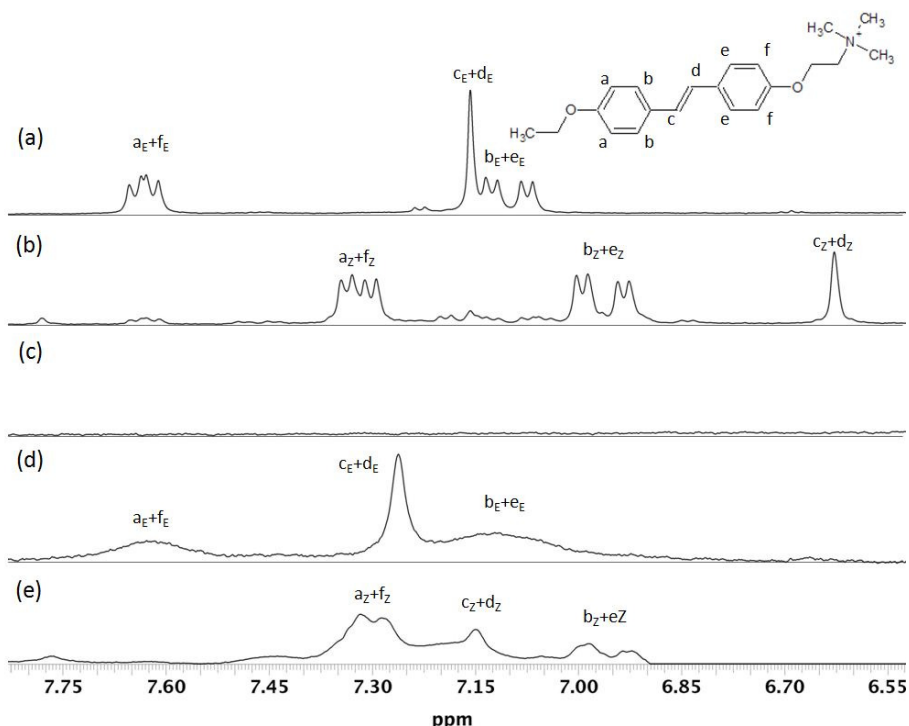


Figure 3. ^1H NMR spectra for CTAB, lipid and CTAB/lipid bilayer mixture in D_2O : a) CTAB before UV irradiation b) CTAB after UV irradiation c) lipid bilayer d) CTAB/lipid bilayer mixture before UV irradiation e) CTAB/lipid bilayer mixture after UV irradiation. The ten protons of stilbene groups are shown by letters a-f. The subscripts E and Z denote (E)- and (Z)- isomers, respectively.

Thus, we show that the reaction AzoTAB photoisomerization is reversible and CTAB is irreversible. It has been shown that (*E*)-isomers of CTAB and AzoTAB interact with the lipid bilayer. Molecular mobility of (*Z*)-AzoTAB increases under UV irradiation due to weakening of lipid bilayer binding, whereas, CTAB/lipid bilayer binding is irreversibly.

References

1. Magome N., Kanaporis G., Moisan N., Tanaka K., Agladze K. Photo-control of excitation waves in cardiomyocyte tissue culture // *Tissue Eng Part A*. 2011. V. 17 I. p. 21–22
2. Sheyda R. Frolova¹, Olga Gaiko¹, Valeriya A. Tsvelaya¹, Oleg Y. Pimenov², Konstantin I. Agladze Photocontrol of Voltage-Gated Ion Channel Activity by Azobenzene Trimethylammonium Bromide in Neonatal Rat Cardiomyocytes // *PLoS One*. 2016 V. 11(3) p. 1–2

Comparison of low-field and high-field MR for the diagnosis of brain metastases

P. I. Simeschenko, V. M. Cheremisin, I. G. Kamyshanskaya

St. Petersburg State University, Faculty of Medicine

The course of radiation diagnosis and radiotherapy Oncology Department

199106, Saint Petersburg, 21 line VO, 8.

SPb "Mariinsky city hospital"

194104, St. Petersburg, Liteiny pr., 56

E-mail: simeschenko@gmail.com

Relevance

Magnetic resonance imaging (MRI) is a relatively safe and highly informative diagnostic method. MR imaging is essential for appropriate treatment in modern oncology due to the ability of MR imaging to determine the presence of tumors of variable localization

The number of MR scanners per 1 million residents varies in different countries: in the United States - a number equal to 30, Canada, Great Britain and France - about 6. In Russia, this figure ranges from 1 to 5, depending on the region. A small number of CT scanners in Russia is mainly associated with scanners high price and the high costs of the operation, in particular the MR with the induction of the magnetic field is greater than 1.5 T. However, due to the huge demand for this method of diagnosis is high enough widespread MR scanners with magnetic field induction of 0.4 T due to lower costs.

Purpose of the study

To compare the ability of low-field and high-field MR in the diagnosis of brain metastases.

Material and Methods

This study was carried out on high field MRI scanner Siemens Magnetom Avanto 1.5 T magnetic field at St. Petersburg State University in St. Petersburg GBUZ "City Mariinsky hospital" and low-field scanner Hitachi Aperto Lucent with induction magnetic field 0,4 T.

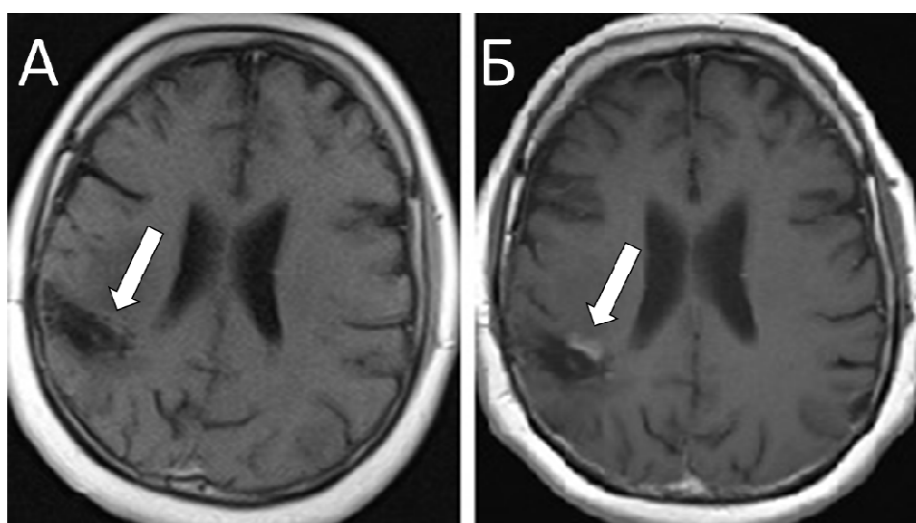


Figure 1. Patient K., 41g. Metastatic ovarian cancer. There is an additional portion of the pathological accumulation of contrast agent for scanning at high field MRI (B) compared to studies carried out in the low-floor imaging (A)

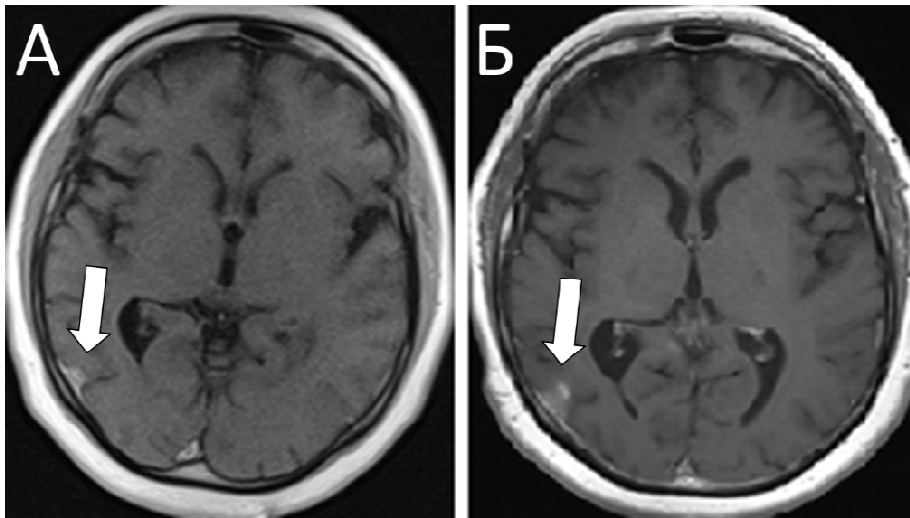


Figure 2. Patient K., 41g. Metastatic ovarian cancer. Increased nodule on MR images formed on 1.5T tomograph (B) compared with the images obtained in the study on tomograph 0,4T (A)

Results

A comparative assessment of MR tomograms of high- and low-field scanners have recently noted a lower resolution, and after contrast enhancement subjectively weaker contrast enhancement was observed, that complicated the differentiation between the pathological and normal, intact brain tissue. Standard routine protocol involving T2, T1-weighted images in three standard projections on tomograph with magnetic field induction 0,4T occupies at least twice more time compared with the MRI magnetic field with induction 1.5T, wherein the number of slices in the first case was 22 while in the second - 25-40, depending on the thickness of the slice. Slice thickness, in turn, affects the ability to detect CKD structures with size less than 5 mm.

Conclusions

The use of low-field MR scanners, primarily due to the economic benefits, as compared to high field scanners, is less expensive, and the cost of the study for the patient, as a rule, is less also. However, the use of MR with a magnetic field below 0,4T can not be considered the best method for diagnosis of brain metastases due to a large slice thickness and a low spatial resolution, that can not afford to diagnose of small secondary lesion in the brain. Another important feature that reduces the overall performance and differential diagnostic possibilities on low-field MR scanners is the absence of software of MR techniques such as DWI, SWI, spectroscopy and tractography.

Currently, only the use of high field MRI scanner with the mandatory implementation of contrast enhancement should be considered as standard MRI method for diagnosis of intracranial metastases.

Application of metasurfaces for magnetic resonance imaging

Alexey P. Slobozhanyuk^{1,2}, Alena V. Shchelokova, Irina V. Melchakova, Pavel A. Belov¹

¹Department of Nanophotonics and Metamaterials, ITMO University, St. Petersburg 197101, Russia

²Nonlinear Physics Center, Australian National University, Canberra ACT 2601, Australia

E-mail: aleksei.slobozhaniuk@anu.edu.au

<http://metalab.ifmo.ru/>

Abstract

We report on a novel ultrathin metasurface resonator design which substantially improve the performance of magnetic resonance imaging (MRI) devices. We fabricate metasurfaces formed by arrays of nonmagnetic metallic wires and place them inside the 1.5T MRI machine under an investigated object. We observe significantly enhanced signal-to-noise ratio (SNR) and minimum values of specific absorption rate (SAR) by exciting particular modes of metasurface resonators.

Introduction

Metamaterials are known as composite artificial electromagnetic structures designed to produce unique properties not observed in nature [1]. These structures allow to control macroscopic electromagnetic fields by engineering the electromagnetic response of their unit cells of the subwavelength dimension. Over the last few years, the concept of metamaterials has been applied to many practical problems, including subwavelength imaging [2] and cloaking [3]. Some approaches how to use metamaterials for improving MRI characteristics has been already discussed in the literature [4-6]. In this study, we propose a novel approach to use two-dimensional metamaterials, or metasurfaces [7], in order to manipulate, redistribute and substantially enhance radiofrequency magnetic field within 1.5 T scanner. We also examine the safety aspects of such metasurfaces for MRI applications.

Results

MRI is a highly innovative, the safest and most informative, non-invasive method for diagnostic medicine. However there are several contemporary challenges in MRI. One of the most relevant is SNR enhancement without increasing the static magnetic field. This, in turn, may reduce the scanning time or allows to reach better image resolution [8] for the same scanning time. Another important challenge is the safety level in MRI which determined by the SAR. The SAR quantifies the absorption of radiofrequency waves and therefore the potential risk of tissue heating during the scan [8] and it is proportional to the square of the electric field. In order to solve aforementioned problems we have employed a metasurface shown in Fig. 1(a). The structure is formed by 14x2 array of parallel thin brass wires located in water with $\epsilon \approx 81$. Such metasurface has a set of eigenmodes [9] with spatially redistributed magnetic and electric fields. For MRI purpose, we are interested in the first eigenmode, for which magnetic field is localized in the central region of the metamaterial and provides a maximum of SNR in the object region, while the electric field is concentrated near the edges of the wires and therefore allowing us to obtain minimal SAR in this region. So we have tuned the length of each wire to the Fabry-Pérot condition for the first eigenmode at the operating frequency of 1.5 T MRI machine, i.e. $f = c/(\sqrt{\epsilon}L) \approx 63.8$ MHz and obtained the length equal to $L = 25.5$ cm. The period of the structure was optimized to 1 cm to achieve a homogeneously enhanced SNR. The studied object is placed on top of the metasurface. Figure 1(b) demonstrates numerically the calculated electromagnetic fields distribution near the object region at the 1.5 cm from the metasurface. The structure was excited by the plane wave polarized along the wires. It is clearly seen that there are a maximum of magnetic field in the

middle part of the metasurface (sample region) and a minimum of electric field in the same region.

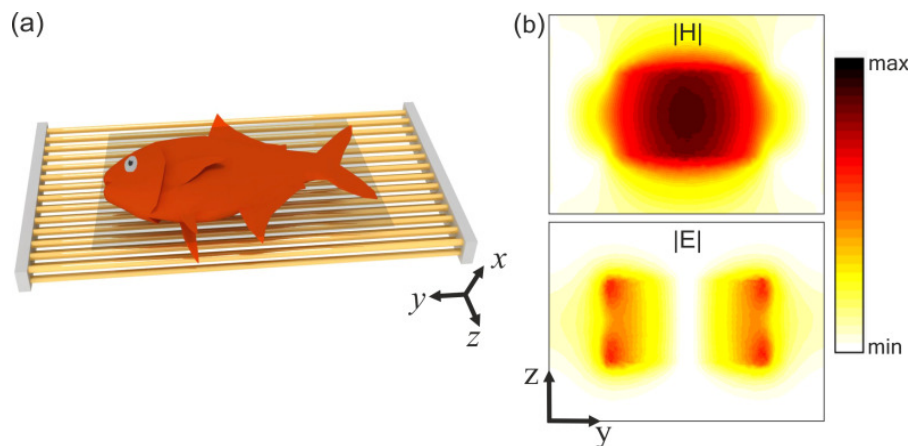


Figure 1. (a) Artist's view of a biological object placed on a metasurface resonator. (b) Numerically calculated magnetic and electric field distributions in the region of the object near the metasurface

The quality of the MRI image is evaluated by SNR. We perform experimental measurements of SNR in the region of interest (sample area) under the metasurface (Fig 2(a)). Based on results of the separate scans of signal and noise in two configurations (phantom with the metasurface (with and w/o the radiofrequency pulse) and empty phantom (with and w/o the radiofrequency pulse) we determined the ratio $SNR_2/SNR_1 \approx 2.7$, where SNR_2 corresponds to the ratio with the metasurface inside the phantom and SNR_1 corresponds to the ratio for the empty phantom. The increase of the SNR by more than a factor of two effectively corresponds to an MRI system with two times higher static magnetic field. The SNR enhancement effect is observed up to 7 cm of the scan depth from the surface (Fig. 2(b)). The enhancement depth and homogeneity could be further optimized by bending the metasurface around an object, using different eigenmode and the period [10]. Another optimization can be offered by changing the substrate. For lossless media, the higher penetration into a human body is expected.

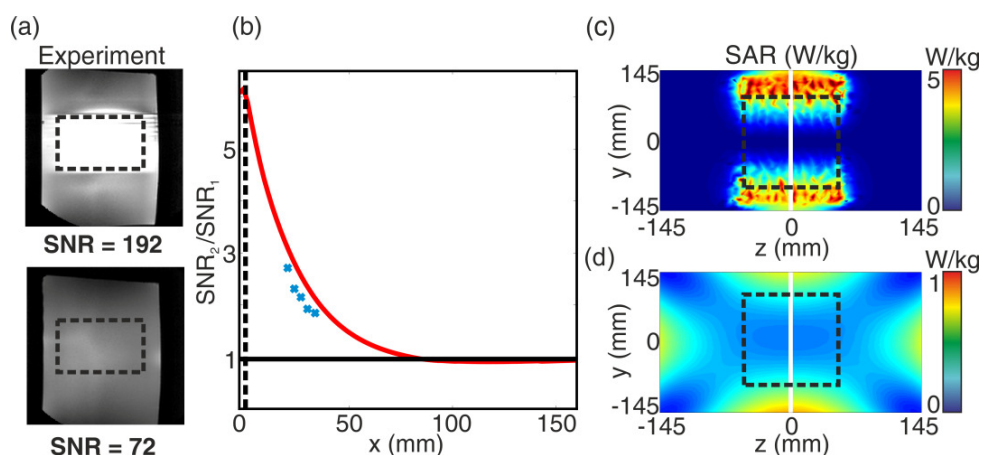


Figure 2. (a) MRI images and SNR values for the phantom with the presence of metasurface (upper figure) and without it (bottom figure). The black dashed rectangle corresponds to the safe – “object” – zone. (b) Numerically calculated (red curve) and experimentally measured (blue symbols) ratio between SNR with the metasurface and without it in depth (along the x direction). SAR (10g) map calculated in the phantom (c) near the metasurface and (d) without it

Figures 2(c,d) show numerically the calculated SAR value. The Food and Drug Administration specified that average SAR value should not exceed 4 W/kg for a whole body scan. In order to evaluate SAR near the metasurface we performed a set of numerical simulations. A birdcage coil, which is usually embedded in the bore of MRI machine, was employed as a source [10]. We use a phantom filled with water as an object under study, which was placed next to the wires. Figure 2(c) demonstrates that with the presence of metasurface SAR has a maximum near the edges of the wires, where the electric field is localized. In the case without the metasurface (see Fig. 2(d)) the electric field has approximately homogeneous distribution, without expressed maximum. In Figs. 2(c,d) we estimated the so-called safe – “object” region (marked as black dashed rectangle), where the SAR value for applied continuous power of 16.6 W is smaller than 4 W/kg in the presence of the metasurface. This region is equal to 68% of the metamaterial length. Moreover, it should be mentioned that if the object is placed near the central part of the metasurface, the SAR values are even smaller than without the metasurface. This happens due to the specific resonant mode structure of the metamaterial with the region of minimum value of radiofrequency electric field. This region is equal to 18% of the metasurface length and can be expanded by using longer wires and the dielectric host with a smaller permittivity value. Moreover, if it is impossible to place the object only near the center of metamaterial, the metasurface can be bent substantially in order to place the edges of wires further from the examined object, while keeping the effect of SNR enhancement.

Conclusions

We have realized unique metasurfaces based on metallic wire arrays with the resonance mode spectrally tuned to the nuclear magnetic resonance. This has allowed to observe a substantial enhancement of the signal-to-noise ratio, and also provided an opportunity to locally control the electric field near the object which makes an MRI examination absolutely safe. The similar concept can potentially be used for low-field MRI techniques as an approach to increase SNR and independently for ultra-high field MRI where the issue of safety remains the main problem due to the fact that SAR increases with frequency.

Acknowledgements

This work was supported by Russian Science Foundation (Project No. 15-19-20054).

References

1. N. Engheta and R. W. Ziolkowski, *Metamaterials: Physics and Engineering Explorations*, Piscataway, NJ: Wiley-IEEE Press (2006).
2. X. Zhang and Z. W. Liu, *Nature Mater.* 7, 435 (2008).
3. A. V. Shchelokova, I. V. Melchakova, A. P. Slobozhanyuk, E. A. Yankovskaya, C. R. Simovski, P. A. Belov, *Phys. Usp.* 58, 167–190 (2015).
4. M. C. K. Wiltshire, J. B. Pendry, I. R. Young, D. J. Larkman, D. J. Gilderdale, and J. V. Hajnal, *Science* 291, 849-851 (2001).
5. M. J. Freire, L. Jelinek, R. Marques, and M. Lapine, *J. Magn. Reson.* 203, 81-90 (2010).
6. X. Radu, D. Garray, and C. Craeye, *Metamaterials* 3, 90-99 (2009).
7. S. B. Glybovski, S. A. Tretyakov, P. A. Belov, Y. S. Kivshar, C. R. Simovski, *Physics Reports*, doi:10.1016/j.physrep.2016.04.004 (2016).
8. E. M. Haacke, R. W. Brown, M. R. Thompson, R. Venkatesan, *Magnetic Resonance Imaging: Principles and Sequence Design*, New York: Wiley, 1999.
9. F. Lemoult, G. Lerosey, J. d. Rosny, M. Fink, “Resonant metalenses for breaking the diffraction barrier”, *Phys. Rev. Lett.*, vol. 104, p. 203901, 2010.
10. A.P. Slobozhanyuk et al., “Enhancement of magnetic resonance imaging with metasurfaces,” *Adv. Mater.* 28, 1832 (2016).

Spin kinetics of ^3He in contact with ordered Al_2O_3 aerogel

*A. A. Stanislavovas¹, E. M. Alakshin¹, A. V. Klochkov¹, V. V. Kuzmin¹, T. R. Safin¹,
K. R. Safiullin¹ and M. S. Tagirov^{1,2}*

¹*Kazan (Volga region) Federal University, Kazan, 420008 Russia*

²*Institute for Perspective Studies, Academy of Sciences,*

Republic of Tatarstan, Kazan, 420011 Russia

E-mail: hectkctk@yandex.ru

Aerogels are materials with mechanical properties of solids with a very low density (pores occupy 90-99% of the aerogel volume). Because of that aerogels are used as detectors of Cherenkov radiation. In addition specific porosity of these materials allows to create the electric double layer capacitors [1]. Processes taking place on the border of the aerogel and liquid ^3He research is an actual problem of modern low temperature physics, because the aerogel acts as impurity in liquid ^3He . In present work the spin-lattice relaxation time T_1 of ^3He nuclei was studied by pulsed NMR methods in contact with the ordered Al_2O_3 aerogel (published in [2]).

Ordered Al_2O_3 aerogel (Nafen-90, ANF Technology Ltd, Tallinn, Estonia) was used as a sample. The SEM image of used aerogel is shown in Fig. 1.

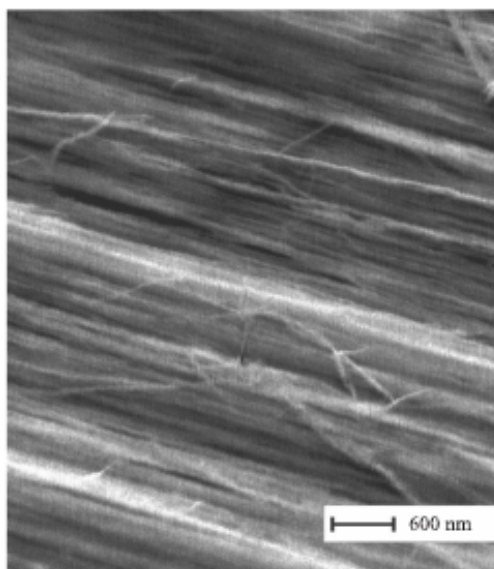


Figure 1. The image of Al_2O_3 “Nafen-90” ordered aerogel (ANF Technology Ltd, Tallinn, Estonia), obtained by scanning electron microscopy. The main parameters of this sample are: 0.5-cm diameter, 2.5-cm length, 8-nm fibers diameter, 90-mg/cm³ density, and the distance between fibers of 50–80 nm

NMR experiments in present work were carried out on a homebuilt pulsed spectrometer described in [3]. The resonance circuit with a “hot capacitor” scheme was used to measure relaxation times at various frequencies. According to this scheme only the detection coil is located inside the ^4He cryostat, while tuning and matching capacitors are located outside the cryostat, i.e at room temperature. In our experiments frequency was varied in the range of 5 - 17 MHz and the temperature was varied in the range of 1.6 – 4.2 K, that obtained by helium vapor pumping.

Preliminary experiments were carried out in order to determine the ^3He adsorbed volume on the sample surface. The ^3He adsorption isotherm on ordered Al_2O_3 aerogel was measured by a Pfeiffer Vacuum RPT 200 AR pressure detector at 4.2 K and 1.6 K

temperatures. The ^3He volume of adsorbed layers obtained from approximation of the linear range of isotherm are following: 6.1 cm^3 at 4.2 K and 12.2 cm^3 at 1.6 K .

The measured ^3He spin-lattice time T_1 dependence on amount of ^3He in the experimental cell is shown in Fig. 2 ($f_0 = 16.32\text{ MHz}$, $B_0 = 0.5\text{ T}$).

Earlier similar experiments have been performed using the chaotic SiO_2 aerogel in S. A. Altshuler laboratory [4-6]. These experiments confirm the dominant role of the adsorbed layer in the process of relaxation of gaseous and liquid ^3He . Our results indicates on the presence of an additional relaxation channel. It is evident from the fact that during the completion of the adsorbed ^3He layers on the Al_2O_3 aerogel surface, the dependence of the ^3He spin-lattice relaxation time T_1 on ^3He amount behaves in the same way as for case of the silicate aerogel (point A of Fig. 2), but in the gas phase that dependence disappears for a wide range of ^3He amount.

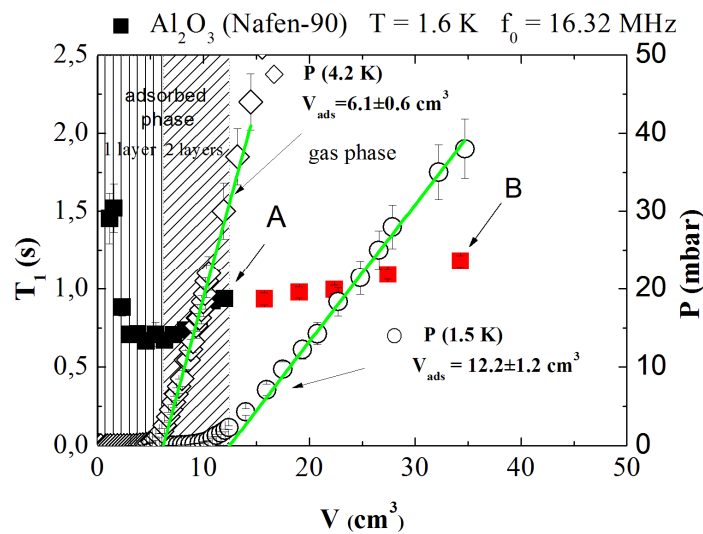


Figure 2. The dependence of spin-lattice time T_1 on the amount of the ^3He (n.c.) in Al_2O_3 aerogel (\blacksquare). The dashed line separates the filling region of the first and the second adsorbed layers. The pressure dependence on amount of ^3He in Al_2O_3 ordered aerogel at the 4.2 K (\diamond) and 1.6 K (\circ) (green lines – approximations of the linear region of the dependence performed in order to determine volumes of adsorbed layers)

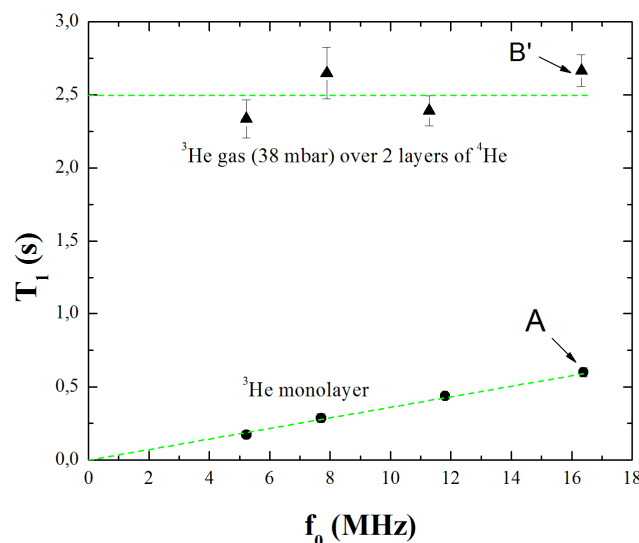


Figure 3. Frequency dependence of the ^3He spin-lattice relaxation time in the Al_2O_3 aerogel

To test this hypothesis the sample surface was covered by two layers of ^4He (16 cm^3) at the 4.2 K temperature. Then the temperature was lowered to 1.6 K the experimental cell was filled by ^3He gas (38 mbar) and the frequency dependence of ^3He gas T_1 relaxation time was measured (Fig. 3). The T_1 frequency dependence of ^3He nuclei in adsorbed layer is also presented on Fig. 3 for comparison.

As seen from Fig. 3 the ^3He spin-lattice relaxation time T_1 in the ^3He adsorbed layer linearly depends on frequency, which is typical for surface relaxation mechanism of ^3He described by Cowan [7]. In contrast to the adsorbed layer, the spin-lattice relaxation time of gaseous ^3He in contact with sample covered by two ^4He monolayers is independent frequency. This means that sample coverage by ^4He completely exclude the surface channel of gas ^3He relaxation. Also after coating the surface of the aerogel by two layers of ^4He , relaxation time of ^3He gas does not increase significantly (about 2 times – point B on Fig. 2 and point B' on the Fig. 3). Earlier in similar experiments with SiO_2 the value of the T_1 relaxation time of ^3He nuclei increased by more than 10 times [5, 6]. So we can suggest that our experimental results confirm that the additional relaxation mechanism is not associated with the fast exchange between the adsorbed and gas phases of ^3He .

Probably the mechanism of the relaxation of ^3He in gas phase is relaxation in fluctuating inhomogeneous magnetic fields created by paramagnetic centers occurs in our experiments. Actually the previous EPR studies of the sample revealed the presence of two types of paramagnetic centers near g-factor 2 with the concentration of about $2 \cdot 10^{16}$ spin/g [8]. We have to note that intrinsic paramagnetic centers were not observed in SiO_2 aerogels.

However, further studies are necessary to build a complete model of the ^3He nuclear magnetic relaxation in this type of aerogel, because the experimental data can not uniquely confirm or deny the influence of paramagnetic centers on the relaxation of ^3He . It is also possible that the unique ordered structure of the aerogel influence on the relaxation of ^3He .

This work was supported by the Russian Science Foundation (project no. 16-12-10359).

References

1. J. M. Miller, B. Dunn, T. D. Tran, R. W. Pekala, J. Electrochem. Soc. **144**, 309 (1997).
2. A.V. Klochkov, A.A. Stanislavovas, V.V. Kuzmin, K.R. Safiullin, M.U. Zakharov, M. S. Tagirov, JETP lett. **104**, 325 (2016).
3. E.M. Alakshin, R.R. Gazizulin, A.V. Klochkov, V.V. Kuzmin, A.M. Sabitova, T.R. Safin, M.S. Tagirov, Magnetic Resonance in Solids **15**, 1 (2013).
4. A.V. Klochkov, V.V. Kuzmin, K.R. Safiullin, M. S. Tagirov, D. A. Tayurskii, N. Mulders, JETP Lett. **88**, 823 (2008).
5. A. Klochkov, V. Kuzmin, K. Safiullin, M. Tagirov, A. Yudin, N. Mulders, J. Phys.: Conf. Ser. **150**, 1 (2009).
6. E. M. Alakshin, R. R. Gazizulin, A. V. Klochkov, V. V. Kuzmin, N. Mulders, M. S. Tagirov and D. A. Tayurskii, JETP Lett. **93**, 223 (2011).
7. B.P. Cowan, Journal of Low Temperature Physic **50**, 135 (1983).
8. G. V. Mamin, S. B. Orlinsky, A.A. Rodionov, M. S. Tagirov, JETP Lett. **102**, 714 (2015).

Impact of copper on water diffusion in sodium mordenite

L. Surova¹, E. Krylova¹, A. F. Privalov², M. G. Shelyapina¹

¹*Saint Petersburg University, Department of Nuclear-Physics Research Methods, Nuclear magnetic resonance*

²*Darmstadt TU, Department of Physics, Institute for Condensed Matter Physics*

E-mail: liudmilasurova@gmail.com

Introduction

Composite materials in which nanoparticles of transition metals are introduced into the crystal matrix of voids of a crystal matrix, such as a zeolite, are becoming more widely used [1, 2]. Copper-exchange zeolites are highly promising materials for heterogeneous catalysts and are used in numerous of chemical reactions, especially for reduction of NO_x (de-NO_x catalysts). According to recent studies of water behavior in zeolite catalysts, water can positively influence reaction rates. From this perspective the study of water dynamics in zeolites are highly required.

Being sensitive to the rate of molecular displacements over submicrometric distances during observation times of hundred microseconds till seconds, the nuclear magnetic resonance (NMR) has proved to be a powerful tool for studying the translational dynamics of guest molecules in porous materials including zeolites.

In this contribution we report on the results of our recent study of water dynamics in copper-exchanged mordenites by static field gradient NMR methods.

Sample preparation and experimental methods

Copper-exchanged zeolites were prepared from Na⁺-mordenites supplied by Zeolist Int. with Si/Al ratios equal to 6.5. To prepare copper-exchange samples, the starting material was treated in 0.05 M CuSO₄ aqueous solution, taking the volume with the twofold excess of copper amount in the solution to the estimated ion-exchange capacity of mordenite. The zeolite-solution mixtures were heated at 100° C into Synthos 3000 Anton Paar microwave oven at 1400 W for 2 hours. For more details see Ref. [3].

To increase the copper content the exchange procedure was repeated several times (up to six copper-exchange procedures). After that, samples obtained by both methods were filtered, thoroughly washed, and dried at room temperature overnight. We studied five samples: NaMor – the starting sample, and four copper exchanged samples CuNaMorM1, CuNaMorM2, CuNaMorM3 and CuNaMorM6.

The proton diffusion measurements were performed using NMR in a static field gradient (SFG NMR) applying the stimulated echo pulse sequence presented in Fig. 1. This method allows to measure diffusion coefficients in systems with short T_2 values, which are typical for solids. If the nuclear system evaluates in a magnetic field gradient \mathbf{g} , the observed echo amplitude can be described by the following function:

$$S(t_m, \tau) = S_0 \exp\left(-(\gamma \mathbf{g})^2 D \left(\frac{2}{3} \tau^3 + \tau^2 t_m\right)\right) \exp\left(-\frac{2\tau}{T_2}\right) \exp\left(-\frac{t_m}{T_1}\right). \quad (1)$$

As one can see from Eq. (1) to determine the diffusion coefficient one needs to know both the spin-lattice and spin-spin relaxation times (T_1 and T_2). Similar to relaxation measurements T_1 is measured using the saturation-recovery method. To measure spin-spin relaxation times we use a standard two pulse 90° – τ – 180° experiment (the *Hahn spin echo*).

The NMR experiment was carried out using relaxometer at 91 MHz in a static field gradient of 134.1 ± 0.3 T/m within the temperature range from 300 K to 380 K. Waiting time between series was more than T_1 in 10 times. The temperature of the samples was controlled with the accuracy of 1 K.

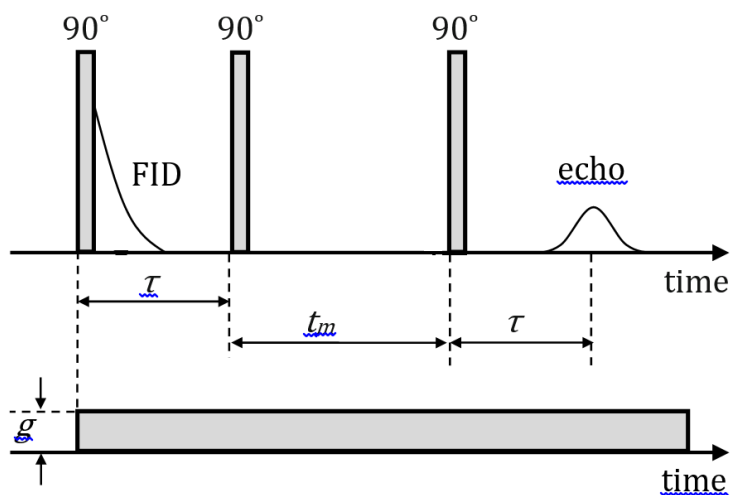


Figure 1. Timing schemes for the stimulated echo pulse sequence:
top – rf pulses, bottom – field gradient

Results and discussion

Recovery magnetization can be fitting one exponential curve for all samples. Diffusion coefficients were taken from global approximation Hahn echo and three Stimulated echoes that were measuring over τ (Fig.2).

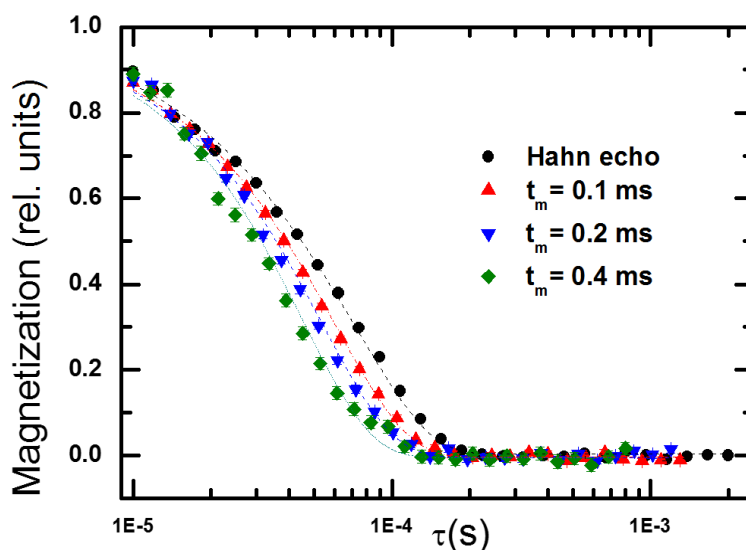


Figure 2. Global fitting Hahn and three Stimulates echoes at 340K for CuNaMorM3

In Fig. 3 we plotted the diffusivity (D) and spin-lattice relaxation time (T_1) of protons versus invers temperature for all the studied samples. The activation energy of water motion E_a was determined from Arrhenius law:

$$D = D_0 e^{-\frac{E_a}{RT}} \quad (2)$$

It has been found that in initial NaMor sample the water diffusion coefficient is close to the value in the bulk water $D^{300K} = 5.2 \times 10^{-10} \text{ m}^2/\text{s}$. However, a partial exchange of Na^+ to Cu^{2+} slow it down to $0.5 \div 1.4 \times 10^{-10} \text{ m}^2/\text{s}$, depending on copper content (see Fig. 3a). The activation energy of water diffusion are about 22 kJ/mol (0.226 eV) for Na^+ mordenites and slightly increases for copper-exchanges samples: 26÷32 kJ/mol (0.27÷0.32 eV) (Fig. 4)

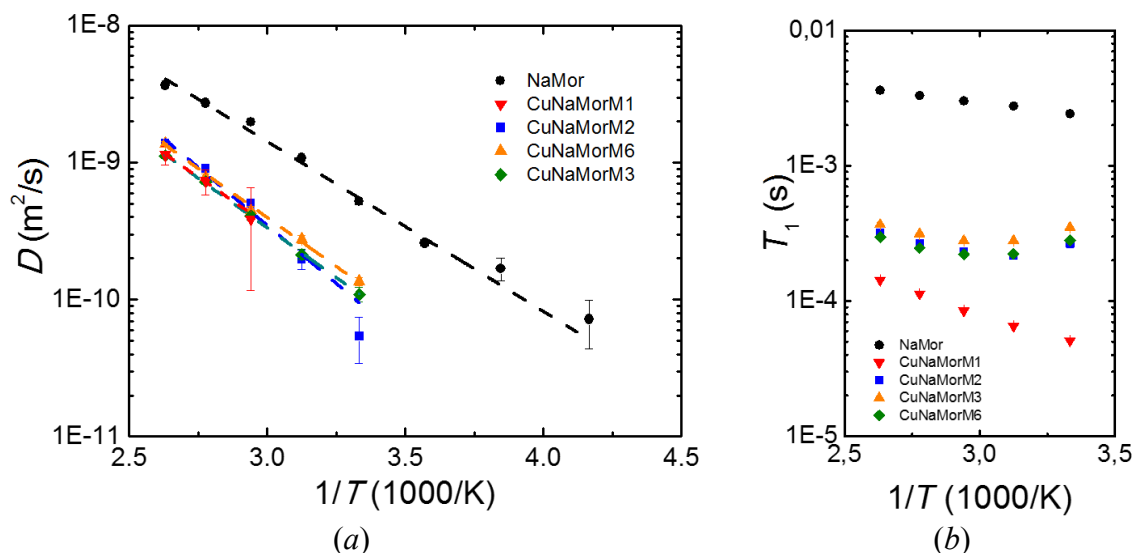


Figure 3. Proton diffusivity (a) and spin-lattice relaxation time (b) versus inverse temperature

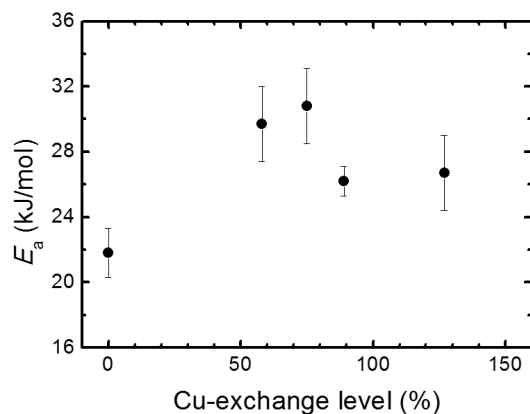


Figure 4. Activation energy of water diffusion in studied samples

Conclusion

The both diffusivity and activation energy values obtained for Na^+ zeolite are in fair agreement with results reported in Ref. [4, 5] for Na-BEA and NaX zeolites and can be attributed to the intracrystalline diffusivity. For zeolites in the Na^+ -form, the heat of water adsorption and, correspondingly, the activation energy of long-range diffusion, is about of 60 kJ/mol [6]. This value notably exceeds the activation energies obtained from NMR experiment. Such a deviation points out that the water molecules remain in the matrix of the host materials.

Acknowledgements

This work is supported by the German-Russian Interdisciplinary Science Center (G-RISC) and student mobility program.

References

1. Stucky G.D., McDougall J.E. – *Science*, **274**, 669-678 (1990).
2. Vanelderren P., Vancauwenbergh J., Sels B., Schoonheydt R. – *Coord. Chem.*, **257**, 483-494 (2013)
3. Y.M. Zhukov et al. – *Microporous Mesoporous Mater.*, **224**, 415–419 (2016)
4. R. Valiullin et al. – *Microporous and Mesoporous Mater.*, **142**, 236-244 (2011)
5. H. Pfeifer – *NMR Basic Princ. Prog.*, **7**, 53-153 (1972)
6. J. Kärger, P. Volkmer – *J. Chem. Soc. Faraday Trans. I*, **76**, 597-615 (1980)

Mechanism of cytotoxicity of GO peptides and some other cysteine-containing peptides

Irina I. Tyuryaeva^{1,2}, Olga G. Lyublinskaya¹, Ivan S. Podkorytov², Nikolai R. Skrynnikov^{2,3}*

¹*Institute of Cytology, Russian Academy of Sciences, St. Petersburg 194064, Russia*

²*Laboratory of Biomolecular NMR, St. Petersburg State University, 199034, Russia*

³*Department of Chemistry, Purdue University, West Lafayette IN 47907, USA*

**E-mail: nikolai@purdue.edu*

Antitumor GO peptides have been designed as dimerization inhibitors of prominent oncoprotein mucin 1. In this study we demonstrate that activity of GO peptides is independent of the level of cellular expression of mucin 1. Furthermore, these peptides prove to be broadly cytotoxic, causing cell death also in normal cells such as dermal fibroblasts and endometrial mesenchymal stem cells. To explore molecular mechanism of their cytotoxicity, we have designed and tested a number of new peptide sequences containing the key CxC or CxxC motifs. Of note, these sequences bear no similarity to mucin 1 except that they also contain a pair of proximal cysteines. Several of the new peptides turned out to be significantly more potent than their GO prototypes. The results suggest that cytotoxicity of these peptides stems from their (moderate) activity as disulfide oxidoreductases. It is expected that such peptides, which we have termed DO peptides, are involved in disulfide-dithiol exchange reaction, resulting in formation of adventitious disulfide bridges in cell proteins. In turn, this leads to a partial loss of protein function and rapid onset of apoptosis. We anticipate that coupling DO sequences with tumor-homing transduction domains can create a potentially valuable new class of tumoricidal peptides.

This work was supported by Russian Science Foundation grant №15-14-20038.

NMR investigations of atomic mobility of sodium embedded in porous glass with pore size 3.5 nm

*A. V. Uskov¹, D. Yu. Nefedov¹, E. V. Charnaya¹, J. Haase², D. Michel²,
Yu. A. Kumzerov³, A. V. Fokin³, A. S. Bugaev⁴*

¹Physics Department, St. Petersburg State University, St. Petersburg 198504, Russia

²Faculty of Physics and Geophysics, Leipzig University, Leipzig D-04103, Germany

³A.F. Ioffe Physico-Technical Institute RAS, St. Petersburg 194021, Russia

⁴Moscow Institute of Physics and Technology, Moscow 141700, Russia

E-mail: yskov@yandex.ru

Introduction

Recent studies have shown influence of nanoconfinement on properties of materials. Alterations in temperatures of phase transitions and new phase transitions which are absent in bulk materials were observed experimentally in nanomaterials [1]. Size effects have strong influence on atomic mobility and electronic properties of small metallic particles. Previous NMR investigations of small metallic particles revealed the size-induced changes of resonance frequency which indicate changes in electronic properties. Magnetisation recovery curves were used for investigation of atomic mobility in liquid gallium [2]. The gallium has two isotopes ⁶⁹Ga and ⁷¹Ga having with spin 3/2 and different resonance frequencies and quadruple moments what simplifies determination. Sodium has only one stable isotope what makes determination of atomic correlation time more complicated.

Methods

In order to investigate properties of sodium nanoparticles the liquid sodium was embedded into porous glass with pore size 3.5 nm. Size of pores was controlled by means of mercury porosimetry. Samples were cut into pieces with size 3x3x5 mm. NMR measurements were performed using pulse NMR spectrometers Bruker Avance 400 and Bruker Avance 750. The longitudinal magnetisation recovery curve was measured using the two-pulse sequence consisting of 180° and 90° pulses. Measurements were performed in temperature range from 80 K to 360 K.

Correlation time of atomic motion could be found from time dependence of longitudinal magnetisation [2]:

$$\frac{M(t)}{M_0} = 1 - b \left[\frac{4}{5} \exp\left(-\frac{C\tau_c t}{1 + 4\omega_0^2 \tau_c^2}\right) + \frac{1}{5} \exp\left(-\frac{C\tau_c t}{1 + \omega_0^2 \tau_c^2}\right) \right] \exp\left(-\frac{t}{T_{1m}}\right), \quad (1)$$

where M_0 is initial magnetisation, b accounts for nonideal inversion of magnetisation, C is constant of quadruple interaction, ω_0 is Larmor frequency, τ_c is correlation time of atomic motion, T_{1m} is time of longitudinal relaxation due to magnetic interaction which is inversely proportional to temperature. The value of T_{1m} could be determined using low temperature

experiments when atomic motion slows down and the approximation $\frac{1 + 4\omega_0^2 \tau_c^2}{C\tau_c} \gg T_{1m}$

becomes valid. In order to illustrate this method the dependence of T_1 on temperature is shown in Fig. 1. It should be mentioned that magnetization recovery could not be interpolated with single exponent, thus the value of T_1 could not be defined strictly, but it could be used in order to illustrate changes in relaxation speed.

Correlation time and quadruple constant were found for every temperature by simultaneous fitting of magnetisation recovery with expression (1).

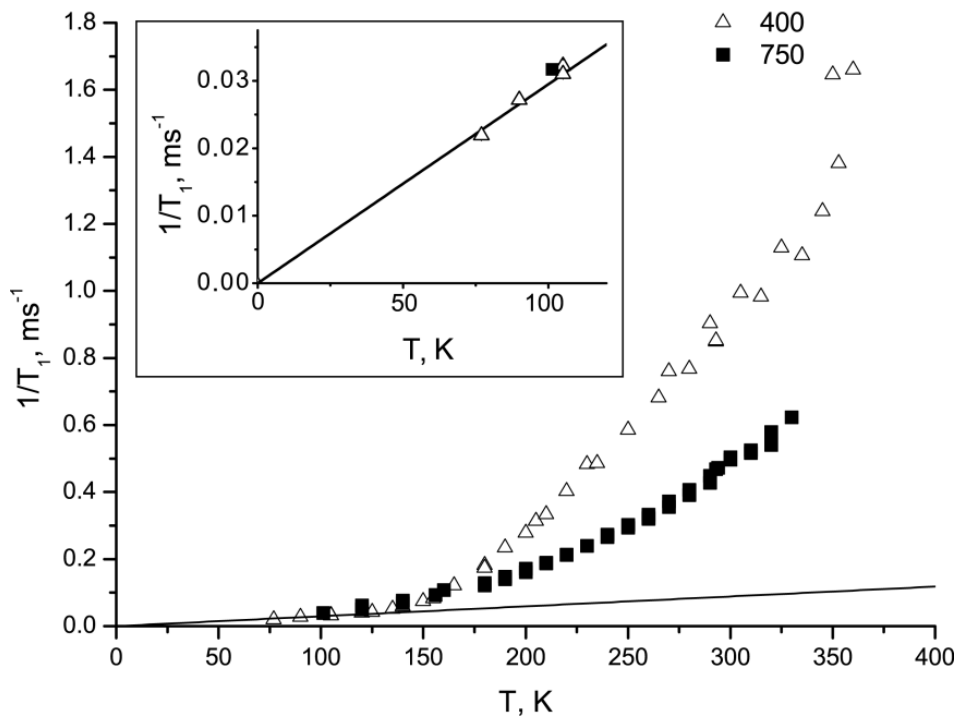


Figure 1. Dependence T_1 on temperature

Results

The correlation time of atomic motion in solid sodium varies from 15 μs at 90 K to 3 ns at 360 K. The obtained dependence of correlation time is shown in Fig. 2. The activation energy of atomic motion obtained using Arrhenius plot is equal to (0.087 ± 0.010) eV. This value is less than activation energy in liquid sodium which is equal to 0.096 eV [3]. The obtained result shows that nanoconfinement accelerates atomic motion in metallic particles.

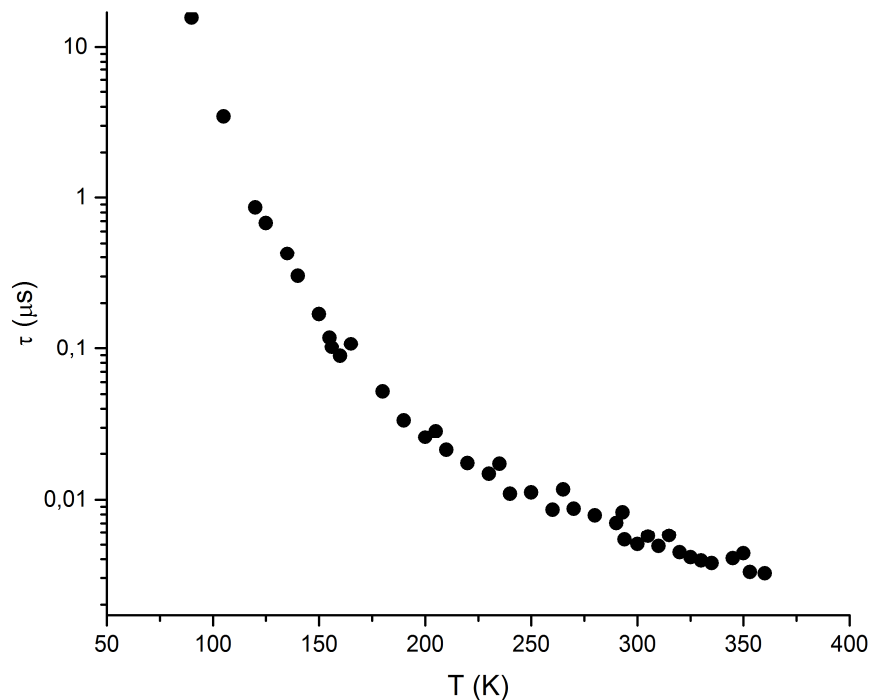


Figure 2. Dependence of correlation time in sodium on temperature

The atomic motion impacts not only spin-lattice relaxation but the position and shape of NMR line. The observed values of Knight shift are shown at Fig. 3. Knight shift measured at the spectrometer Avance 750 is shown by solid circles, Knight shift measured at the spectrometer Avance 750 is shown by empty circles. The difference between the obtained values for different spectrometers appears due to dynamic shift of resonance line. This effect was observed previously [4] and could be observed only if the Larmor frequency is comparable to correlation time. The line shapes of NMR lines and value of dynamic shift could be calculated using the values of correlation time obtained previously. The comparison of the experimentally measured at room temperature line shapes and the line shapes calculated using model of dynamic shift is shown at the insert at Fig. 3.

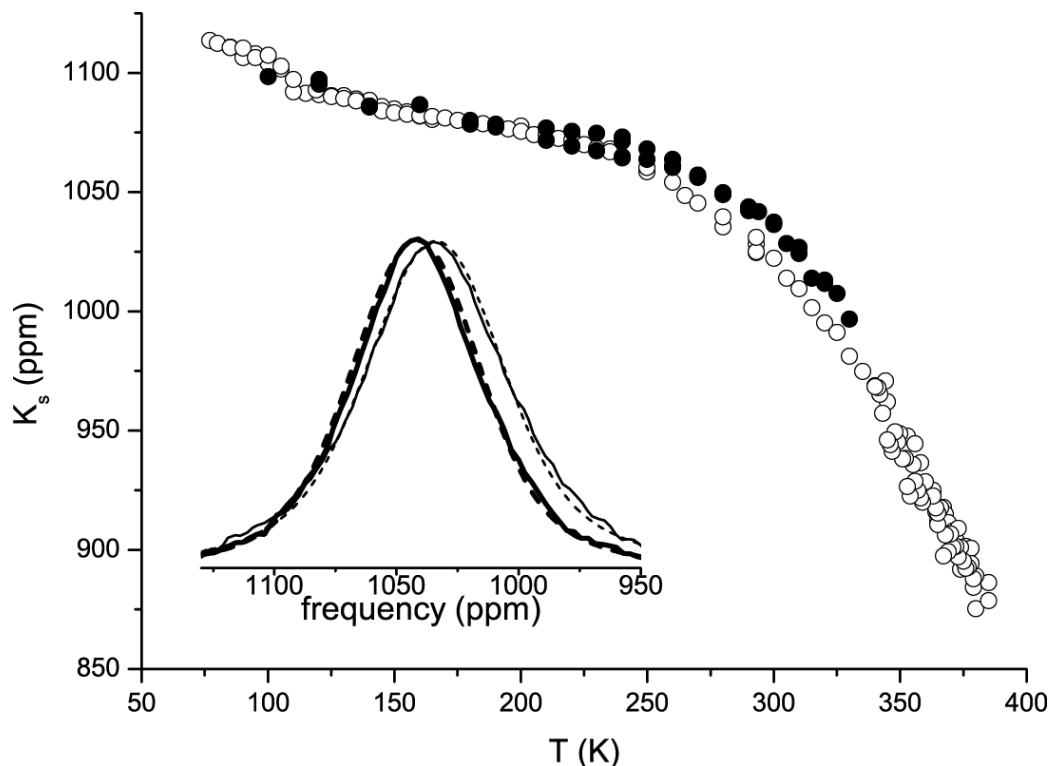


Figure 3. Dependence of Knight shift on temperature

References

1. A. V. Uskov, D. Yu. Nefedov, E. V. Charnaya, J. Haase, D. Michel, Yu. A. Kumzerov, A. V. Fokin. Polymorphism of Metallic Sodium under Nanoconfinement. – *Nano Letters*, 16, 791-794 (2016)
2. Min Kai Lee, E.V. Charnaya, Cheng Tien. Self-diffusion slowdown in liquid indium and gallium metals under nanoconfinement. – *Microelectronics Journal*, 39, 566-569 (2007)
3. Guo-Xin Qian. First-Principles Calculation of the Activation Energy for Diffusion in Liquid Sodium. – *Physical Review Letters*, 64, 1146-1149 (1990)
4. R. Poupko, A. Baram, Z. Luz. Dynamic frequency shift in the E.S.E. spectra of transition metal ions. – *Mol. Phys.*, 27, 1345-1357 (1974)

Spectroscopic Analyses of Nanometer Scale Heterogeneity in PEG-based Polyacrylate Gel

Bing Wu^{1,2,3}, Mingwen Tian³, Jianjun Xu³, Junyu Li³, Dermot Brougham², Victor Litvinov³

¹National Institute for Cellular Biotechnology, Dublin City University, Glasnevin, Ireland

²School of Chemistry, University College Dublin, Belfield, Ireland

³DSM Resolve, Urmonderbaan 18, 6160 RD, Geleen, The Netherlands

E-mail: bing.wu2@mail.dcu.ie

Introduction

Due to its biocompatibility, PEG-based polyacrylate material has been widely used in the field like biomedical coating and tissue engineering. On the other hand, UV-curing has been extensively implemented to produce these material in large scale in industry partially because of its easy applicability. However, the rather uncontrollable radical polymerization often results in a heterogeneous product with complicated morphological property. These distributed microstructures traditionally are probed by atomic force microscopy (AFM), electron microscopy (EM) and X-ray and neutron diffraction. However, solid state NMR spin diffusion experiments opened up a new possibility in this area with its unique feature which does not require any sample preparation like staining.

'Nano-gel' Formation During the UV-curing process

As one of the most used soft material, PEG-based polyacrylate material has been used in various industrial applications like biomedical coating and tissue engineering. [1] While UV-curing, due to its simple procedure and easy applicability, has been widely in the industrial production of polyacrylate gels. One of the shortcoming of implementing this radiation-induced radical polymerization approach is the widely presented micro-phase-separation in the resulted materials. While Krzeminski et al. used AFM to study the morphological heterogeneity in gels synthesized by similar oligomer diacrylates, and argued the formation of rodlike 'microgel' (as shown in Figure 1) at the early stage of curing procedure when the acrylate double bond conversion is still low. [2] Therefore, it is of great interest to systematically probe microheterogeneity in these UV-cured polyacrylates via a combination of different analytical approaches.

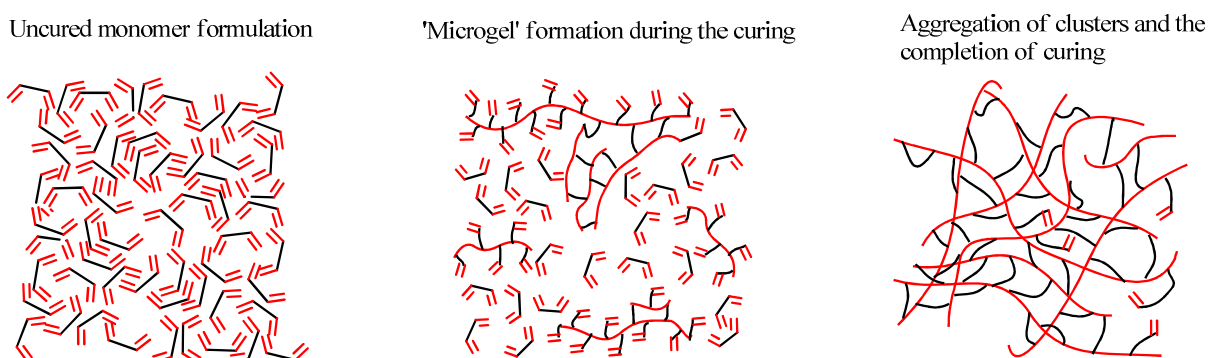


Figure 1. The proposed scenario for structure development in UV-cured diacrylate networks

Spectroscopic Analyses on Micro-morphology

Small-Angle X-ray Scattering Analyses

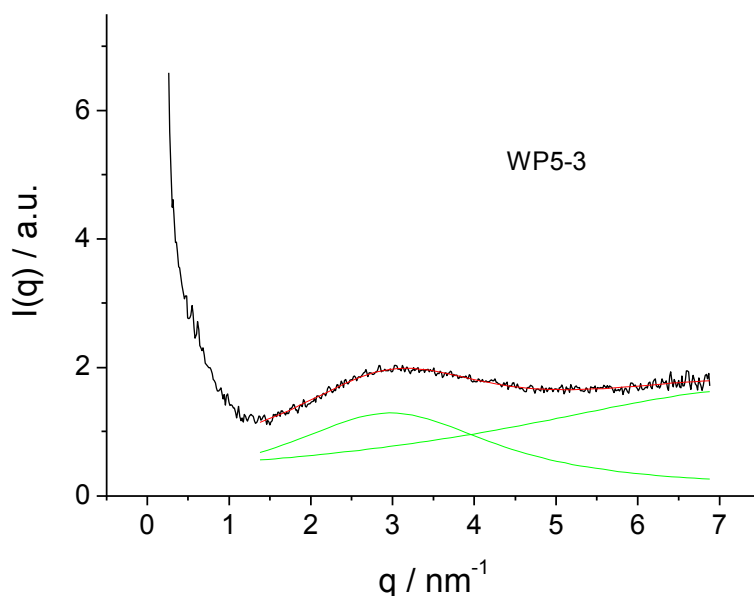


Figure 2. SAXS profile of 50% cured PEG-polyacrylate gel

Small-angle scattering techniques are well-known for their applications in probing structural heterogeneity on the scale from 10 to 10^4 c. As shown in Figure 2, two domains are clearly shown in the 50% cured PEG-polyacrylate gel.

Atomic Force Microscopy Analyses

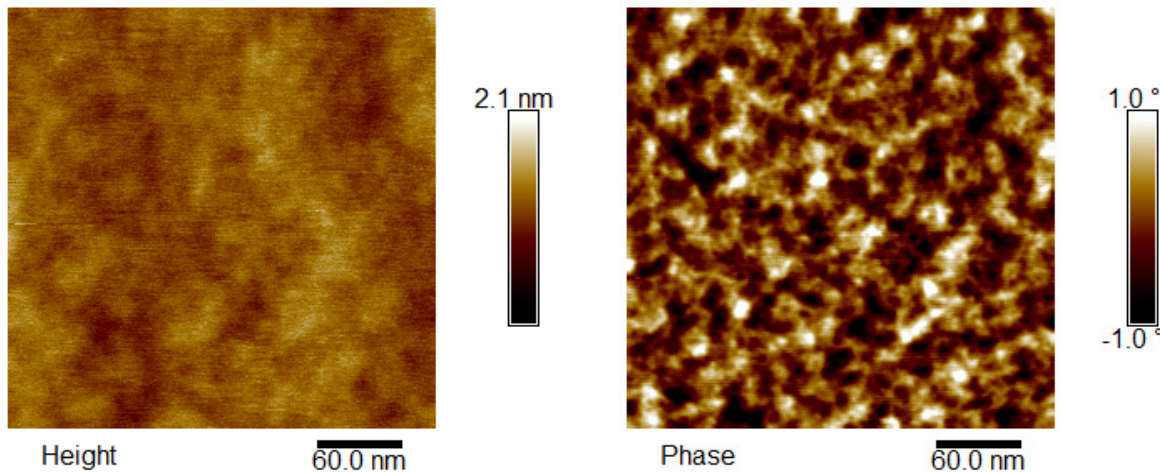


Figure 3. Tapping mode AFM phase images of dry 50% cured PEG-polyacrylate gel

AFM is another key instrument for evaluating polymers at small length scale, notably around 1 to 10^6 Å. Figure 3 shows a clear phase separation in 50% cured PEG-polyacrylate gel. The domain size is measured by averaging the distance between domains with similar phase angle.

NMR Spin Diffusion Analyses

NMR spin diffusion experiment offers information on different aspects of heterogeneity (structural and dynamic) in a broad range of spatial dimensions from 10 to 2000 Å. Figure 4 demonstrates the feasibility of using NMR spin diffusion to probe the ‘nanogel’ type heterogeneity inside the 50% cured PEG-polyacrylate.

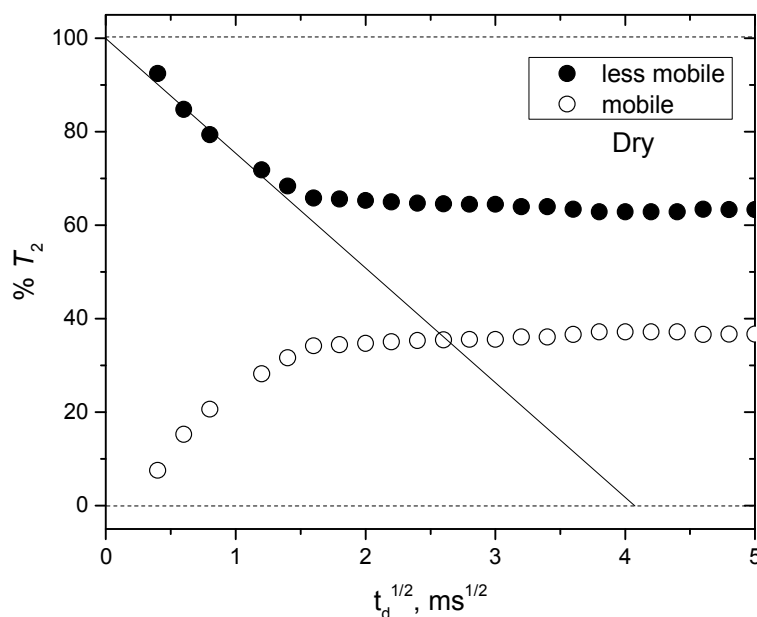


Figure 4. Build-up curve of the magnetization of mobile domain and less mobile domain in 50% cured PEG-polyacrylate gel: (left) dry sample; (right) 20% H₂O swollen sample

Conclusions

In this study, we focused on using various spectroscopic techniques to probe the ‘nanogel’ formation during the curing procedure. As suggested by AFM and SAXS analyses, a two-phase-system was formed during the curing stage, and this two-phase system would gradually disappear when the curing reaction completed. By analyzing domain size with these three techniques, the ‘nanogel’ formation is discussed under the context of changing swelling degree and sample curing degree. (these are not shown in this abstract).

Table 1. ‘Nanogel’ domain size calculated by different techniques

Methodology	SAXS	AFM	NMR Spin Diffusion
Domain Size (nm)	2.2 nm	3.1 nm	4.1 nm

Acknowledgements

This work is financially supported by the Marie-Sklodowska-Curie actions (Grant #316973).

References

1. F. P. W. Melchels, J. Feijen, D. W. Grijpma, A review on stereolithography and its applications in biomedical engineering. *Biomaterials* **31**, 6121 (Aug, 2010).
2. M. Krzeminski, M. Molinari, M. Troyon, X. Coqueret, Characterization by Atomic Force Microscopy of the Nanoheterogeneities Produced by the Radiation-induced Cross-linking Polymerization of Aromatic Diacrylates. *Macromolecules* **43**, 8121 (Oct, 2010).

Structure investigation of bovine insulin by two-dimensional NMR spectroscopy

Yuriy O. Zgadzay, Sergey V. Efimov, Vladimir V. Klochkov

Kazan Federal University, Kazan

E-mail: yurchubuk@yandex.ru

Introduction

Knowledge of protein structures in solution or in complex with supramolecular assemblies (such as phospholipid micelles) is of obvious pharmaceutical interest for understanding their action. Insulin is an irreplaceable preparation for people suffering from diabetes mellitus; that is why it is important to study its structure and the mechanism of interaction of insulin with different ligands.

Materials and methods

Bovine insulin was chosen as an object to investigate. The sample was water solution (90% H₂O, 10% D₂O) of bovine insulin (3.6 mg, $c = 1.1$ mM); KCl was added to the solution ($c = 0.05$ mM); NaN₃ served as antiseptic means and DSS (sodium 3-(trimethylsilyl)-1-propane sulphonate) was used for referencing the chemical shift scale. pH level was 2.86. At higher acidity levels, protein is denatured or NH protons become invisible in NMR spectra due to fast exchange. For this reason quality of spectra obtained at a lower pH does not allow total signal assignment. Two-dimensional homonuclear experiments TOCSY and NOESY and heteronuclear spectra (¹H,¹³C)-HSQC recorded on a Bruker Avance III HD 700 spectrometer were used for signal assignment (proton resonance frequency was 700 MHz). Sample temperature was set to 20 or 35°C.

Results and discussion

Signal assignment in the TOCSY and NOESY spectra at two mentioned temperatures was made. NOESY spectra show cross-peaks not only between NH and H α protons in adjacent groups, but also in NH–NH pairs, and between NH–H α atoms in residues ($i, i+2$) and ($i, i+3$), which is an evidence of formation of a helical structure [1]. This fact complicates signal assignment. Heteronuclear spectra were used as additional sources of information [2]. Figure 1 shows the distribution of sequential ($i, i+1$) and medium-range ($i, i+2,3,4$) distance restraints $d_{\alpha N}$, $d_{\beta N}$, d_{NN} . It can be seen that there are α -helices between residues 3–7 and 12–18 in the A chain. A similar diagram for the B chain reveals a long helical structure involving residues from 8 to 18.

Based on ¹H and ¹³C chemical shifts, dihedral angles ϕ and ψ in the protein chain were predicted with the aid of the TALOS+ program [3]. These values will be used together with NOESY data for modelling the protein structure in solution.

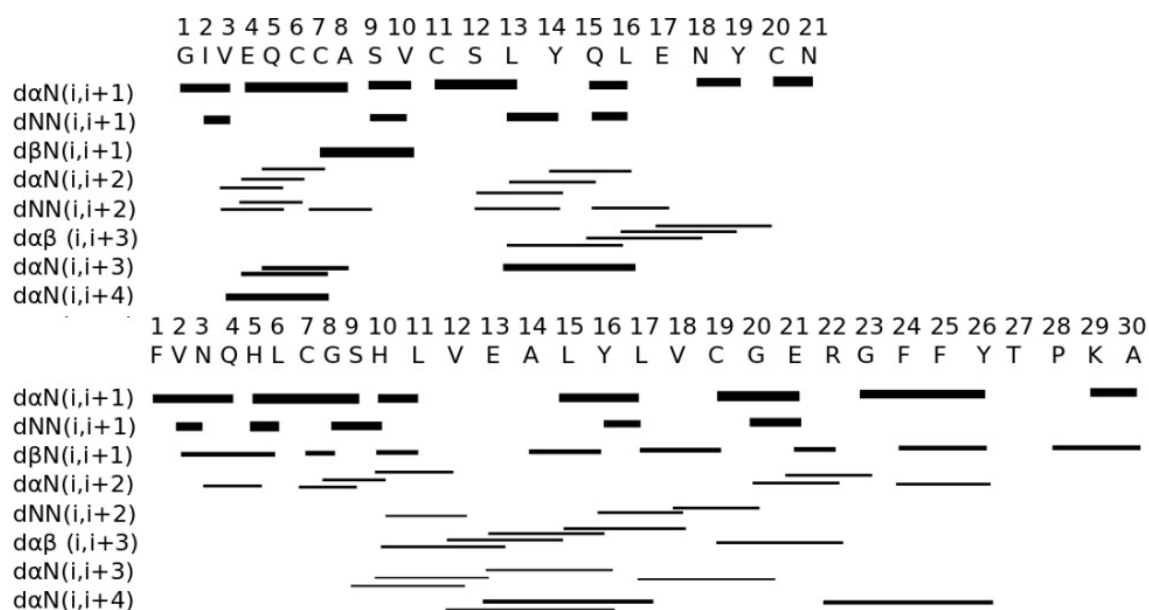


Figure 1. Sequential and medium-range NOE restraints (for A chain in the top and for B chain in the bottom)

After full NMR assignment was achieved, the structure of bovine insulin was obtained by molecular modelling in XPLOR-NIH [4]. Obtained structure is presented in Figure 2.

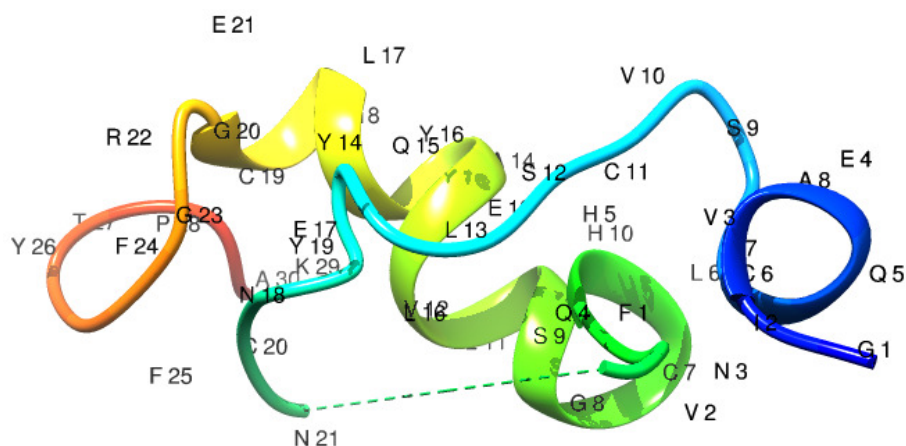


Figure 2. Three-dimensional structure of bovine insulin in water solution

In future we plan to obtain NMR spectra of porcine and human insulins and to add micelles into the samples to compare the protein structures in solution and in complex with metal ions. Note that differences in structure and in the protein chain composition lead to noticeable differences in NMR spectra, which allows comparing drug samples on a qualitative level by 2D spectroscopy [5]. Also obtaining spectra of isotope-labelled (^{15}N and $^{15}\text{N}/^{13}\text{C}$) samples of human insulin to make more comprehensive signal assignment including ^{15}N resonances is planned.

Acknowledgements

This work was funded by the subsidy of the Russian Government to support the Program of Competitive Growth of Kazan Federal University among World's Leading Academic Centers and by the subsidy allocated to Kazan Federal University for the state assignment in the sphere of scientific activities (Center of Shared Facilities).

References

1. Olsen, H. B. Investigations of Structure and Dynamics of Insulin Mutants using NMR Spectroscopy : PhD dissertation / H. B. Olson. – Roskilde University, 1996. – 63 p.
2. Rule, G. S. Fundamentals of protein NMR spectroscopy / G. S. Rule, K.T. Hitchens. Dordrecht : Springer, 2006. – P. 21-25.
3. Talos+: a hybrid method for predicting protein backbone torsion angles from NMR chemical shift/ Y. Shen [et al.] // J. Biomol. NMR. – 2009. – V. 44. – P. 213-223.
4. Using Xplor-NIH for NMR molecular structure determination / C. Schwieters, J. Kuszewski, G. Clore // Progr. NMR Spectroscopy 48 – 2006 – V. 48 – P.47-62.
5. Heteronuclear NMR provides an accurate assessment of therapeutic insulin's quality / M. Quinternet [et al.] // J. Pharm. Biomed. Anal. – 2013. – V. 78-79. – P. 252-254.

Poster Session

Magnetic Resonance Imaging of the blood and its derivates

V. Y. Adelson¹, V. V. Frolov¹, V. M. Cheremisin²

¹*Saint-Petersburg State University, Faculty of Physics
198504, St. Petersburg, Peterhof, st. Ulyanovskaya, 1*

²*Saint-Peterburg State University, Faculty of Medicine
199034, St. Petersburg, V.O. 21-line, 8a
E-mail: adelson_v@outlook.com*

Introduction

Magnetic resonance imaging (MRI) is one of the most modern and advanced technologies for the production of diagnostic images in a clinical setting. In order to interpret the MRI data with hemorrhages, very important to know the development features of hematoma and its visualization on MR-tomograms in different modes.

There are some types of intracranial hemorrhage, depending on their localization: subarachnoid, subdural, epidural, intraparenchymal, intraventricular, intratumoral. The causes of intracranial hemorrhage may be hypertension, aneurysm rupture or bleeding from vascular malformations, poorly differentiated tumors, or metastases, trauma, encephalitis, venous thrombosis and (or) dural sinus [1].

Table 1 give us information about the MRI signal intensity in T1 mode and T2-weighted images in the different phases of the different haemorrhages.[2] However, MRI SWI mode allows you to visualize the traces of small hemorrhages after a long time, the deposition of iron-containing substances in certain brain structures in diffuse axonal injury, and a well-track venous blood. [3-4] In order to enhance the contrast of MRI essential is local magnetic field inhomogeneity. They are caused by different values of the magnetic susceptibility of substances such as deoxyhemoglobin, iron and calcium.

Table 1. The intensity of the MR signal on T1 and T2 - WI in different phases of intraparenchymal, sub- and epidural hemorrhage

Hemorrhage		Hemoglobin form, localisation	MR-signal intensity	
Phase	Time		T1-WI	T2-WI
Hyperacute	< 1day	Oxyhemoglobin, Intracellular	Iso-	Iso-
Acute	1-3 days	Deoxyhemoglobin, Intracellular	Hypo-	
Early subacute	3-7 days	Methemoglobin, Intracellular	Hyper-	Hyper-
Late subacute	7-14 days	Methemoglobin, Extracellular	Hyper-	Hypo-
Chronic	>14 days	Hemosiderin, Extracellular	Iso-	Iso-

As an example, you can see the image of the dynamics of changes on MRI-T1 and T2-weighted images in intracerebral hemorrhage in the left hemisphere of the brain [5].

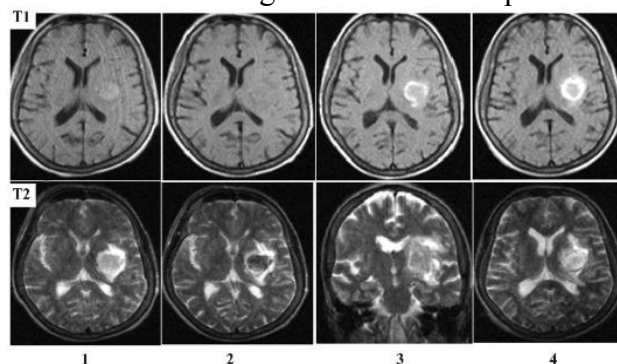


Figure 1. Dynamics of changes on MRI-T1 and T2-weighted images in intracerebral hemorrhage in the left hemisphere of the brain. 1 - day 1, 2 - 3rd day, 3 - day 7, 4 - day 4 of development of hemorrhagic stroke

Experiment

In this work, we will do an experiment involving 20 samples of 0.9% NaCl solutions with different concentrations of blood in them. Research is being conducted on the high field MRI 1,5T in modes T1, T2, SWI, GSE and diffusion-weighted sequences, and low-field unit 0,23T in T1 and T2 modes. Sections were oriented in a plane parallel to the long axis of the tubes, mounted in a vertical position. Studies carried out on the first day repeatedly every 2 hours for 7 hours after formation samples. Samples of blood concentration at a dosage of from 1:10 to 10: 1 scale factor, 1 times a day for 14 days. Thus 10 different samples of blood concentration at the next study exposed shaken, and the remaining 10 are unmixed. The blood is mixed in a sterile 10 ml tubes. Storage of samples is carried out at a temperature of 5°C in a household refrigerator.

Conclusion

Continued work in this direction will allow us to identify the most optimal parameters of pulse sequences, not previously described, and compare the performance of sequences for imaging blood derivatives. Optimization of these sequences will identify the place of hemorrhage, and calcium and iron deposits, which, in turn, will identify a series of diseases.

References

1. Галкина Т.Н., Кондаков Е.Н. Эпидемиологические аспекты нетравматических внутричерепных кровоизлияний. // *Нейрохирургия*. - 2000. - № 1. - С. 28-32.
2. Магнитно-резонансная томография (руководство для врачей)/ под ред. В.А. Фокина, Т.Е. Труфанова, из-во Фолиант, СПб, 2007, -688с.
3. Haacke EM., Xu Y., Cheng YN., JR Reichenbach. Susceptibility weighted imaging (SWI) // *Magnetic Resonance in Medicine*, Vol.52(3), 2004. – P. 612 - 618.
4. Haacke EM., Xu Y., Cheng YN., JR Reichenbach Susceptibility-Weighted Imaging: Technical Aspects and Clinical Applications Part1 and Part 2// *Physics Review, AJNR Am J Neuroradiol* 30:19 –30, Jan 2009
5. Неврология и нейрохирургия / под ред. А.Н. Коновалова, А.В. Козлова; Е.И. Гусев, А.Н. Коновалов, В.И. Скворцова : учебник : - т. 1. - 2009. - 624 с.

NMR ^{125}Te in the topological insulator Bi_2Te_3

A. O. Antonenko¹, E. V. Charnaya¹, V. V. Marchenkov^{2,3}, S. V. Naumov²

¹*St. Petersburg State University, 198504, 1 Ulyanovskaya street, St. Petersburg, Russia*

²*M.N. Miheev Institute of Metal Physics of Ural Branch of Russian Academy of Sciences
620990, 18 S. Kovalevskaya street, Ekaterinburg, Russia*

³*Ural Federal University, 620002, 19 Mira street, Ekaterinburg, Russia*

E-mail: nastya5555@mail.ru

Nowadays there is a great interest on the new class of materials — topological insulators (TIs). The TIs' existence was recently theoretically predicted and later discovered experimentally [1]. The bismuth telluride semiconductor, which as has been shown to belong to the three-dimensional topological insulators, previously have been widely known for its thermoelectric properties and has been studied a lot experimentally. But despite this, NMR studies of this material began relatively recently, and so far there are only a few published studies [2-4] dedicated to the research of Bi_2Te_3 .

Topological insulators are characterized by an energy gap in the volume and conductivity at the surface of the material as the metal. Due to the gapless states on the surface there is a possibility of the flow of spin-polarized current almost without energy loss. These unusual properties of topological insulators' surface give the potential for their use in new spintronic and magneto-electric devices, as well as for the creation of quantum computers. Experimental studies of Bi_2Te_3 by NMR open up new vistas for the investigation of topological insulators.

In [2], devoted to NMR studies of bismuth telluride as a powder, at room temperature the NMR line consisted from the one peak with its position near 500 ppm. Studies [3] for the different size nanoparticles of Bi_2Te_3 at room temperature revealed the weak additional line near -500 ppm for the line which was visible for the powder. Its presence was interpreted as a signal from the nuclei on the surface of the nanoparticles. In [4] there was studied the spectrum ^{125}Te which consisted of two lines with shifts about 400 and -600 ppm at room temperature. Also in this work low-temperature measurements were carried out for the high-frequency component of the NMR line.

In this work low-temperature NMR measurements of single-crystal plates of a topological insulator Bi_2Te_3 were performed in a wide temperature range.

Research was performed at the Center for Diagnostics of Functional Materials for Medicine, Pharmacology and Nanoelectronics of Research park of St. Petersburg State University using NMR spectrometer Bruker Avance 400 in the magnetic field of 9.4 T. The measurements were carried out in a temperature range from 12.5 to 293 K at ^{125}Te nuclei. Accuracy of temperature stabilization was 0.2 K, the number of scans due to the weakness of the signals was not less than 2^{11} . For the detection of the NMR signals the pulse sequence of spin echo $\pi / 2 - \tau - \pi$ was used. Duration of 90-degree pulse depending on the temperature was chosen between 2.5 and 4 μs . Bismuth telluride samples were studied in two orientations: the crystallographic axis c was oriented parallel and perpendicular to the external magnetic field B_0 .

It was found that the NMR spectrum ^{125}Te consists of two lines at room temperature with a positive (about 500 ppm) and negative (approximately -500 ppm) shifts of the resonant frequency for the single crystal plate when the axis c was perpendicular to the external magnetic field. These lines strongly moved towards lower frequencies with decreasing temperature. The distance between them was maintained, in addition, the lines themselves broadened approximately 1.5 times compared with room temperature.

A completely different situation was observed in the case of axis c was parallel to the external magnetic field. At room temperature ^{125}Te spectrum consisted of two lines with positive shifts in frequency: the maximum of main line was at 750 ppm, but in addition to it there was the line of a little intensity with its position at 2250 ppm. Lines were also shifted to lower frequencies as the temperature decreases from room to the helium, but these shifts were less observable than it was for another orientation. Thus at 16.5 K the intensity of the left line increased significantly and it began to dominate, in contrast to the situation at room temperature.

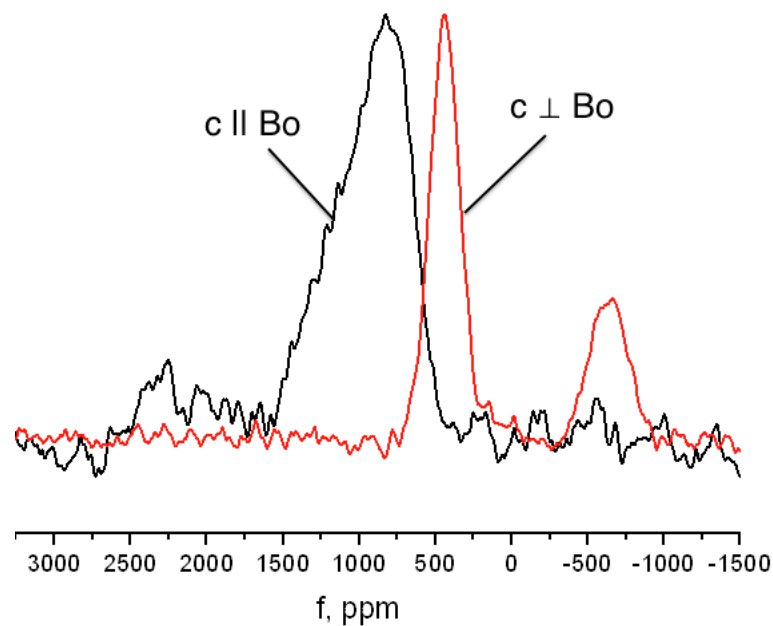


Figure 1. ^{125}Te NMR spectral lines of Bi_2Te_3 single crystal in two orientations at room temperature

References

1. L. Fu, C.L. Kane. Phys. Rev. B **76**, 045302 (2007).
2. R. E. Taylor, B. Leung, M. P. Lake, L. S. Bouchard. J. Phys. Chem. C **116**, 17300 (2012).
3. D. Koumoulis, T. C. Chasapis, R. E. Taylor, et al. Phys. Rev. Lett. **110**, 026602 (2013).
4. D.Yu. Podorozhkin, E.V. Charnaya, A. Antonenko, et al. Phys. Sol. State **57**, 1741 (2015).

Investigation of Ce³⁺ emitters in scintillating garnets by pulsed EPR and ENDOR

A. G. Badalyan¹, E. V. Edinach¹, Yu. A. Uspenskaya¹, N. G. Romanov¹, H. R. Asatryan¹,
G. V. Mamin², S. B. Orlinski², P. G. Baranov^{1,3}

¹Ioffe Institute, 194021 St. Petersburg, 26 Politekhnicheskaya str., Russia

²Kazan Federal University, Institute of Physics, 420008 Kazan, 18 Kremlyovskaya str., Russia

³Peter the Great St. Petersburg Polytechnic University, 195251 St. Petersburg, 29

Politekhnicheskaya str., Russia

E-mail: elena.edinach@mail.ioffe.ru

Introduction

Garnet single crystals and ceramics doped with cerium are widely used as scintillator materials that convert high energy radiation into visible or infrared light [1]. Yttrium aluminum garnet (YAG) doped with cerium is a key component in light emitting diodes (LEDs) and lasers [2]. The phosphor absorbs part of the blue light emitted by an (In,Ga)N LED and converts it into yellow emission, which together with partly transmitted blue light yields white light.

Recently coherent properties of rare-earth single-spin qubits in YAG have been demonstrated [3, 4]. It was declared that rare-earth-doped crystals are excellent hardware for quantum storage of optical information. Combined with the high brightness of Ce³⁺ emission and the possibility of creating photonic circuits out of the host material, this makes cerium spins an interesting option for integrated quantum photonics.

Garnets crystallize in a cubic form and are described by the formula C₃(AD)₅O₁₂, where three different cation sites are indicated. C is a dodecahedral site, A and D are an octahedral and a tetrahedral sites, respectively. The site C can be occupied by Y or Lu. In these materials, sites A and D are occupied by aluminum but can also be substituted by other elements, for example gallium. As we show in this paper where pulsed EPR and ENDOR techniques are used in diagnosing the cerium environment in garnet powders and ceramics.

Experimental

All ceramic samples were prepared at Philips Research Eindhoven by sintering of oxide raw materials. Based on X-ray diffraction patterns it was concluded that all samples consist of a single garnet phase. Lu₃Al₅O₁₂ samples were doped with cerium at concentration 0.2%. The X-band ESE detected EPR spectra were measured by using the Hahn-echo decay sequence $\pi/2 - \tau - \pi$, with $\pi/2 = 16$ ns and $\tau = 180$ ns. To measure T_2 the ESE signal amplitude was monitored by using the Hahn-echo decay sequence $\pi/2 - \tau - \pi$, where τ was varied from 180 ns up to 2.2 μ s, $\pi/2 = 16$ ns. ENDOR was measured by using Mims sequence $\pi/2 - \tau - \pi/2 - T - \pi/2 - \tau - \text{ESE}$, $\tau = 228$ ns, $T = 19.8$ μ s, for RF pulse $T_{\text{RF}} = 18$ μ s.

Results and discussion

Fig. 1 shows the X-band (9.4 GHz) ESE detected EPR signal of Ce³⁺ ions in Lu₃Al₅O₁₂:Ce (0.2% Ce) ceramics. The ENDOR spectra were measured at magnetic fields marked in Fig. 1 (a) as $B_1 = 708.0$ mT, $B_2 = 649.9$ mT and $B_3 = 371.5$ mT.

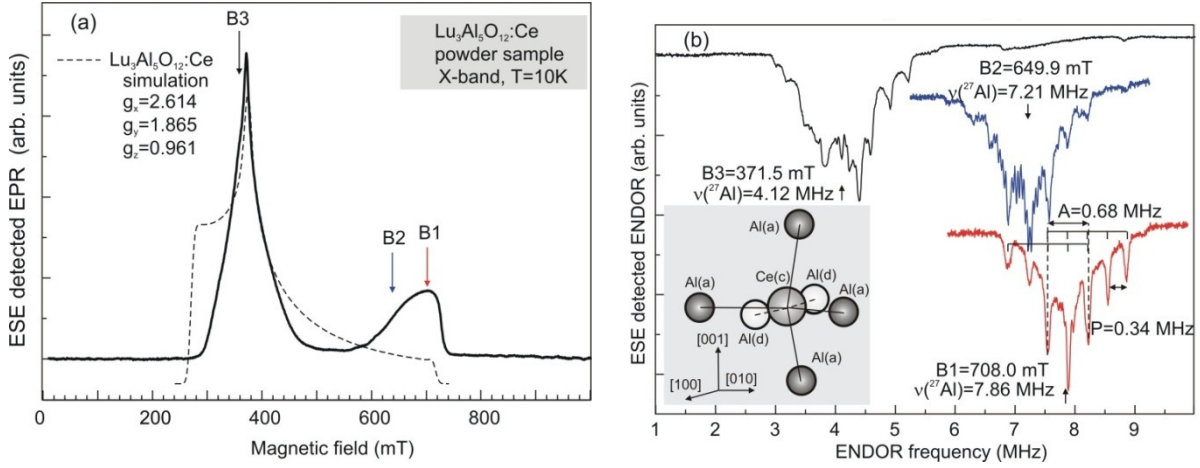


Figure 1. ESE detected EPR (a) and ENDOR (b) signals of Ce^{3+} ions in $\text{Lu}_3\text{Al}_5\text{O}_{12}:\text{Ce}$ powder sample. The inset in (b) shows a sketch of the nearest environment of the Ce^{3+} ion with aluminum atoms in two positions A and D; the distances between the Ce^{3+} ion and aluminum atoms in the nearest octahedral and tetrahedral positions are 3.33 \AA and 2.98 \AA , respectively

Fig.1 (b) shows the groups of lines arranged symmetrically with respect to the ^{27}Al nuclear Zeeman frequencies $\nu(^{27}\text{Al})$ indicated by arrows. These groups are related to the hyperfine (HF) and quadrupole interactions with the neighboring aluminum atoms.

To analyze the Ce^{3+} EPR and ENDOR spectra the following spin Hamiltonian with $S=1/2$ has been used:

$$\hat{H} = \mu_B \vec{B} \cdot \hat{g} \cdot \hat{S} + \sum_i (\hat{S} \cdot \hat{A}_i \cdot \hat{I}_i + \hat{I}_i \cdot \hat{P}_i \cdot \hat{I}_i - g_N \mu_N \vec{B} \cdot \hat{I}_i), \quad (1)$$

where the first term describes electron Zeeman interaction, the second term - describes the HF, quadrupole, and nuclear Zeeman interactions with ligand ions (cerium has only even isotopes), respectively. The term in Eq. (1), which describes the quadrupole interaction of the aluminum nuclei, can be written as $H_Q = P \left[I_z^2 - \frac{1}{3} I(I+1) \right]$, here $P = 3/2 P_{zz} = 3q$ [6].

For the nuclear spin $I > 1/2$ the quadrupole interaction of the nucleus with an electric field gradient must be taken into account by $q = \frac{eQ}{4I(2I-1)} V_{zz}(r)$. Here Q is the electric quadrupole moment in multiples of $|e| \times 10^{-24} \text{ cm}^2$, $V_{zz}(r_i)$ is the electrical field gradient, and $m_q = \frac{(m_I + (m_I + 1))}{2}$ is the average value of the nuclear quantum states m_I between which the nuclear transition takes place. For ^{27}Al the nuclear spin is $I = 5/2$, giving five m_q -values: ± 2 , ± 1 and 0. Thus, the quintet in Fig. 1(b) is due to the quadrupole interaction of ^{27}Al . Natural abundance of ^{27}Al is 100%, the nuclear g -factor $g_N = 1.4566$, and the electric quadrupole moment $Q = 0.15$ (Appendix A in [7]).

The value of the isotropic HF interaction allows for estimating the spin density of the s -electron on the aluminum nuclei as $A = 0.68 \text{ MHz}$. The wave function for the unpaired electron can be approximated by a linear combination of atomic orbitals centered on the aluminum atoms near the Ce^{3+} ion as $\Psi = \alpha(\psi_{3s}) + \beta(\psi_{3p})$, $\alpha^2 + \beta^2 = 1$.

Since the anisotropic part of the HF interaction for aluminum atom is about 20 times smaller than the isotropic one (3911 MHz) [8] we ignore the contribution of the anisotropic part $\beta(\psi_{3p})$. Thus α is very small ($\alpha^2 \cong 0.017\%$).

The quadrupole splitting depends on the orientation of the magnetic field relative to the direction of the electric-field gradient. The magnitude of this splitting between the neighboring lines varies from P for the perpendicular orientation of the magnetic field to $2P$

for the parallel orientation, passing through zero at an angle of about 55° . Furthermore, we must consider the complex combination of the HF and quadrupole interactions, which also depend on orientation.

Resolved nuclear quadrupole splitting allows for the direct determination of the electric field gradient at the nuclear position. Usually two sources of the electric field gradient $V_{zz}(r_i)$ are considered: intrinsic electric-field gradients in different crystal lattice positions, which are due to the crystal structure of a garnet, and the unpaired charge density in the np orbital ($3p$ -orbital of the ^{27}Al ion). We can estimate the contribution of the garnet electric field gradient. The quadrupole splitting, caused by ^{27}Al nuclei surrounding the Ce^{3+} ion, is $P \cong 0.34$ MHz, and the electric field gradient $V_{zz}(\text{Al}) = 1.25 \times 10^{21}$ V/m².

In Fig. 1 (b) there are at least two types of ENDOR spectra for aluminum, differing in magnitude of the quadrupole interaction. It is known that aluminum can occupy two positions in the garnet crystal lattice ($\text{C}_3\text{A}_2\text{D}_3\text{O}_{12}$), an octahedral position (a) and a tetrahedral one (b). Since the electric field gradients can be different in these positions, the quadrupole splitting for ^{27}Al nuclei should be different.

Summary

In conclusion, EPR and ENDOR techniques were applied to measure hyperfine and quadrupole interactions for Ce^{3+} in garnet based scintillator powders and ceramics for assessment of the unpaired electron spatial distribution and definition of the electric field gradient at aluminum and gallium sites. The Ce^{3+} g -factor anisotropy can be used in ENDOR experiment for diagnostic of the cerium environment in mixed garnet ceramics, to distinguish between aluminum and gallium in the nearest neighborhood of Ce^{3+} . First results were obtained on the quadrupole interaction for aluminum nuclei in garnet ceramics and an octahedral and a tetrahedral Al positions were separated. Pulsed EPR and ENDOR techniques enable determining the coherence of the Ce^{3+} spin system.

Acknowledgements

This work has been supported by the Russian Science Foundation under Agreement #14-12-00859 and by Philips.

References

1. H. Ogino, A. Yoshikawa, M. Nikl, J.A. Mares, J. Shimoyama, K. Kishio, J. Cryst. Growth **311**, 908 (2009).
2. V. Bachmann, C. R. Ronda, A. Meijerink, Chem. Mater. **21**, 2077 (2009).
3. P. Siyushev, K. Xia, R. Reuter, M. Jamali, N. Zhao, N. Yang, C. Duan, N. Kukharchyk, A. D. Wieck, R. Kolesov, J. Wrachtrup, Nature Communications **5**, 3895 (2014).
4. R. Kolesov, K. Xia, R. Reuter, M. Jamali, R. Stohr, T. Inal, P. Siyushev, J. Wrachtrup, Phys. Rev. Lett. **111**, 120502 (2013).
5. A. Vedda, M. Martini, D. Di Martino, V. V. Laguta, M. Nikl, E. Mihokova, J. Rosa, K. Nejezchleb, K. Blazek, Radiat. Eff. Defect. S. **157**, 1003 (2002).
6. J.-M. Spaeth, J.R. Niklas, R.H. Bartram, *Structural Analysis of Points Defects in Solids* (Springer-Verlag Berlin Heidelberg, 1992).
7. J. R. Morton, K. F. Preston, J. Magn. Reson. **30**, 577 (1978).
8. R. L. White, T. G. Phillips, R. A. Lefever, J. Appl. Phys. **38**, 408 (1967).

NMR proton's relaxation efficiency research in aqueous solutions of composite magnetic nanoparticles

Yu. V. Bogachev¹, A. V. Nikitina¹, A. A. Kostina¹, V. A. Sabitova¹, V. V. Pankov²,
V. O. Natarov², E. G. Petrova², D. A. Kotikov², T. G. Shutova²

¹Department of Physics, Saint-Petersburg Electrotechnical University "LETI",
5, prof. Popov st., Saint-Petersburg, 197376, Russia,
E-mail: Yu.Bogachev@mail.ru

²Department of Chemistry, Belarusian State University,
4, Nezavisimosti avenue, Minsk, 220030, Republic of Belarus,
E-mail: val_natarov@mail.ru

Introduction

Magnetic nanoparticles (MNP) is currently finding increasingly wide application in medicine and biology for diagnostics, magnetic separation, drug delivery, etc. [1]. The magnetic nanoparticles should have certain magnetic characteristics, to be stable, biocompatible, non-toxic, have the ability of functionalization, to interact or bind with specific biological objects. One of the most common methods for the synthesis iron oxide MNP is the co-precipitation method. Due to the high sensitivity to different parameters (nature of the precipitant, concentration of reagents, temperature of synthesis, pH of the reaction medium, etc.), it allows to widely vary the size and properties of the resulting nanoparticles.

The aim of this paper is research the NMR relaxation properties of protons in aqueous solutions of composite nanoparticles based on solid solutions of zinc ferrites, magnesium and iron (magnetite).

Experimental methods

Composite MNP substituted with zinc and/or magnesium magnetite were obtained by the method of co-precipitation from solutions of the corresponding salts using different precipitants – NaOH and Na₂CO₃. The solution taken in stoichiometric ratio of initial reagents at room temperature was introduced into the solution of precipitator, taken with some excess, and stood for 1 h with intensive mixing until the completion of crystallization processes. The pH of the system during the reaction was maintained at ~ 11, due to which it is managed to achieve full deprotonation aqua complexes ions of all metals, but to prevent the formation of water-soluble hydroxocomplexes. In the event carbonate co-precipitation, the reaction mixture was rapidly heated to the temperature of 90°C, after that heating was stopped. Obtaining colloidal solutions of nanoparticles was carried out using ultrasonic bath (Sapfir, Russia) and submersible ultrasonic disperser (USG-13-0,1/22, Russia). Magnetic nanoparticles were functionalized polyelectrolyte shell PDDA - olydiallyldimethylammonium chloride. Nomenclatures of the samples are presented in table 1.

The NMR measurements have been made using NMR relaxometer (Spin Track, Russia) with the magnitude of the magnetic field of 0.33 Tesla. The resonance frequency for protons - 14 MHz. To measure the time of spin-lattice relaxation T₁ pulse sequence "inversion-recovery" was used 180°-τ-90° (90° pulse of 2.6 μs; the duration of the 180° pulse of 5.2 μs). To measure the time of the spin-spin relaxation T₂ pulse sequence used is the Carr-Purcell-Meiboom-Gill (CPMG) (90° pulse of 2.6 μs; the duration of the 180° pulse of 5.2 μs).

Table 1

N ^o	Structure	M _s , Am ² kg ⁻¹	Method of synthesis	r ₁ , c ⁻¹ mMol ⁻¹ L	r ₂ , c ⁻¹ mMol ⁻¹ L
1	Mg _{0.1} Fe _{2.9} O ₄	65	Co-precipitation with carbonate	33.9	302.4
2	Mg _{0.12} Zn _{0.08} Fe _{2.8} O ₄	59	Co-precipitation with carbonate	43.1	260.9
3	Mg _{0.1} Zn _{0.2} Fe _{2.7} O ₄	59	Co-precipitation with carbonate	31.7	146.5
4	Mg _{0.12} Zn _{0.08} Fe _{2.8} O ₄	34	Co-precipitation with alkali (without heating)	15.4	77.9
5	Fe ₃ O ₄	63	Co-precipitation with carbonate	-	-
6	Mg _{0.1} Fe _{2.9} O ₄	29	Co-precipitation with alkali (without heating)	-	-

Results and discussion

The results of x-ray phase analysis (XRA) confirmed the formation of single-phase crystalline compound with a spinel structure when used alkaline and carbonate co-precipitation. According to electron microscopy, the average size of the nanoparticles is ~ 10 nm when used as a precipitant of a hydroxide and ~20 nm for sodium carbonate. At room temperature for all investigated compositions is marked superparamagnetic behavior with no coercivity and remanent magnetization. The values of saturation magnetization M_s for studied samples are given in Table 1.

According to the results of the NMR relaxation measurements graphs of longitudinal R₁ (Figure 1) and transverse R₂ (Figure 2) nuclear magnetic relaxation rates of water protons on the concentration of magnetic compositenanoparticles were constructed.

As can be seen from the figures 1, 2 for the samples 1, 3, 4 and 6 the concentration dependence of the relaxation rates correspond to a linear dependence of the general form $R_i = r_i \cdot C + A$, where C is the concentration of MNP, expressed in mmol, A is constant determined by the relaxation rate of water protons in the absence of MNP, r_i is the relaxation efficiency coefficient. The analysis of concentration dependencies allows to determine the relaxation efficiency coefficient r_i as derived functions of the experimental dependence $R_i = f(C)$ at this point and in the case of linear dependence to calculate this angular coefficient as the ratio: $r_i = (1/C \cdot T_i)$ (mmol·s/l)⁻¹.

The analysis of relaxation efficiency of the studied samples shows that:

1. relaxation efficiency r₁ and r₂ for the samples MNP, obtained by co-precipitation with carbonate, higher than the relaxation efficiency of MNP samples, obtained by co-precipitation with alkali (without heating);
2. relaxation efficiency r₂ is much higher than the relaxation efficiency r₁ for all samples MNP on the basis of iron oxide, regardless of synthesis, which confirms the fact that the investigated MNP are negative contrast agents in MRI;
3. relaxation efficiency r₂ for the samples obtained by co-precipitation with carbonate lower for the composite MNP in the structure of the nucleus which is Zn. For the samples 2 and 5 the concentration dependence of the transverse R₂ nuclear magnetic relaxation rates of water protons have been nonlinear. The analysis of these dependencies shows a decrease in the relaxation efficiency by increasing the

concentration MNP in the solution. This indicates instability of these MNP in aqueous solution and their aggregation ability to form clusters with increasing concentration MNP in the solution increases. This effect of clustering MNP was observed in these samples visually and increased with increasing residence time of the sample in the magnetic field of the NMR relaxometer. Similar results were obtained earlier in the NMR relaxation study of protons in aqueous solutions of iron oxide MNP with Si-Cshell [2].

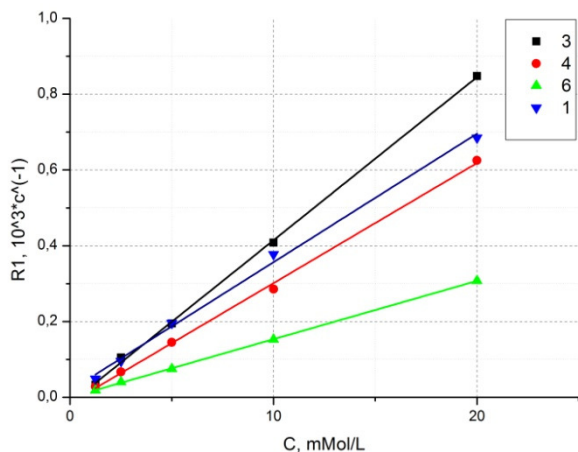


Figure 1. The dependence of the longitudinal relaxation rate R_1 on the concentration of magnetic nanoparticles

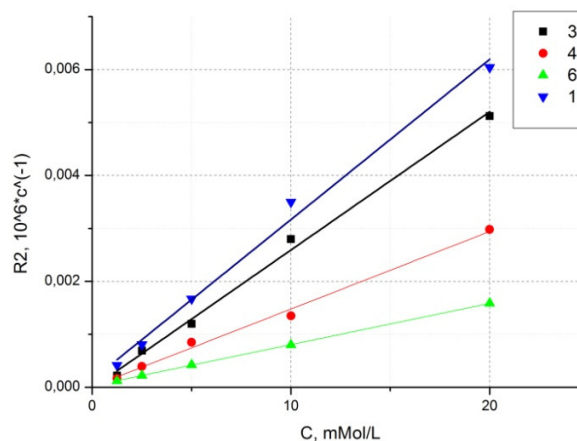


Figure 2. The dependence of the transverse relaxation rate R_2 on the concentration of magnetic nanoparticles

Conclusions

Research of the NMR relaxation of protons in aqueous solutions of composite MNP iron oxide show that their relaxation efficiency r_2 is much higher than relaxation efficiency r_1 and depends on the composition, method of synthesis MNP, which allows the use this parameter to assess the stability of MNP in aqueous solutions and estimation of their aggregation behavior.

References

1. Jinhao Gao, HongweyGu, Bing Hu. Multifunctional Magnetic Nanoparticles: Design, Synthesis, and Biomedical Applications.// Accounts of chemical research, 2009, vol.42, No.8, pp.1097-1107.
2. Yu.V.Bogachev, Ju.S.Chernenko, K.G.Gareev, I.E.Kononova, L.B.Matyushkin, V.A.Moshnikov. S.S.Nalimova. The Study of Aggregation Processes in Solutions of Magnetite-Silica Nanoparticles by NMR Relaxometry, AFM and UV-Vis-Spectroscopy. // Appl. Magn. Reson., 2014, vol.45, pp. 329-337.

Microscale vector magnetic field sensor based on NV centers in diamond for biology and medicine applications

Alexander Dmitriev, Anton Vershovskii

*Ioffe Institute, St. Petersburg, Russia
E-mail: alexdmk777@gmail.com*

Introduction

Since the 1960s, the main tool in quantum magnetometry has been the optically pumped quantum magnetometer (OPQM) based on relatively large centimeter-scale alkali vapor cells [1]. However this type of magnetometers can retain high sensitivity with millimeter-scale only in ultra-low magnetic fields (< 100 nT). The problem of the spatial resolution of a magnetic field sensors was solved when the application of methods based on optically detected magnetic resonance (ODMR) to negatively charged nitrogen-vacancy (NV^- , or just NV) color centers in diamond crystals allowed to expand the field of optical quantum magnetometry to micro- and nanometer scales [2]. Various NV magnetometers based on the ODMR in diamond achieve extremely high spatial resolution combined with maintaining magnetic sensitivity even at room temperature and therefore are quite promising for the investigation of biological and medical objects [3].

The advantage of NV color centers in application to quantum magnetometry lies in their high concentration (10^{17} – 10^{19} cm^{-3}), combined with lifetimes T_1 and T_2 as high as several milliseconds and their optical properties (most NV centers in bulk diamond gave a stable fluorescence signal that did not bleach or blink).

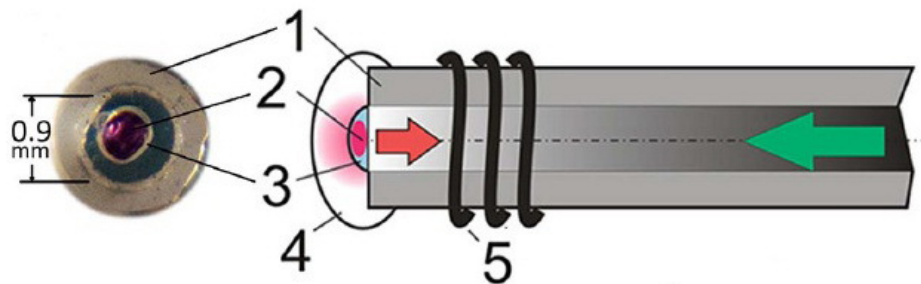


Figure 1. View of the fiber end, and a schematic diagram of magnetometer sensor: (1) optical fiber, (2) diamond crystal, (3) transparent glue, (4) reflective coating, (5) microwave antenna. (from [9])

Experimental setup

The experimental setup was described in [4]: a synthetic diamond of SDB1085 60/70 grade (manufactured by Element Six) with dimensions $0.1 \times 0.3 \times 0.3$ mm was subjected to electron irradiation ($5 \cdot 10^{18}$ cm^{-2}) and subsequent annealing in Ar at 800°C over 2 h. The crystal was used at room temperature; it was attached by optically transparent glue [Fig. 1] to the end of an optical fiber. We used a fiber with a core diameter of 0.9 mm, which ensured effective collection of the photoluminescence (PL) signal at the cost of losing $\sim 90\%$ of pumping light. The pumping beam (15 mW at a wavelength of 532 nm) was focused on the second end of the fiber, and the PL signal was collected from the same end. A three turn copper wire coil reeled on the fiber at a distance of ~ 2 mm from the crystal acted as a MW antenna.

Results

The ODMR spectrum of a singular NV center is determined [2] by the center gyromagnetic ratio $\gamma/2\pi = 28$ GHz/T, axial zero-field splitting (ZFS) parameter $D/2\pi = 2.87$

GHz, and transverse ZFS parameter E, varying from kHz to MHz. There are four ($i = 1, \dots, 4$) possible orientations of the NV center axes with respect to the crystal lattice [Fig. 2]. In the presence of a field B with projection B_i onto the i -th NV axis, the transition frequencies are as follows [5]:

$$2\pi \cdot f_{i\pm} = D \pm [E^2 + (\gamma \cdot B_i)^2]^{1/2} \quad (1)$$

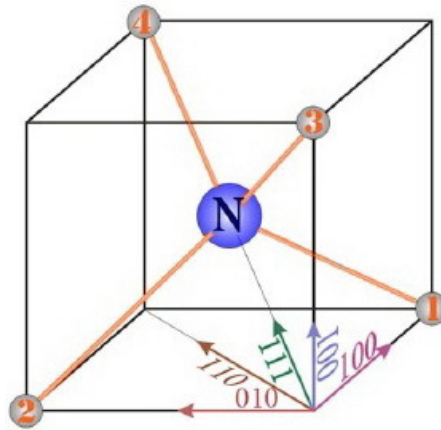


Figure 2. Possible NV center configurations in the diamond crystal, comprising nitrogen atom (N) at the center and carbon atoms or vacancies (1–4) at the vertices; arrows indicate crystallographic directions. (from [9])

The plus/minus sign here corresponds to $|m_s = 0\rangle \leftrightarrow |m_s = \pm 1\rangle$ (shortly $-|0\rangle \leftrightarrow |\pm 1\rangle$) transitions. Magnetic field B splits each of the two spectral lines corresponding to these transitions into four resonant components, which may overlap depending on the field direction. Additional structure arises due to the interaction of unpaired electron with nuclear spin of ^{14}N [6], which splits each spectral line into a partially resolved triplet. Finally, the NV ODMR spectrum consists of 24 spectral lines in two symmetrical wings [Fig. 3(a)].

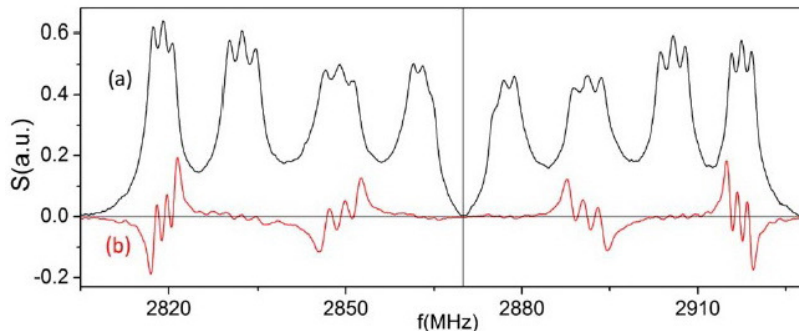


Figure 3. Panoramic ODMR spectra of NV color centers in diamond at $B = 3$ mT: (a) amplitude modulation of MW field; (b) modulation of magnetic field in $\langle 011 \rangle$ direction (from [9])

Our NV magnetometer belongs to the class of M_z OPQMs [7] that detect population difference signals, normally using frequency modulation of the RF or MW field for tuning it to the resonance line. However this method in application to diamond is only applicable if no overlap of resonances occurs. Moreover, it is incapable of identifying resonances in the spectrum. Therefore, in [4] we used instead a weak modulating AC field B_{mod} superimposed on B. According to (1), choosing the direction of B_{mod} makes it possible to control the relative amplitudes of the ODMR responses corresponding to four orientations of NV centers. The use of six modulating fields oriented along crystallographic directions $\langle 110 \rangle$, $\langle 1\bar{1}0 \rangle$, $\langle 101 \rangle$,

$\langle 10\bar{1} \rangle$, $\langle 011 \rangle$, $\langle 0\bar{1}\bar{1} \rangle$ (each of these fields forms a spectral pattern containing just two triplets in each wing of the spectrum [Fig. 3(b)]) might appear excessive; but it allows us to 1) identify all the spectral lines, and 2) exclude the twelve dead zones that appear when two or even three triplets in each wing of the spectrum overlap. The patterns containing overlapping lines can be excluded from consideration, and the remaining lines are still sufficient to determine all components of B , – save for the cases when B is directed along one of the directions $\langle 001 \rangle$, $\langle 010 \rangle$, and $\langle 00\bar{1} \rangle$ [Fig. 2].

Further sensitivity enhancement was achieved [8] by simultaneous microwave excitation of all three components of the hyperfine triplet; to achieve this, resonant MW field was modulated at the frequency of hyperfine splitting. As expected, this led to a change in the shape of the observed resonances [Fig. 4]. Overlaying the resonance responses leads to an increase in the contrast of the central peak and to an increase in total signal due to the involvement of hyperfine levels $|0, \pm 1\rangle$.

All in all, in a balanced scheme where the effective gyromagnetic ratio $df/fB = 2df_+/dB = 56$ GHz/T, application of this combined ODMR excitation technique resulted in an estimated sensitivity increase to $\delta B \approx 1.5$ nT·Hz^{-1/2}. The expected shot-noise limited sensitivity amounts to $\delta B \approx 0.3$ nT·Hz^{-1/2}. [9]

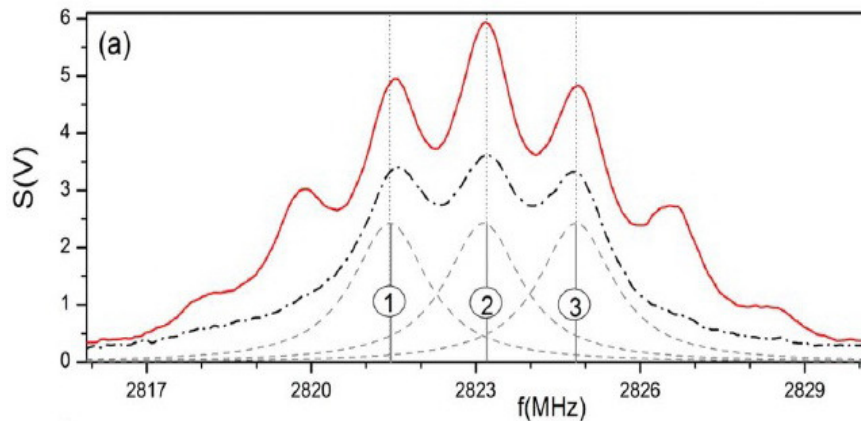


Figure 4. ODMR signal corresponding to $|m_s = 0\rangle \leftrightarrow |m_s = -1\rangle$ transition at 100% amplitude modulation of the MW field. Dashed-dotted line, single-frequency excitation; solid red line, combined multifrequency excitation; dashed line, the triplet approximation by three Lorentz contours characterized by a HWHM of (1.67 ± 0.1) MHz (from [9])

Conclusion

The DC NV magnetometer sensitivity achieved in our experiment is still inferior to that reported for scalar alkali vapor OPQMs. Nevertheless, the sensor of our NV magnetometer is small enough to provide spatial resolution of order of 100÷300 μ m. In a far zone, the field of a magnetic dipole is inversely proportional to the cube of the distance to its center. Therefore, in magnetometry of small objects (particularly, in medical and microbiological tasks), reducing the size of the sensor allows one to reduce the distance R between the centers of the sensor and the object, thus decreasing the sensitivity requirements proportionally to R^3 .

References

1. D. Budker and M. Romalis, Nature Physics 3, 227 (2007).
2. J.M. Taylor, P. Cappellaro, L. Childress, L. Jiang, D. Budker, P. R. Hemmer, A. Yacoby, R. Walsworth, M. D. Lukin, Nat. Phys. 4, 810 (2008).

3. G. Balasubramanian, I. Y. Chan, R. Kolesov, M. Al-Hmoud, J. Tisler, C. Shin, C. Kim, A. Wojcik, P. R. Hemmer, A. Krueger, T. Hanke, A. Leitenstorfer, R. Bratschitsch, F. Jelezko, and J. Wrachtrup, *Nature* 455, 648 (2008).
4. A.K. Vershovskii, A. K Dmitriev, *Technical Physics Letters*, 41, 393 (2015).
5. V.M. Acosta, D. Budker, P. Hemmer, J. Maze, and R. Walsworth, in *Optical Magnetometry*, D. Budker and D. F. Kimball, eds. (Cambridge University, 2013), p. 142.
6. V.M. Acosta, E. Bauch, M. P. Ledbetter, C. Santori, K.-M. C. Fu, P. E. Barclay, R. G. Beausoleil, H. Linget, J. F. Roch, F. Treussart, S. Chemerisov, W. Gawlik, and D. Budker, *Phys. Rev. B* 80, 115202 (2009).
7. E.B. Alexandrov and A. K. Vershovskii, in *Optical Magnetometry*, D. Budker and D. F. Kimball, eds. (Cambridge University, 2013), p. 60.
8. A.K. Vershovskii, A. K Dmitriev, *Technical Physics Letters*, 41, 1026 (2015).
9. A.K. Dmitriev, A.K. Vershovskii, *JOSA B.*, v.33, no.3, pp. B1-B4 (2016).

Observation of spin-wave self-modulation instability in a perpendicularly magnetized magnonic crystal

A. V. Drozdovskii, A. B. Ustinov, B. A. Kalinikos

*St. Petersburg Electrotechnical University
197376 Russia, St. Petersburg, prof. Popov st. 5
E-mail: drozdovskyav@gmail.com*

During last years a great attention has been given to the study of tunable materials both for their properties and for the high number of potential applications. Magnonic crystals (MCs) are new class of tunable materials with the periodically modulated magnetic properties where spin waves (SW) can propagate [1]. Reviving interest to such structures is stimulated by fundamental and applied researches. In particular, the periodic magnetic waveguides were used for development of the tunable resonators and filters, signal-to-noise enhancers, logic elements, sensors and other [2]. Microwave properties of such structures can be tuned in a wide frequency range with magnetic field. Most attention was given to study the linear properties of MCs and possibilities of their reconfiguration. However, the magnonic crystals produced from the ferrite films may demonstrate strong nonlinearity for high spin wave power.

The phenomenon of modulation instability that appears due to four-wave parametric process is typical of many nonlinear media. The modulation instability is commonly classified by two types, spontaneous and induced instability. Induced instability arise from the interaction of two initial monochromatic signals owing to nonlinearity of the medium. Spontaneous modulation instability (called also “self-modulation instability”) appears due to the decay of an initial monochromatic signal into waves with close wave numbers. As is known, both types of modulation instability can lead to the formation of envelope solitons.

In this work, we report the first experimental study of self-modulation spin-wave instability in perpendicularly magnetized magnonic crystals.

The magnonic crystal was fabricated from an yttrium-iron garnet (YIG) film with chemical etching. The fabricated sample of the magnonic crystal had a width of 2 mm and a length of 30 mm. The YIG film with thickness of 9 μm and saturation magnetization of 1750 Gs was grown by liquid-phase epitaxy on a gadolinium-gallium garnet substrate. The half-width ΔH of the ferromagnetic resonance curve of the YIG film was 0.55 Oe measured for the frequency of 4500 MHz. The film had free surface spins. To avoid possible unwanted reflected spin waves, the edges of the MC were cut at an angle less than 45° . The experimental periodic structure had a period Λ of 400 μm , a groove length of 50 μm , and a groove depth of 1.5 μm .

A delay line structure was used for the measurements. Spin waves were excited and received using short-circuited input and output microstrip antennas having a length of 2 mm and a width of 50 μm . The distance between the antennas was 5.2 mm. Thus, there were 13 periods of the structure between the transmitting and receiving antennas. The experimental device was placed between poles of an electric magnet generating a uniform magnetic field with strength of 3050 Oe. The field was directed perpendicular to the plane of the magnonic crystal. Such mutual orientation of the field and the propagation direction of spin waves corresponds to the excitation of forward volume spin waves in the magnonic crystal. For this magnetic field direction, the nonlinear self-interaction coefficient N is positive.

The experiment was carried out in several stages. First, the transmission characteristics of spin waves in a knowingly linear regime of their excitation and propagation were studied. The measured amplitude–frequency characteristic is shown by solid lines in figure 1. As is seen, the spin-wave spectrum of the magnonic crystal has pass bands and stop bands (band

gaps) with strong group velocity dispersion and high damping of spin waves. The stop bands are formed due to Bragg resonances.

The numerical calculation of the amplitude–frequency characteristic was performed with the use of the method similar to that described in [3], i.e., in terms of the transmission matrix. The calculation did not take into account the losses for the excitation and reception of the spin waves. Nevertheless, the plots indicate good quantitative agreement between measured and calculated frequencies of the stop bands.

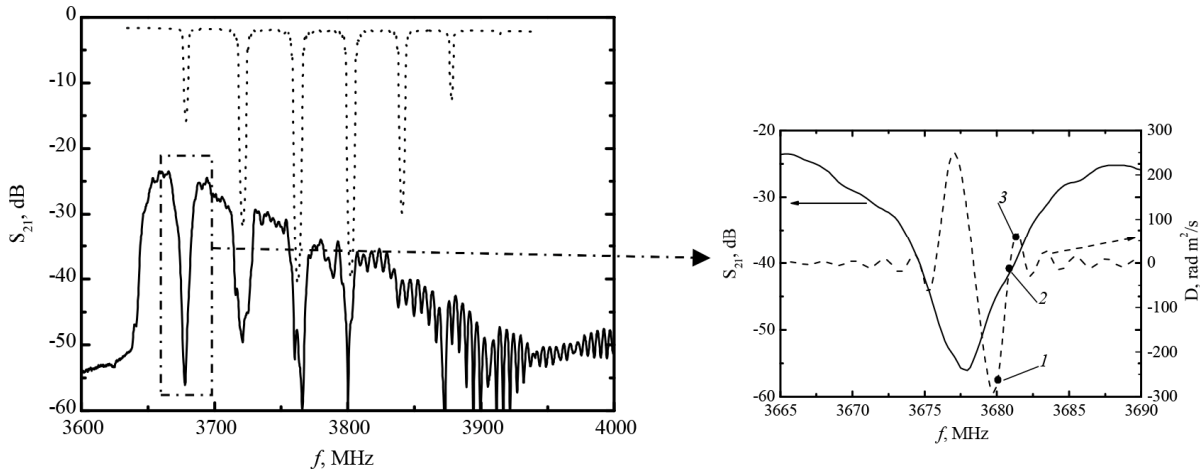


Figure 1. The experimental (solid line) and theoretical (dotted line) transmission characteristics of magnonic crystal. Dashed line shows the frequency dependence of the spin-wave dispersion coefficient near the frequency of the first Bragg resonance

At the second stage of the experiments we studied the possibility of the emergence of self-modulation instability of the spin-waves propagating in the magnonic crystal. We measured the spectra and envelopes of the output microwave signal under the systematic variation of the power and frequency of the input monochromatic signal. The results show that the spin-wave instability in the magnonic crystal emerged in a threshold manner at $P_{in} = 18$ dBm for frequencies within high-frequency slope of the stop band. For these parameters, low-amplitude satellites emerged in the spectrum of the output signal. The amplitude of these frequency harmonics increased and the spectrum was enriched with an increase in the input power. The frequency region of the self-modulation instability was also broadened.

The shape of output waveform depends not only on the power, but also on the frequency of the input microwave signal. Figure 2 exemplifies the frequency spectra (left panel) and the corresponding envelopes of the output microwave signal (right panel) measured for frequencies near the first Bragg resonance for $P_{in} = 20$ dBm.

Figure 2,a shows the measured results for the frequency of the input signal of $f_{in} = 3680$ MHz and negative dispersion coefficient (see point 1 on figure 1). In this case the output bright pulses were observed. This agrees with the theoretical concepts of the Lighthill criterion for solitons ($D \cdot N < 0$) [4]. In the region where the dispersion coefficient changes its sign (see point 2 on figure 1) the pairs of bright and dark pulses were observed (see figure 2,b). For areas with a positive dispersion coefficient (see point 3 on figure 1) and $D \cdot N > 0$ the formation of dark pulses was observed as is shown in figure 2,c.

It should be mentioned that the self-modulation instability was observed also near the second and the third stop bands of the magnonic crystal. Outside the stop bands, i.e., in the regions where the dispersion coefficient is low, the inherent modulation instability was not observed in the entire power range of the experimental setup.

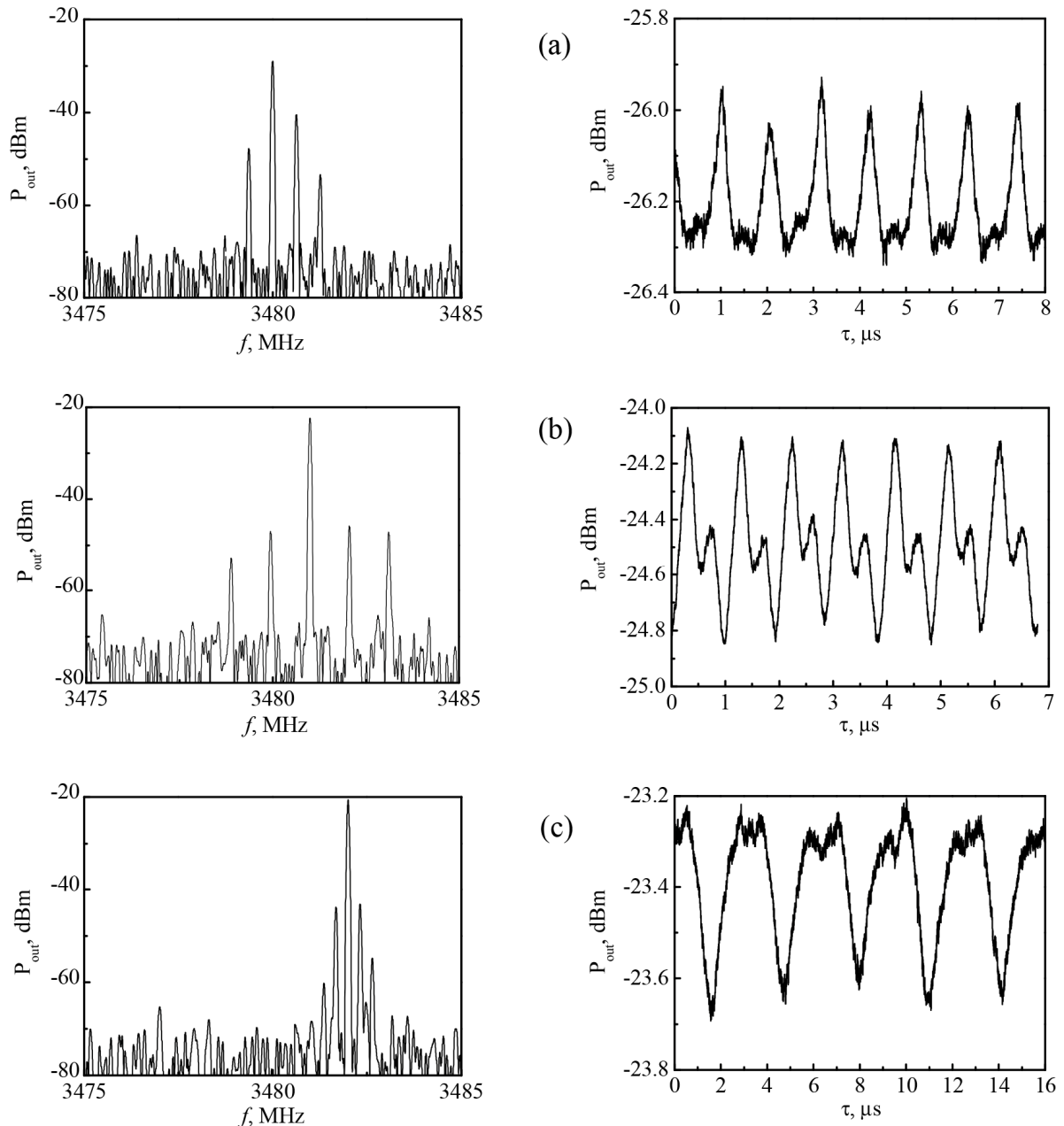


Figure 2. Frequency spectra (left) and the respective envelopes (right) of the output signal measured for various frequencies of input microwave signal:
 (a) $f_{in} = 3680$ MHz, (b) $f_{in} = 3681$ MHz, (c) $f_{in} = 3680$ MHz

In conclusion, self-modulation spin-wave instability in a magnonic crystal has been studied for the first time. The formation of periodic bright and dark spin-wave envelope soliton trains has been detected at the edges of stop bands.

References

1. Nikitov S.A., Tailhades Ph., Tsai C. S. JMMM, 2001, Vol. 236 p. 320-330.
2. Serga A.A., Chumak A.V., Hillebrands B. Journal of Physics D: Applied Physics, 2010, Vol. 43, № 26, p. 264002.
3. Seshadri S.R. J. Appl. Phys., 1986, Vol.60, p. 1758.
4. Nikitin A.A., Ustinov A.B., Semenov A.A., Chumak A.V., Serga A.A., Vasyuchka V.I., Hillebrands B. Appl. Phys. Lett., 2015, Vol. 106(10), p. 102405.

Concomittent gradients in low fields

V. V. Frolov, V. I. Chizhik, P. A. Kupriyanov

Faculty of Physics, Saint Petersburg State University, St. Petersburg, Russia
E-mail:vfrolovv@bk.ru

To reconstruct a magnetic resonance image from a NMR signal linear dependence of the magnetic field on a coordinate is used. Then the frequency of a NMR signal from a voxel also linearly depends on a coordinate. Thus in magnetic resonance imaging (MRI) an encoding of the position of voxel is carried out. In tomograph there is the gradient system that creates gradients of magnetic field in three mutually ortogonal directions. The encoding field $\mathbf{B}_{\text{encod}}$ is the sum of the basic magnetostatics field \mathbf{B}_0 and field \mathbf{B}_G , created with the gradient system. One supposes $\mathbf{B}_G = \mathbf{G} \cdot \mathbf{r}$, where $G_i = \partial B_z / \partial u_i$ ($u_i \equiv x, y, z$), id est

$$\mathbf{B}_{\text{encod}} = \mathbf{B}_0 + \mathbf{G} \cdot \mathbf{r} \quad (1)$$

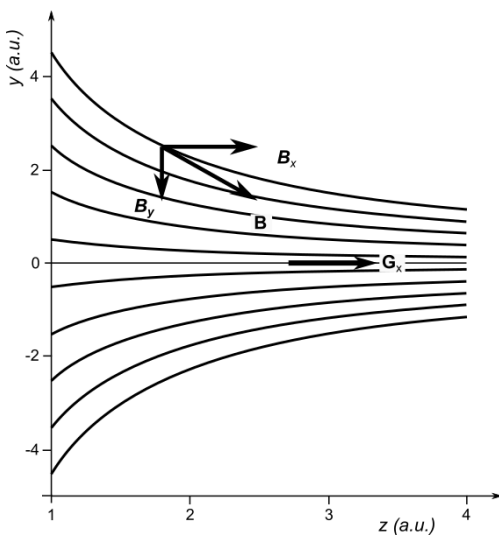


Figure 1. A map of field lines of magnetic field with x-gradient. One may see the evidence of appearance of transversal component B_y

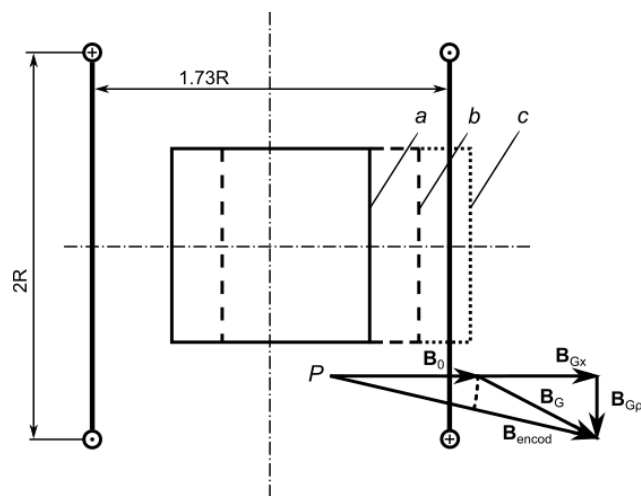


Figure 2. Gradient system with a pair of thin ringed coils of radius R interspaced as $\sqrt{3} \cdot R$. The vector diagram demonstrates concomitant field B_{Gp} and the forming of encoding field B_{encod} at point P . Indexes a , b and c are related with three positions of investigated object (see text)

During acquisition of NMR signal only one component of gradient, which determines direction of encoding, operates. However (1) ignores the fact that a gradient is a not vector, but tensor of 2nd rank [1]. It results in that the total encoding field is not linear on a coordinate [2 - 4] due to appearance of traversal components (Fig 1). This circumstance appears important in very low field NMR experiments but may be ignored in high field. In the presented report the simplest gradient system is examined in form of two ringed coils with oppositely directed currents (Fig.2). Such system is intended for creation of gradient along an axis z . However, in accordance with above said, the appearance of gradients along z accompanies appearance of gradient in other direction, and an dependence of encoding field becomes non-linear.

Non-linearity runs high

1. by small ratio of working field B_0 towards maximum field of gradient system in the volume of object $B_{G\text{max}}$;
2. by big dimensions of object relatively to coil radius;
3. by a shift of investigated objet towards negatives values gradient field.

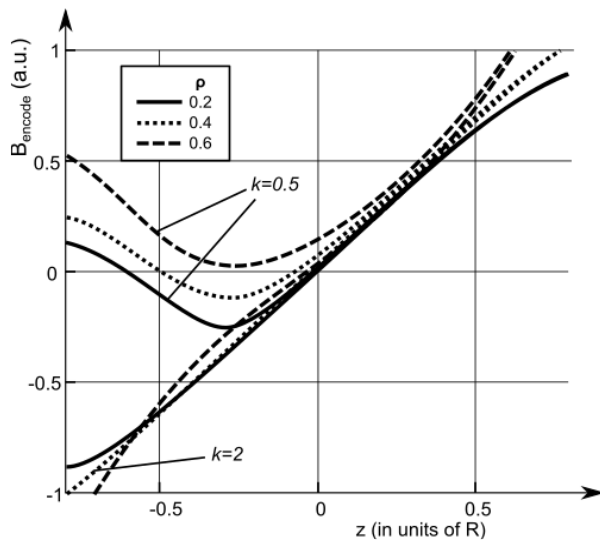


Figure 3. The dependences of encoding field on z at varies distances from axis ρ for an ratio working field/gradient field $k = B_0/B_{Gmax} = 0.5$ and 2 and for symmetrical position of investigated object

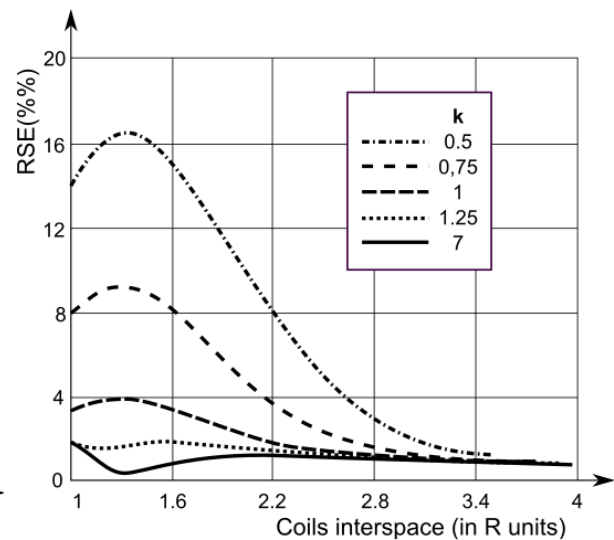


Figure 4. The dependences of relative mean quadratic error on distance between coils for various ratios working field/maximum gradient field k and for symmetrical position of investigated object

We have carried out calculation of z -dependences of encoding field on z for varies distances from the axis and values of working field (Fig 3). For that we used expressions of off-axis field from [5]. Relative mean quadratic errors for different working fields depending on coils interspace was calculated too (Fig. 4). The calculation was executed in media Matcad 15.

Conclusion

It is shown a concomitant with magnetic field longitudinal gradient results in appearance the nonlinearity of co-ordinate dependence of the field. This misrepresents MRI because of scale variations within investigated object. To minimize the artefact, it is necessary to change parameters of the system generating magnetic field gradients. As example, in system consisting in two ringed coils the distance between the coils should be incremented in comparison with Maxwell position to 1.35 coil radius. In so doing in the worst extreme case when the main homogenous magnetic field is negligible, the standard deviation from linearity within object in the size about of half-radius of coils will make no more than 4 %.

References

1. Frolov V. V. The generalized approach to reconstruction of spin magnetic resonance images. In: *Nuclear Magnetic Resonance*, Issue 7, p. 27- 41. Ed. Saint Petersburg State University, Saint Petersburg, Russia. - 1988 (in Russian)
2. Norris D.G., Hutchison, J. (1990). *Concomitant magnetic field gradients and their effects on imaging at low magnetic field strengths*. *Magnetic resonance imaging*, **8**(1), 33-7.
3. M.A. Bernstein, K.F. King, X.J. Zhou. *Handbook of MRI Pulse Sequences*. Elsevier – Academic Press, 2004. 1017 p.
4. Ilina O.G. Concomitant gradients terms in low-field MRI. International Symposium and Summer School in Saint Petersburg “Nuclear Magnetic Resonance in Condensed Matter. 10th meeting: NMR in Life Sciences”. July 8—12 2013. Abstracts. “SOLO” Publisher, Saint Petersburg, 2013. 128 p.
5. B.L. Alievsky, V.L. Orlov. *The calculation of the axially symmetric coils magnetic field parameters* (in Russian) - Energoatomizdat, Moscow. 1983.

On the decoupling of dipole transceive antennas for 7 Tesla with mushroom metasurface structures

Anna A. Hurshkainen¹, Stanislav B. Glybovski¹, Ingmar J. Voogt, Irina V. Melchakova¹, Pavel A. Belov¹, Cornelis A. T. van den Berg² and Alexander J. E. Raaijmakers²

¹*ITMO University, 197101 St. Petersburg, Russia*

²*University Medical Center Utrecht, 3584 CX, Netherlands*

E-mail: a.hurshkainen@metalab.ifmo.ru

http://www.metalab.ifmo.ru

Introduction

Metasurfaces are usually defined as two-dimensional periodic structures with electromagnetic parameters of artificial continuous boundaries comprising useful electromagnetic properties [1]. Unit cells of a metasurface can have different parameters of the microstructure and different periodicity affecting the macroscopic response of the equivalent boundary. Among various known types of metasurfaces there is one referred to as High Impedance Surfaces (HIS). HIS exhibit two important electromagnetic properties: full in-phase reflection of an incident wave and suppression of all propagating surface waves in a particular frequency range. The second property can be used for decoupling of closely-spaced antennas in the microwave range.

In order to improve homogeneity or local SNR of body imaging at 7 Tesla arrays of densely spaced antennas are used in the parallel-transmit mode [2]. In this regime each antenna is driven with the individual magnitude and phase. Recently dipole antennas have been proposed as efficient multi-channel array elements for 7 Tesla [3] instead of conventional magnetic loops. Dipole antennas provide better penetration of a transmit RF-field for the same value of the maximum local SAR. However, neighboring dipole antennas in a body array suffer from a strong electromagnetic coupling destructively affecting the array transmit efficiency and the amplifier safety.

In the present work we first experimentally realize and test a HIS for suppression of mutual coupling of two dipole antennas of a transceive body array for 7 Tesla MRI.

Design of the decoupling structure

In order to mitigate strong electromagnetic coupling between dipole antenna elements of a 7T MRI coil the structure inspired by *mushroom*-type metasurfaces [4] was used by the authors [5]. The metasurface structure forms a resonator consisting of multiple coupled resonant unit cells. Each unit cell comprises metallic patches at two layers of the same thin dielectric substrate. Every patch is connected to the common ground plane by thin metal wires. A high capacity between the two layers allows the unit cells to be resonating at a relatively low frequency of 298 MHz (Larmor frequency of Hydrogen at 7 Tesla).

The two layers of patches were manufactured as a printed circuit board (PCB). The same technique was used to manufacture a common ground plane. The two PCBs were arranged as a multi-layered structure and separated by a foam insulator with the epsilon equal to 1. Each patch was manually connected to the ground plane by soldering small wires. In the experiment the metasurface structure was positioned above two identical fractionated half-wave dipole antennas with the separation of 30mm. The distance between the resonator and each of the dipoles was varied and the decoupling capabilities of the structure were measured.

For the smaller distance to the structure (5 mm) a strong decoupling regime was achieved. In contrast, for the larger distance (45mm) the structure exhibited weak decoupling capabilities.

In order to evaluate electromagnetic properties of two dipole antennas in a presence of the metasurface structure in both the strong and the weak decoupling regimes we performed

measurements with a vector network analyser (VNA) and a 7 Tesla MR research system. The measurement setup schematic as well as the summary of the measured transmit RF-field pattern and the isolation of the dipoles are given in Figure 1. The setup contained two dipole antennas in the presence of the metasurface structure and the phantom mimicking the properties of a human body. The isolation of two dipole antennas measured by VNA was -16.7 dB in the strong decoupling regime, and -6.9 dB in the case of a weak decoupling. For comparison, the isolation without the metasurface structure for the same separation of the dipoles was only -2.8 dB. Moreover, the B1+ field distributions were measured on the 7T Philips Achieva scanner in a central axial plane of the phantom.

Results and Conclusion

The measurement results demonstrate efficient decoupling provided by the mushroom metasurface structure. The isolation between two closely spaced dipole antennas improves from -2.8 dB up to -16.7 dB for the 5 mm distance to the structure and to -6.9 dB for the 45 mm distance to the structure. For the weak decoupling regime, the magnetic RF-field distribution remains almost the same. In the strong decoupling regime, the penetration depth of the B1+ slightly decreases. On the other hand, fair comparison of the field distribution requires evaluation of the $\frac{B_1^+}{\sqrt{\maxLocalSAR}}$ ratio. In the strong decoupling regime, the maximum local SAR value drops down by 40% due to the presence of the structure. In the weak decoupling regime, the maximum local SAR remains almost the same. The experimental results demonstrated that for both the two regimes the $\frac{B_1^+}{\sqrt{\maxLocalSAR}}$ increases. As a conclusion, the small distance of 5 mm from the dipoles to the metasurface structure is preferable due to high isolation improvement and higher $\frac{B_1^+}{\sqrt{\maxLocalSAR}}$ ratio.

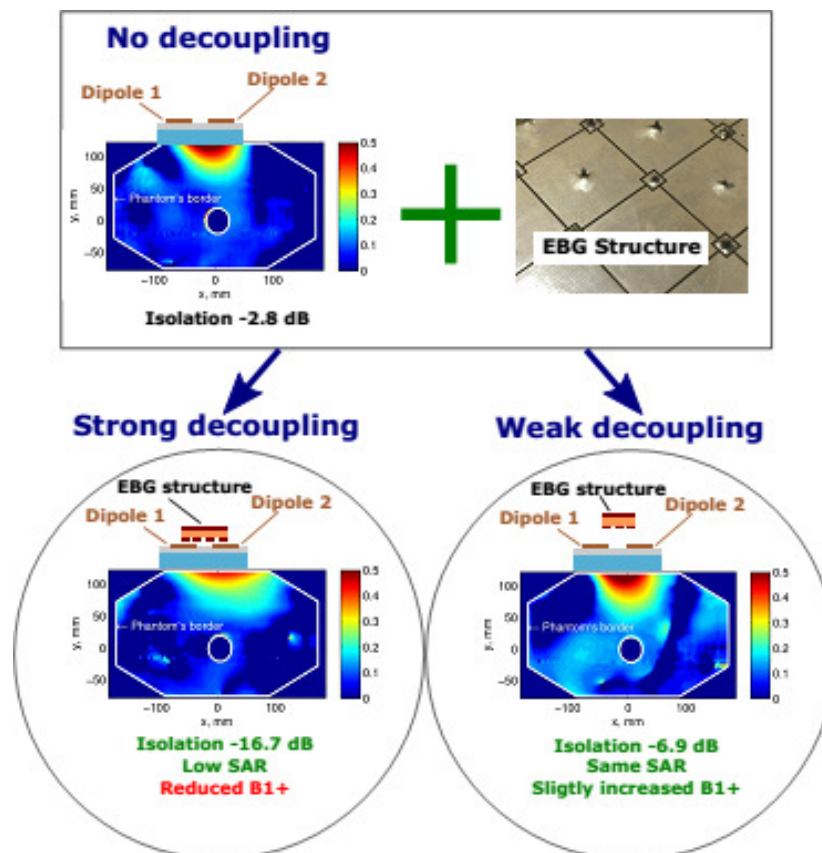


Figure 1. Schematic of the measurement setup and summary of the measured results

Acknowledgements

This work is supported by the Russian Science Foundation (Project No. 15-19-20054).

References

1. Stanislav B. Glybovski, Sergei A. Tretyakov, Pavel A. Belov, Yuri S. Kivshar, Constantin R. Simovski. Metasurfaces: From microwaves to visible – *Phys. Rep.*, **634**, 1-72 (2016).
2. P.B. Roemer, W.A. Edelstein, C.E. Hayes, S.P. Souza, O.M. Mueller. The NMR phased array - *Magn. Resonance in Medicine*, **16(2)**, 192-225 (1990).
3. A.J.E. Raaijmakers, O. Ipek, D.W.J. Klomp, C. Possanzini, P.R. Harvey, J.J.W. Lagendijk, C.A.T. van den Berg. Design of a radiative surface coil array element at 7 T: the single-side adapted dipole antenna – *Magn. Resonance in Medicine*, **66(5)**, 1488-1497 (2011).
4. D. Sievenpiper, L. Zhang., R.F. Jimenez Broas, N.G. Alexopolous, E. Yablonovitch. High-impedance electromagnetic surfaces with a forbidden frequency band – *IEEE Trans. on Microwave Theory and Techniques*, **47(11)**, 2059-2074 (1999).
5. A.A. Hurshkainen, T.A. Derzhavskaya, S.B. Glybovski, I.V. Melchakova, A.J.E. Raaijmakers, I.J. Voogt, C.A.T. van den Berg. Element decoupling of 7T dipole body arrays by EBG metasurface structures: experimental verification – *Journal of Magnetic Resonance*, **269**, 87-89 (2016).

NMR-visualization of spatial distribution of the self-diffusion coefficient in ultra-low magnetic field

S. V. Ievleva, N. V. Luzhetckaia, K. V. Tyutyukin, V. V. Frolov

Faculty of Physics, Saint Petersburg State University

Ulyanovskaya st. 1, Petrodvorets, St. Petersburg, 198504, Russia

E-mail: ievlevasvetlanka@mail.ru

Introduction

The important feature of magnetic resonance imaging (MRI) is a possibility to visualize various characteristics of investigated object. For diagnostic of internal human organs this possibility is based on the high water content in the human organism (approximately 70%), since protons in water molecules are a source of an intense nuclear magnetic resonance signal.

Contrasting of images by the certain parameter is changing of the NMR images in dependence on the sensitivity to this parameter. Contrasted images could be divided into two groups. The first one is parametric images, i.e. the images of the spatial distribution of the parameter, where the brightness is proportional to the value of the displayed parameter. And the second one is parameter-weighted images, where the brightness of the image is determined not only by the parameter of interest, but also by all other factors affecting the intensity of the NMR signal.

The most common imaging techniques are weighting on the relaxation times and diffusion weighting, which is far less widespread. In last case, the image weighting parameter is the self-diffusion coefficient. The features of water molecules diffusion can be explained with the features of biological tissues structure. For medicine the great interest is presented in those cases when DWI (Diffusion Weighted Imaging) of a normal tissue differs from DWI of pathologically changed one [1-4].

We studied the possibility of obtaining DWI in ultra-low magnetic field [5]. We conducted the experiments and obtained diffusion weighted images at magnetic field 7 mT using the laboratory homebuilt nuclear magnetic resonance imager. The results are presented in this work.

DWI technique

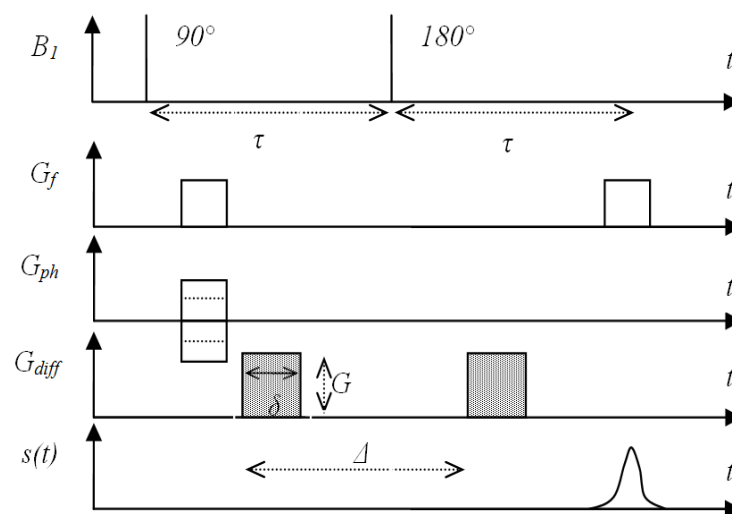


Figure 1. Pulse sequence for DWI

The method of obtaining DWI represents a combination of methods for measuring self-diffusion coefficient and methods of spatial encoding in MRI. Earlier we have used the pulse sequence based on gradient echo [5]. Nevertheless better part of clinical diffusion imaging sequences rely on spin-echo signal formation with balanced diffusion-encoding magnetic field gradients G_{diff} on each side of the refocusing radio-frequency pulse sequence (Fig. 1). The combination of radio-frequency pulses with an amplitude B_1 (90° RF-pulse and 180° RF-pulse) and magnetic field gradient pulses (G_f – frequency-encoding gradient, G_{ph} – phase-encoding gradient) allows us to obtain an 2D-image contrasted with self-diffusion coefficient after twofold Fourier transform of the echo-signal $s(t)$.

Rectangular magnetic field gradient pulses of amplitude G , duration δ , and with their leading edges separated by Δ , produce attenuation of the NMR signal k_{diff} due to self-diffusion:

$$k_{diff} = \exp[-bD],$$

where b is so-called b -factor defined as:

$$b = \gamma^2 G^2 \delta^2 (\Delta - \delta/3),$$

where γ stands for the gyromagnetic ratio, D – self-diffusion coefficient [2].

For realization of the imaging pulse sequence (Fig. 1) the special programs were created in the LabVIEW environment.

Experiments and results

In this work three combined samples were used: acetone-water (Fig. 2), agarose-oil (Fig. 3), oil-ethanol (Fig. 4). Different types of magnetic resonance images were obtained: with diffusion contrast and without.

A DWI contrast depends on differences in mobility of water molecules. Water molecules diffusivity of the research object is characterized by the signal intensity on these images.

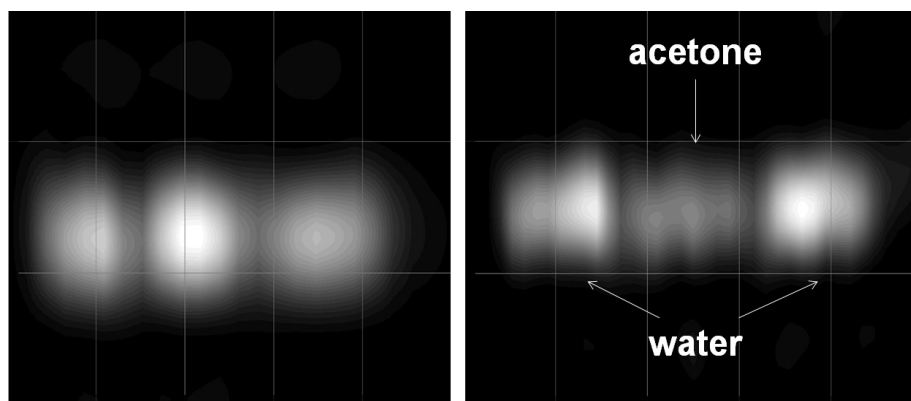


Figure 2. Sample acetone-water:
DWI (right) and standard MRI (left)

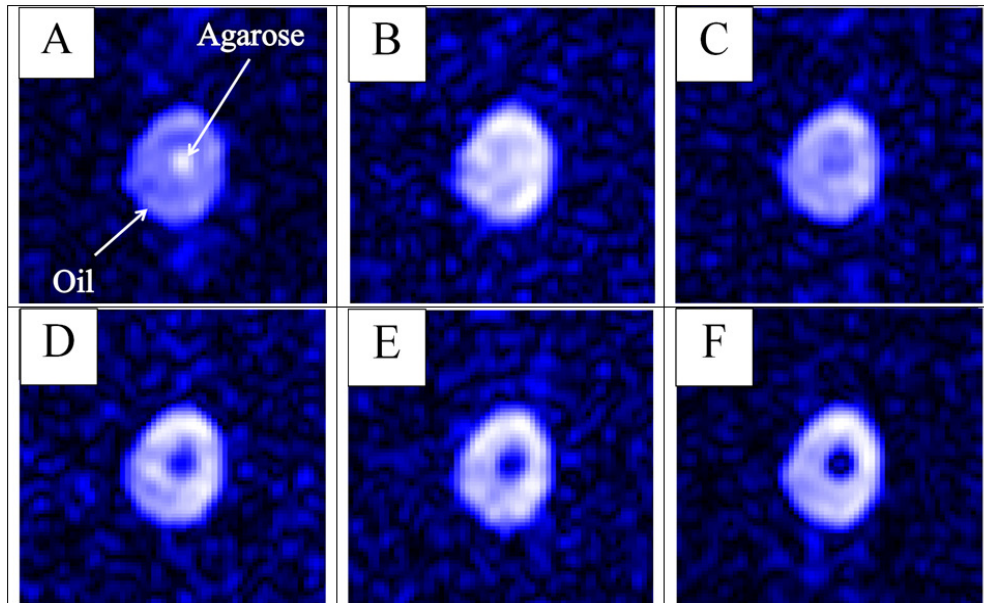


Figure 3. Sample agarose-oil: A) $b=0$ s/sm², B) $b=330$ s/sm², C) $b=750$ s/sm², D) $b=1330$ s/sm², E) $b=2080$ s/sm², F) $b=3000$ s/sm²

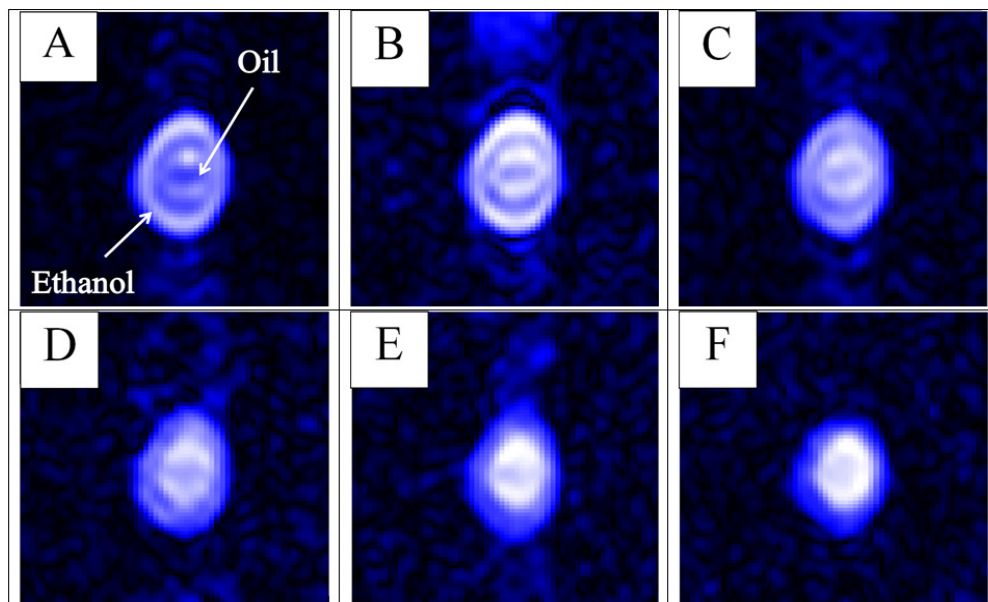


Figure 4. Sample oil-ethanol: A) $b=0$ s/sm², B) $b=330$ s/sm², C) $b=750$ s/sm², D) $b=1330$ s/sm², E) $b=2080$ s/sm², F) $b=3000$ s/sm²

References

1. V. Perrin. MRI Techniques. – Wiley, 2013. – 225 p.
2. S. E. Maier, Y. Sun, R. V. Mulkem. Diffusion Imaging of Brain Tumors // NMR Biomed, 2010. – 23(7). – pp. 849-864.
3. F. Schik, T. Nagele, D. Wildgruber, J. Trubenbach et al. Ultrafast Diffusion-Sensitive MR Imaging of Brain on an Open Scanner at 0.2 T // AJNR, 1999. – 20. – pp. 53-61.
4. C. K. Okorie, G. I. Ogbol, M. O. Owolabi, O. Ogun et al. Role of DWI in acute stroke management using low-field MRI in resource-limited settings // WAJR, 2015. – (22). – pp. 61-66.
5. С. В. Иевлева, Н. В. Лужецкая, К. В. Тютюкин, В. В. Фролов. Диффузионно-взвешенные изображения в очень слабом магнитном поле // Вестник СПбГУ, 2016. – Сер.4 Т.3(61). – с. 76-81.

Magnetic nanoparticles SPION-cmHsp70.1 for diagnosis of the orthotopic C6 glioma

Roman A. Illarionov¹, Marina A. Parr², Lyudmila Yu. Yakovleva³, Yaroslav Yu. Marchenko³, Boris P. Nikolaev³ and Maxim A. Shevtsov^{4,5}

¹*Faculty of Chemical and Biotechnology, Saint-Petersburg State Institute of Technology (Technical University), Saint-Petersburg, Russia*

²*Peter the Great St.Petersburg Polytechnic University, Saint-Petersburg, Russia*

³*Research Institute of Highly Pure Biopreparations, Saint-Petersburg, Russia*

⁴*Institute of Cytology of the Russian Academy of Sciences (RAS), Saint-Petersburg, Russia*

⁵*Klinikum rechts der Isar, Technical University of Munich, Munich, Germany*

E-mail: r.a.illarionov@gmail.com

Introduction

Glioblastoma is the most common and most aggressive primary brain cancer and is characterised by high mortality. Despite combined approach that currently includes surgical removal of the tumor with subsequent radio- and chemotherapy with temozolomide (TMZ) the survival does not exceed 15 months. Nanotechnology based on the application of magnetic nanoparticles could be an alternative approach for early detection and treatment of brain tumors. To further increase the targeting potential of particles the latter could be decorated with tumor-targeting bioligands. The stress-inducible 72-kDa heat shock protein Hsp70, which is known to be expressed on the membrane of highly aggressive tumor cells including high-grade gliomas, but not on corresponding normal cells, can be used as the tumor-specific marker for new therapeutic approaches. Superparamagnetic iron oxide nanoparticles (SPIONs) due to their high transverse relaxivity (r_2) characteristic and increased susceptibility effect (T_2^*) are used as contrast negative agents in magnetic resonance imaging (MRI). Conjugating of the SPIONs with anti-Hsp70 monoclonal antibody (cmHsp70.1) could increase the specificity of glioma targeting.

Materials and methods

Synthesis of the SPION-cmHsp70.1 nanoparticles

Superparamagnetic iron oxide nanoparticles (SPIONs) were prepared from iron salt (FeSO_4 and FeCl_3) solutions by co-precipitation in alkaline media at 80°C [1]. For preventing aggregation low molecular weight dextran (MW 10 kDa, Sigma) was added to the dispersion of magnetic nanoparticles during the process of ultrasound application. For conjugation with antibodies the dextran-coated magnetic nanoparticles were crosslinked with epichlorohydrin and aminated. Activated by water-soluble carbodiimide, dextran was coupled to the carboxyl groups of cmHsp70.1, producing a superparamagnetic conjugate SPION-cmHsp70.1. Size distribution of SPIONs and its conjugates were studied by transmission electron microscopy (TEM) (JEOL-2000 microscope, Japan) and dynamic light scattering (DLS) (Malvern). For analysis of SPION-cmHsp70.1 interaction with soluble Hsp70 the conjugates ($[\text{Fe}]=150 \mu\text{g/ml}$) were co-incubated with protein for 4 hours. Following incubation the particle size was assessed with the help of DLS method. The determination of specific ability of SPION-cmHsp70.1 to bind Hsp70 was performed by temporal measurement of T2 relaxation times (Bruker NMR-spectrometer CXP-300 7.1 T, Germany) of nanoparticles suspension according to [2]. The hydrodynamic size and electrophoretic properties were measured on Zetasizer Nano (Malvern Instruments, UK).

Magnetic resonance imaging of the intracranial glioma

For assessment of the magnetic nanoparticles accumulation in the tumor animals were randomly divided into four groups (3 animals each) on the 14th day after inoculation: (1) i.v.

injection of the phosphate-buffer solution (PBS) (control group); (2) i.v. injection of the SPIONs (2.5 mg/kg) for 24 hours; (3) i.v. injection of SPION-cmHsp70.1 conjugates (2.5 mg/kg) for 24 hours; (4) single dose irradiation (10 Gy) with i.v. injection of SPIONcmHsp70.1 conjugates (2.5 mg/kg) for 24 hours. On the 15th day after inoculation the irradiation of the tumors was performed. Following 24 hours after irradiation magnetic nanoparticles were intravenously administered. Assessment was performed using high-field 11.0 T MRI scanner (Bruker) with a custom rat coil. High-resolution anatomical T2-weighted, T1-weighted and FLASH scans in coronal planes were obtained. For estimation of the accumulation of the nanoparticles in the tumor we utilized multi-slice multi-echo (MSME) sequences. The obtained images were analyzed with software Analyze (AnalyzeDirect, Inc., Overland Park, KS).

Results

Dextran-coated superparamagnetic nanoparticles had the size of 42.7 ± 2.3 nm. Following conjugation of cmHsp70.1 antibody the size of the SPIONs increased up to 54.8 ± 1.1 nm and the Z-potential decreased from 14 mV to -14.9 mV. Significant increase in relaxation time R_2 and R_2^* indicates high MR negative contrast of SPION-cmHsp70.1. Superparamagnetic properties of the SPION-cmHsp70.1 were confirmed with method of longitudinal nonlinear sample's response to a weak ac magnetic field with measurements of second harmonic of magnetization [3]. The absence of field hysteresis evidences superparamagnetic regime of SPIONs and their conjugates.

The interaction of cmHsp70.1 conjugates with soluble Hsp70 was assessed with DLS. Following co-incubation with Hsp70 we observed a significant increase in the hydrodynamic size of the SPION-cmHsp70.1 conjugates that was not observed when control dextran-coated SPIONs or SPION-isotype IgG conjugates were applied. Co-incubation with BSA did not influence the size of the cmHsp70.1 conjugates.

In vitro NMR T2-relaxometry of SPION-cmHsp70.1 co-incubated with soluble Hsp70 demonstrated formation of conjugates that resulted in increased relaxation time. With addition of Hsp70 to SPION-cmHsp70.1 conjugates the T2 transverse time of relaxation increased from 200 ms to 325 ms in a homogenous magnetic field of 7.1 T. This growth of T2 relaxation time is caused by subsequent chain of events in aggregation and sedimentation of conjugate nanoparticles.

To prove that magnetic nanoparticles preserve their superparamagnetic characteristics in cell C6, K562 and HeLa tumor cells were incubated with SPION-cmHsp70.1, then cell suspensions in agarose gel were analyzed in a high-field (11 T) MR scanner with estimation of T2 relaxation values. The uptake of the cmHsp70.1-conjugates into the cells led to the hypertensive T2-weighted MR images that indicates nanoparticles contrast enhancing properties in cells. In C6 cells treated with unconjugated SPIONs a drop of T2 values from 67.8 ± 3.3 ms to 55.5 ± 2.9 ms was observed. Incubation with SPION-cmHsp70.1 conjugates further decreased the T2 signal to 29.8 ± 1.7 ms. After a single dose irradiation (10Gy) the T2 values of cell suspensions further dropped to 17.5 ± 2.1 ms.

MR images obtained after intravenous administration of magnetic nanoparticles (Fig. 1) showed increased accumulation of SPION-cmHsp70.1 in the tumors in comparison to unconjugated SPIONs. In control nontreated animals the T2* values constituted 45 ± 6 ms. Following infusion of SPIONs there was a drop of T2* values to 32 ± 3 ms, that were further decreased when SPION-cmHsp70.1 conjugates were applied – 21 ± 6 ms.

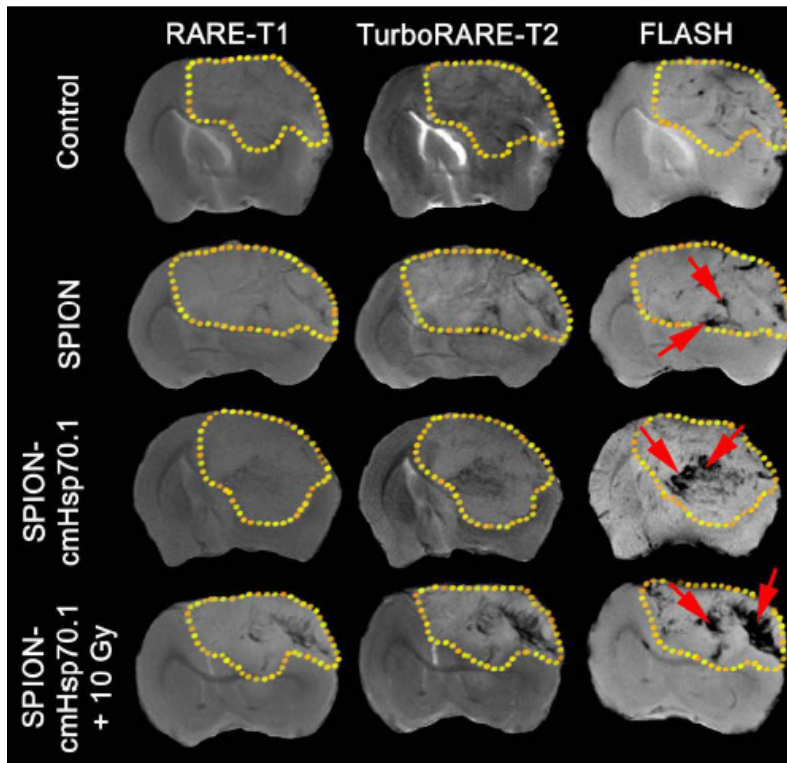


Figure 1. The high-resolution MR images of the animals following intravenous administration of the anti-Hsp70 targeting magnetic conjugates

Subsequent administration of the SPION-cmHsp70.1 conjugates in the irradiated animals (10 Gy single dose irradiation) resulted in a significant drop of T2* values to 15 ± 2 ms. We assessed whether irradiation causes the increase of Hsp70 expression in the tumor tissue and observed the elevated levels of Hsp70 in the tumor in comparison to non-irradiated animals. This overexpression was associated with increased retention of the SPION-cmHsp70.1 articles in the glioma cells.

Conclusion

Hsp70-targeting superparamagnetic nanoparticles (SPION-cmHsp70.1) were shown to specific target the glioma following administration via clinically relevant route. The retention of the particles in the tumor site resulted in the significant contrast enhancement of the glioma on the MR scans that could be applied for the diagnosis of the central nervous system malignancies.

Acknowledgements

The study was supported by the Russian Foundation for Basic Research 15-08-08148A.

Authors would like to thank Vyacheslav A. Ryzhov for analysis of the superparamagnetic state of synthesized conjugates and Olga G. Genbach for assistance in animal experiments.

References

1. R. Massart. - *IEEE Trans Magn.*, 17, 1247–1248 (1981).
2. C. Tassa, S.Y. Shaw, and R. Weissleder. - *Accounts of chemical research.*, 44, 842–852 (2011).
3. M.A. Shevtsov, B.P. Nikolaev, V.A. Ryzhov, L.Y. Yakovleva, A.V. Dobrodumov, Y.Y. Marchenko, B. Margulis, E. Pitkin, and I.V. Guzhova. - *JMMM.*, 388, 123–134(2015).

Research of ionic liquid in mixture of glycerol and water by algorithm for detecting clusters

Aleksey A. Kazarinov, Andrei V. Komolkin

Faculty of Physics, Saint-Petersburg University, Russia

E-mail: aleksey.kaz@mail.ru

Ionic liquids, which actually are salts with low melting temperatures (lower than 100 degrees Celsius), are interesting as the new substance class, which is not completely researched. One of their properties is formation of aggregates in aqueous solution, when the concentration of ionic liquids exceeds critical micelle concentration (CMC) [1].

At the present work are researched two types of ionic liquids solutions. First one contains water, and second one has a "water + glycerol" mixture as a solvent. Both systems have been calculated by molecular dynamics during a time interval. Octyl-methyl imidazolium chloride is a molecule of ionic liquid used in this computer experiment. The program, based on pre-developed algorithm [2], which can find clusters in micellar system, was used for analysis of the systems. According to theoretical statements [3], aggregates could not be formed in the second system. However, in the first system aggregates can be formed, because concentration of $[C_8mim^+][Cl^-]$ exceeds CMC 4 times, that allows to compare results of processing via the program for both systems and confirm these statements. Special for that purpose, algorithm has been modified.

The program has such possibilities as finding distribution of aggregate size, proportion of ions in clusters, an estimate of residence time with corresponding plot. In figures below are presented results of calculations by the program. Figure 1 corresponds to the second system. Obviously, recognized aggregates with $N_{agg} \leq 6$ prevail, and there are not significant sizes for 10 ns interval of registrations.

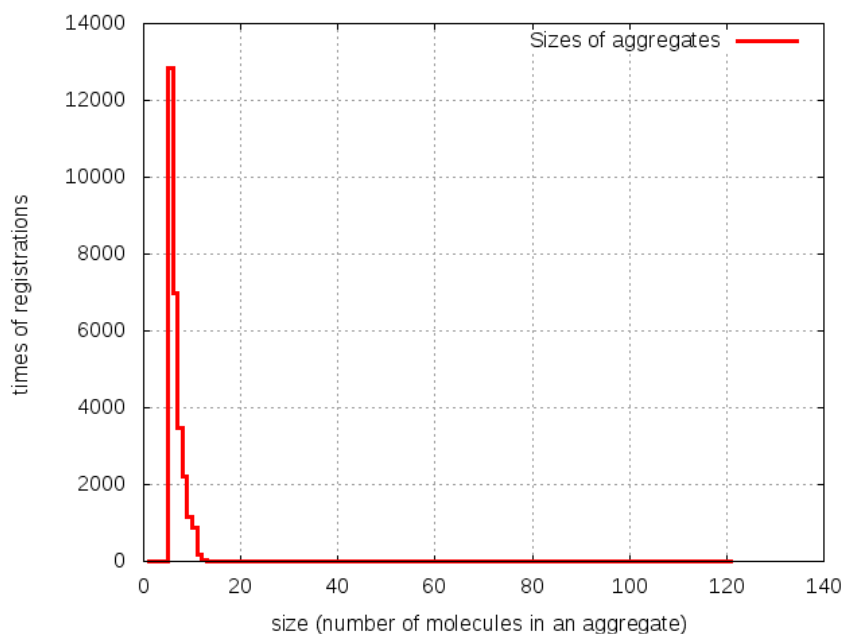


Figure 1. Distribution of aggregation number (size) for second system

Same calculations have been performed for the first system. The corresponding results are shown in Figure 2. This micellar system contains three aggregates, which have varying sizes for investigated interval (10 ns). Sizes of aggregates are similar to earlier findings [4, 5].

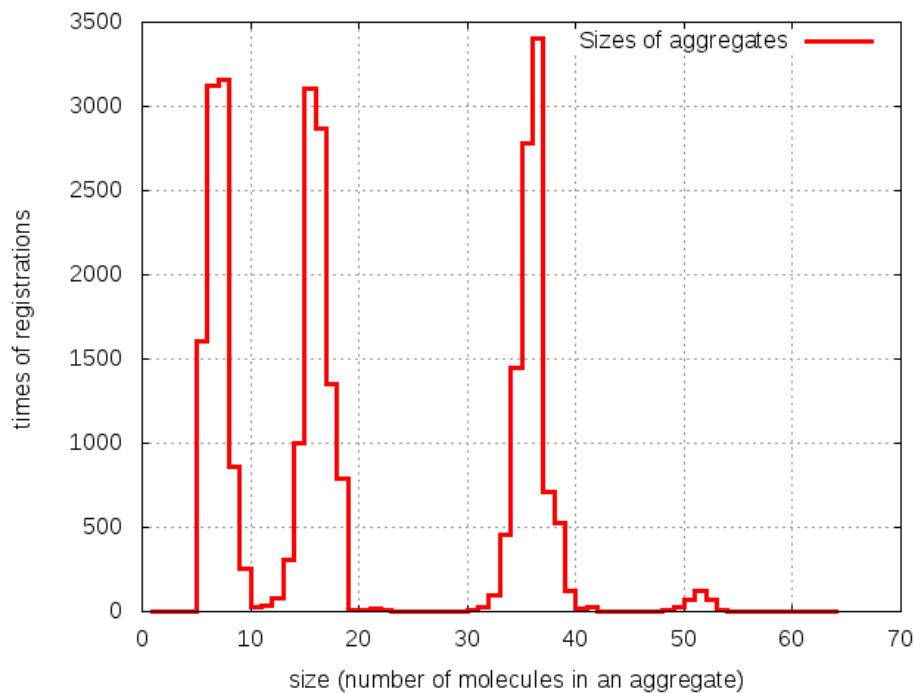


Figure 2. Distribution of aggregation number (size) for first system

Also proportion of molecules in aggregates and residence time of both systems have been compared, that is presented in Figures 3 and 4. It can be noticed, that addition of glycerol into system “ionic liquid - water” decreases percentage of molecules formed aggregates.

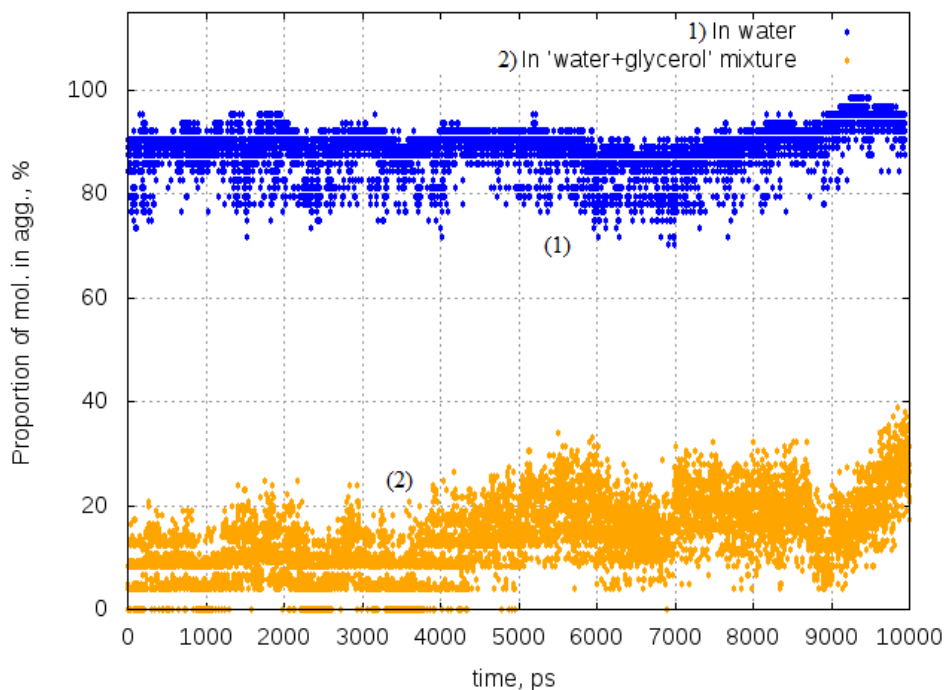


Figure 3. Comparison of aggregate molecules proportion of both systems

In Figure 4 are presented results of residence time estimating. As seen, in water solution of ionic liquid the number of registered cases of residence higher than the similar

number for other system, containing mixture of glycerol and water. Parameters of approximation are collected in the Table 1.

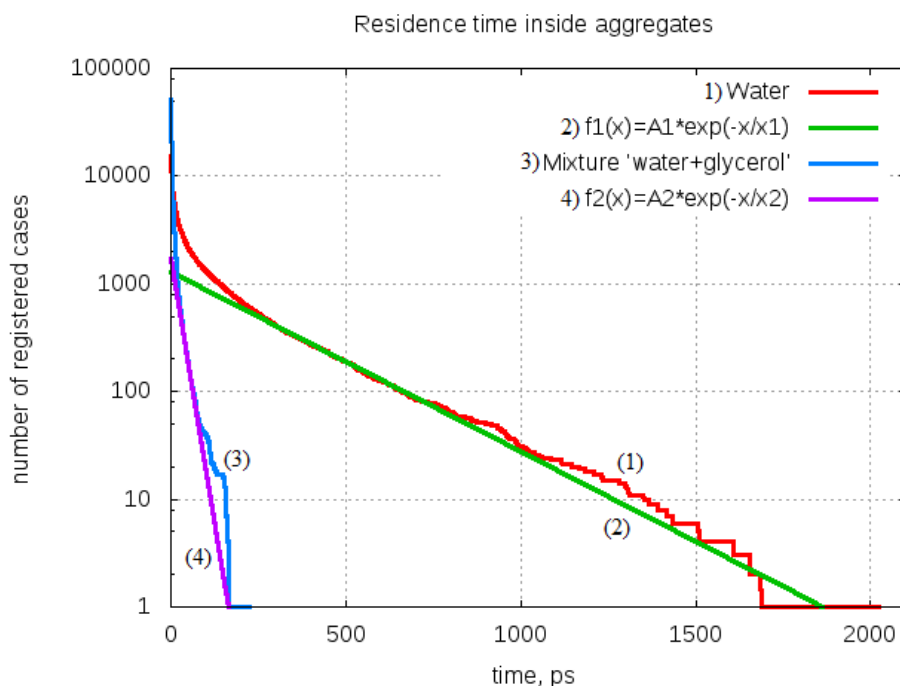


Figure 4. The estimate of residence time

Table 1. Parameters of approximation

Parameter	Value	Time interval, ps
A1	(1298.48±4.84) times	[260;1000]
x1	(260.08±0.62) ps	
A2	(1799.54±47.08) times	[30;100]
x2	(22.0±0.3) ps	

Acknowledgements

The calculations were performed by equipment of “Research Park SPbSU” resource center.

References

1. Мицеллообразование // Химическая энциклопедия. Т. 2. — М.: Большая Российская энциклопедия, 1992. С. 95–96.
2. Казаринов, А. А. Разработка алгоритма выделения кластеров в молекулярной системе «ионная жидкость – вода» / А. А. Казаринов, А. В. Комолкин // Материалы конференции : тез. конф., 12-я Зимняя молодёжная школа-конф. «Spinus» - Санкт-Петербургский гос. университет. – С.-Петербург, 2015. – С. 174-177.
3. Лиофильность и лиофобность // Химическая энциклопедия. Т. 2. — М.: Большая Российская энциклопедия, 1990. С. 595–596.
4. Jianji Wang*, Huiyong Wang, Sheli Zhang, Hucheng Zhang, and Yang Zhao // J. Phys. Chem. B, 111, p. 6181-6188 (2007).
5. B. L. Bhargava* and Michael L. Klein // J. Phys. Chem. B, 113, p. 9499-9505 (2009).

EPR study of $[\text{Co}^{2+} - \text{F}_{\text{int}}^-]$ associative defects formed in the $\text{BaF}_2:\text{Co}$ crystals: reasons of their stability

Aydar I. Khamzin, Radik R. Zaynullin

Kazan State Power Engineering University, Kazan, 420066, Russia

Zavoisky Physical-Technical Institute, Kazan, 420029, Russia

E-mail: aydarham@gmail.com

Introduction

Fluorite type crystals (CdF_2 , CaF_2 , SrF_2 , BaF_2) are well known ionic compounds which are used as materials for various applications. For these purposes the fluorites must be activated by various impurities. If the impurity metal belongs to transition metal group one gets a cubic paramagnetic center. Physical properties of such center depends significantly on what energetic level occurs as ground one. In a free states the impurity d -ions have the following ground orbital terms: 2D , 3F , 4F , and 6S [1]. The S -terms are orbital singlets but D - and F -terms correspond to degenerated orbital states. In the fluorite type crystals the cubic crystal field produces a splitting of D - or F -term. First gives orbital doublet and orbital triplet and second the orbital singlet and two triplets. When the ground state of an impurity d -ion is orbital doublet or triplet, the Jahn-Teller effect realizes driving to a distortion of coordination cube of the d -ion.

It was found that the activation of fluorites by d -ions needs in special condition for crystal growing process: the inert atmosphere must contain fluorine gas. In such cases the defects of interstitial fluorine ions will be formed in the crystal. If an impurity d -ion brings into ionic crystal lattice an excess of positive charge, the interstitial anion can play the role of charge compensating defect. Obviously, an association of the charge compensating interstitial anion with such impurity d -ion is energetic profitable. It leads to formation of the stable associative defects in the body of activated crystal. It was surprising, but such stable associative $[\text{Co}^{2+} - \text{F}_{\text{int}}^-](\text{C}_{4v})$ defects were observed in the BaF_2 crystals activated by cobalt impurities [2]. The present work was devoted to clarify the reasons of thermal stability of these defects. As physical properties of single Co^{2+} impurity defects are of interest too in such analysis, the latest defects (which were not studied in [2]) were considered as well.

Paramagnetic centers formed in $\text{BaF}_2:\text{Co}$ during activation process

The crystalline $\text{BaF}_2:\text{Co}$ samples were grown by Bridgman method in the helium atmosphere containing fluorine gas (2%). Three type paramagnetic centres were observed in the samples by EPR method (let's denote them as I, II and III).

The EPR spectrum of I centres (Fig. 1) demonstrate hyperfine (HFS) and superhyperfine (SHFS) structures and corresponds to the $[\text{CoF}_8]^{6-}(\text{O}_h)$ impurity paramagnetic complexes with $S = 1/2$. Spin-Hamiltonian describing the angular dependencies in the EPR spectra of these complexes is:

$$\hat{H}_s = g\beta_e \vec{H} \cdot \hat{S} + f\beta_e \{ (S_x^3 H_x + S_y^3 H_y + S_z^3 H_z) - (1/5)(\hat{S} \cdot \vec{H})[3S(S+1) - 1] \} + \hat{H}_{HFI} + \hat{H}_{SHFI}, \quad (1)$$

where H_{HFI} and H_{SHFI} are the terms describing hyperfine and superhyperfine structures of the spectra observed in the EPR experiments. The values of the Zeeman interaction parameters were evaluated ($g = 2.325$; $f = -0.011$).

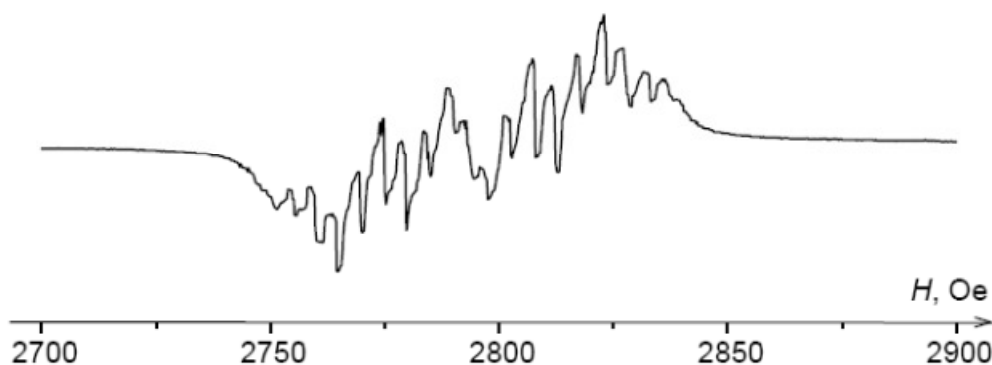


Figure 1. EPR spectrum of a $\text{BaF}_2:\text{Co}$ sample containing the $[\text{CoF}_8]^{6-}(\text{O}_h)$ impurity complexes ($f_{\text{EPR}} = 9.3 \text{ GHz}$; $T = 4.2 \text{ K}$; $H \parallel \langle 111 \rangle$)

The EPR spectrum of II centres (see in [2]) contained more information about their magnetic properties and molecular structures. It was found that the concentration of the associative $[\text{CoF}_4\text{F}_{\text{int}}]^{7-}(\text{C}_{4v})$ complexes is high (relative to cubic Co^{2+} centers). As the superhyperfine structure of EPR spectra arising due to magnetic moment of the nucleus of interstitial fluorine ion was observed in the EPR spectra, the positions of the interstitial ion and Co^{2+} ion were determined from analysis of the EPR parameters of the centers under discussion. To find the reasons for lowering of the energy of the pair defect “ $\text{Co}^{2+}-\text{F}_{\text{int}}^-$ ”, the calculations of a shape of the ground adiabatic potential sheet of Co^{2+} substituting a basic Ba^{2+} ion were performed (results see in Fig. 2).

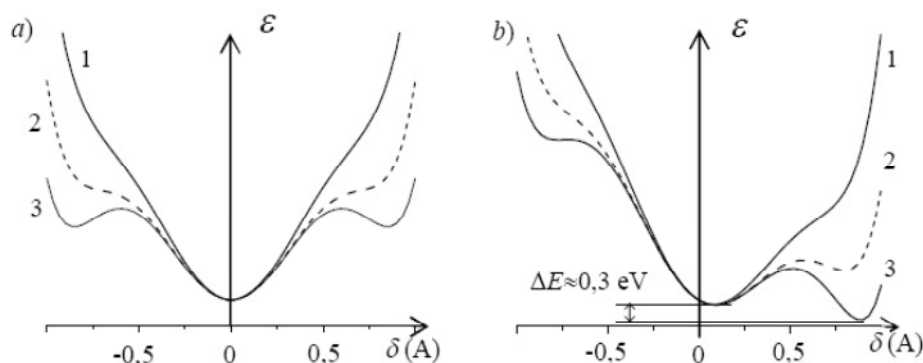


Figure 2. The shapes of the ground adiabatic potential sheet of Co^{2+} substituting a basic Ba^{2+} ion: (a) there is no interstitial ion in vicinity of the Co^{2+} ; (b) in the centre of body of a nearest (to Co^{2+} ion) “octahedral hole” of crystal lattice is localized an interstitial fluorine ion

These calculations using Born-Maier approximation showed that the interstitial fluorine ion can lead to a lowering of energy of the $[\text{CoF}_4\text{F}_{\text{int}}]^{7-}(\text{C}_{4v})$ complexes when Co^{2+} ion demonstrated a pseudo-Jahn-Teller properties.

References

1. A. Abragam, B. Bleaney. Electron Paramagnetic Resonance of Transition Ions. Clarendon Press, Oxford, 1970.
2. M.M. Zaripov, V.A. Ulanov, E.P. Zheglov. – *Sov. Phys. Solid State*, 36, 411-417 (1994)

Heteroatomic ^1H - ^{13}C HSQC and HMBC correlations are given in the Table 1. Analysis of these data allowed performing complete assignment of signals of the NMR ^1H and ^{13}C spectra of spiran **3** (Fig. 1 (B)).

Table 1. Coordinates of cross-peaks in the HMBC and HSQC spectra of compound **3**

^1H , δ , ppm	HMBC, ^{13}C , δ , ppm	HSQC, ^{13}C , δ , ppm
7.77	129.9, 137.2, 163.6	129.5
7.51	191.4, 126.5	129.8
7.51	142.9, 127.5	128.2
7.51	129.8, 134.8, 137.2 сЛ.	126.5
7.47	129.5, 137.2	129.9
7.42	163.6 сЛ., 142.9 сЛ., 137.3, 134.8, 127.7,	129.1
7.41	137.2, 142.9, 128.2, 126.5 сЛ.	127.5
7.38	129.1, 137.3	127.7
7.23	140.7 сЛ., 139.5, 126.9, 47.7	121.5
7.06	121.5, 139.5	126.9
7.06	140.7, 111.3, 47.7 сЛ.	123.4
6.99	140.7, 123.4	111.4
6.96	–	140.1
6.66	–	133.4

Confirmation of the spiran structure using the ^1H - ^{15}N HMBC method

In the ^1H - ^{15}N HMBC correlation spectrum of compound **3**, obtained at 0°C , cross-peaks of *o*-quinone proton are observed at 6.96 ppm with the signals of both pyrrole - at 134.4 ppm, and pyridine nitrogen atom at 276.6 ppm (Fig. 2), which confirms the spiran molecule structure. A cross-peak of proton at 7.06 ppm with pyrrole nitrogen atom is also present.

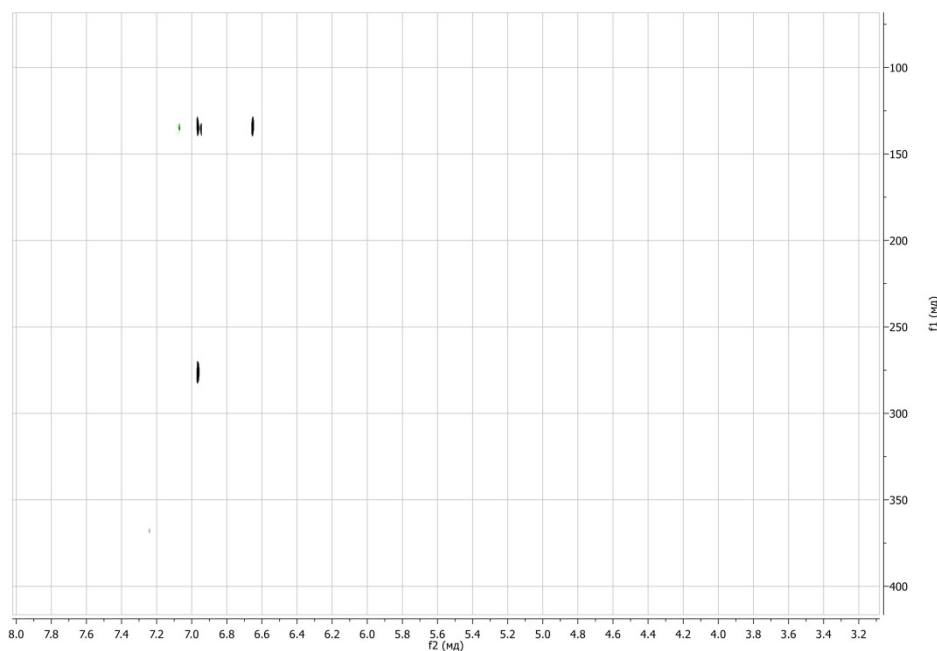


Figure 2. Fragment of the ^1H - ^{15}N HMBC spectrum of compound **3** (0°C)

Dynamic processes in the NMR spectra of spiran **3**

In the ^1H NMR spectrum of compound **3** in the CDCl_3 solvent at room temperature an anomalous broadening of signals of protons of quinone cycle δ_{H} 6.66 and 6.96 ppm, of *tert*-butyl groups at δ_{H} 1.06 and 1.36 ppm, and methyl groups of the indoline fragment at δ_{H} 1.59 and 1.98 ppm is observed. At temperature increase to 57°C the abovementioned signal pairs coalescent (Fig. 3).

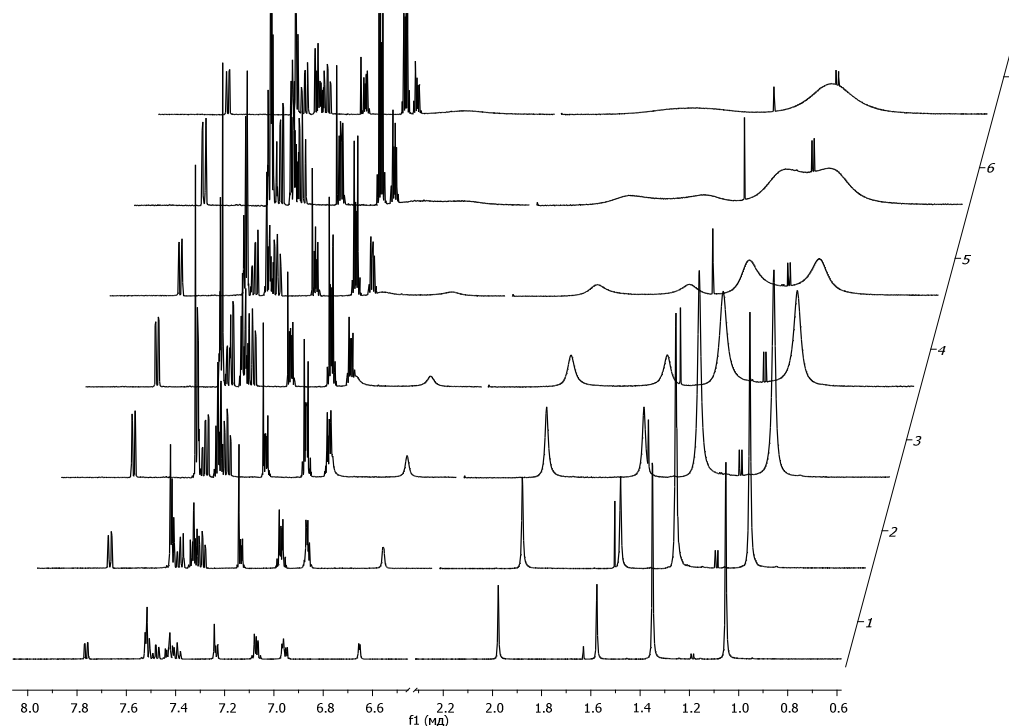


Figure 3. Coalescence of signals at increasing temperature in the NMR ^1H spectrum of compound **3** [from 0°C (1) to 60°C (7) with 10°C step]

The dynamics is observed only for paired groups, whose magnetic nonequivalence is due to their spatial position with respect to the noncoplanar molecular structure, i.e., the absence of symmetry plane of the molecule leads to divergence of the signals of protons of the quinone cycle, *tert*-butyl groups, and methyls of the pyrrole cycle. Thus, the most probable reason for the coalescence of NMR spectra signals is the inversion of the molecule by inversion of the pyramidal pyrrole nitrogen.

Acknowledgements

The work was performed with Presidium of the Russian Academy of Sciences within the framework of Program No. 8 "The development of methods for the preparation of chemical compounds and the creation of new materials", Russian Foundation for Basic Research (grant 14-03-00672), the Grants NSh-8201.2016.3 and the Internal SFedU grant № 213.01-2014/005.

References

1. Yu.A. Sayapin, E. A. Gusakov, Bang Nghia Duong, I. O. Tupaeva, V. N. Komissarov, I. V. Dorogan, V. V. Tkachev, S. M. Aldoshin, V. I. Minkin. – *Russian Chemical Bulletin*, **2**, 480-491 (2013).

Structural studies of the antimicrobial peptide protegrin-5 in membrane mimicking environment by high-resolution NMR spectroscopy

O. A. Kolosova, K. S. Usachev, V. V. Klochkov

Institute of Physics, Kazan Federal University

E-mail: kolosova.olga11@gmail.com

Introduction

Antimicrobial peptides (AMPs) are small peptides with a strong antibiotic activity which play an important role in the immune system of many different animals. Naturally occurring AMPs probably represent one of the very first evolved forms of chemical defense of living eukaryotic cells against invasion by bacteria, protozoa, fungi, and virus. AMPs are less susceptible to the development of bacterial resistance because they disrupt the membrane of bacteria through nonspecific peptide–lipid interactions. Natural AMPs have such properties as the broad-spectrum antibacterial activity, high selectivity, and the disruption of bacterial cell membranes, which allow to suggest that these molecules are potentially useful as antibiotics. So, it is important to investigate their structure and function at high resolution in order to increase their potency and selectivity.

There are five known naturally occurring porcine protegrins: PG-1 (RGGRL⁵CYCRR¹⁰RFCVC¹⁵VGR¹⁸), PG-2 (RGGRL⁵CYCRR¹⁰RFCIC¹⁵V¹⁶), PG-3 (RGGGL⁵CYCRR¹⁰RFCVC¹⁵VGR¹⁸), PG-4 (RGGRL⁵CYCRG¹⁰WICFC¹⁵VGR¹⁸), and PG-5 (RGGRL⁵CYCRP¹⁰RFCVC¹⁵VGR¹⁸), with a high content of cysteine (Cys) and several positively charged arginine (Arg) residues. In this study we represent PG-5 (Fig. 1).



Figure 1. Amino acid sequence of PG5

Materials and method

The protegrin peptides were synthesized by solid-phase peptide synthesis by Dr. Andrey Filippov in the Chemistry of Interfaces Laboratory at the Luleå University of Technology.

The NMR investigation was done on a Bruker Avance 700 spectrometer equipped with a cryoprobe. The peptide (4 mg) was solubilized in an aqueous solution (H₂O or ²H₂O, 500 μl) containing 20 mg perdeuterated dodecylphosphocholine (DPC) (molar ratio ~1:12). 3-(Trimethylsilyl)-propionic-2,2,3,3-²H₄ acid (TMSP-2,2,3,3-²H₄) (98 % atom ²H, Aldrich) was added as an internal chemical shift standard for ¹H NMR spectroscopy. Perdeuterated d₃₈ DPC (98 % ²H) and TSP-d₄ were purchased from Aldrich. Chemical shift assignments of PG-5 in DPC micelles were obtained using standard methods of protein NMR spectroscopy by 2D NMR 1H–1H TOCSY and NOESY (Nuclear Overhauser Effect Spectroscopy) experiments. Interproton NOE distance constraints determined from NOESY experiments were used for the structural calculations by molecular dynamic method calculations of the Xplor-NIH program.

Results

In this study, a 2D NMR ^1H - ^1H COSY, ^1H - ^1H TOCSY and ^1H - ^1H NOESY methods of protein NMR spectroscopy approaches was used for sequential assignment of the backbone and sidechain resonances for antimicrobial peptide protegrin-5 in the presence of DPC micelles (detergent/protein ratio of ~1:12) as a membrane mimicking environment (Table 1). Final chemical shifts values were deposited in the BioMagResBank database (<http://www.bmrb.wisc.edu>) under accession number 26009.

Table 1. ^1H chemical shifts in ppm measured in water for PG-5 in the presence of perdeuterated DPC micelles(detergent/peptide molar ratio ~1:12) at 293 K.

Residue	NH	C_αH	C_βH	C_γH	C_δH	$\text{C}_\epsilon\text{H}$
R1	–	3.97	1.83	1.58	3.10	7.38
G2	8.98	3.89				
G3	8.46	3.89				
R4	8.65	4.20	1.71	1.53	3.04	7.52
L5	8.54	4.21	1.62	1.51	0.83, 0.77	
C6	8.01	4.28	2.73			
Y7	8.07	4.43	2.97, 2.82		7.05	6.74
C8	7.88	4.35	2.74			
R9	8.40	4.25	1.75, 1.64	1.52	3.03	7.53
P10	–	4.28	1.93	1.64	3.77, 3.46	
R11	8.20	4.07	1.67, 1.53	1.47	3.00	7.42
F12	8.00	4.45	3.06, 3.00		7.22	7.15
C13	8.20	4.28	2.78			
V14	7.91	4.02	2.05	0.85		
C15	8.29	4.35	2.80			
V16	7.95	4.09	2.05	0.79		
G17	8.33	3.87				
R18	8.02	4.17	1.79	1.60, 1.50	3.05	7.42

A total of 164 distance constraints derived from NOE experiment recorded in H_2O and D_2O were used for structure calculations by molecular dynamics method in the Xplor-NIH program. A total of 1000 structures were calculated and 20 with minimal energy were chosen. None of the 20 structures had any violated NOE distances. The final NMR ensemble of 20 structures has been deposited in the Protein Data Bank with the code 2NC7. Superimposed conformations of the minimized structures for the PG-5 in a solution of H_2O + D_2O with DPC micelles are shown in Fig. 2. The overall quality of the structures was assessed by the program MolProbity. The Ramachandran analysis of the best 20 structures showed that all ϕ and ψ angles were localized to allowed (100 %) and favored (72.8 %) areas of the Ramachandran plot. The mean value of the overall backbone root-mean-squared deviation (RMSD) for backbone was 0.53 ± 0.21 Å and for heavy atoms 1.34 ± 0.27 Å.

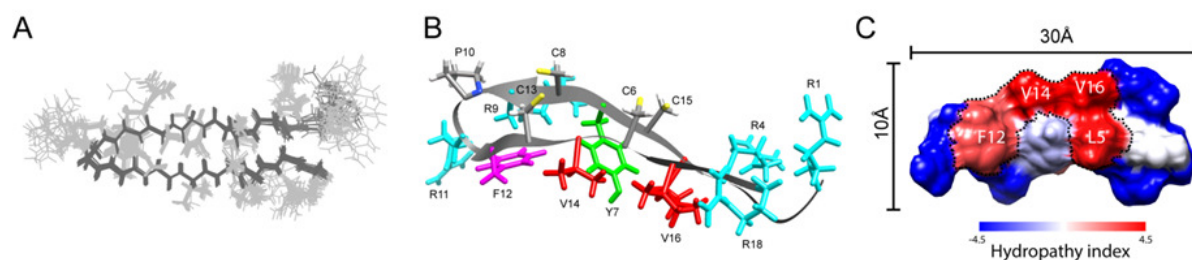


Figure 2. Spatial structure of protegrin-5. **A** Overlay of the ensemble of 20 final energy-minimized XPLOR structures in stereo (PDB ID: 2NC7). The main and side chains are shown in black and light gray, respectively. **B** Ribbon diagrams of the lowest energy structure. Aliphatic amino acid residues are marked in red (Leu and Val), polar residue (Tyr) are marked in green, phenylalanine residue is marked in magenta and positively charged residues (Arg) are marked in cyan. **C** Kyte–Doolittle hydrophobicity surface structural model for PG-5: from blue for the most hydrophilic, to white, to red for the most hydrophobic (50). An apolar cluster (Leu5, Phe12, Val14 and Val16) marked by dotted line

Protegrin dimerization in the presence of DPC micelles was observed for PG-1 and PG-3[1] from 2D ^1H – ^1H NOESY spectra, where there were observed several additional NOEs between side chains, which appear inconsistent with the β -sheet structure, and it was assumed that these NOEs appear due to formation of an additional antiparallel β -sheet between two monomers. We also observed such “inconsistent” NOEs for PG-5, which are an indication that PG-5 adopts an antiparallel dimer [2]. Several experimental and computational studies shown by potentials of mean force (PMF) calculations and atomic force microscopy that protegrins could associate and insert into an anionic membrane forming an octameric or decameric β -barrels. According to PMF data, octamers were more stable and exhibit a favorable binding energy to the pore so we used this model for our further calculations of pore structure for PG-5 based on the observed intermonomer NOEs (the final structure in Fig. 3).

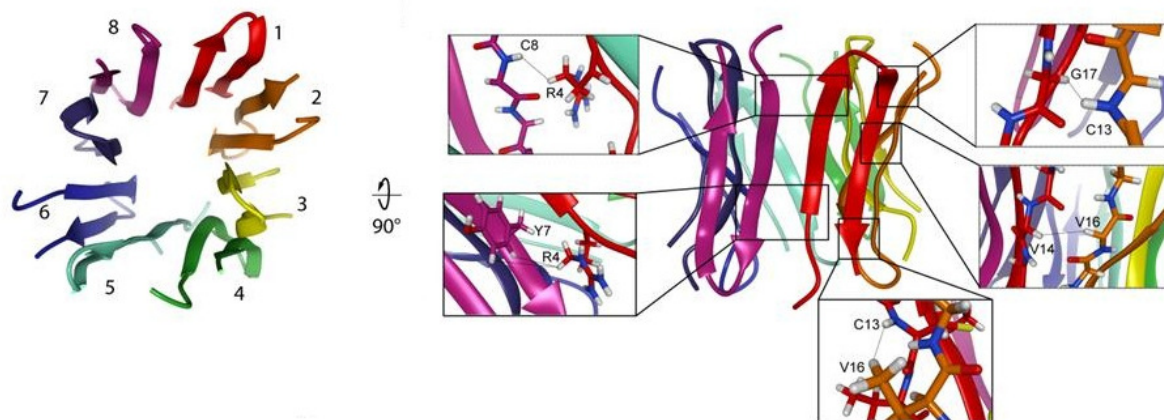


Figure 3. Structure of the transmembrane pore of protegrin-5

References

1. Usachev K.S., Efimov S.V., Kolosova O.A., Klochkova E.A., Aganov A.V., Klochkov V.V. (2015) Antimicrobial peptide protegrin-3 adopt an antiparallel dimer in the presence of DPC micelles: a high-resolution NMR study. *J. Biomol NMR* 62:71–79S.
2. Usachev K.S., Efimov S.V., Kolosova O.A., Klochkova E.A., Yulmetov A.R., Aganov A.V., Klochkov V.V. (2016) Oligomerization of the antimicrobial peptide Protegrin-5 in a membrane-mimicking environment. Structural studies by high-resolution NMR spectroscopy. *Eur Biophys J.* DOI 10.1007/s00249-016-1167-5

Investigation of magnetically doped topological insulators and 2D Rashba system by EPR

*A. V. Koroleva¹, A. M. Shikin¹, A. A. Rybkina¹, I. I. Klimovskikh¹, O. E. Tereshchenko^{1,2,3},
A. S. Bogomyakov⁴, K. A. Kokh^{1,2,5}*

¹*Saint Petersburg State University, Saint Petersburg, 198504, Russia*

²*Novosibirsk State University, Novosibirsk, 630090 Russia*

³*A.V. Rzhhanov Institute of Semiconductor Physics, Novosibirsk, 630090 Russia*

⁴*International Tomography center, SB RAS, Novosibirsk, Institutskaya, 3a, 630090, Russia*

⁵*V.S. Sobolev Institute of geology and minerology SB RAS, Novosibirsk, 630090, Russia*

E-mail: dalika@inbox.ru

Introduction

There is currently actively investigated new class of materials - topological insulators. Particular interest is the possibility of using these structures in spintronics. The possibility of such application is conditioned by the unique properties of topological insulators: the surface states of a three-dimensional topological insulator are characterized by the Dirac cone structure, where the spin of the electron is locked perpendicular to momentum. The same properties are observed in other materials - 2D Rashba system, where the anomalously large spin-orbit splitting of the surface states is observed. Doping with magnetic impurity can not only change the concentration of charge carriers in the volume, but also the magnetic properties change, which may lead to the opening of an energy gap in the spectrum of the surface states [1]. In this kind of material predicted by monitoring a number of interesting phenomena: the quantum anomalous and zero-plateau quantum anomalous Hall (QAH) effect [2, 3]. Magnetic properties of the investigated systems depends on the bulk properties, including the crystallographic structure. EPR is a powerful method for studying the crystal structure of impurity centers in the matrix crystals [4, 5].

Experimental procedure

For the study we selected samples of the topological insulator Sb_2Te_3 and Rashba system BiTeI doped with different iron concentration. The samples were grown by modified Bridgman method. The EPR study was conducted in the St. Petersburg State University Research Park in the laboratory of EPR on a Bruker ELEXSYS-580 spectrometer with using nitrogen cooling

The first results and discussion

To determine the optimal conditions several samples Sb_2Te_3 and BiTeI , doped with Fe, Mn, Cr and V were studied. As a result of studies several features of samples complicating interpretation of the results were found. Since the samples belong to the class of layered single crystals, they are prone to delamination, it lead to a strong asymmetry of the resonance lines and complicates the deciphering of the EPR spectra. It is necessary to improve the method of sample preparation.

The best results were obtained with samples $\text{BiTeI:Fe}(0.5\%)$ (Fig.1). The fine structure is not permitted because of the strong exchange interaction. Permissions of fine structure can be achieved by decreasing the concentration of the magnetic impurity. Type of the line indicates that the Fe-ion is in place of crystal lattice which characterized by the lowest symmetry (triclinic, monoclinic or rhombic symmetry).

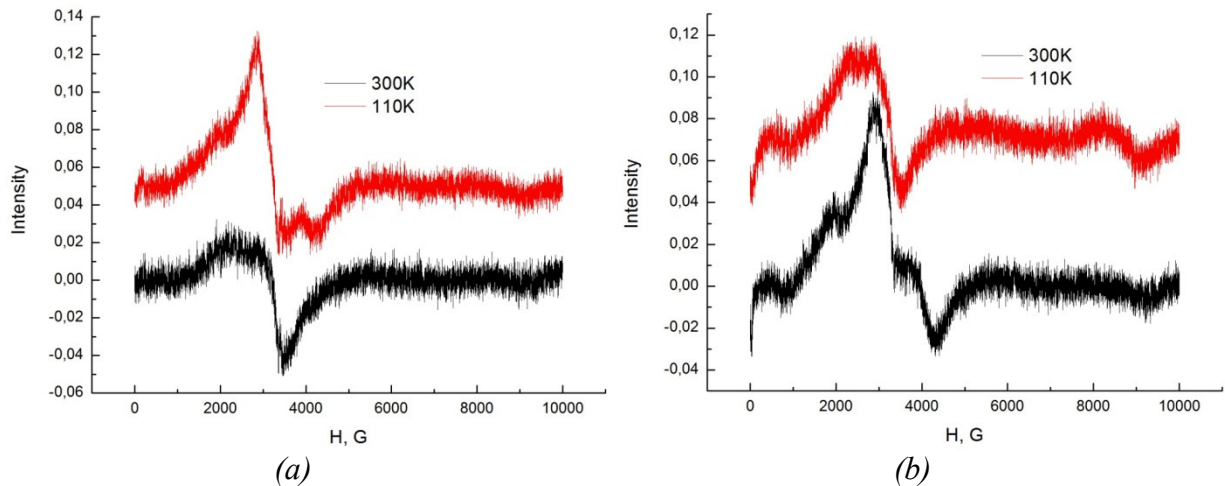


Figure 1. The EPR spectrum of the sample $\text{BiTeI:Fe}(0.05\%)$ (a) – obtained when an external magnetic field parallel to the axis of symmetry C_3 (perpendicular to the plane of the sample), (b) – obtained when an external magnetic field perpendicular to the axis of symmetry C_3 (parallel to the plane of the sample)

Crystal structure and symmetry group is shown in Figure 2. It is known from literature that the single crystals BiTeI have complete symmetry group 156 ($P3m1$) [6]. This group contains a total of 5 non-equivalent positions (Tab.1). Items $3m$ symmetry occupied by the atoms of the main substance [7], two other items are described by groups m and 1 , they belong to the lowest symmetry. If we assume that the impurity ions occupy these positions, the EPR line will be just such a kind which we found experimentally. This hypothesis needs further investigation and confirmation. It is worth noting that topological insulator Bi_2Te_3 has a similar structure, but as shown in [8] the iron ions would replace Bi rather than embedded in the interstices.

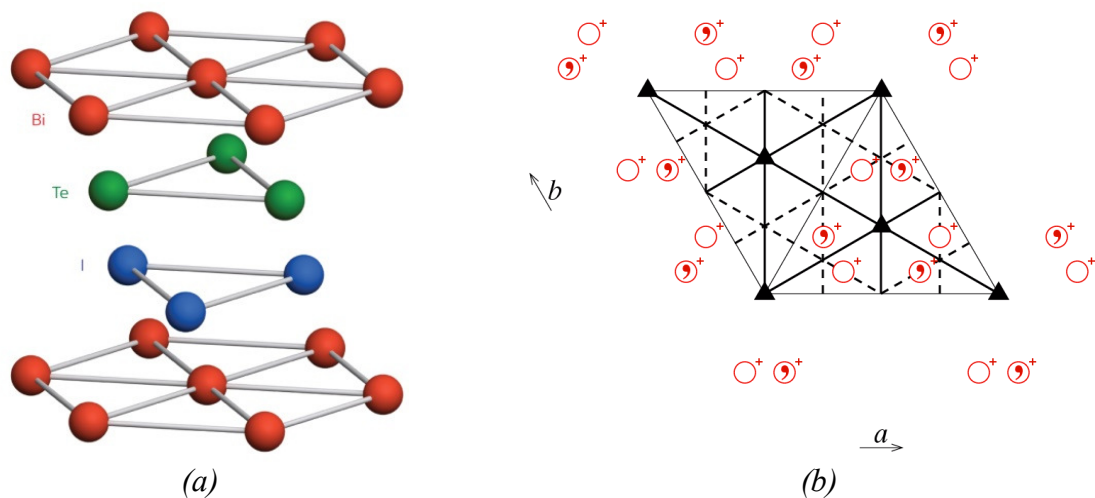


Figure 2. The crystal structure of the bismuth tellurium iodide (BiTeI) is made up of stacked layers of bismuth, tellurium and iodine atoms (a), the complete symmetry group of BiTeI - $P3m1$ (b)

Conclusion

We plan to investigate the topological insulator Sb_2Te_3 , and Rashba systems BiTeI doped with magnetic impurities (Fe, Mn, V, Cr) with different concentrations. The first study of our samples have revealed several difficulties. It is necessary to improve the method of sample preparation, choose the optimum concentration of the magnetic impurity to reduce the

influence of the exchange interaction. On the one hand it is possible to observe the fine structure of the EPR lines, on the other hand the concentration should be sufficient to observe effects related to the breaking of time-reversal symmetry. Preliminary results give information about position of the impurity ion in the lattice of BiTeI, which should be checked by other methods. The location of the ion in the lattice can have a significant impact on the electronic structure and magnetic properties of the crystal.

Table 1. Wyckoff Positions of Group 156 ($P3m1$)

Multiplicity	Wyckoff letter	Site symmetry
6	e	1
3	d	m
1	c	3m
1	b	3m
1	a	3m

References

1. J. G. Checkelsky, J. Ye, Y. Onose, Y. Iwasa, and Y. Tokura, *Nat Phys* 8, 729 (2012),
2. R. Yu, W. Zhang, H.-J. Zhang, S.-C. Zhang, X. Dai, and Z. Fang, *Science* 329, 61 (2010),
3. C.-Z. Chang, W. Zhao, D. Y. Kim, H. Zhang, B. A. Assaf, D. Heiman, S.-C. Zhang, C. Liu, M. H. W. Chan, and J. S. Moodera, *Nat Mater* 14, 473 (2015),
4. A. Wolos, A. Drabinska, M. Kaminska, A. Hruban, S.G. Strzelecka, A. Materna, M. Piersa, M. Romaniec, R. Diduszko, *Journal of Magnetism and Magnetic Materials*, 419 (2016)
5. T. M. Garitezi, G. G. Lesseux, C. B. R. Jesus, T. Grant, Z Fisk, R. R. Urbano, C. Rettor, P. Pagliuso, *Journal of Physics: Conference Series* 592 (2015)
6. Sümeyra Güler-Kılıç and Çetin Kılıç, *Phys. Rev. B* 91, 245204 (2015)
7. Tomokiyo, A.; Kawano, S.; Okada, T. *Japanese Journal of Applied Physics*, 16 (1977)
8. Kulbachinskii V.A., Kaminsky A.Yu., Kindo K., Narumi Y., Suga K., Lostak P., Svanda P., *Phys. Lett. A*. V.285, (2001)

Investigation of parametric excitation of the spin-wave pulses in magnetic films

A. V. Koryukin, A. V. Kondrashov, A. B. Ustinov

Department of Physical Electronics and Technology, St. Petersburg Electrotechnical University St. Petersburg, 197376, Russia.

Introduction

It is well known that the oscillations in any physical systems can be excited parametrically with periodical variation of a parameter of a system. The phenomenon of parametric excitation of oscillations known for a long time and has been studied in a large number of oscillatory and wave systems [1]. However, a question about the possible phase jumps of excited oscillations have not been studied previously. The aim of the present work is an experimental study of parametric excitation of the spin-wave pulses in magnetic films.

Experimental setup

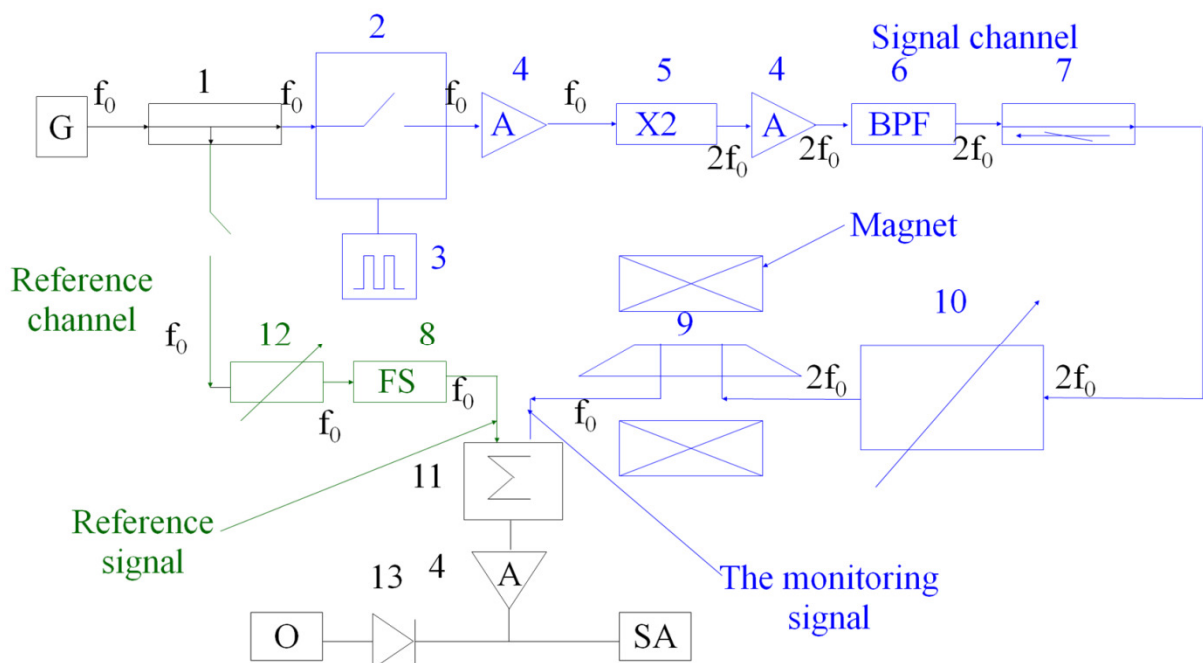


Figure 1. Block-diagram of experimental setup

Experimental setup is shown in Fig. 1. The experiments were carried out with experimental prototype of delay line (9) fabricated with 5.7- μm -thick yttrium iron garnet film. The film was magnetized in the film plane and parallel to the direction of spin-wave propagation. The value of the bias magnetic field was of 1070 Oe. The principle of parametric excitation of the spin-wave pulses consisted of local modulation of bias field by a variable magnetic field produced with the microstrip antenna. For this purpose, the antenna was fed by a microwave signal of double frequency. Excitation of spin-wave pulses detected by other microstrip antenna that is located at a distance of 6.5 mm.

To determine the phase of the exciting pulses the experimental setup was designed as a phase detector. Microwave switch (2), frequency doubler (5), microwave amplifiers (4) and variable attenuator (10) were in the signal channel. The reference channel consisted of attenuator (12) and phase shifter (8). Signal applied to the input of the circuit had a frequency f_0 . Part of it is coupled to the reference channel. To produce the signal of the double frequency we used the frequency doubler (5). This method of obtaining the double frequency signal is

preferred over a direct feed to the delay line (9) the signal from generator, since for implementation of the phase detection signals should have the same frequency.

Experimental results

First, the study of parametric excitation was performed in a continuous mode. The measurements were performed by systematic changing the frequency f_0 and pump power. In this mode, the reference channel has been disabled, and microwave switch remained open. The output of the delay line is fed to the measurement equipment. Above a threshold pump power for signal with frequency $2f_0$ we observed the parametric excitation of spin waves with a frequency f_0 . The results showed that there was some level of pump power at which a stable spin wave is excited.

Further studies were carried out in a pulsed mode. The experimental prototype was fed by pumping microwave pulses having carrier frequency of $2f_0$. Experimental setup was constructed as a phase detector so as to obtain zero output power for the case of destructive interference of the test and reference signals. The measurements showed random jumps of the pulse phase by 180 degrees. Graphical representation of this phenomenon is shown in Fig. 2.

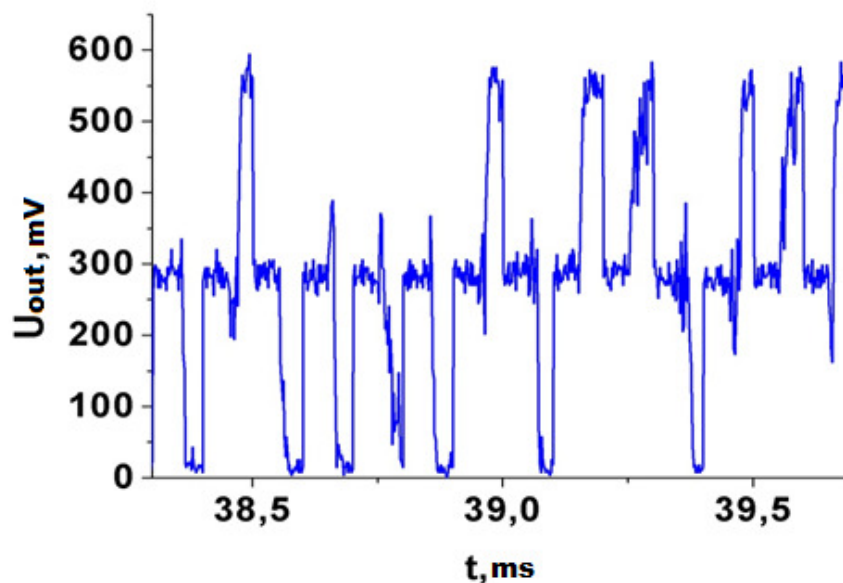


Figure 2. A waveform demonstrating observed phenomenon

Conclusion

The continuous and pulsed parametric excitations of the spin waves in magnetic film were studied. We demonstrate experimentally that phase of parametrically excited pulses jumps randomly by 180 degrees.

Acknowledgements

This work was supported with RFBR grant № 15-32-20357 mol_a_ved.

References

1. Demokritov S. O., Serga A. A., Demidov V. E. and etc. Experimental observation of symmetry-breaking nonlinear modes in an active ring, Nature, vol. 426, 159-162 p., 2003.

Study of the novel cationic spiropyran structure by NMR spectroscopy

Maria Lukyanova, Boris Lukyanov, Ilya Ozhogin, Gennadiy Borodkin, Oksana Komissarova, Artem Pugachev, Vasiliy Malay, Anastasia Kozlenko and Eugene Mukhanov

Institute of Physical and Organic Chemistry at Southern Federal University, Rostov-on-Don, Russian Federation

E-mail: lab811@ipoc.sfedu.ru

Introduction

Spiropyrans are one of the most important classes of photochromic compounds due to high quantum yield of their photoinduced rearrangements, accompanied by the reversible photochemical cleavage of the C_{spiro}-O bond in the 2H-chromene ring. Investigation of new compounds, belonging to one of the most perspective and interesting in terms of practical application classes of organic photochroms – spiropyrans, is of interest in the field of molecular electronics.

Synthesis of novel cationic spiropyran

Novel cationic spiropyran **1** has been prepared from 1,2,3,3-tetramethyl-3H-indoleum perchlorate and 2-hydroxy-5-methyl-benzene-1,3-dicarbaldehyde:

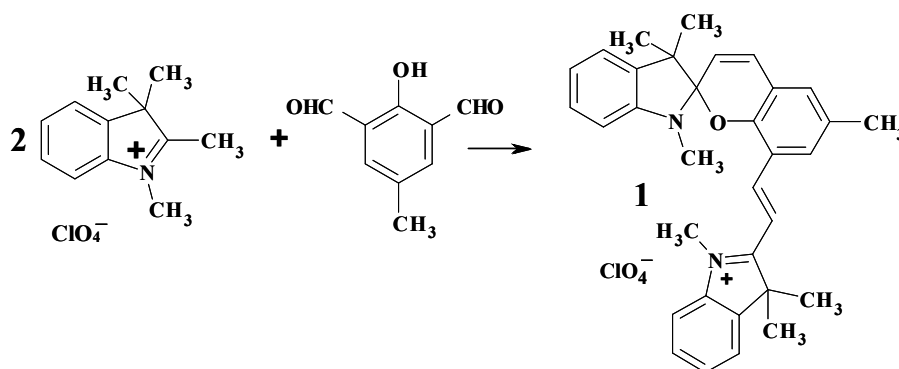


Figure 1. Synthesis scheme of spiropyran 1

Study of the cationic spiropyran structure

The structure of new cationic spiropyran **1** has been studied with the NMR ¹H, NMR ¹³C and COSY ¹H-¹H NMR spectroscopy. There are two groups of indoline protons observed in the ¹H NMR spectrum (Figure 2).

Gem-dimethyl groups protons signals in the 3 and 3'' position are at the 1.16, 1.25 and 1.30, 1.33 ppm, signals of the methyl protons at indoline cycle positions 1 and 1'' are at 2.67 and 3.65 ppm. The slight difference in the chemical shifts of the gem-methyl groups at the 3'' confirms the presence of only one asymmetric carbon atom, and the shift downfield signals indicates the presence of the positively charged quaternary nitrogen atom. The 3' and 4'-protons signals appear at 6.00 and 7.13 ppm respectively, vinyl fragment S12'-C13' appear as two doublets at 7.45 and 8.05 ppm with spin-spin coupling constant of 16.5 Hz.

The NMR spectroscopy COSY ¹H-¹H data (Figure 3) were used for an unambiguous classification of aromatic protons signals.

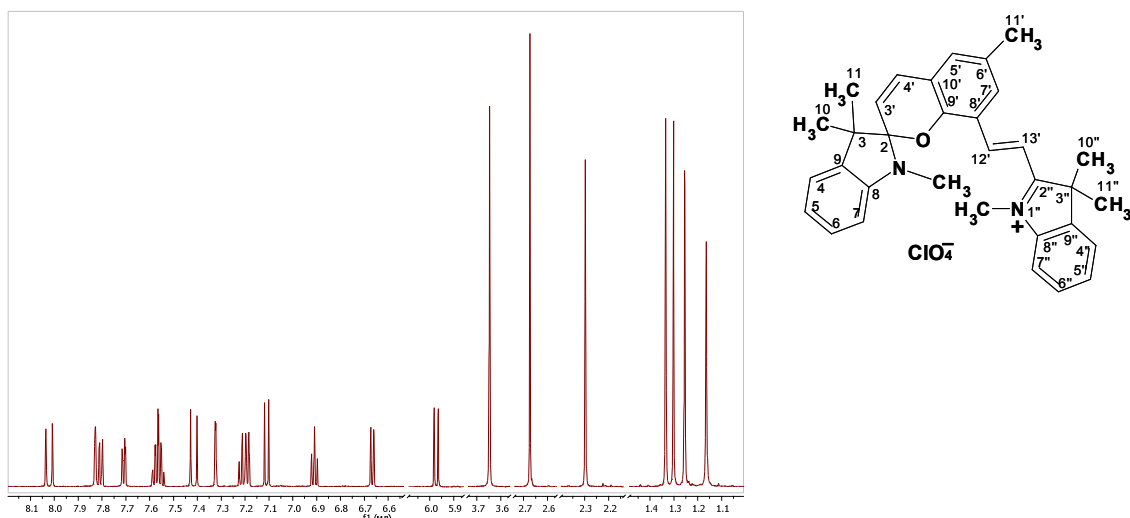


Figure 2. Spiropyran **1** NMR ^1H spectra (DMSO- d_6)

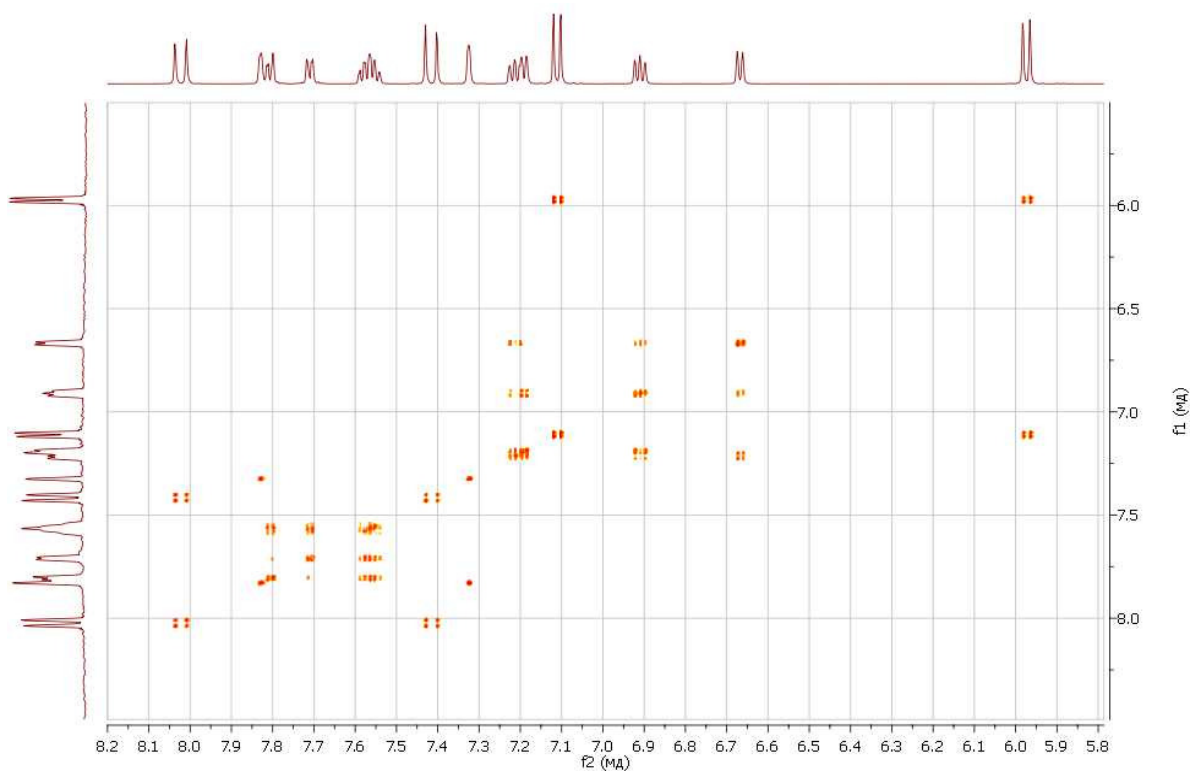


Figure 3. Spiropyran **1** COSY ^1H - ^1H NMR spectra

The structure of the compound **1** was confirmed by X-ray analysis [1].

Acknowledgements

This research was supported by The Ministry of education and science of Russian Federation in the framework of the State Assignment for Research, project № 1895.

References

1. Tkachev V.V., Lukyanova M.B., Lukyanov B.S., Pugachev A.D., Aldoshin S.M., Minkin V.I. The study of a new condensation reaction product of 1,2,3,3-tetrametilindoleniliya perchlorate with 2,6-diformyl-4-methyl-phenol. – *Journal of Structural Chemistry*, **57**, 6, 1312 – 1313 (2016)

Electron paramagnetic resonance investigations of ZnSe:Mn nanocrystals

D. S. Mazing¹, A. V. Nikiforova¹, A. S. Osinin¹, V. A. Moshnikov¹, Yu. V. Bogachev², S. M. Sukharzhevskii³

¹*Faculty of Electronics, St. Petersburg Electrotechnical State University, Russia*

²*Department of Physics, St. Petersburg Electrotechnical State University, Russia*

³*Magnetic Resonance Research Center, St. Petersburg State University, Russia*

E-mail: dmazing@yandex.ru

Introduction

Wide range of prospective applications, such as lightning, display technology and biomedical diagnostics, induces intensive development of colloidal quantum dots technology. One of important directions in material science is doping of nanocrystals. Controllable incorporation of dopants could be instrumental for regulating of electrical, optical and magnetic properties. Luminescent semiconductor nanocrystals doped with paramagnetic ions are good candidates for multimodal imaging probes [1]. Therefore, adequate assessment of the state of dopant centres within nanoparticle crystal lattice is of the essence. In case of paramagnetic nature of the dopant electron paramagnetic resonance (EPR) is a very useful method for investigation of doping procedure. In this work colloidal nanocrystals of ZnSe doped with manganese were synthesized by means of hot-injection technique in organic solvent and investigated using EPR as a primary tool for determination of dopant localization.

Experimental

Colloidal ZnSe:Mn²⁺ nanocrystals were obtained via hot-injection technique in organic solvent octadecene. Zinc oleate precursor solution was prepared by dissolving of ZnO (3 mmol) in 16 ml of octadecene and 12 mmol of oleic acid (OA) at 305 °C under nitrogen gas flow. Selenium powder suspension (0.5 mmol in the mixture of 1.5 ml of octadecene and 0.5 ml of oleylamine in total) was chosen as source of selenium. Firstly selenium suspension was injected into heated solution of zinc oleate (0.1 mmol) and manganese stearate (0.05 mmol) in 20 ml of octadecene at 290 °C. Then multiple injections of the zinc oleate solution were carried out at 260 °C (approximately 1 ml of precursor solution every 5 min, total amount of zinc oleate equals 0.75 mmol). The solution was annealed at this temperature for 1 hour to promote dopant diffusion into ZnSe lattice. Synthesized nanoparticles were precipitated from stock solution by means of centrifugation adding acetone as precipitant and were dissolved in toluene for further assay.

EPR measurements were performed on Bruker Elexsys E580 spectrometer. Photoluminescence spectra were obtained using spectrofluorimeter based on monochromator MDR-206 (LOMO), absorption spectra were acquired by means of spectrophotometer PE-5400UV (190 – 1000 nm).

Discussion

Photoluminescence and absorption spectroscopies results

Obtained nanoparticles exhibit bright photoluminescence with a single maximum at 575 nm and full width at half maximum less than 60 nm (figure 1). This type of emission is typical for Mn²⁺ dopant centers within crystal lattice of zinc chalcogenides and is thought to be d-d transition (⁴T₁ – ⁶A₁) within host bandgap. The absence of additional transitions in visible range implicitly indicates effective recombination via dopant centers and successful incorporation of individual Mn²⁺ centers inside ZnSe crystal lattice. Absorption onset is positioned around 425 nm.

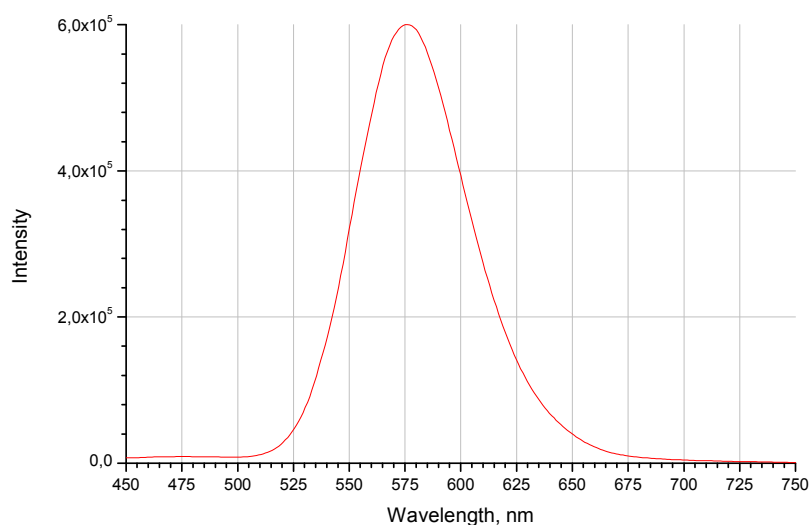


Figure 1. Photoluminescence spectrum of ZnSe:Mn nanocrystals

EPR spectroscopy results

EPR spectra were obtained at different concentrations of ZnSe:Mn²⁺ nanocrystals and all of them exhibit a well resolved set of six lines of almost equal intensity and separation (Figure 2). Based on the general spectral features [2], as well as on the results of experimental investigations and theoretical evaluations of spin Hamiltonian parameters of Mn²⁺ ions in cubic and lower symmetry crystal lattice [2-5], this set of six lines was attributed to the six hyperfine structure components of Mn²⁺. Due to the larger linewidth and smaller intensity, it is not possible to distinguish the hyperfine forbidden transitions in our EPR spectra. Hyperfine splitting constant $|A| = 83,34 \cdot 10^{-4} \text{ cm}^{-1}$, $g = 2,0055$. Comparing these values with other reports [2-5] a conclusion may be made that dopant Mn²⁺ centers are predominantly localized near nanocrystal surface. Slightly asymmetrical form of the spectrum components points at axial distortion of crystal lattice (crystal field) around manganese atoms. The presence of wide spectral EPR line at all EPR spectra in this work may be caused by strong dipole-dipole interaction between neighboring ions of manganese. This signal could have its origin due to the Mn pair or cluster formation.

Additionally, the EPR spectra showed four EPR lines supposedly corresponding to free radicals (R1) of inorganic origin. Notably with decreasing concentration this component of free radicals becomes more prominent than that of the dopant.

Also at low concentrations weak single EPR line is visible (~ 3365 Gs) which is attributed to defects (D1) of crystal lattice. The value of g-factor of this line is 2,0049 which is close to g-factor of unpaired electron. The same line was found in EPR spectrum of undoped ZnSe nanocrystals prepared using similar synthetic technique proving that it is not related to Mn²⁺.

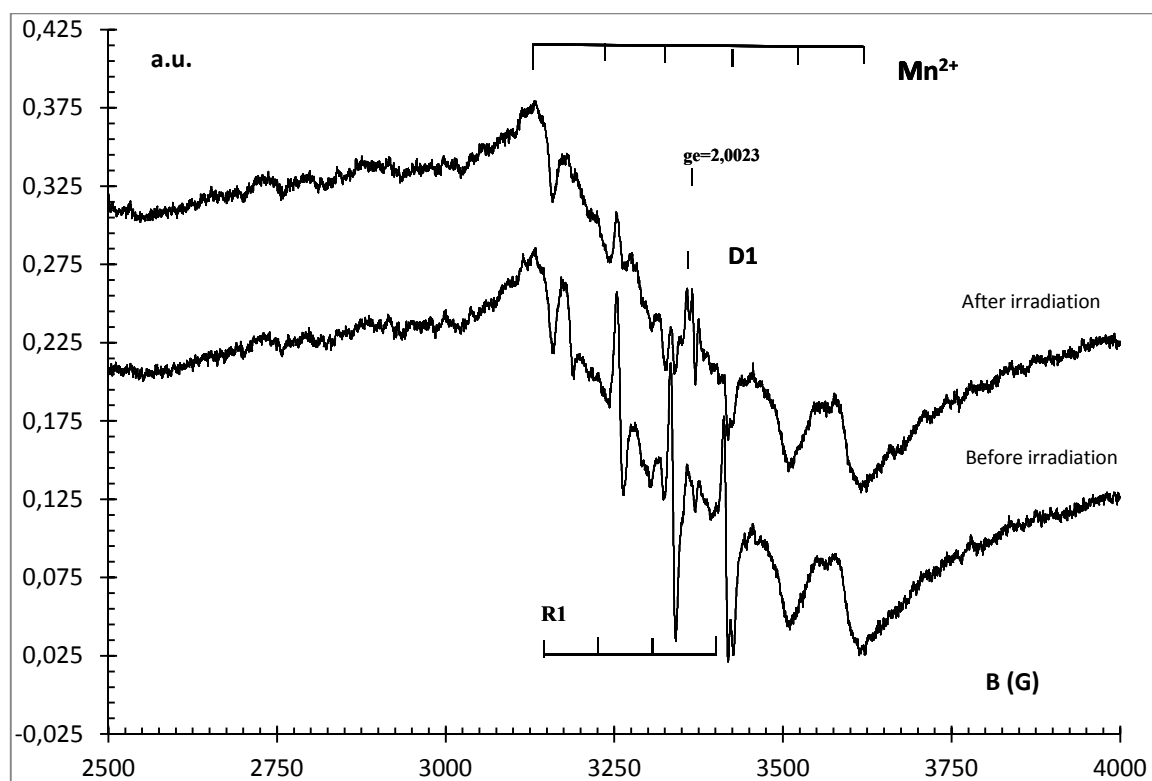


Figure 2. EPR spectrum of ZnSe:Mn nanocrystals

In another experiment the sample of nanocrystals was exposed to prolong laser irradiation (maximum wavelength 405 nm, < 10mW). This led to gradual decreasing of quartet of EPR lines till eventual full extinguishing which was irreversible implying transition of corresponding centers to non-paramagnetic state. At the same time the EPR signal amplitude attributed to crystal lattice defects increased.

Acknowledgements

This work is supported by the Russian Science Fund (project №14-15-00324).

EPR measurements were carried out at the Centre for Magnetic Resonance of Saint Petersburg State University.

References

1. L. Jing, K. Ding, S. V. Kershaw, I. M. Kempson, A. L. Rogach, M. Gao. – *Advanced Materials*, 26(37), 6367-6386 (2014).
2. A. Abragam and B. Bleaney, *Electron Paramagnetic Resonance of Transition Ions*, Clarendon Press, Oxford, 1970.
3. A. D. Lad, C. Rajesh, M. Khan, N. Ali, I. K. Gopalakrishnan, S. K. Kulshreshtha, S. Mahamuni. – *Journal of applied physics*, 101(10), 103906. (2007)
4. B. Yang, X. Shen, H. Zhang, Y. Cui, J. Zhang. – *Physical Chemistry*, 117(30), 15829-15834 (2013).
5. S. Acharya, D. D. Sarma, N. R. Jana, N. Pradhan. – *The Journal of Physical Chemistry Letters*, 1(2), 485-488 (2009).

Investigation of stationary and chaotic regimes of microwave signal generation in the spin-wave microwave photonic oscillator

K. K. Metelkina, A. V. Kondrashov, A. B. Ustinov

Department of Physical Electronics and Technology, St. Petersburg Electrotechnical University St. Petersburg, 197376, Russia.

Introduction

In recent years interdisciplinary research fields become important. Interdisciplinary studies enables one to combine advantages of different technologies [1]. Microwave photonics is a research area combining optoelectronic and microwave technologies. Microwave photonic oscillators are one of the most promising ways to generate different microwave signals. Thus, they provide a monochromatic signal generation with low phase noise [2]. Also, they demonstrate broad band chaotic signal generation [3]. The aim of the present work is to study the nonlinear effects which occur during self-generation of microwave signal in the spin-wave microwave photonic oscillator.

Experimental setup

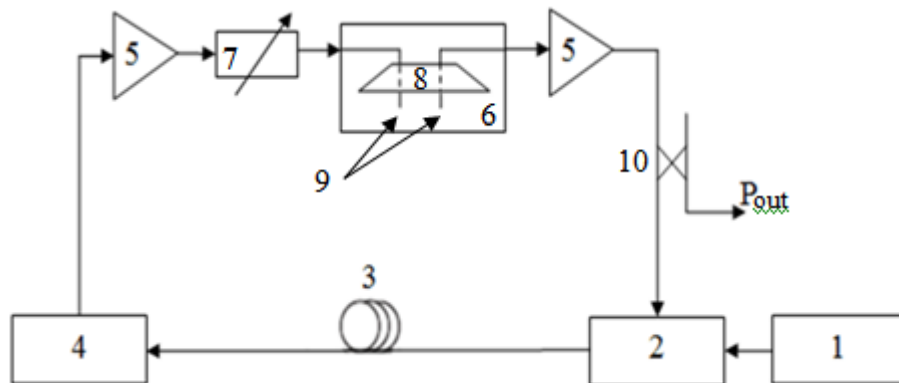


Figure 1. Block diagram of the microwave spin-wave photonic oscillator

Figure 1 shows the block diagram of the proposed prototype of the oscillator. The ring structure of the oscillator consists of the optical and radio-frequency parts. The optical part contains commercially available components: a semiconductor laser (1), an electro-optical modulator (2), an optical fiber with length of 100 m (3), and a semiconductor photodetector (4). The main radiofrequency components are two identical microwave amplifiers (5) and an original spin-wave microwave filter (6). The total gain of the microwave circuit is controlled using an attenuator (7). The original spin-wave microwave filter based on the epitaxial yttrium iron garnet (YIG) film (8). The filter is used for electronic tuning through changing an applied bias magnetic field. In this filter, microstrip antennas are used for the excitation and detection of spin waves.

Consider the principle of operation of the oscillator. Laser diode (1) emits cw optical radiation that serves as the optical carrier signal. The electro-optical modulator (2) modulates the amplitude of the optical radiation using the microwave signal that is generated by the radiofrequency circuit. The modulated optical radiation propagates along optical fiber (3) with delay time τ_{opt} and is detected with the photodiode (4) (Fig. 1). An output signal after amplification is applied to the electro-optical modulator, completing the ring. A minor part of the microwave signal couples out from the ring via directional coupler (10) with a coupling coefficient of -10 dB.

Results and discussion

The studies were carried out with a systematic increase in the ring gain G above the self-generation threshold. The monochromatic signal generation occurred at the frequency of 5.28 GHz for $G = 0$. An increase in G led to development of the self-modulation instability. As a result, we observed the self-generation of periodic sequence of solitons. Further increase in G led to bifurcation, after which the oscillations become stochastic. The stochastic waveforms had a broad spectrum with noise pedestal.

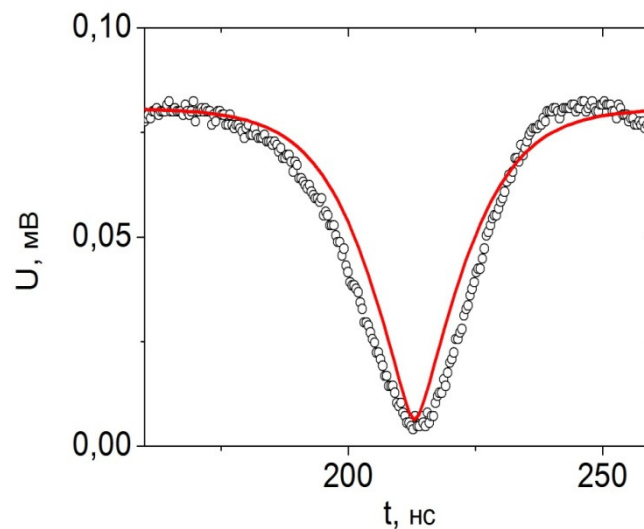


Figure 2. Experimental (dots) and theoretical (solid curve) dark soliton profiles

A computer modelling was performed to confirm the solitonic nature of the observed dark nonlinear pulses that are shown in figure 2. The nonlinear Schrödinger equation model was used for modelling. In the course of the experiment it was shown that the dispersion and nonlinear properties of the the ring were determined by spin waves propagating in the YIG film. Therefore, the dispersion and nonlinear coefficients in the modelling were taken for the YIG film used in the experiments. The group velocity was used as a fitting parameter. It is clear from figure 2 that the observed experimental waveforms have a profile close to the classical dark envelope soliton. The obtained data prove the solitonic nature of the observed nonlinear excitations.

Conclusion

We observed, for the first time, a self-generation of dark envelope solitons in the microwave spin-wave photonic oscillator. The solitons were formed as a balance between spin-wave dispersion spreading and spin-wave nonlinear self-steepening effects introduced by the magnetic film. A microwave chaos developed in the oscillator beyond the soliton generation.

This work was supported by a grant from RNF № 16-12-10440.

References

1. Belkin M.E., Sigov A.S. // Journal of Communications Technology and Electronics. 2009. Vol. 54. No. 8. pp. 855-868.
2. Ustinov A.B., Nikitin A.A., Kalinikos B.A.// Technical Physics. 2015. Vol. 60. No. 9. pp. 1392-1396.
3. Ustinov A.B., Kondrashov A.V., Kalinikos B.A.// Technical Physics Letters. 2016. Vol. 42. No. 4. pp. 403-406.

Development of contrast complexes based on manganese for high field MRI

M. S. Muravyeva¹, E. A. Kluev², N. B. Koroleva³, M. A. Katkova³, I. V. Mukhina²

¹*Lobachevsky State University of Nizhni Novgorod
603950, Nizhniy Novgorod, Prospekt Gagarina, 23*

²*Nizhny Novgorod State Medical Academy
603950, Nizhniy Novgorod, Minin & Pozharsky sq., 10/1*

³*Razuvaev Institute of Organometallic Chemistry
603137, Nizhniy Novgorod, Tropinina st., 49*

E-mail: masha-muravyeva@mail.ru

Introduction

Magnetic resonance imaging (MRI) is one of the most sensitive methods of diagnosis and assessment of nervous system's pathology. MRI is used for detection brain tumors, stroke, inherent anomalies of brain tissue and vessels like cyst and aneurism, structural damage of tissue in case of dementia and multiple sclerosis.

Usage of contrast agents allows receiving more discrete and detailed images of nervous system and especially brain. In our country there are four contrast agents based on gadolinium, which are registered and used: magnevist, omniscan, dotharem and gadovist. However, they have serious contraindication and side effects. Injection of big doses of gadolinium contrast agent leads to nephrogenic systemic fibrosis with death. In addition, it's important to underline that gadolinium based contrast agents are non-specific and incapable to cross brain-blood barrier (BBB). Thus, they can detect only disorders, which cause BBB damage.

Therefore, development of modern class of MRI contrast agents is one of the most significant aims. Recently manganese based contrast agents as alternative to gadolinium based ones attracts more and more attention. Unlike gadolinium manganese is a microelement that compounds take part in metabolism of nervous and other types of tissue. However, the study of manganese contrast agents is limited to simple salts or similar compounds of gadolinium and may be therefore they lose to known gadolinium based commercial products. Accordingly, the synthesis of novel water-soluble chelated manganese compounds for creation a safe and effective contrast agents is an urgent task that is not only of fundamental but also of practical interest.

Experiments

The aim of our study was development and synthesis of manganese chelates for generation contrast substance for MRI diagnostic and assessment of its properties as contrast agent (relaxometry and test on the models of different brain pathologies like stroke and brain injury). Object of investigation were compounds of manganese (II) of bioactive organic acids.

Mn(II) — EDTA and Mn(II) — DTPA complexes have contrast properties (paramagnetic efficacy) similar to Gd(III) complex. Intravenous injection to healthy animals shown enhancement of contrast in liver and kidney notably excretory organs. Preclinical studies shown low toxicity and high efficiency of different brain disorders.

Manganese lactate(II) was synthesized in reaction of manganese carbonate and lactic acid.

Conclusion

With the aim of further testing manganese lactate(II) as potential contrast agent we studied it's relaxation properties on spectrometer Agilent DDR2 400WB (9.4 T). We measured values of relaxation r_1 and r_2 on linear dependence of reverses values of relaxation

time to concentration of manganese lactate. Our studies shown following relaxation's values $r_1 = 6.5 \text{ s}^{-1}\text{mM}^{-1}$, $r_2 = 180.9 \text{ s}^{-1}\text{mM}^{-1}$ in 9.4T field. On animal studies, increase of contrast in areas of stroke and brain injury was shown.

This work was supported by RFBR grant №15-43-02285.

The study of nonsymmetrical bis-spiropyrans of 1,3-benzoxazin-4-one series using two-dimensional ^1H NMR spectroscopy

Ilya Ozhogin, Eugene Mukhanov, Boris Lukyanov, Maria Lukyanova, Oksana Komissarova, Artem Pugachev, Yulia Schekina, Vasily Malay, Anastasia Kozlenko

Institute of Physical and Organic Chemistry at Southern Federal University, 344090, Russia, Rostov-on-Don, Stachka ave. 194/2

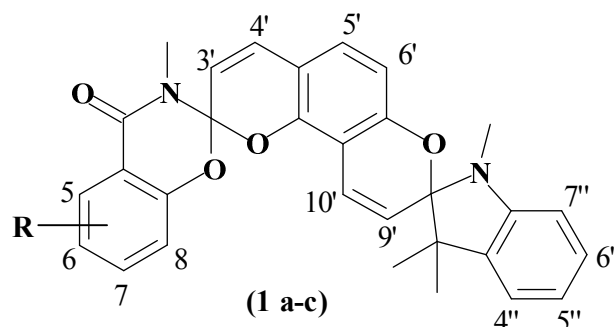
E-mail: iozhogin@sfedu.ru, ilyuh@ya.ru

Introduction

Spiropyrans represent one of the most interesting classes of photochromic compounds, which can undergo reversible photoisomerisation from spirocyclic form to a colored merocyanine form under activating irradiation. More complicated molecules of bis-spiropyrans contain two photoswitchable centers, so they have at least four isomeric forms, which could be potentially switched between each other. This possibility makes bis-spiropyrans promising prototypes of the multipositional molecular switches for molecular electronics [1].

Synthesis and investigation of new bis-spiropyrans

In this study three novel nonsymmetrical indoline-benzoxazine bis-spiropyrans (1 a-c), in which the photoactive centers are conjugated through a common pyranochromene moiety, was synthesized by a multistage procedure [2].



R = a) 7- CH_3 ; b) 8- CH_3 ; c) 8- OCH_3

The structure of the synthesized mono and bis-spirocompounds has been proven by IR and ^1H NMR spectroscopy. The ^1H NMR spectra of the target products, with presence of characteristic signals of proton-containing groups, fully comply with the proposed structure. There are characteristic signals of gem-dimethyl groups of indoline part in the "strong" field spectra area of bis-spiropyrans (1a-c), represented as two 3H-singlets at 1.0-1.2 ppm, which confirm the adjacency to an asymmetric carbon spiro-atom. The proton signals of methyl groups linked to the nitrogen atoms of the indoline and oxazine fragments appear at 2.6 and 3.1 ppm respectively. Characteristic signals of 3' and 9' protons of benzopyran fragment appear as doublets about 5.8 and 5.5 ppm and form the AB-system with the protons 4' (6.9-7.0 ppm) and 10' (6.6-6.7 ppm) with the J-constants equal to 9.8 и 10.5 Hz. That fact confirms the *cis*-configuration of vinyl fragments adjacent to spiro -centers of bis-spiropyran molecules.

Two-dimensional NMR spectroscopy study

For the correct assignment of aromatic protons signals, which appear as a rather complex multiplet pattern, the compound (1c) was studied using two-dimensional NMR techniques, namely COSY ^1H - ^1H correlation spectroscopy (Fig. 1) and spectroscopy of

nuclear Overhauser effect NOESY ^1H - ^1H (Fig. 2). The set of these two-dimensional NMR techniques allowed us to unambiguously isolate the signal of each of the aromatic protons from the overall view of the spectrum. In particular, doublet signal at 6.48 ppm was assigned to the proton 7", since, based on the NOESY ^1H - ^1H experiment, it has cross-peak with the signal of the methyl group at the indoline nitrogen atom. Paired hydrogen atom 6" was identified as a triplet at 7.1 ppm signal through correlation spectra COSY ^1H - ^1H . In addition to this signal in the region 7.0-7.2 ppm there were identified the triplet signal of the proton 6 and the doublet signals of the protons 7 and 4". The latter two are correlated through the space with hydrogen atoms of methoxy-group of the benzoxazine moiety and the methyl group in position 3' of the indoline moiety, respectively. Signals of protons 5' and 6' are shown as two doublets at 6.38 and 6.95 ppm with the J-constant equal to 8.35 Hz. Doublet signal at 7.68 ppm corresponds to the proton 5 and shifted to downfield due to the proximity to the carbonyl group of the benzoxazinone cycle.

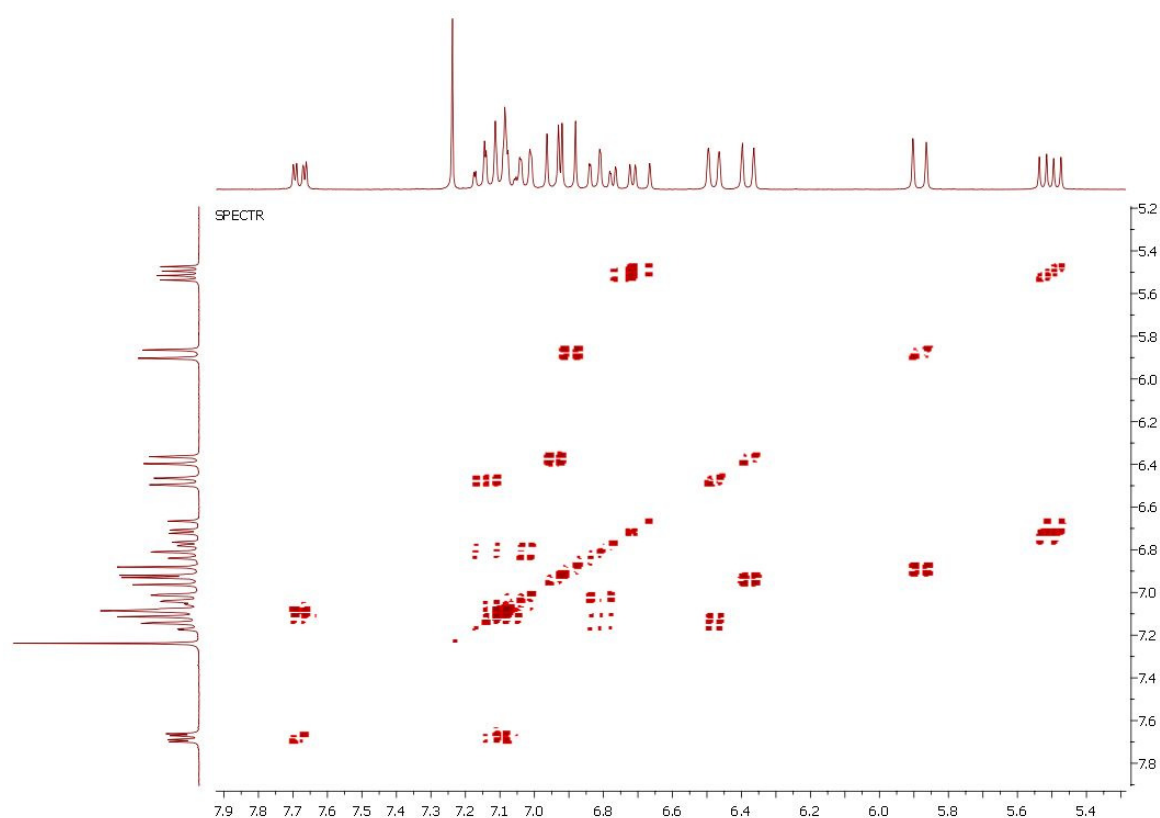


Figure 1. COSY ^1H - ^1H NMR spectra of compound (1c), aromatic protons area

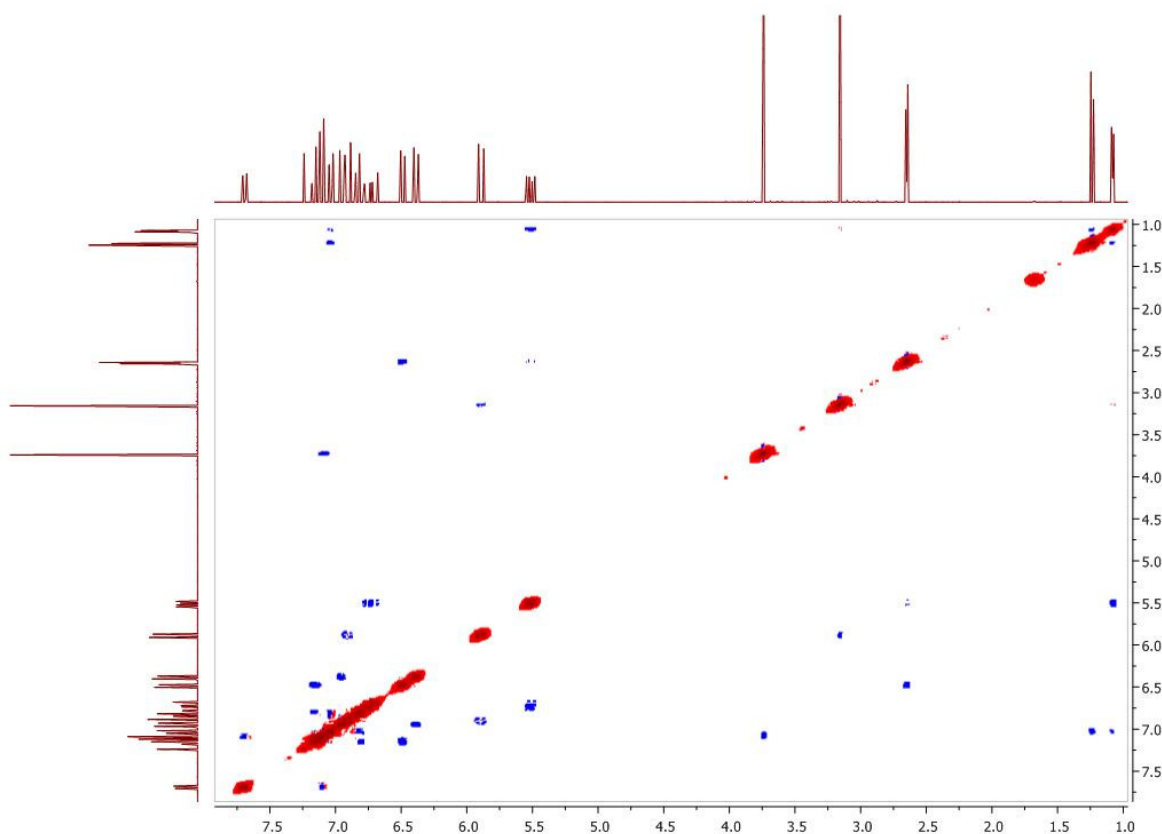


Figure 2. NOESY $1H-1H$ NMR spectra of compound (**1c**)

Acknowledgements

This research was supported by The Ministry of education and science of Russian Federation in the framework of the State Assignment for Research, project № 1895.

References

1. V. I. Minkin. In *Molecular Switches*, eds. B.L. Feringa, W.R. Browne. – Weinheim: Wiley-VCH, 2011.
2. E. L. Mukhanov, Y. S. Alekseenko, B. S. Luk'yanov et al. – *High Energy Chem.*, 3, 220–223 (2010).

Structure analysis of mixed matrix membranes based on polysulfone and polyvinyl alcohol

Anastasia V. Penkova, Anna I. Kuzminova, Maria E. Dmitrenko

St. Petersburg State University, St. Petersburg, 199034 Russia

E-mail: anast.chem@gmail.com

Nowadays, the essential improvement of the transport properties of polymer membranes can be achieved by the modification of the polymer matrix by inorganic filler that yields in developing the mixed – matrix membranes (MMM). The introduction of inorganic filler in the polymer matrix of the membrane allows attaching additional functional properties. Hybrid or mixed matrix membranes (MMMs) prepared by dispersing inorganic filler in a polymeric matrix offer the possibility to overcome the trade-off between the permeability and selectivity of the polymeric membranes. Among the inorganic particles fullerene takes an important place as this nanoparticle saves its unique π -electron structure inside of the polymer matrix.

This work focuses on preparation and characterization of mixed matrix membranes based on two polymers (polysulfone (PS) and poly(vinyl alcohol) (PVA)) modified by the incorporation of small amounts of fullerene and fullerene derivatives (water soluble forms of fullerene). The most important investigation of influence of fillers inclusion to polymers is analysis of membranes by spectroscopy methods. Nuclear magnetic resonance (NMR) allows understating interaction between fullerene and polymer matrix. The study of structure of the hybrid membranes leads to understanding the change of physic-chemical and transport properties of the polymer membranes as well as mechanism of mass transfer of small penetrants through non-porous films in pervaporation separation of liquid mixtures. Thanks to NMR the structure changes were investigated in the present work.

The additional characterizations of the polymer samples were carried out by microscopy methods (SEM and AFM) and X-ray diffraction. Transport properties of the membranes were studied during the dehydration of organic mixtures by pervaporation. The correlation of structure peculiarity with transport properties of developed mixed matrix membranes was studied. It was shown that the structure and transport characteristics of mixed matrix membranes were essentially changed as compared to membranes based on parent polymers.

Acknowledgements

This work was supported by grant of RFBR No. 15-58-04034. The experimental work was facilitated by equipment from Resource Centers: for Nanotechnology, Research center for X-ray Diffraction Methods, Research Centre for Physical Methods Surface Investigation, Thermal Analysis and Calorimetry, Chemical Analysis and Materials Research Centre and GEOMODEL at St. Petersburg State University.

Non-magnetic heat controller in scheme of quantum magnetometer and the angular velocity sensor

V. I. Petrov¹, R. K. Speranskiy^{1,2}, E. N. Popov³

¹Concern CSRI "Electropribor" JSC SRC RF

²ITMO University

³Peter the Great Saint-Petersburg polytechnical university

E-mail: font133@yandex.ru

Introduction

Quantum magnetometers, built on the basis of hot atoms atomic spin, electronic or nuclear, have high requirements to the uniformity of the magnetic field B_0 , which determines the angular rate of the spin's precession f .

$$f = \gamma \cdot B_0, \quad (1)$$

where γ – a gyromagnetic ratio. Nonuniformity of the magnetic field leads to the widening of resonant lines and, as a result, to the deterioration of the device resolution. In this regard, the problem of magnetic interference, generating by peripheral units in measure circuit, is especially relevant in applied tasks.

In this paper we will focus on the one of the strongest sources of magnetic interference in a volume of quantum sensor: the heating element, which maintains a constant temperature on the surface of the cell. That's why the developing of device for the temperature stabilization of gas cell (the heat controller) is not a trivial task. It requires the account of heat controller's influence on the sensitive element of the quantum sensor: the cell with the active substance.

The sensitive element of the quantum sensor on the basis of magnetic resonances

At the core of the considered sensor is the longitudinal electronic paramagnetic resonance, which provides the ability to measure the magnitude and direction of the external magnetic field's projection to the plane, perpendicular to the selected axis of quantization (determined by the direction of the constant field B_0). This effect occurs in alkali metal vapor, which is in the dense buffer gas under the continuous laser radiation. The saturated vapors concentration depends on the magnitude of signal, the rate of relaxation processes, and shifts of the resonant lines, which measure the induction of the magnetic field or the angular rate of rotation. The number of active atoms in the cell determines by the temperature of its surface, that's why the problem of the quantum sensor's thermostabilization is very important. In practice, the temperature has to be continuously supported at the level, determines by the maximum amplitude of the detection laser's signal, which is linearly dependent on the rotation of the plane of polarization in the medium by Faraday effect. This value of the temperature is individual for every alkali metal (60°C for Cs, 90°C for Rb). Generally, the cell's cooling arises by the convection with ambient air. Due to the requirement to the uniformity of the magnetic field, the heat controller has to be realized as a non-magnetic heater.

Construction of the heat controller

The sensitive element of quantum sensor of magnetic field (the cell with alkali metal vapors) have to be heated for creating the optimal concentration of alkali vapors. As such, the cell is placed into the thermostat with the non-magnetic heat controller. Both of them are made of non-magnetic material. For instance, the material for heating element could be a copper. Heat winding is made of bifilar cable or in the form of a bifilar printed circuitry so as

magnetic flux generating by every part of the cable will be compensated by the magnetic flux of opposed direction (Fig. 1).

For another thing, for further reducing of magnetic interference, the heating element's supply performs with an alternating current. With that in every elemental part of the heating element for the entire period the current flows in two opposite directions and therefore reduces the joint magnetic flux to nothing. To exclude the coincidence between the heating element frequency, its nearest harmonics and operational frequency of radio-field, the heating element frequency is selected higher than operational frequency of the sensor. For the Cesium sensor and the value of magnetic field below 20 mT the maximum operational frequency determines according to the Larmor's equation (1) as 70 kHz. In that case a reasonable value of heating element frequency is around 300 kHz.

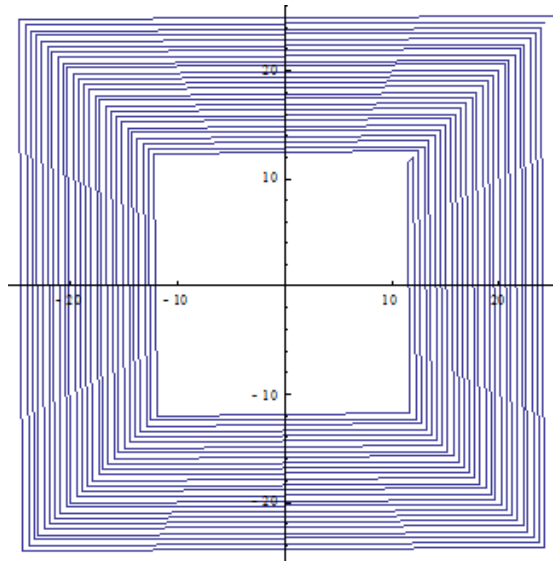


Figure 1. The location of tracks on one side of the PCB. Units are millimeters. The location of tracks on the another side is similar, but current flows to the opposite direction

Besides the heating element's current in the thermostat, the current flows in thermistor and lead wires can be the source of magnetic interference. Despite a small value of this current (around 100 mA), field generating by it leads to the systematic error of the quantum sensor, because its source is placed directly close to the gas cell. For reducing the error, generated by the thermistor's current, is used the same technique as for the reducing the influence of the heating plates magnetic field — the current conversion from DC to AC. For this purpose the low-resistance keys switch are used.

Some quantum sensors have high requirements to the accuracy of thermal stabilization. In case of requirements about 10^{-3} °C (1 mK) it's necessary to provide the enough contrast of thermistor's resistance in the operating range of temperature. For the ^{133}Cs -sensor the operating range is 50 – 70 °C, the resistance of thermistor PT1000 in this range is 650 – 1500 Ohm, what gives the minimum ratio adjustment 0,065 V/K 65 mV/mK. Using the thermistor PT100 could lead to the value 6,5mV/mK, what is already on the verge of the sensitivity of certain electronic circuits. Increasing of measuring current is also undesirable because it leads to the growth of the magnetic interference.

For tuning the temperature of the cell is used the temperature setting device (adjuster), which contains switchable resistors, matched according to the measured law of change of the thermistor's resistance. The thermistor, the adjuster's resistor and two sources of calibrated current form a measuring bridge, providing the ability to compensate the interference when it occurs in supply circuits. The unbalance signal of the bridge is amplified by the pre-amplifier and transmitted to the controller, constructed according to the proportional-integrative (PI)

scheme. The gain of proportional term sets the ramp time of set temperature, and the time constant of the integrator affects the duration of transition process. The thermostat which is used in the heat controller has a significant latency – in order of 5 s. So much time required for the thermistor to react to a change of the heating current. Systems with transport delay [1] require a setting the time of integration ten times greater than the value of latency to exclude its influence on the accuracy. Thus the integration circuit requires the time constant about 50 s. [2]. Because of such a high value of latency the need for rapid regulation by the differential term is eliminated. The manipulation signal of the controller goes on the generation unit (Fig. 2) where it affects the regulatory element, controlling the output power. The generation unit contains the clock generator, the regulatory element and the output stage. The clock generator produces a rectangular signal of frequency 307 or 614 kHz in depending of the quantum sensor's operating frequency. The regulatory element controls the output stage power. The output stage is built on two field switches with followed filtration of the output signal to the first harmonic.

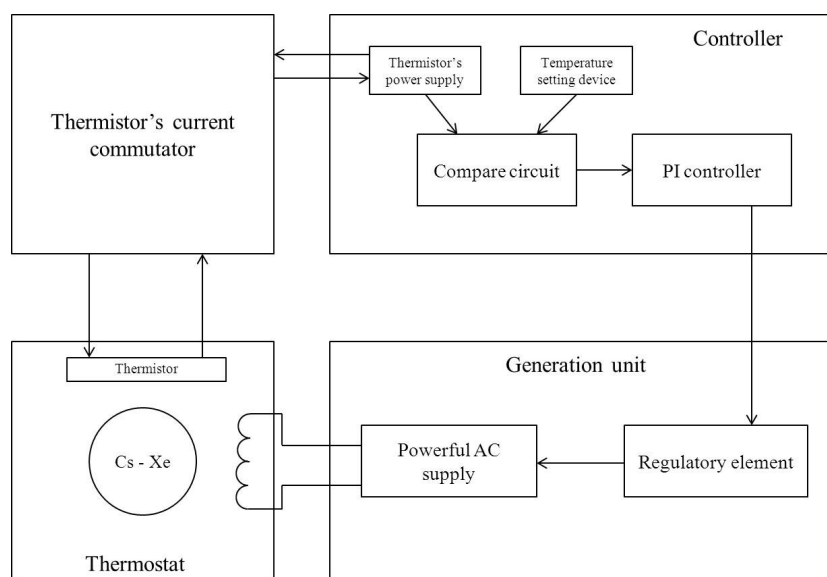


Figure 2. Block diagram of the heat controller

Results

The non-magnetic heat controller for quantum sensors or sensitive elements of quantum electronic devices – magnetometers, atomic clocks or NMR-gyros. The build-up time is about 15 min, accuracy of the temperature stabilization in operating volume is about 10^{-2} °C. In the course of the further development of the controller and the generation unit the accuracy is expected about 10^{-3} °C or better. According to the experiment the widening and shifts of resonant lines were not detected.

Acknowledgements

The work was carried out with the financial support from Federal Special-Purpose Programm «Research and development in priority areas development of scientific and technological complex of Russia for 2014-2020» (contract №14.578.21.0211).

References

1. V.A. Besekerskiy, Ye.P. Popov. The theory of automatic control systems (in Russian). – “Nauka” Publ., Moscow, 1975.
2. U. Tietze, Ch. Schenk. Electronic Circuits. Design and Applications. 12-th edition, vol. II (in Russian). – “DMK Press” Publ., Moscow, 2007.

Investigation of the nonlinear oscillations in ferromagnetic films taking into account a nonlinear frequency shift and nonlinear damping

Ansar Safin¹, Alexey Ustinov²

¹*National Research University "MPEI", Moscow, Russia*

²*Saint Petersburg Electrotechnical University "LETI", St. Petersburg, Russia*

E-mail: arsaftin@gmail.com

Introduction

Resonators based on high-quality ferromagnetic thin films, such as single-crystalline yttrium iron garnet (YIG) films, can find various applications in microwave electronics (see, e.g., [1]). As is known increasing of the microwave power supplied to the ferromagnetic film resonator is accompanied by various nonlinear effects. On the one hand, the development of nonlinear effects is frequently undesired, and their possible existence must be taken into account in developing linear spin-wave microwave devices. On the other hand, nonlinear effects in ferromagnetic films can provide a basis for the development of new method and devices for processing and generating microwave signals [1, 2].

In this work dynamics of the magnetic oscillations in the yttrium iron garnet (YIG) films with simultaneous influence of nonlinear frequency shift (nonisochronism) and positive damping has been studied theoretically. On the first step, using the method of slowly varying amplitudes from the Landau-Lifshitz-Gilbert equation, which describe the YIG magnetization dynamics, we consider the truncated equations for the spin wave amplitude and phase. Then we find stationary states of this system and analyze their stability by varying the basic physical parameters. We show, that presence of nonlinear damping for sufficiently high input power limits and compensates the influence of the nonlinear frequency shift of the magnetization oscillations which reduces the resonance frequency shift.

Mathematical Model

The mathematical model of the YIG-resonator in single-harmonic approximation for the complex amplitude $u(t)$ can be described by the following equation:

$$\frac{du}{dt} + i(\omega_0 + N|u|^2)u + \omega_{r0}(1 + \nu_1|u|^2 + \nu_2|u|^4)u = \Lambda(P_{inc}) \cdot e^{-i\omega_{inc}t}, \quad (1)$$

where ω_0 is the resonance frequency of the YIG-film, N is the nonlinear frequency shift, ω_{r0} – relaxation frequency on the $u=0$, $\nu_{1,2}$ are the nonlinear relaxation parameters, $\Lambda(P_{inc})$ the nonlinear function of the external power P_{inc} .

Now let's turn to the truncated equations based on the slowly varying amplitude $U(t)$ and phase $\varphi(t)$ using the expression

$$u(t) = U(t) \cdot e^{-i\omega_0 t - i\varphi(t)}. \quad (2)$$

After substitution (2) in (1) on the period $T_0 = 2\pi/\omega_0$ and dividing real and imaginary parts, we receive the following equations

$$\begin{cases} \frac{1}{U} \frac{dU}{dt} + \omega_{r0}(1 + \nu_1 \cdot U^2 + \nu_2 \cdot U^4) = \frac{\Lambda}{U} \cos[(\omega_0 - \omega_{inc})t + \varphi], \\ -\frac{d\varphi}{dt} + N \cdot U^2 = \frac{\Lambda}{U} \sin[(\omega_0 - \omega_{inc})t + \varphi]. \end{cases} \quad (3)$$

After rewriting system (3) based on the phase difference $\psi = \Delta\omega \cdot t + \varphi$ (we accept $\omega_0 - \omega_{inc} = \Delta\omega$) we receive:

$$\begin{cases} \frac{dU}{dt} = -\omega_{r0} \left(1 + \nu_1 \cdot U^2 + \nu_2 \cdot U^4\right) U + \Lambda \cdot \cos \psi, \\ \frac{d\psi}{dt} = \Delta\omega + N \cdot U^2 - \frac{\Lambda}{U} \cdot \sin \psi. \end{cases} \quad (4)$$

Let's find stationary points of the system (4) and analyze it's stability.

Results

The stationary points of the system (4) are U_0, ψ_0 and one can find them by solving the following equation:

$$\Lambda^2 = \omega_{r0}^2 P_0 \left(1 + \nu_1 \cdot P_0 + \nu_2 \cdot (P_0)^2\right)^2 + P_0 (\Delta\omega + N \cdot P_0)^2, \quad (5)$$

Using numerically solving of the equation (5) we plot (see Fig.1) the resonance frequency f_0 versus incident microwave power P_{inc} and (b) spectra $S_0(f)$ for three cases (with and without hysteresis). Here we see, that that presence of nonlinear damping for sufficiently high input power limits and compensates the influence of the nonlinear frequency shift of the magnetization oscillations which reduces the resonance frequency shift.

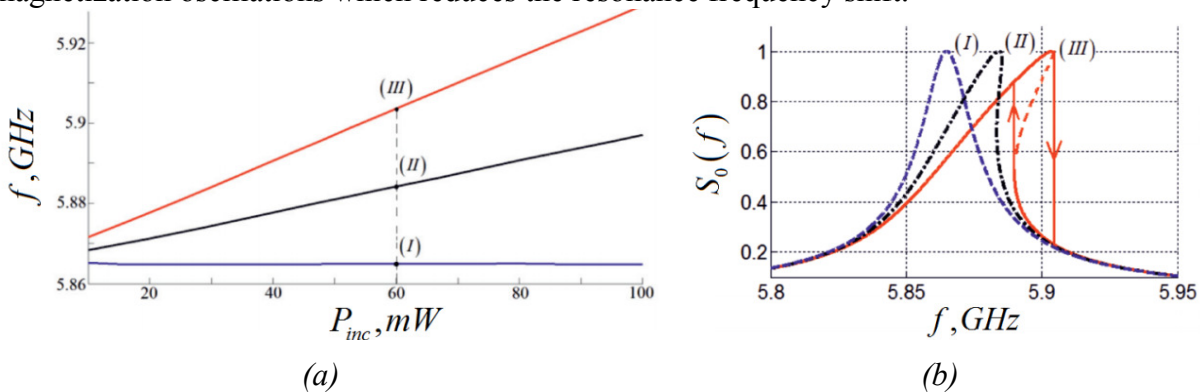


Figure 1. Plots of the (a) resonance frequency f_0 versus incident microwave power P_{inc} and (b) spectra $S_0(f)$ for three cases (with and without hysteresis)

Acknowledgements

This work is supported by the Russian president grant for young scientists (grant MK-7026.2016.8).

References

1. B.A. Kalinikos, A.B. Ustinov, S.A. Baruzdin. Spin-wave devices and echo-processors (in Russian). – “Radiotechnica” Publ., Moscow, 2013.
2. A.V. Drozdovskii, A.B. Ustinov. – *Technical Physics Letters*, 36, № 9, 834-837 (2010).
3. A.R. Safin, A.B. Ustinov. – *Fundamental Research*, 12, 509-513 (2014).

The Matlab toolbox for fitting the two-dimensional NMR spectra

Ali Shaban¹, Sevastyan Rabdano^{1,2}

¹*Saint Petersburg State University, Department of Physics.*

²*Saint Petersburg State University, Laboratory of Biomolecular NMR*

E-mail: shaban-a@live.com

NMR spectroscopy is a powerful tool of scientific research. It helps to obtain information about the studied material on the molecular and atomic levels without destroying the sample. The obtained data from the NMR spectrometer can be then analysed using different software packages to get important molecular properties of the sample. Those packages, although available and not so hard to use, are written on non-popular programming languages. Matlab, on the other hand, is a popular numeric computing environment amongst young scientists, yet it does not have a comfortable means of spectra fitting and analysis. The need to use Matlab for 2D NMR spectra fitting is the motivation for this work.

“2D NMR spectra fitter” is a toolbox [1] that allows the researchers to fit 2D spectra and obtain their useful parameters such as peak width. After the NMR signal is obtained, a Fourier transform gives us a spectrum that consists of peaks with Lorentzian and Gaussian lineshape. 1D NMR spectra can be used to obtain a lot of useful information about the atoms, but it suffers from peak overlapping when system studied is not trivial. 2D NMR spectra allow overcoming this discrepancy and can be used, for example, to study a protein’s structure. Homonuclear and heteronuclear two-dimensional NMR experiments are good examples of this approach.

Our toolbox uses as input two files: one that has spectrum data and one that has peaks’ coordinates. As an output it provides a table of fitted peaks’ parameters. It imports data from the files into Matlab. To fit 2D spectrum we either need to fit all the peaks at a time and thus spend too much time waiting for the results or we need to fit the spectrum as separated peaks and thus we will not have correct results for overlapping peaks. So we had to find an algorithm that can save both time and accuracy.

Such algorithm starts with dividing the spectrum into clusters of close-positioned peaks and then fits each cluster separately. The clustering part of the algorithm starts with each peak at a time, checks whether it has in vicinity other peaks or not, builds a cluster that includes those peaks and returns a matrix that contains each cluster’s center, dimensions and the number of peaks that it includes. The toolbox fits the peaks with 2D Gaussians and then moves on to fit the next cluster. It returns a matrix that contains each peak’s center, width and the calculation uncertainty.

This toolbox was successfully used to fit a series of two-dimensional pulsed field gradient NMR spectra of RRM2 domain of TDP-43. The obtained peak volumes were used to calculate the diffusion coefficient and the molecular mass of the diffusing particle.

References

1. Matlab Central File ID: #52300,
<http://www.mathworks.com/matlabcentral/fileexchange/52300-2d-nmr-spectra-fitter>.
Accessed on 31.10.2016.

Investigations of $Y_2SiO_5:Nd^{143}$ by ESR method[☆]

Alexey V. Shestakov^{1,2}, *Rushana M. Eremina*^{1,2}, *Tatiana P. Gavrilova*^{1,2}, *Ivan V. Yatsyk*^{1,2},
*Andrey A. Sukhanov*¹, *Yuri D. Zavartsev*³, *Alexandr I. Zagumennyi*³, *Sergey A. Kutovoi*³

¹Kazan E. K. Zavoisky Physical-Technical Institute (KPhTI) of the Kazan Scientific Center of the Russian Academy of Sciences, Sibirsky tract, 10/7, Kazan, 420029, Russia

²Kazan (Volga Region) Federal University, Kremlevskaya st., 18, Kazan, 420008 Russia

³Prokhorov General Physics Institute of the Russian Academy of Sciences (GPI RAS), Vavilov Str., 38 Moscow, 119991 Russia

E-mail: REremina@yandex.ru

http://kfti.knc.ru/en/

Introduction

One of the research areas in the field of advanced materials and their applications modern information technologies of processing and transmission of information through a quantum memory modules is the study of dielectric crystals activated by rare-earth ions. To create high-performance modules can be used the group of crystals, to which $Y_2SiO_5:^{143}Nd^{3+}$ belongs. These crystals have properties, required to create highly efficient optical quantum memory, namely, large optical density, and large phase relaxation times, the presence of long-lived hyperfine states [1]. For the realization of quantum bits it is important to suppress the spin relaxation of the neodymium nuclei due to the interaction with the nuclear spin of the ligand ^{29}Si with $I=1/2$, therefore, it is necessary to grown isotopically pure single crystal.

The aim of this work was to study the paramagnetic centers of neodymium ion isotope 143 with $I=7/2$ doped in the Y_2SiO_5 (^{28}Si) single crystals by ESR method.

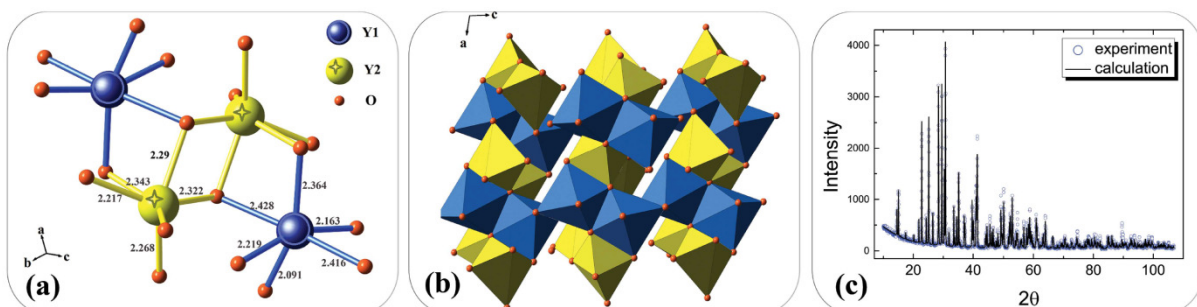


Figure 1. (Color online) Crystal structure of Y_2SiO_5 (space group $C2/c$): (a) two structurally non-equivalent positions of Y ions, which substituted by Nd^{3+} ions; distances are given in Å; (b) pairs of distorted octahedrons YO_6 in (ac) -plane; non-equivalent octahedrons are shown by yellow and blue colors, respectively to (a); (c) - diffraction pattern of Y_2SiO_5 sample at room temperature

Samples preparation and experiment technique

Monocrystal samples of Y_2SiO_5 were synthesized in Prokhorov General Physics Institute of the Russian Academy of Sciences (GPI RAS) (Moscow, Russia). All crystals have been grown in irridium crucibles with a diameter of 40 mm by the Czochralski method at industrial installations with induction heating "Crystal-2" and "Crystal-3M". The samples were oriented by x-ray diffraction to within $\pm 0.5^\circ$ and cut in the (ab) , (ac) , and (bc) crystallographic planes to form rectangular parallelepipeds measuring $1.5 \times 2 \times 3$ mm. The X-ray diffraction pattern of the sample was obtained using a DRON-7 diffractometer equipped with the CuK_α radiation source. The system was calibrated using a Standard Reference Material 300104 (annealed nickel foil). The diffractometer parameters were 40 kV, 20 mA, a 2θ scan range of 10° to 110° , step size of 0.02° and a scan speed of 5s/step.

Experiments were performed using an X-band (9.7 GHz) Bruker electron spin resonance (ESR) spectrometer (Elexys E580) and (EMX+) equipped with a helium cryostat. Microwave (mw) $\pi/2$ and π pulses were 16-200-32 ns long.

Experimental results and discussion

The X-ray analysis of the Y_2SiO_5 monocrystal showed that the compound is in single-phase state and its structure belongs to the space group $C2/c$, lattice parameters are $a=10.410\text{\AA}$; $b=6.721\text{\AA}$; $c=12.490\text{\AA}$, $\alpha=90^\circ$, $\beta=102.65^\circ$, $\gamma=90^\circ$ and in agreement with literature data [2]. Yttrium ions in the unit cell are located in two positions in Y(1) and Y(2) substituted by Nd^{3+} (see Fig. 1a and 1b). The diffraction pattern of the sample is shown in Fig. 1c. The atom position parameters are listed in Table 1.

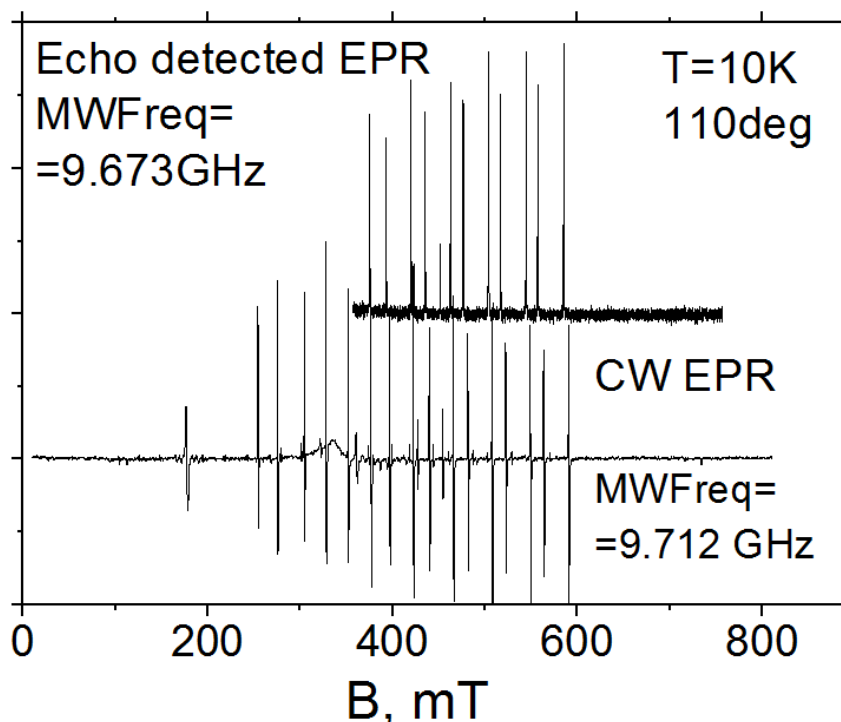


Figure 2. ESE and CW spectrums for a magnetic field ($T = 10\text{ K}$) showing two sets of ESR transitions from two magnetically inequivalent Nd^{3+} positions

Table 1. Position of atoms in Y_2SiO_5 sample (space group $C2/c$) at $T=300\text{ K}$

	Y(1)	Y(2)	Si	O(1)	O(2)	O(3)	O(4)	O(5)
x	0.806	0.929	0.873	0.800	0.946	0.968	0.763	0.882
y	0.378	0.743	0.907	0.713	0.998	0.843	0.071	0.398
z	0.141	0.963	0.181	0.118	0.089	0.298	0.203	0.985

The observed ESR spectrum Nd^{3+} in Y_2SiO_5 exhibits two groups of eight nonequidistant lines, which represent the hyper fine structure (HFS) components due to the odd neodymium isotope ^{143}Nd for two structurally nonequivalent positions; the line from the even isotope is absent. Figure 2 shows the field swept electron spin echo (ESE) and CW spectrums obtained for a magnetic field in (a*b) plane. The 16 intense lines correspond to the allowed ESR transitions for the two magnetically inequivalent classes of one site. These results suggest that Nd^{3+} ions preferentially occupy one of the Y^{3+} crystallographic sites.

To fit the experimental data we used the effective electron spin $S = 1/2$ and the nuclear spin $I = 7/2$ for ^{143}Nd and the following Spin Hamiltonian:

$$H = \mathbf{S} \cdot \mathbf{A} \cdot \mathbf{I} + \mathbf{g} \cdot \mu_B \cdot \mathbf{B} \cdot \mathbf{S}, \quad (1)$$

where \mathbf{A} – tensor of HFS and \mathbf{g} – g-tensor, \mathbf{B} – magnetic field, μ_B – Bohr magneton.

The Zeeman \mathbf{g} and hyperfine \mathbf{A} tensors were determined from CW spectra obtained by rotating the sample in (a*b) and (a*c) planes. A least squares fit to the ESR line positions gives the principal values of the \mathbf{g} tensor and \mathbf{A} local coordinate system: $g_{xx}=4.203$, $g_{yy}=1.8384$, $g_{zz}=0.7187$; in crystallographic system $A_{aa}=0.0632\text{K}$, $A_{bb}=0.0273\text{K}$, $A_{cc}=0.0168\text{K}$. Obtained here \mathbf{g} values are close to the values from [3]. The electron spin-lattice and spin - spin relaxation times T_1 and T_2 , respectively, were measured by an inversion-recovery sequence as a function of temperature between 5 and 10 K. The values of T_1 and T_2 are presented in Table 2.

Table 2. The parameters of spin-lattice and spin-spin time relaxations at 5,8 and 10 K for the paramagnetic centers of Nd^{3+} ions doped in Y_2SiO_5

T(K)	T_1 (μs)	T_2 (μs)	B (mT)
5	716	13.7	586.43
8	13	8.603	585.1
10	1.064	1.119	585.1

Conclusions

The crystal structure parameters of Y_2SiO_5 monocrystals doped by isotopically pure $^{143}\text{Nd}^{3+}$ (0.025%) were determined. Hyperfine structure parameters and g-tensors, times of spin-spin and spin-lattice relaxation of two nonequivalent Nd^{3+} paramagnetic centers were obtained.

Acknowledgements

This work was supported by the Russian Science Foundation (grant number 16-12-00041).

References

1. C.W, Thiel, Y. Sun, R.M. Macfarlane, T. Böttger, R.L. Cone, Rare-earth-doped LiNbO_3 and KTiOPO_4 (KTP) for waveguide quantum memories, *J. Phys. B: At. Mol. Opt. Phys.* 45, 124013 1-14 (2013).
2. W. Zhou, J. Yang, J. Wang, Y. Li, X. Kuang, J. Tang, H. Liang, Study on the effects of 5d energy locations of Ce^{3+} ions on NIR quantum cutting process in $\text{Y}_2\text{SiO}_5:\text{Ce}^{3+}$, Yb^{3+} , *Optics express* 20, A510-A518 (2012).
3. G. Wolfowicz, H. Maier-Flaig, R. Marino, A. Ferrier, H. Vezin, J.J.L. Morton, P. Goldner, Coherent storage of microwave excitations in rare-earth nuclear spins, *Phys. Rev. Lett.* 114, 170503 1-5 (2015).

Cis/trans isomerism of peptide bonds: the case of cardiotoxins from cobra venom

Alexey N. Shumsky¹, Tatyana M. Ilyasova², Peter V. Dubovskii²

¹Emanuel' Institute of Biochemical Physics, RAS, 4 Kosygin str., Moscow 119334, Russian Federation

²Shemyakin-Ovchinnikov' Institute of Bioorganic Chemistry, RAS, 16/10 Mikluho-Maklay str., Moscow 117997, Russian Federation

E-mail: shumsk@mail.ru

Introduction

Peptide bonds are planar, and the two successive C α atoms, flanking the bond can be either in *trans* or in *cis* conformation. For peptide bonds before non-proline residues (non-prolyl bonds), the *trans* state is favored. This is not the case for Xaa-Pro peptide bonds, or prolyl bonds (Fig. 1). Here, the *trans* isomer is only slightly favored over the *cis* one. About 7% of all prolyl bonds in proteins were found to be in *cis* conformation, compared to only 0.03% of non-prolyl bonds [1]. In this work we illustrate occurrence of *cis* peptide bonds, their manifestation in NMR spectra and ways of their detection in cobra cardiotoxins.

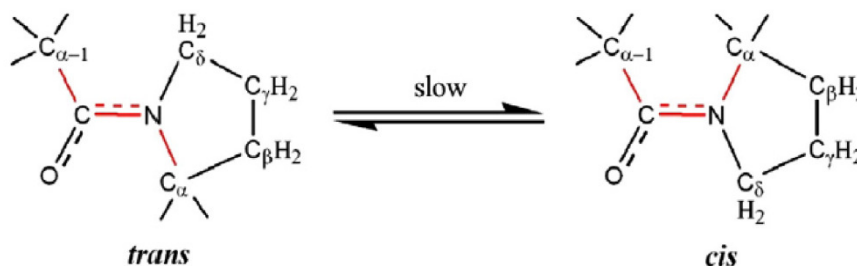


Figure 1. Peptidyl-prolyl bond isomerization

Cobra cardiotoxins

Cobra cardiotoxins (59-61 residue-long polypeptides, often also called cytotoxins) belong to the family of disulphide-rich toxins. These are all- β -sheet molecules adopting three-finger fold (Fig. 2) [2]. They possess as many as 4 disulfide bonds, connecting 8 conservative Cys-residues. The elements of antiparallel β -structure take origin from hydrophobic core, formed by the disulfides.

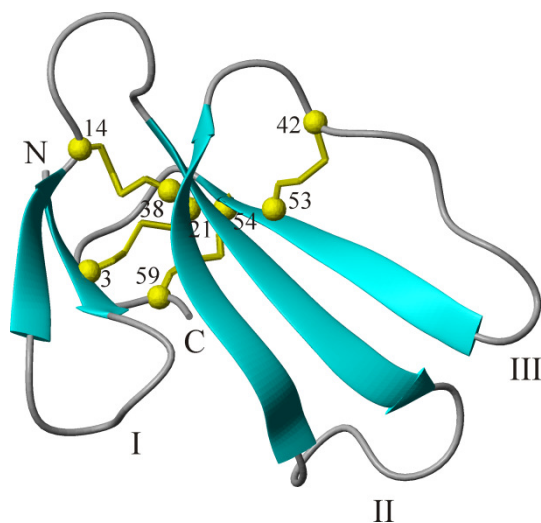


Figure 2. Structural organization of a cobra cardiotoxin in ribbon representation. The direction of β -strands, forming antiparallel β -sheets is shown with arrows. The fingers formed are numbered with roman numerals. The N- and C-termini of the molecule are marked with the respective letters. The C α -atoms of Cys-residues are shown with spheres and marked with the residue numbers (for 60-residue long cytotoxin molecule). The side-chains of the disulfide bonds are shown with yellow sticks

Up to now, there are several cardiotoxins, investigated with respect to *cis-trans* isomerism of their prolyl bonds (Table 1).

Table 1. Cardiotoxins and their database identifiers

Uniprot ¹	Name	Amino-acid sequence ²	PDB ³
P01441.1	CTII	1 10 20 30 40 50 60 LKCKKLVPLFSKTCPAGKNLCYKMFMVAAAPHVPVVRGCIIDVCPKSSLLVKYVCCNTDKCN	1CB9/1CCQ
P01451.1	CTI	LKCNKLVPIAYKTCPEGKNLCYKMFMMSDLTIPVVRGCIIDVCPKNSLLVKYVCCNTDRCN	1RL5/-
-	rCTI	MLKCNKLVPIAYKTCPEGKNLCYKMFMMSDLTIPVVRGCIIDVCPKNSLLVKYVCCNTDRCN	5T8A/5LUE
P01448.1	CTINm	LECNKLVPIAHKTCPAGKNLCYQMYMVSKSTIPVVRGCIIDVCPKSSLLVKYVCCNTDRCN I II III	-/-

¹ - <http://www.uniprot.org/>

² - Residues, forming the I-III fingers are shaded grey and marked below the sequence (see Fig. 2 for reference to fingers). Residue numbering starts with N-terminal Leu-residue, for rCTI the N-Met residue is zero numbered;

³ - <http://www.rcsb.org/pdb/home/home.do> (Major/minor forms).

NMR-detection of *cis*-prolyl bonds

Manifestation of *cis-trans* isomerism

All cardiotoxins investigated by NMR-spectroscopy in aqueous solution (Table 1) display two sets of signals in either homonuclear, or heteronuclear NMR-spectra (Fig. 3). They arise due to non-equality of the chemical shifts of the respective forms of the toxins. As a rule, heterogeneity in the spectra arises due to *cis-trans* isomerism of Val7-Pro8 peptide bond (all other Pro-residues feature *trans*-configuration). The *trans*-isomer features higher population, compared to its *cis*-analog (approximately, 5:1). This is reflected in intensity of the respective cross-peaks (Fig. 3).

Chemical shift analysis for identification of the conformation of Pro-residues

After the signals of the both forms of cytotoxin molecule have been assigned, there are two ways to establish their origin. One is analysis of the NOESY spectra. In this way CTII from *N. oxiana* venom was analyzed [4]. Another one – analysis of the chemical shifts of Pro-residues with PROMEGA program [5]. This approach was used for analysis of recombinant CTI (rCTI) [3]. In this case ¹³C-chemical shifts were available, because ¹³C,¹⁵N-labelled toxin was recombinantly produced [6]. However, these assignments can also be obtained at natural abundance of ¹³C-nuclei for native toxin (CTI). Indeed, comparison of ¹³C-HSQC spectra of rCTI and native CTI exhibit nearly coincident chemical shifts (except the N-terminus, where Met-residue is attached to rCTI) [6]. All CTs feature rather conservative spatial organization (Fig. 2) and thus, as far as concerned their ¹³C-HSQC spectra, conservatism of the chemical shifts is also seen, when comparing the spectra of different cardiotoxins. Having assigned ¹³C-HSQC spectra of native CTI, we were able to assign the respective spectra for CTINm from *N. melanoleuca* (Table 1) and determine conformation of all prolyl peptide bonds in this toxin.

Conclusion

¹³C-chemical shifts of Pro-residues are reliable means for identification of *cis/trans* isomerism for cardiotoxins. Their analysis with PROMEGA-program can be used as a fast-way-analysis for characterising equilibria, often observed in aqueous solutions of these polypeptides. We assume the method used is fast, convenient and suitable for analysis of *cis/trans* isomerism of Pro-residues in cobra cardiotoxins featuring similar number of prolyl peptide bonds (to those listed in Table 1).

Acknowledgements

This work is supported by Russian Foundation for Basic Research (RFBR) (grants #13-04-02128, 16-04-01479).

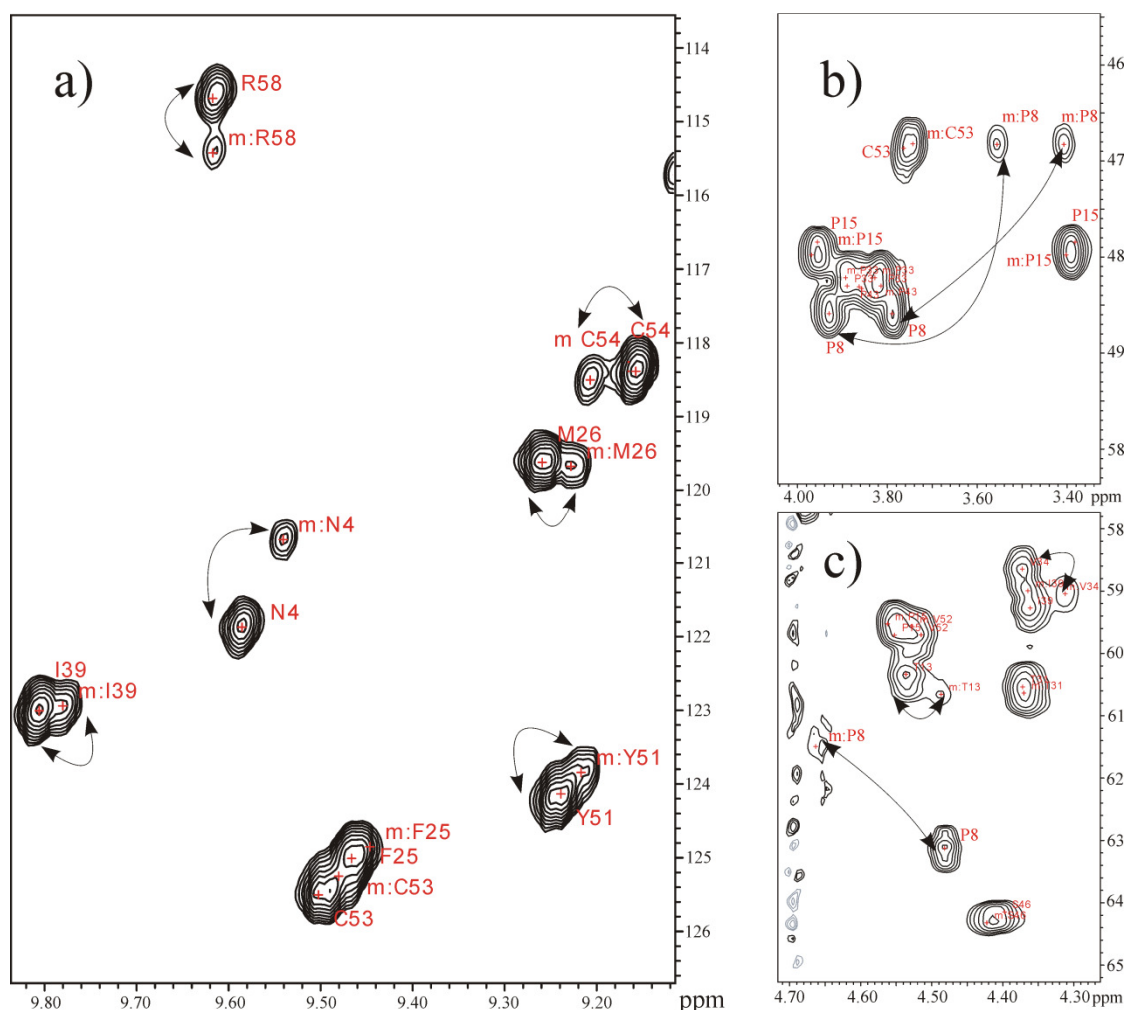


Figure 3. Conformational equilibrium in aqueous solution of ^{13}C , ^{15}N -rCTI (pH 6.0, 30°C, $\text{H}_2\text{O}/\text{D}_2\text{O}$, 95:5). Fragments of ^{15}N -HSQC (a) and ^{13}C -HSQC (b, c) spectra. The cross-peaks are marked with the names of residues in a single-letter abbreviation. A small letter “m:” is added to those corresponding to the “minor” conformer (with *cis* Val7-Pro8 bond). “Major” and “minor” cross-peaks are connected with a double-headed arrow, when they are well-resolved. The HD/CD and HA/CA regions of ^{13}C -HSQC spectrum are represented in (b) and (c) panel, respectively. The similarly-named cross-peaks in the panel (b) correspond to non-equivalent delta-protons. This figure is adapted from [3]

References

1. D. E. Stewart, A. Sarkar, J. E. Wampler. – J. Mol. Biol., 214, 253-260 (1990).
2. A. G. Konshina, P. V. Dubovskii, R. G. Efremov. – Curr. Protein Pept. Sci., 13, 570-584 (2012).
3. P. V. Dubovskii, M. A. Dubinnyi, A. G. Konshina, E. D. Kazakova, G. M. Sorokoumova, T. M. Ilyasova, M. A. Shulepko, R. V. Chertkova, E. N. Lyukmanova, R. G. Efremov. Cytotoxin I from *N. oxiana*: structure and dynamics of the recombinant and native protein (unpublished work).
4. D. V. Dementieva, E. V. Bocharov, A. S. Arseniev. – Eur. J. Biochem., 263, 152-162 (1999).
5. Y. Shen, A. Bax. – J. Biomol. NMR, 46, 199-204 (2010).
6. M. A. Shulepko, E. N. Lyukmanova, Z. O. Shenkarev, P. V. Dubovskii, M. V. Astapova, A. V. Feofanov, A. S. Arseniev, Y. N. Utkin, M. P. Kirpichnikov, D. A. Dolgikh. – Protein Expr. Purif., (2016) in press.

Application of modified Fe₃O₄ nanoparticles as MRI contrast agents: in vitro and in vivo study

N. A. Shvets¹, A. S. Mazur¹, T. I. Vinogradova², V. D. Semenov¹, O. M. Osmolovskaya¹, M. G. Osmolovsky¹

¹*Institute of Chemistry, Saint-Petersburg State University, 199034, Russian Federation*

²*St. Petersburg Research Institute of Phthisiopulmonology, 194064, Russian Federation*

E-mail: Shvets.natasha@mail.ru

Introduction

The Magnetic Resonance Imaging (MRI) is one of the most powerful non-invasive method which is widely used for diagnosis of diseases [1]. This method is based on the analysis of the spin-lattice and spin-spin relaxation time of protons in the human body (T1 and T2 mode, correspondently). To enhance the images definition the contrast agents which accumulated in the diseased area were used.

For T1 mode the commercial available contrast agents based on gadolinium complexes (Magnevist, Omniscan, Multihance, Gadavist) were used. Superparamagnetic iron oxide nanoparticles (NPs) (Feridex, Resovist, Combidex, Lumirem) were suggested for T2 mode [2]. But the ways to obtain the contrast agents with high chemical and aggregative stability based on superparamagnetic Fe₃O₄ and biocompatible coating are still under discussion.

In this work the original approach to improve the Fe₃O₄ NPs stability by forming the Fe₂O₃ surface layer was presented.

NPs synthesis and characterization

Fe₃O₄ NPs obtained by precipitation method were treated under hydrothermal conditions in the temperature range from 140 to 240°C.

XRD, TEM, BET, DLS and VSM methods, Mössbauer and IR spectroscopy were used to establish the optimal conditions of the process. It was shown that at low temperatures the surface layer of g-Fe₂O₃ were formed. At the temperatures above 200°C the NPs were aggregated and formed the a-Fe₂O₃ crystals.

At the second stage the absorption of dextran and xanthan which used as biocompatible coatings on Fe₃O₄ and Fe₃O₄@Fe₂O₃ NPs was carried out at 37 and 60°C, respectively. For both types of NPs the isotherms at low polysaccharides concentrations are the Langmuir type.

So 6 types of NPs were synthesized and used for further experiments (Table 1).

Table 1. The types of NPs used for MRI measurements

Sample	F	FF	FX	FD	FFX	FFD
Abbreviate	Fe ₃ O ₄	Fe ₃ O ₄ @ Fe ₂ O ₃	Fe ₃ O ₄ @ Xanthan	Fe ₃ O ₄ @Dextran	Fe ₃ O ₄ @Fe ₂ O ₃ @ Xanthan	Fe ₃ O ₄ @Fe ₂ O ₃ @ Dextran

MRI measurements

This part of the work was carried out in SPBU Magnetic Resonance Research Centre on Bruker Avance III 400 MHz WB Three channel Solid State NMR spectrometer with MRI/Diffusion capability.

In vitro study

The measurements were conducted using a special test tube and 2% agarose gel as the model of human tissue. The tubes contain the alternating layers of agarose and 6 types of NPs with different concentration in agarose.

The three modes were used (flash, T1 and T2). The experiments showed that nanoparticles (non-modified NPs, Fe_3O_4 @dextran/xanthan, and Fe_3O_4 @ Fe_2O_3 @dextran/xanthan) demonstrated the negative contrast (Fig. 1) in both T1 and T2 modes.

In vivo study

In vivo study was carrying out using healthy male mice. Distribution of nanoparticles (modified and non-modified) in organism of mice was studied. The average weight of a mouse about 20 g. All particles were entered intravenously. For comparison the native mouse was used.

MR images were shown that all the types of NPs accumulated in the livers, kidneys and lungs of mice. For example, the results for a liver are presented in Fig. 2. It is important to note that the walls of vessels become more visible by using of all NPs as contrast agents. In addition, non-modified F-NPs have toxic effects on mouse.

So the proposed approach for Fe_3O_4 surface stabilization is an effective and allows to use the obtained nanomaterials for MRI contrast agents.

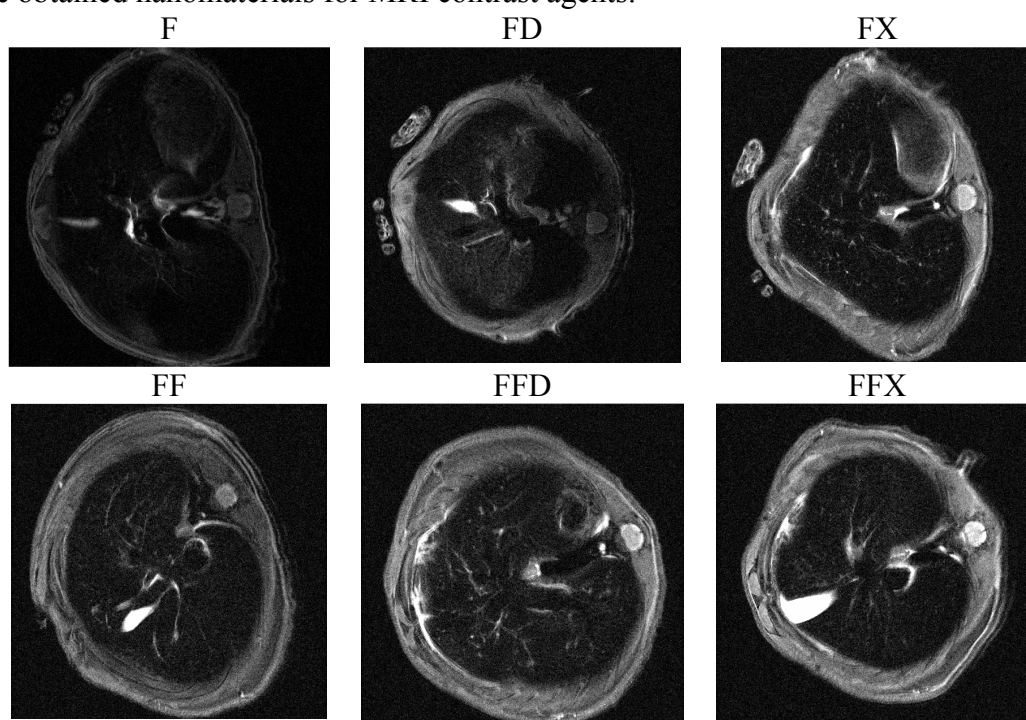


Figure 1. The liver mouse tomograms with different intravenous NPs, T2 mode

Acknowledgements

Authors appreciate Resource Centers of the Research Park of St. Petersburg State University, including Centre for X-ray Diffraction Studies, Magnetic Resonance Research Centre, Centre for Innovative Technologies of Composite Nanomaterials.

References

1. Jia-Kun Xu, Fang-Fang Zhang. – *Molecules*, 19, 21506-21528 (2014).
2. Michele K. Lima-Tenório, Edgardo A. Gómez Pineda. – *International Journal of Pharmaceutics* 493, 313–327 (2015).

Study of the relaxation efficiency of Gd and Fe ions inside fullerenols and they complexes with PVP and Dextrine in aqueous solutions

S. V. Sokratilin¹, Yu. S. Chernyshev¹, V. I. Chizhik¹, A. V. Ievlev¹, A. A. Shogina², M. V. Suyasova², V. P. Sedov², V. T. Lebedev²

¹St. Petersburg State University 198504, St. Petersburg, Petergof, str. Ulyanovskaya, 1.

²NRC "Kurchatov Institute", PNPI the name of Academician B.P. Konstantinov, PNPI, 1, Orlova roscha mcr., Gatchina, Leningrad region, 188300, Russia

E-mail: Sergey.Sokratilin@gmail.com, szhogina_aa@pnpi.nrcki.ru

Introduction

Nowadays there are many different methods of studying the internal human tissues: radiography, computed tomography (CT), positron emission tomography (PET), but one of the most promising is magnetic resonance imaging (MRI). Today, MRI is used in neurology, neurosurgery, orthopedics, endocrinology, gynecology and many other branches of medicine. The great advantage of this method is high resolution without radiation exposure. Sometimes to increase diagnostic accuracy it is necessary to use special paramagnetic contrast agents (MRI contrast agents). Salts-chelates are usually used as a contrast agent, rare-earth metal of the lanthanide group. Endohedral metallofullerenes with greater efficiency also can be used as a contrast agent.

Fullerene is a molecular carbon formation in the shape of a truncated icosahedron. In the molecules of fullerene carbon atoms are arranged at the vertices of regular hexagons and pentagons that make up the surface of a sphere or ellipsoid. All atoms are equivalent, as evidenced by the spectrum of nuclear magnetic resonance (NMR) on ¹³C - it comprises only one spectral line. Fullerol is a molecular compound, which is a fullerene, an upgraded OH - hydroxyl groups, that provide good solubility.

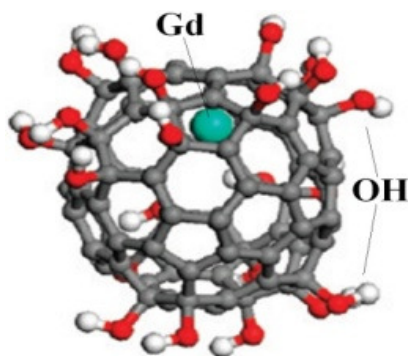


Figure 1. Endohedral metallofullerenol with Gd ions inside

In this paper we investigated paramagnetic ion (Gd and Fe) in aqueous solutions of metallofullerenols [1-5]. Solutions with different concentrations of the fullerenes and with different pH factors were investigated. Solutions were tested with different concentrations: 0,1; 0,5; 1,0; 2,0; 4,0; 6,0; 8,0; 10 mMol/L. And with different pH: 3; 3,7; 7,8. Besides, water-soluble metallofullerenols (Fe@C₆₀(OH)₃₀) and Fe@C₆₀ complexes with biocompatible polymers (polyvinylpyrrolidone (PVP) and dextrin) have been synthesized.

In Fe@C₆₀(OH)₃₀, Fe@C₆₀-PVP and Fe@C₆₀-Dextrin, iron preserves magnetic properties, exhibits low toxicity, and can be used in high doses in diagnostic investigations of liver, spleen, lymphatic system, and gastrointestinal tract.

The choice of the object of study, Gd and Fe ions in aqueous solutions fullerenols explained the relevance of [6, 7] to find effective relaxant for MRI. The work was conducted

in collaboration with the staff of The Petersburg Nuclear Physics Institute. They provided samples fullerenes, fullerenols, metallofullerenes synthesized in their laboratory, and investigate them of methods of neutron scattering.

Results and discussion

In this paper we made a series of measurements of relaxation rates of the concentration for different series of samples dependence. The first series of samples contained ions of Fe and endohedral metallofullerenes with Fe ions with different pH, and the second series contained ions Gd and endohedral metallofullerenes with Gd ions with different pH. A series of measurements was carried out on two different spectrometers with different proton resonance frequency of 20 MHz and 90 MHz, with constant temperature $T = 30\text{ }^{\circ}\text{C}$. The spin-lattice relaxation time T_1 was determined by the "inversion-recovery" method with pulse sequence $180^{\circ}-\tau-90^{\circ}$. The 180° - pulse duration is a $25\text{ }\mu\text{s}$, 90° -pulse - $12,5\text{ }\mu\text{s}$. Initial interval between pulses $500\text{ }\mu\text{s}$, the final 200-ms . The delay between the series - 200 ms . The spin-spin relaxation time T_2 was determined by the Carr-Purcell multi-pulse sequence $90^{\circ} - \tau - (180^{\circ} \times n - 2\tau) - n$. The RF pulse parameters: 90° ($12,5\text{ }\mu\text{s}$) - τ ($200\text{ }\mu\text{s}$) - 180° ($25\text{ }\mu\text{s}$). The delay between the series is a 1 s .

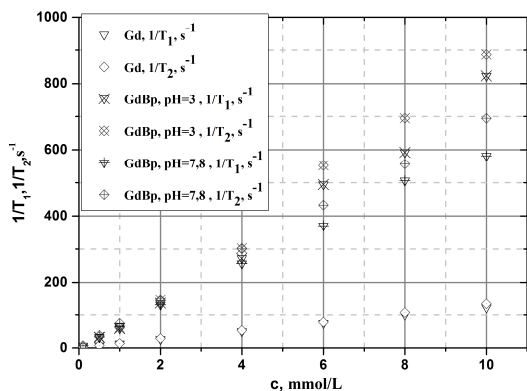


Figure 2. The dependence of the relaxation rates ($1/T_1, 1/T_2$) on solution concentration ($C\text{ mmol/l}$), 20 MHz

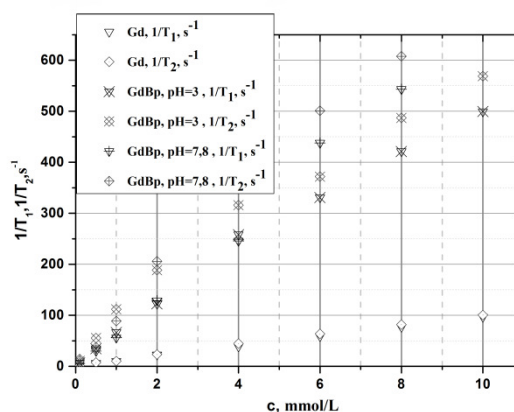


Figure 3. The dependence of the relaxation rates ($1/T_1, 1/T_2$) on solution concentration ($C\text{ mmol/l}$), 90 MHz

Frequency dependence for four different solutions were obtained. For two solutions of endohedral metallofullerenami with $\text{pH} = 4$ and for two solutions with metal ions.

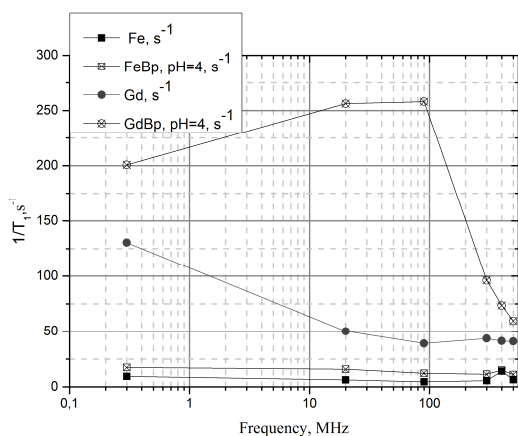


Figure 4. The dependence of the relaxation rate ($1/T_1$) on the proton resonance frequency

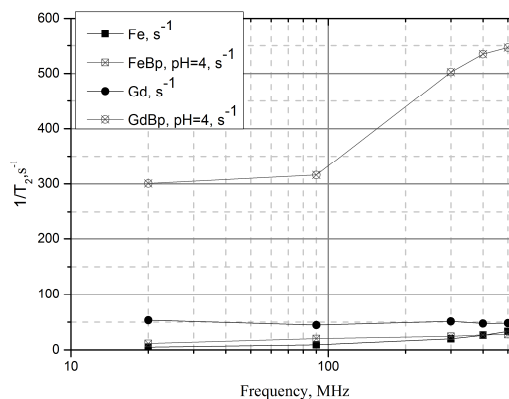


Figure 5. The dependence of the relaxation rate ($1/T_2$) on the proton resonance frequency

Temperature dependence of fullerenols with Fe and Gd ions at 500 MHz in the temperature range of 295-338 Kelvin were obtained. Fe@C₆₀-PVP and Fe@C₆₀-Dextrin showed a negative contrast ($r_1 \ll r_2$) in MRI. The ability of a contrast agent to enhance the proton relaxation rate is defined in terms of its relaxivity (relaxation efficiency) ($R_{1,2}$) (Tab.1).

Table 1. The relaxation efficiency of contrast agents

MR contrast agent	$R_2, \text{mM}^{-1}\text{s}^{-1}$	$R_1, \text{mM}^{-1}\text{s}^{-1}$
Fe@C ₆₀ -PVP	300.0±6.0	9.80±0.20
Fe@C ₆₀ -Dextrin	85.7±2.0	1.80±0.01
Fe@C ₆₀ (OH) ₃₀	5.0±0.5	3.0±0.06
Fe ₃ O ₄	187.0±3.7	1.60±0.03

The lower value of the relaxation efficiency of complexes with dextrin compared with complexes with PVP can be explained by an increase in the thickness of the polymeric shell around the fullerene “core”. The water protons movement near the local magnetic field gradients generated by paramagnetic iron atom in the fullerene is restricted by the polymeric shell.

Conclusion

The effectiveness of the solutions with Gd ions inside of endohedral metallofullerenes is 6,5 times greater than the effectiveness of water solutions with Gd ions. The efficiency of solutions with Fe ions inside of endohedral metallofullerenes is 1,5 times greater than the efficiency of water solutions with Fe ions. The effectiveness of relaxation in solutions with Gd and Fe ions inside of endohedral metallofullerenes is weakly dependent from the pH. Relaxation effectiveness of Gd@C₈₂(OH)₃₈₋₄₀ much higher contrast than the commercial agents «Magnevist» and «Gadovist».

References

1. Lin A., Fang S., Chou C., Luh T., Ho L. Local Carboxyfullerene Protects Cortical Infraction in Rat Brain, *Neuro Science Research*. 2002. V. 43. P. 317-321.
2. Tabata Y., Ishii T., Aoyama T., Oki R., Hirano Y., Ogawa O., Ikada Y. Perspectives of Fullerene Nanotechnology. Dordrecht – Boston – London: Kluwer Academ. Publ., 2001.
3. Nikolaev I. V., Lebedev V.T., Grushko Yu. S., Sedov V. P., Shilin V. A., Török Gy., Melenevskaya E. Yu. Ordering of Hydroxylated Fullerenes in Aqueous Solution: Fullerenes, Nanotubes and Carbon Nanostructure, V. 20 No. 4-7, P. 345-350, 2012.
4. Lebedev V.T., Grushko Yu. S., Török Gy. Structure and self-assembly of fullerene-containing molecular systems, *Journal of optoelectronics and advanced materials*, V. 15, No. 3-4, P. 193-198, 2013.
5. Файнгольд И. И., Полетаева Д. А., Котельников Р. А., Корнев А. Б., Трошин П. А., Кареев И. Е., Бубнов В. П., Романова В. С., Котельников А. И., Мембранотропные и релаксационные свойства водорастворимых производных гадолинийсодержащего эндометаллофуллерена, ISSN 00023353, Известия Академии наук. Серия химическая, 2014, № 5
6. Calucci L., Ciofani G., Mattoli V., Mazzolai B., Boni A., Forte C., NMR relaxation enhancement of water proton by Gd-doped boron nitride nanotubes, *The journal of physical chemistry*, 118, 6473-6479, 2014.
7. Koenig S., Epstein M., Ambiguities in the interpretation of proton magnetic relaxation data in water solutions of Gd³⁺ ions, *The journal of chemistry physics*, Vol. 63, No. 6, 1975.

NQR spectroscopy of intermetallic compounds CrGa₄ and MnGa₄

*Anton Trofimenko¹, Sergei Zhurenko¹, Kirill Okhotnikov, Valeriy Verchenko²,
Andrei Shevelkov² and Andrei Gippius¹*

¹*Faculty of Physics, M. V. Lomonosov Moscow State University, Moscow 119991, Russia*

²*Faculty of Chemistry, M. V. Lomonosov Moscow State University, Moscow 119991, Russia*

E-mail: trofim992@rambler.ru

Introduction

Intermetallic compounds with cubic crystal structure of the PtHg₄ type demonstrate unusually rich variety of thermodynamic properties. In particular, CrGa₄ can be described as a bad nonmagnetic metal with the Fermi level located near a pseudo-gap, which is formed by the strong *d-p* hybridization. In contrast, the isostructural compound MnGa₄ exhibits a typical metallic behavior. Our neutron diffraction experiments show that MnGa₄ is antiferromagnetically ordered at least up to room temperature. In this work we report on *ab-initio* calculations of electric field gradient (EFG) as well as NQR spectroscopy study of CrGa₄ and MnGa₄.

Methods

Single phase polycrystalline MnGa₄ and CrGa₄ samples were synthesized using standard ampoule technique. The *ab-initio* numerical calculations of electronic band structure of Mo₈Ga₄₁ were performed in frames of the density functional theory (DFT) with the linearized augmented plane wave (LAPW) method using the Wien2k code [1]. NQR experiments were performed using phase-coherent home-build pulsed spectrometer. ^{69,71}Ga NQR spectra were measured using a frequency step point-by-point spin-echo technique at 4.2 K.

Results

XPD data analysis show that both systems are characterized by cubic cell with $a=5.6497$ Å (CrGa₄) and $a=5.5967$ Å (MnGa₄) with the space group Im-3m. Atoms are situated in the following positions: Mn/Cr (0,0,0) and Ga (¼, ¼, ¼).

The numerically calculated EFG values and corresponding ^{69,71}Ga NQR frequencies obtained for the Ga site in both CrGa₄ and MoGa₄ crystal structures are listed in Table 1.

Table 1. EFG values and NQR frequency for Ga site in CrGa₄ and MnGa₄

Compound	EFG, 10 ²¹ V/m ²	Assymetry η	⁶⁹ Ga NQR MHz	⁷¹ Ga NQR MHz
CrGa ₄	-18.44	0,00	38.12	23.85
MnGa ₄	-15,80	0,00	32.66	20.43

Experimental ⁶⁹Ga NQR spectrum demonstrates qualitative difference in local Ga surrounding in CrGa₄ and MnGa₄ (Fig. 1). In antiferromagnetic MnGa₄ compound ⁶⁹Ga NQR spectrum consists of intensive single Lorentzian line. No traces of Zeeman splitting were observed since Ga atoms are situated symmetrically in relation to magnetic Mn atoms and therefore the hyperfine field on Ga site is equal to zero.

In contrast, ⁶⁹Ga spectrum in CrGa₄ unexpectedly exhibits complex satellite structure indicating deviation of local Ga symmetry from stoichiometric. One of the possible reason might be Cr shift from (0,0,0) position caused by removing of the orbital degeneracy similar to the Jahn-Teller effect. However, simple non-correlated shift of the Cr atoms cannot satisfactory explain the observed structure of the Ga NQR spectrum.

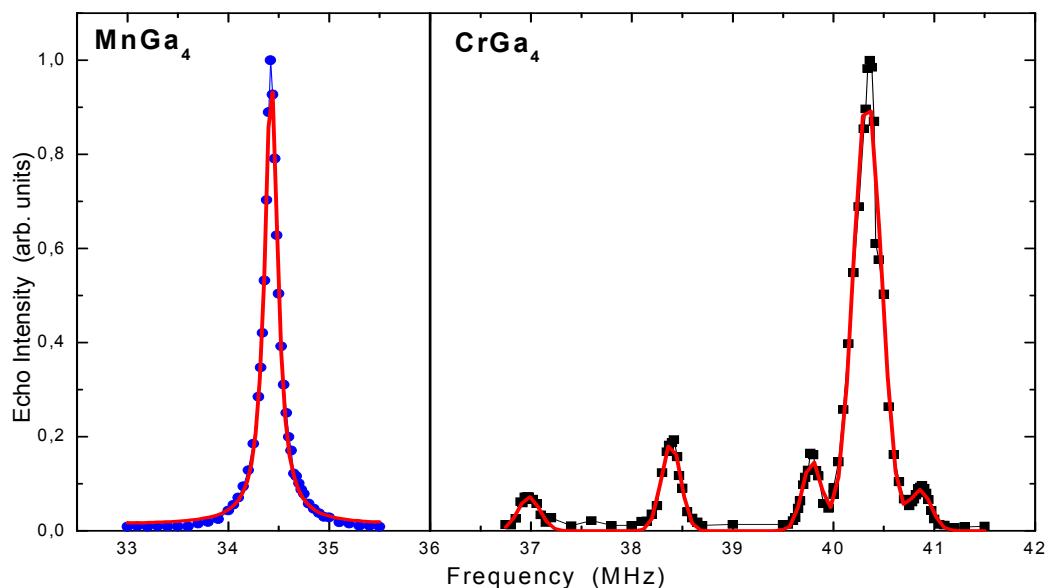


Figure 1. Experimental ^{69}Ga NQR spectrum of MnGa_4 (left) and CrGa_4 (right) measured at 4.2 K. Red solid lines are approximation by Lorentz function and set of Gauss functions for MnGa_4 and CrGa_4 , respectively

Conclusions

The EFG values for Ga site in CrGa_4 and MnGa_4 were calculated using the Wien2k code. Experimental $^{69,71}\text{Ga}$ NQR spectra measured at 4.2 K revealed qualitative difference in local Ga surrounding in CrGa_4 and MnGa_4 possibly connected with correlated shift of Ga atoms from stoichiometric position in CrGa_4 .

Acknowledgements

This work is supported by the Russian Foundation for Basic Research (grant #16-53-52012).

References

1. P. Blaha et al., WIEN2k, Techn. Universität Wien, Austria, 2001.

Investigation of double-frequency excitation of spin-wave chaotic solitons in magnetic films

D. E. Troshkin, A. V. Kondrashov, M. A. Cherkasskii, A. B. Ustinov

Saint Petersburg Electrotechnical University "LETI"

197376, Saint-Petersburg, 5 Professor Popov st.

E-mail: dimatroshkin@mail.ru

Introduction

In recent years, one of the important research directions was the study of chaotic dynamics of solitons in a various systems and media [1-3]. Chaotic dynamics of spin-wave solitons was observed in the magnetic films with a single-frequency excitation of the spin wave [2]. It arised from the development of a chain of self-modulation instabilities. The aim of this work was to study the dynamics of chaotic soliton excitations formed during the double-frequency excitation of spin waves in yttrium iron garnet (YIG) films through the development of induced modulation instability.

Experimental setup

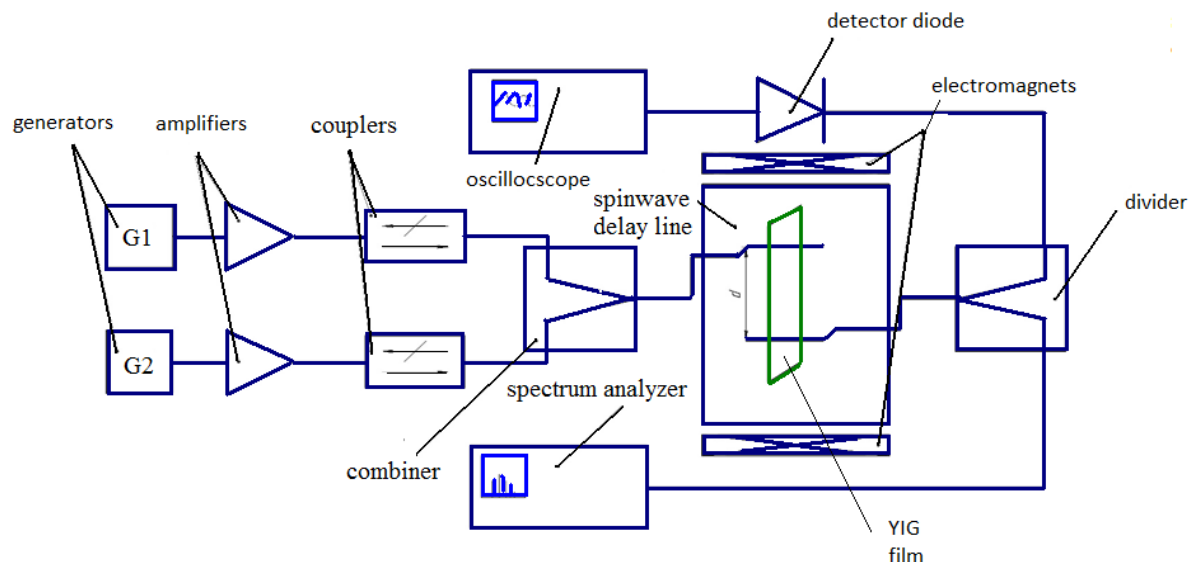


Figure 1. Experimental setup

Figure 1 shows experimental setup. It consisted of the spin-wave delay line, which was made with a 13.6- μm -thick YIG film, two microwave generators, a microwave combiner and some auxiliary components. Spin waves were excited and received by microstrip antennas having a width of 50 μm . The distance between the antennas d was 4.9 mm. The experiment was carried out as follows. Two microwave signals of close frequencies fed to the combiner, and then to the input port of the spin-wave delay line, thereby exciting two spin waves in the YIG film. Frequencies of the spin waves were denoted as f_1 and f_2 . The waveforms formed during the propagation of the two spin waves in the YIG film were received and investigated with an oscilloscope and a spectrum analyzer. During the measurements the frequency and power of the first and second signals were systematically changed.

Experimental results

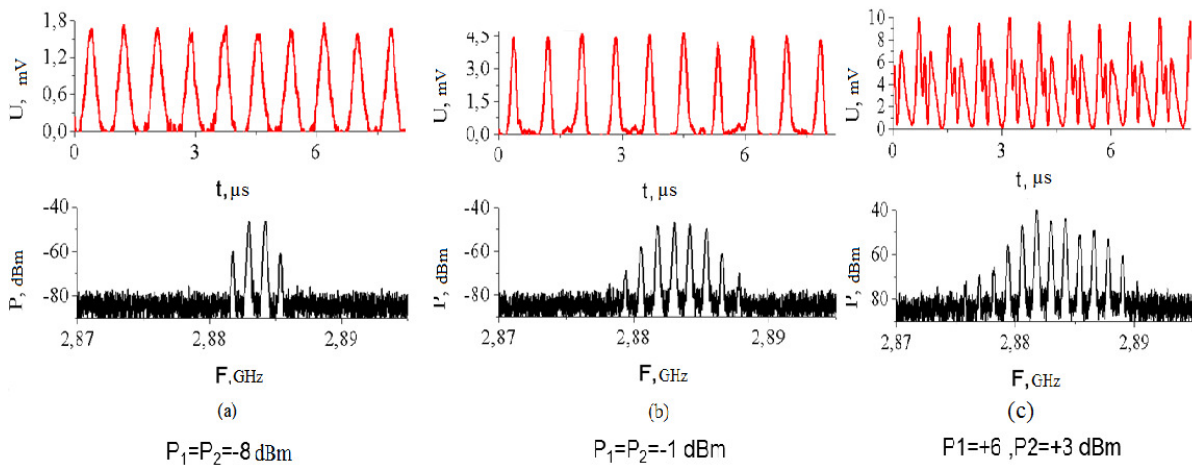


Figure 2. Bright solitonic (a), chaotic solitonic (b) and aperiodic (c) regimes of the spin-wave excitation

The first part of experiments was carried out for constant frequencies of the input signals $f_1 = 2283$ MHz and $f_2 = 2284,2$ MHz. Input power of the signals was changing. Results showed that for $P_1 = -14$ dBm and $P_2 = -10$ dBm solitons were not formed, a linear beating of two signals took place at the delay line output (Fig. 2(a)). With an increase in power up to $P_1 = P_2 = -8$ dBm the bright solitons were observed in agreement with the Lighthill criterion (Fig. 2(b)). With further increase in input power, the transition to a chaotic soliton dynamics was observed. The additional increase in power led to the destruction of the solitons and an aperiodic complex signal on the waveform appeared (Fig. 2(c)).

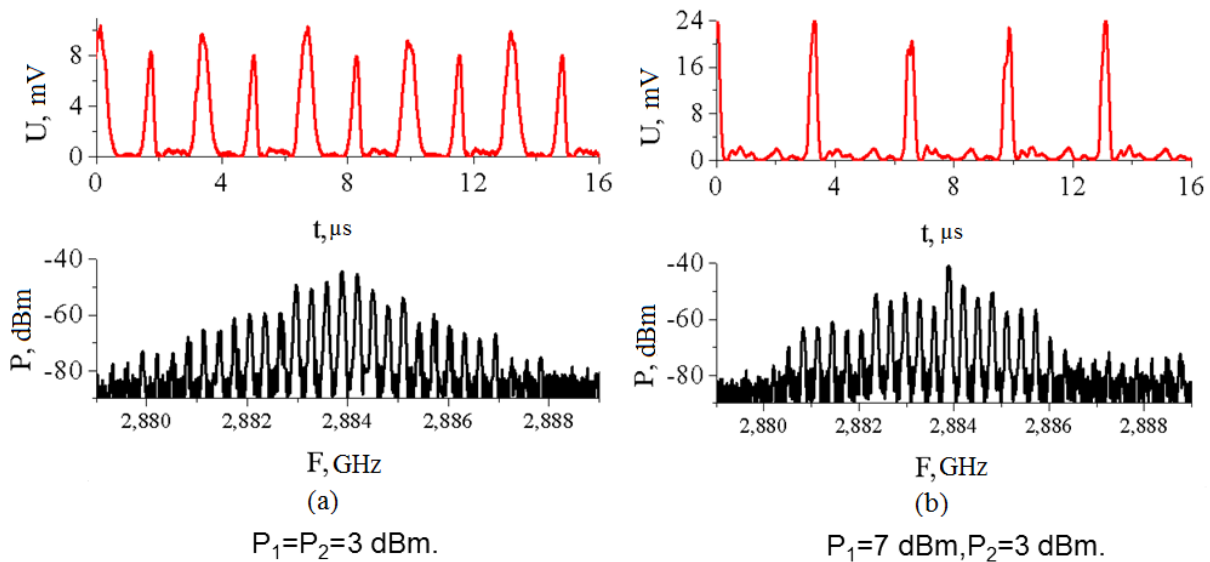


Figure 3. Doubling of the soliton pulse frequency effect

The next part of experiments was carried out for input signal frequencies of $f_1 = 2283,9$ MHz and $f_2 = 2284,2$ MHz. For values of the input power $P_1 = P_2 = 3$ dBm we observed a bifurcation of the soliton sequence period doubling. With further increase in power of the first generator a weakening of this effect was seen, until the complete disappearance with the power $P_1 = 7$ dBm (Fig. 3). A further increase in power led to the destruction of stable soliton regime and the formation of a complex aperiodic signal. Soliton nature of the

chaotic nonlinear pulses was confirmed by numerical simulations with the model of the nonlinear Schrödinger equation.

Thus, our findings demonstrate for the first time the chaotic soliton sequences formed through double-frequency excitation of spin-waves in YIG film as well as the period doubling of the sequences.

This work was supported by RFBR grant № 15-32-20357 mol_a_ved.

References

1. Soto-Crespo J.M., Akhmediev N., Phys. Rev. Lett. 95, 024101 (2005);
2. Ustinov A.B., Demidov V.E. , Kondrashov A.V., Kalinikos B.A., Demokritov S.O., Phys. Rev. Lett. 106, 017201 (2011);
3. Anderson J. Q., Ryan R. A., Wu M., Carr L. D., New Journal of Physics 16, 023025 (2014).

Logic gate based on microwave ferrite-ferroelectric interferometer

Irina A. Ustinova, Andrey A. Nikitin, Alexey B. Ustinov

*St. Petersburg Electrotechnical University, St. Petersburg, Russia
E-mail: ustinovairin@yahoo.com*

Introduction

An interest to ferrite–ferroelectric structures (which are now usually called “artificial multiferroic layered structures”) has greatly increased in the last decade [1, 2]. Microwave (MW) hybrid spin-electromagnetic waves (SEWs) can propagate in structures of this type [3-6]. The interest to artificial multiferroic structures is caused by a possibility to control the properties of SEWs by magnetic and electric bias fields. Devices based on multiferroic structures have dual electric and magnetic tuning. Electric control has an advantage over magnetic control, since it is potentially faster and is less energy consuming. One promising application of multiferroics for processing of MW signals may be waveguide MW interferometers built similarly to the Mach–Zehnder interferometer.

Another topical trend is development of logic device concepts. Previously, spin wave logic gates based on a Mach-Zehnder-type interferometer were realized both theoretically [7] and experimentally [8, 9]. An electric current controlled spin wave logic gate based on a width-modulated dynamic magnonic crystal was fabricated [10]. Despite the fact that application of Mach-Zehnder interferometers for development of logic gates have been known for a long time [11], the interest to study them still remains high [12]. The aim of the present work is theoretical investigation of a logic NOT-exclusive-OR gate based on MW ferrite-ferroelectric interferometer.

Theory

A block-diagram of the logic gate is shown in Fig.1. The interferometer is implemented according to a bridge scheme with two arms. The both arms comprise ferrite-ferroelectric phase shifters consisting of several layers: a ferrite film (1), a dielectric substrate (2) and a ferroelectric slab (3).

Consider the principle of the operation of the logic gate. A MW signal applied to the input is divided into two signals which propagate in the interferometer arms and acquire different phase shifts. At the output, these signals add and interfere. The intensity of the output signal depends on the phase difference. The variable attenuator changes the amplitude ratio of amplitudes of the signals that interfere at the interferometer output. The electric field applied to the ferroelectric slab serve as logical inputs where a logical zero is represented by $E=0$ kV/cm and a logical one by the field E_s necessary to create a phase shift of π .

Phase shift of MW signal in the arm depends mainly on the phase shift of spin and spin-electromagnetic waves (SEWs) in ferrite-ferroelectric (FF) phase shifter. Microstrip antennas (4) excite and receive the spin waves (SWs) in the ferrite film. The excited SWs propagate to the ferroelectric plate and, having reached it, enters the multiferroic structure and transforms the SEW. This part of waveguiding structure may be called the “active” part of the device because here the phase shift of MW signal is controlled by the changing of the polarization of the ferroelectric layer. After leaving the layered structure, the hybrid wave is transformed back into a spin wave, which is then received by the output microstrip antenna. The phases φ_1 and φ_2 of the interfering signals depend on the applied electric fields E_1 and E_2 .

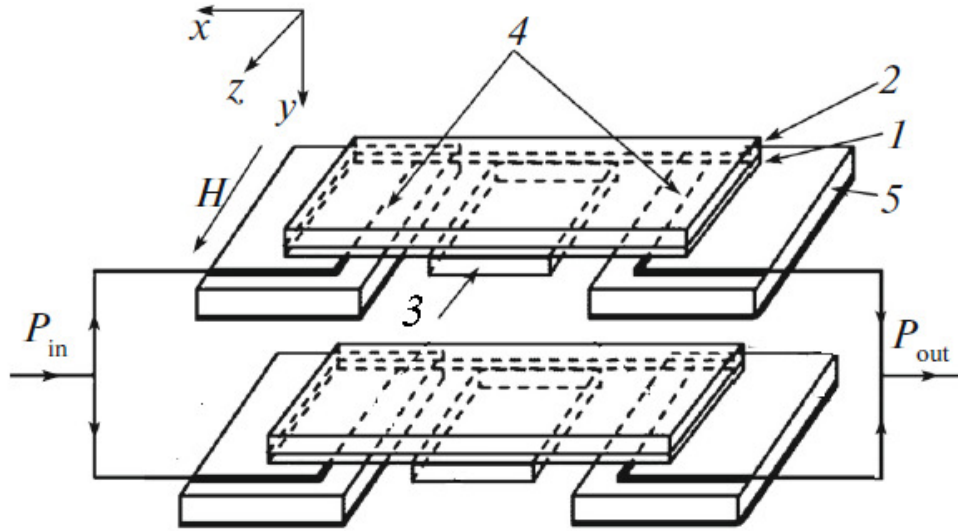


Figure 1. Schematic view of the logic NOT-exclusive-OR gate based on ferrite-ferroelectric interferometer

The theoretical model of the described interferometer is based on the dispersion laws of SEWs propagating in a FF structure [5] and spin waves propagating in free ferrite film [13]. We assumed that the SEWs propagate in the direction opposite to the orientation of the x axis and the multiferroic structure is magnetized by uniform magnetic field H along z axis (Figure 1). This field orientation corresponds to propagation of quasi-surface SEWs with the maximum of the field distribution occurring on the ferrite-ferroelectric interface.

The phase shift of MW signal in the arm of the interferometer was calculated as:

$$\varphi_1 = k_{SW}d_{SW} + k_{SEW}d_{SEW} + \varphi_{01}, \quad (1)$$

where k_{SW} and k_{SEW} are the wave numbers of the SWs and SEWs, respectively, d_{SW} и d_{SEW} are the distances passed by the SWs and SEWs, respectively, and φ_{01} is a phase shift in MW circuit of the first arm. The phase shift of the MW signal in the second arm is denoted φ_2 . In the case of equality φ_1 and φ_2 the suggested scheme is considered to be a logic NOT-exclusive-OR gate. In the case of addition of a permanent phase shifter introducing in one of the interferometer arms the phase shift of 180 degrees the described scheme transforms into a logic exclusive-OR gate.

The ferroelectric was considered to be in the paraelectric phase as a nonlinear dielectric with high permittivity. The change in the permittivity of ferroelectric upon the applying electric field E was described by the square law:

$$\varepsilon(E) = \varepsilon_1 - bE^2, \quad (2)$$

where ε_1 is the dielectric permittivity of the ferroelectric at $E = 0$ and b is the phenomenological parameter depending on the ferroelectric material and defined experimentally.

The power of MW signal in the interferometer output was calculated using a standard formula:

$$P_{out} = P_{out1} + P_{out2} + 2\sqrt{P_{out1}P_{out2}} \cos(\Delta\varphi), \quad (3)$$

where P_{out1} and P_{out2} are the powers of the interfering signals, and $\Delta\varphi = \varphi_1 - \varphi_2$ is their phase difference.

Results and discussion

The simulation of interferometer characteristics was carried out for different parameters of its design. Fig.2 shows the theoretical results calculated for following

parameters of the device: the thickness of the ferrite layer $L_f = 5.2 \mu\text{m}$, its saturation magnetization $4\pi M_S = 1750 \text{ G}$, dielectric permittivity $\epsilon_f = 14$, dissipation parameter $\Delta H = 0.5 \text{ Oe}$; the thickness of the ferroelectric plate $L_d = 200 \mu\text{m}$, dielectric loss tangent of the ferroelectric layer $\tan \delta = 10^{-2}$, dielectric permittivity $\epsilon_1 = 2868$, $\epsilon_2 = 1826$, coefficient $b = 6.25 \text{ cm}^2/\text{kV}^2$; the bias magnetic field $H = 754 \text{ Oe}$. The distance between the antennas was 6.75 mm , which was the sum of $d_{SW} = 2.75 \text{ mm}$ and $d_{SEW} = 4 \text{ mm}$.

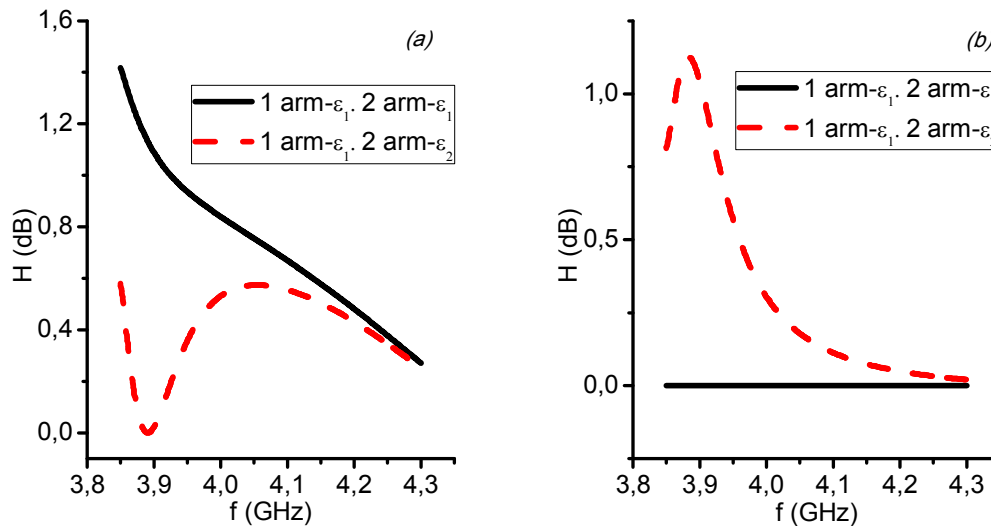


Figure 2. Theoretical results

Fig. 2, a represents amplitude-frequency characteristics (AFCs) for the logic gate NOT-exclusive-OR. Fig.2,b represents AFCs for the logic gate exclusive-OR.

In conclusion, the suggested logic gates can find different application. As examples we can mention modulators of MW signals, cells for measurement of the ferrite and ferroelectric material parameters, etc.

Acknowledgements

This work is supported by the Russian Foundation of Basic Research.

References

1. M. M. Vopson. - Critical Reviews in Solid State and Materials Sciences, **40**, 223-250 (2015).
2. C. A. F. Vaz. - J. Phys.: Condens. Matter, **24**, 333201 (2012).
3. V. B. Anfinogenov, T. N. Verbitskaya, Yu. V. Gulyaev, et.al. - Radiotekh. Electr., **30**, 2032-2039 (1988).
4. V. E. Demidov, B. A. Kalinikos, E. Edenhofer. - J. Appl. Phys, **91**, 100007 (2002).
5. A. A. Nikitin, A. B. Ustinov, V. V. Vitko, et.al. - J. Appl. Phys., **118**, 183901 (2015).
6. A. V. Sadvnikov, E. N. Beginin, K. V. Bublikov, et.al. - J. Appl. Phys, **118**, 203906 (2015).
7. K.-L. Lee, S.-K. Kim. - J. Appl. Phys, **104**, 053909 (2008).
8. T. Schneider, A. A. Serga, B. Leven, et.al. - Appl. Phys. Lett., **92**, 022505 (2008).
9. M. P. Kostylev, A. A. Serga, T. Schneider, et.al. - Appl. Phys. Lett., **87**, 153501 (2005).
10. A. A. Nikitin, A. B. Ustinov, A. A. Semenov, et.al. - Appl. Phys. Lett., **106** (2015).
11. A. B. Ustinov, B. A. Kalinikos. - Appl. Phys. Lett., **90**, 153501 (2007).
12. M. M. Gupta, S. Medhekar. - Optical., **127**, 1221-1228 (2015).
13. R. W. Damon, J. R. Eshbach. - J. Phys. Chem. Sol. **19**, 308-320 (1961).

Atomic mobility in triple eutectic alloy Ga-In-Sn

*E. V. Varzer¹, D. Ju. Podorozhkin¹, A. O. Antonenko¹, D. Ju. Nefedov¹,
E. V. Charnaya¹, Ju. A. Kumzerov², A. V. Fokin²*

¹*Saint-Petersburg State University*

198504 Saint-Petersburg, Petergof, Uljanovskaya str/ 1

²*Ioffe Physico-Technical Institute of RAS*

194021 Saint-Petersburg, Politekhnikheskaya str. 26

E-mail: egor.varzer@gmail.com

Recently interest of the study of triple alloys increased significantly. It is caused by the practical application of these materials. For example, it is possible to use Ga-In-Sn alloy in the production of mercury-free thermometers, to create liquid heat transfers, to cover the surface of electrodes, to apply in medicine and biotechnology. It is also promisingly to use Ga-In-Sn alloy in ferrocolloidal suspensions. In this regard, it becomes especially important to study the influence of nanostructures on viscosity and atomic diffusion into the liquid Ga-In-Sn alloy. It was found significant slowdown of atomic mobility for binary alloys Ga-In and Ga-Sn. This problem has not been investigated for triple alloys before.

In this paper was studied atomic mobility in liquid triple alloy Ga-In-Sn, which was embedded into three different nanoporous matrix. As matrix were used porous glasses with mean pore size $d=7$ nm and $d=18$ nm, and opal matrix, which is a close packing of amorphous silica spheres of 210 nm in diameter. Pore size in porous glasses porous was determined by nitrogen and mercury porosimetry. Diameter of silica spheres was determined by atomic force microscopy. A net of octahedral (size is 87 nm) and tetrahedral (size is 47 nm) pores is located between spheres in opal matrix.

The Ga-In-Sn alloy of eutectic composition was embedded into pores in liquid state under pressure at room temperature. After filling pores the matrix surface was cleaned and samples for study were cut. Sample volume was 0.2 cm^3 . The samples were weighed before and after filling. Filling factor was about 80% for all three samples. The Ga-In-Sn bulk alloy was also prepared for comparison of the results.

NMR measurements were carried out at room temperature on three pulse spectrometers: Avance 400, MSL 500 and Avance 750 in three different magnetic fields: 9.4 T, 11.75 T and 17.6 T, respectively. Longitudinal relaxation time was measured by the recovery of the magnetisation after a 180° -pulse (inversion recovery). The NMR line position was determined by the signal maximum, obtained after the Fourier transform of free induction decay signal after 90° -pulse. Number of scans varied from 2k to 16k. NMR line shift for ^{69}Ga and ^{71}Ga nuclei was calculated relative to line position in a cubic GaAs single crystal and relative to the line position in a weak solution of InNO_3 for ^{115}In .

The experiments established that the NMR lines for the alloy in matrices significantly broadened compared to those in bulk alloy. Recovery of the longitudinal magnetization for bulk sample was single-exponential, as well as for other liquid metals and alloys. Single-exponential and independent of the field relaxation corresponds to the approximation of rapid movement. The measurement results showed that the approach of rapid movement is valid only for Ga-In-Sn alloy introduced into glass with 18 nm pore size and into opal.

Investigation of hydroxylation path of fullerenols $C_{60}(OH)_n$, $n=2, 4, 6, 12, 40$

Aleksandr S. Voronin^{}, Andrei V. Komolkin*

Department of Nuclear-Physics Research Methods, Saint Petersburg state university, 199034, Saint Petersburg, Russia

^{}E-mail: sahkaxz@gmail.com*

Introduction

Hydroxylated fullerenes – fullerenols, have large prospect of use in medicine. However, their precise structure remains unknown. The location of hydroxyl groups is especially interesting. One of the methods for synthesis fullerenols is chemical reaction of fullerene with hydrogen peroxide H_2O_2 [1]. This reaction produces $C_{60}(OH)_n$, where n is equal to mostly 38 ± 2 [2]. Here, we review the results of the research of location of hydroxyl groups in fullerenols $C_{60}(OH)_n$, $n=2, 4, 12, 40$, which was carried out by means of computer simulation.

Method of quantum chemistry

For computer simulation in this research was used a program of computational quantum chemistry GAMESS, which carries out:

- Calculation of molecular wave functions by Hartree–Fock method;
- The accounting of energy of electronic correlation on the basis of density functional theory with functional LYP.

All molecules were modeled with the same basic set 6-31G.

Results and discussions

Initially, to understand how hydroxyl groups most likely join C_{60} , four different locations of two hydroxyl group were simulated:

- Opposite to each other in a hexacarbon ring (Fig. 1a);
- Next to each other along bond of conjugation of two hexacarbon rings (Fig. 1b);
- On the opposite sides of the molecule (Fig. 1c);
- Next to each other along bond of conjugation of pentacarbon and hexacarbon rings (Fig. 1d)

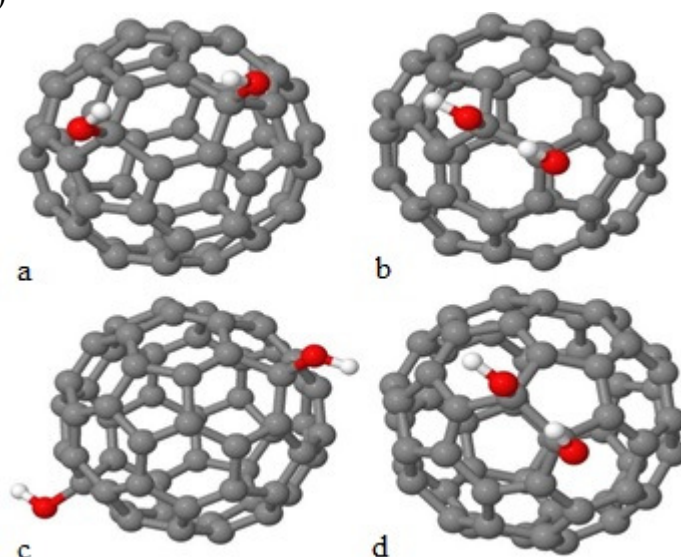


Figure 1. Locations of hydroxyl groups in fullerenols $C_{60}(OH)_2$, which were modeled in this work

According to the simulation results, the second isomer is the most energetically preferable (Fig. 1b). It is caused by the fact that the bond of conjugation of two hexacarbon rings is double, and it is energetically favorable for two hydroxyl groups to break this bond and to join the carbon atoms. It also forms a hydrogen bond, which can be seen from the figure. In other cases two broken double bonds and two unpaired electrons remained. We can also assume that in reaction C_{60} with H_2O_2 hydroxyl groups joins the carbon atoms by pairs.

At the following stage it was necessary to define how pair of hydroxyl groups will join the molecule further. Two most probable cases were simulated:

- Joining along bond of conjugation of two hexacarbon rings independently of position of the first pair (in our case on the opposite side of the molecule, Fig 2a);
- Joining next to the first pair of hydroxyl group along bond of conjugation of two hexacarbon rings (Fig. 2b)

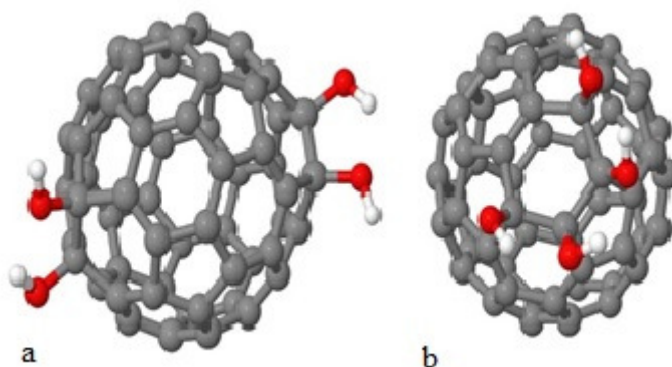


Figure 2. Locations of hydroxyl groups in fullereneols $C_{60}(OH)_4$, which were modeled in this work

The second case was energetically more preferable, probably due to the fact that the larger quantity of hydrogen bonds is formed. At this stage it is possible to assume that pairs of hydroxyl groups are forming a kind of chain along bonds of conjugation of hexacarbon rings.

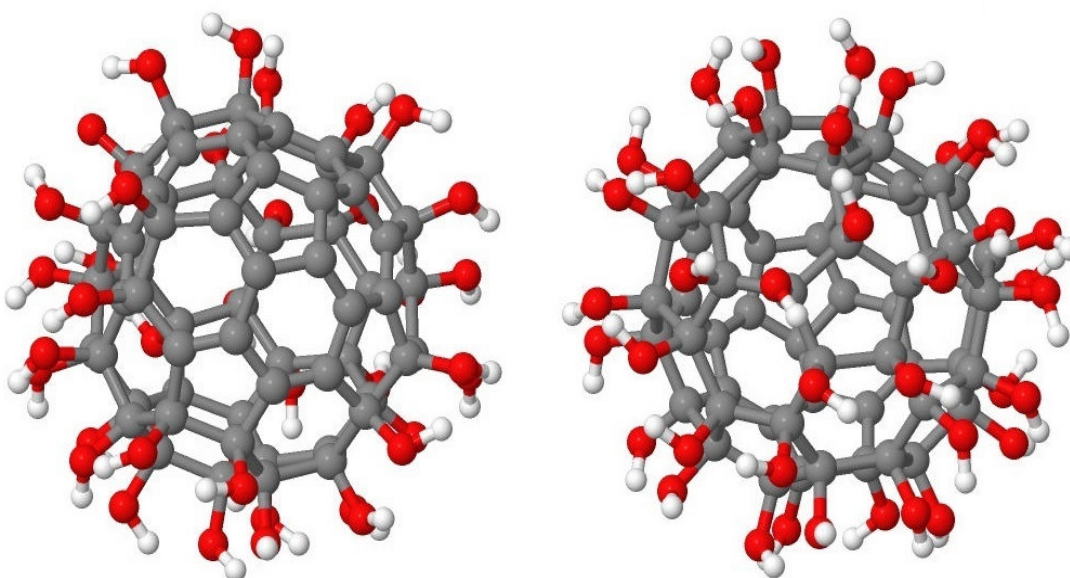


Figure 3. Two views of the first configuration of $C_{60}(OH)_{40}$

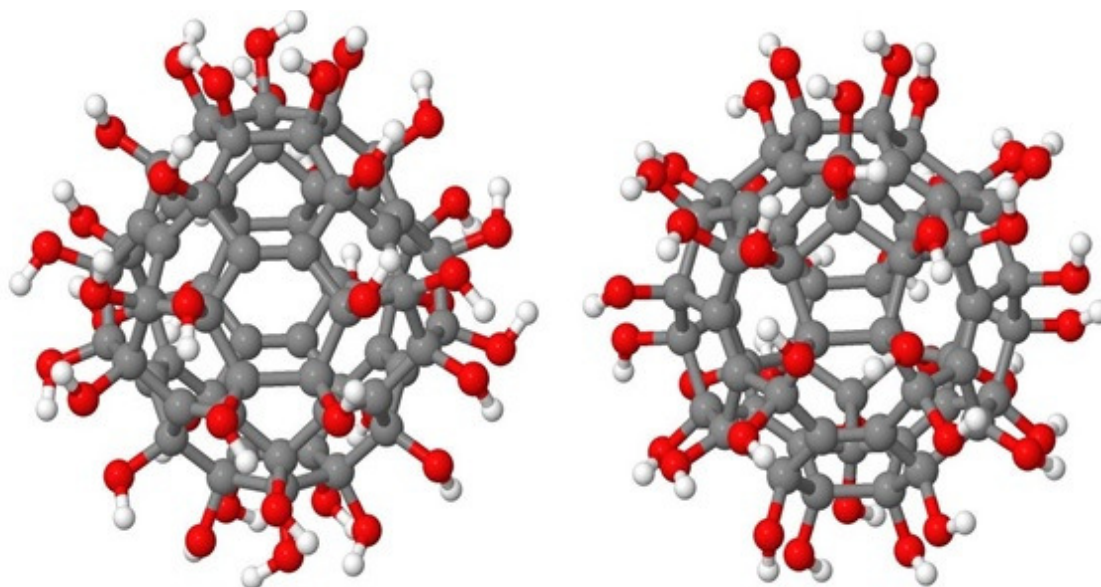


Figure 4. Two views of the second isomer of $C_{60}(OH)_{40}$

As it was already noticed, the reaction of fullerene with hydrogen peroxide H_2O_2 produces $C_{60}(OH)_n$ where n is equal to mostly 38 ± 2 . Therefore, it was simulated the following 2 isomers of the molecules $C_{60}(OH)_{40}$:

- One part of the molecule is evenly filled with forty hydroxyl groups, and other part is empty (Fig. 3);
- The closed chain of 20 hydroxyl groups is placed on the “equator” of the molecule, and star-formed “caps” of 10 hydroxyl groups are on the poles (Fig. 4).

The second isomer is energetically more favorable as all hydroxyl groups located along bond of conjugation of hexacarbon rings and all hydrogen atoms form hydrogen bonds. This configuration has an axis of symmetry of the fifth order.

In the report, fullerenols with number of hydroxyl groups of 6 and 12 are also discussed.

Acknowledgements

Simulation was carried out on the computers of the Department of Nuclear-Physics Research Methods of the Saint Petersburg state university.

References

1. K. Kokubo, K. Matsubayashi, H. Tategaki, H. Takada, T. Oshima, *ACS Nano* 2008, 2, 327.
2. V. T. Lebedev. Small angle neutron and X-ray studies of carbon structures with metal atoms // SANS-YuMO User Meeting, Dubna, 2011.

Ti-Substituted BaFe₁₂O₁₉ Single Crystal Growth Magnetic Properties

Denis A. Vinnik¹, Liubov S. Mashkovtseva¹, Dimitry A. Zherebtsov¹, Sandra Nemrava², Nikolay S. Perov^{3,5}, Anna S. Semisalova³, Lyudmila I. Isaenko^{4,6}, Rainer Niewa²

¹South Ural State University, Faculty of Material Science and Metallurgical Technologies

²Institute of Inorganic Chemistry, University of Stuttgart, Pfaffenwaldring 55, 70550 Stuttgart, Germany

³Moscow State University, Leninskie Gory 1-3, 119991 Moscow, Russia

⁴Institute of Geology and Mineralogy Siberian branch Russian Academy of Sciences, Ac. Koptuyuga ave. 3, 630090 Novosibirsk, Russia

⁵Baltic Federal University, Nevskogo street 14, 236041 Kaliningrad, Russia

⁶Novosibirsk State University, Pirogova street 2, 630090 Novosibirsk, Russia

E-mail: liubov.mash@gmail.com

Introduction

Traditionally, hexagonal ferrites are applied in microwave and millimeter-wave engineering, for example, in gyromagnetic devices for the EHF range (30–300 GHz) [1]. The interest in scientific work directed on structural and magnetic properties modification by partial substitution of iron with different diamagnetic and paramagnetic cations in BaFe₁₂O₁₉ has increased considerably within the latest 20 years [2]. Substitution of Fe by Ti ions has a strong influence on the magnetic properties (saturation magnetization and coercive field) and improves dielectric properties at microwave frequencies [3].

Single crystals growth

We used flux method to grow single crystal. The batch composition for growth of undoped BaFe₁₂O₁₉ crystals consisted of 67.465 wt % Fe₂O₃, 18.64 wt % Na₂CO₃, and 13.895 wt % BaCO₃. To grow Ti-substituted crystals, 2, 4, 8, 12, and 20 mass % TiO₂ (or 1.20, 2.40, 4.80, 7.19, and 11.99 wt % Ti) were added (samples 2–6 in Table 1). The total mass of one batch for crystal growth accounted to up to 50 g.

The initial mixture was ground in an agate mortar and filled into a 30 mL platinum crucible. The crucible was placed in a resistance furnace equipped with a thermocouple type B and a precision thermoregulator RIF-101. To homogenize the starting materials, the furnace was maintained at 1260 °C for 3 h followed by cooling at a rate of 4.5 K/h to 900 °C. The system was then allowed to naturally cool to room temperature. The spontaneously obtained crystals with a size up to 8 mm were separated from the flux by leaching in hot nitric acid. The additional phases such as NaFeO₂ and Fe₂O₃ were found to be present in small amounts. In fig. 1 one sample is presented.

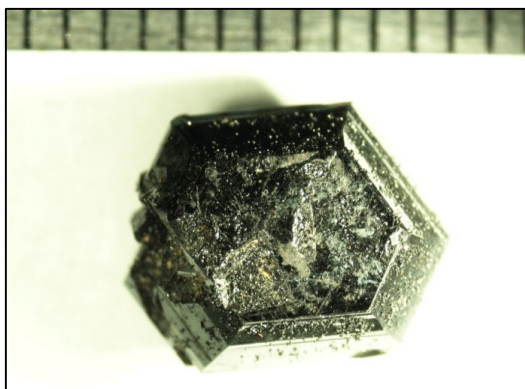


Figure 1. BaFe_{12-x}Ti_xO₁₉ single crystals

Crystal's properties and structure

Measurements

The compositions of the samples were determined using an electron microscope Jeol JSM7001F with an energy dispersive spectrometer Oxford INCA X-max 80. Powder X-ray diffraction analysis was performed on a Rigaku Ultima IV diffractometer in the angular range from 10° to 90° with filtered (Ni foil) CuK α 1,2 radiation. The Curie temperatures were determined using a simultaneous thermal analyzer Netzsch 449C Jupiter. Magnetic measurements of powder and single crystal samples were performed on a vibrating sample magnetometer VSM LakeShore 7407.

Crystal structure and magnetic properties

Diffraction analysis data are presented in table 1. All samples have hexagonal structure. Unit cell parameters grow up to x=0.78 but then values decrease. Curie temperature dramatically reduce. Table 1 present the values of the specific saturation magnetizations at room temperature in an external magnetic field of 12.0 kOe for powder and single crystal samples. The external field is parallel to the easy axis and perpendicular to the main extension directions of the crystal with the shape of a hexagonal platelet. Additionally single crystal samples 1–4 were investigated in different relative orientations with respect to the magnetic field. Magnetic hysteresis curves are typical for a barium ferrite with M-type structure (magnetoplumbite).

Table 1. Unit cell parameters, Curie temperatures and saturation magnetizations of Ti-substituted barium hexaferrites BaFe $_{12-x}$ Ti $_x$ O $_{19}$

№	Ti, wt%	x	a/Å	c/Å	V/Å ³	T _C /°C	M _{Sat} [emu/g]	
							Powder	Crystal
1	0	0	5.8929(4)	23.1943(1)	697.54(7)	452	64.8	-
2	0.7	0.16	5.8952(4)	23.205(2)	698.41(7)	423	63.7	69.98
3	2.0	0.46	5.8977(4)	23.213(1)	699.24(6)	376	61.3	63.71
4	3.4	0.78	5.900(1)	23.237(3)	700.6(2)	322	58.9	60.07
5	3.9	0.9	5.8990(3)	23.2334(2)	700.17(5)	287	51.7	* N/A
6	5.5	1.3	5.8972(4)	23.2238(2)	699.45(5)	251	23.95	* N/A

References

1. Koledintseva, M. Y.; Khanamirov, A. E.; Kitaitsev, A. A. *Ceram.Mater.* 2011, 61–86.
2. S. Fisher, B. I. Halbedel, B.; Hülsenberg, D.; Belau, S.; Schadewald, U.; Jakob, M. *Cfi/Ber. DGK* 2005, 82, 182–188.
3. Quiroz, P.; Halbedel, B. 54th International Scientific Colloquium, Ilmenau University of Technology, 2009.

Crystal structure, *ab-initio* calculations and NQR spectroscopy of novel superconductor $\text{Mo}_8\text{Ga}_{41}$

*Sergei Zhurenko*¹, *Kirill Okhotnikov*¹, *Valentin Popov*¹, *Valeriy Verchenko*²,
*Andrei Shevelkov*² and *Andrei Gippius*¹

¹*Faculty of Physics, M.V. Lomonosov Moscow State University, Moscow 119991, Russia*

²*Faculty of Chemistry, M.V. Lomonosov Moscow State University, Moscow 119991, Russia*

E-mail: zhurenko.sergey@gmail.com

Introduction

Intermetallic compound $\text{Mo}_8\text{Ga}_{41}$ undergoes superconducting transition at $T_c = 9.7$ K with relatively high value of upper critical field $\mu_0 H_{c2} = 8.6$ T [1]. Thermodynamic and transport measurements as well as electronic structure calculations performed both in normal and superconducting state in $\text{Mo}_8\text{Ga}_{41}$ were discussed in [2]. Here we report on the crystal structure, *ab-initio* calculations of electric field gradient (EFG) and preliminary results of NQR spectroscopy study of $\text{Mo}_8\text{Ga}_{41}$.

Methods

Crystals of $\text{Mo}_8\text{Ga}_{41}$ were grown with a high-temperature solution growth method using Ga both as a reagent and a flux medium as described in [2]. The *ab-initio* numerical calculations of electronic band structure of $\text{Mo}_8\text{Ga}_{41}$ were performed in frames of the density functional theory (DFT) with the linearized augmented plane wave (LAPW) method using the Wien2k code [3]. NQR experiments were performed using phase-coherent home-build pulsed spectrometer. $^{69,71}\text{Ga}$ NQR spectra were measured using a frequency step point-by-point spin-echo technique at 4.2 K.

Results

$\text{Mo}_8\text{Ga}_{41}$ crystallizes in the V_8Ga_{41} type of crystal structure where Mo and Ga atoms occupy 2 and 9 crystallographic positions, respectively. MoGa_{10} polyhedra are interconnected by corners and form the arrangement, in which one triangular face of each polyhedron is shared with a cuboctahedron centered by the unique Ga atom (Fig. 1). The Ga atom in the center of a cuboctahedron with crystallographic position (0; 0; 0.5) has no contacts with Mo atoms in its first coordination sphere.

The numerically calculated EFG values and corresponding $^{69,71}\text{Ga}$ NQR frequencies obtained for all 9 different Ga sites in the $\text{Mo}_8\text{Ga}_{41}$ crystal structure are listed in Table 1. The Ga site #1 with almost zero EFG is situated in the center of GaGa_{12} cuboctahedra. The expected Ga NQR frequencies for this site are too low to be detected by our NQR spectrometer. Other 8 Ga sites produce very complex $^{69,71}\text{Ga}$ NQR spectrum in the frequency range of 10-32 MHz with several overlapping peaks of different multiplicity (Fig.2). Our preliminary $^{69,71}\text{Ga}$ NQR spectra measurements at 4.2 K show satisfactory agreement with theoretical prediction.

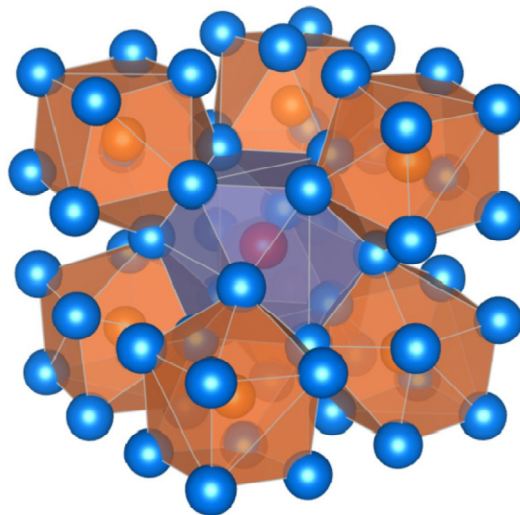


Figure 1. Mo_8Ga_{41} crystal structure constructed by $MoGa_{10}$ polyhedra (orange) and $GaGa_{12}$ cuboctahedra (blue)

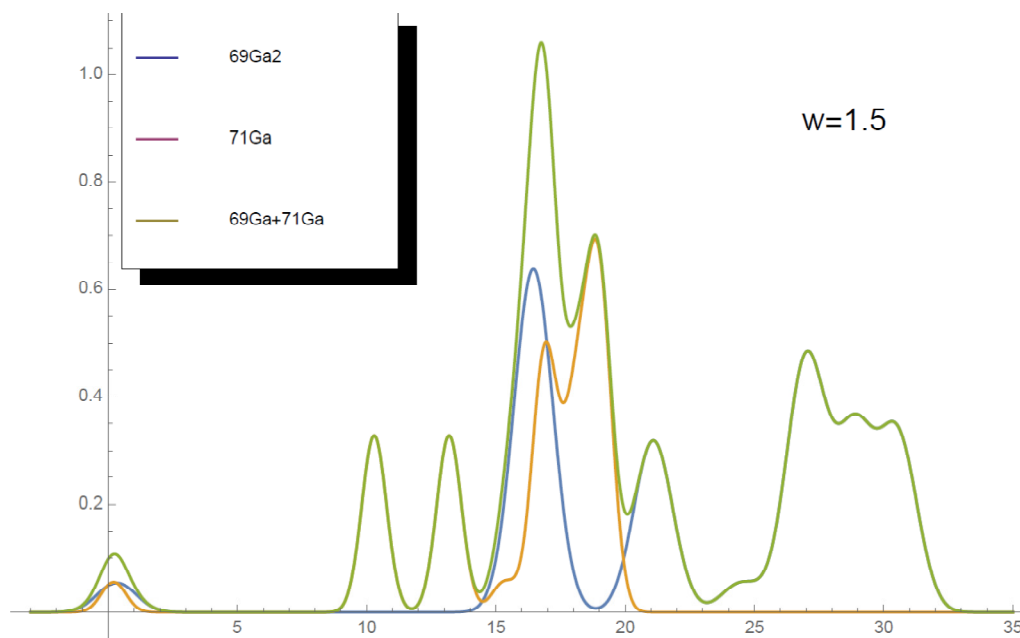


Figure 2. Calculated $^{69,71}Ga$ NQR spectrum of Mo_8Ga_{41} assuming individual ^{69}Ga NQR width of each Ga site of 1.5 MHz

Table 1. EFG values and NQR frequency for Ga sites in Mo_8Ga_{41}

Site	Multiplicity	EFG, $10^{21} V/m^2$	Assymetry η	^{69}Ga NQR MHz	^{71}Ga NQR MHz
1	1	-0,16	0,00	0,33	0,21
2	1	-11,85	0,00	24,50	15,33
3	3	-12,76	0,31	26,80	16,77
4	6	-10,20	0,05	21,09	13,19
5	6	-7,90	0,21	16,45	10,29
6	6	-14,45	0,19	30,06	18,81
7	6	-13,03	0,19	27,10	16,96
8	6	-14,71	0,17	30,56	19,12
9	6	-13,93	0,13	28,88	18,07

Conclusions

Crystals of the intermetallic superconducting compound $\text{Mo}_8\text{Ga}_{41}$ were successfully synthesized. The EFG values for each Ga site were calculated using the Wien2k code. Experimental $^{69,71}\text{Ga}$ NQR spectrum shows satisfactory agreement with theoretical prediction.

Acknowledgements

This work is supported by the Russian Foundation for Basic Research (grant #16-53-52012).

References

1. A. Bezinge and K. Yvon, *J. Less-Common Met.* **99**, L27 (1984).
2. V.Yu. Verchenko et al., *Phys. Rev. B* **93**, 064501 (2016)
3. P. Blaha et al., WIEN2k, Techn. Universität Wien, Austria, 2001.

Poems about School

* * *

Чижик-Spinus, где ты был?
– «Я сигнал за хвост ловил!
Сделал я ему “Фурье” –
Закружилось в голове!»

Цели «Spinus»’а просты:
Дать научные мосты!
Пусть у вас здесь будет шанс
Пообщаться «в резонанс»!

В Школе здесь научат всех
Сочетать с наукой смех,
Дискотеки с Э-Пе-эР,
Я-Ка-эР и Я-эМ-эР!

В Школе много новых лиц,
Будем превращать их в птиц:
Вдруг хотя б одной из ста
Дастся «Нобель-высота»!

2010

* * *

Spinus, Spinus, where you were?
Did you dive in the Resonance world?
– “Yes! I dived with my great joy –
Resonance is a pleasant toy!”

“Spinus” school invited you
To look for a knowledge clue.
We will show the signal birth
In the field of our Earth!

If you wish to have success,
At the School achieve progress!
We will teach you all to fly
In the scientific sky!

We desire you to get
Many victories-побед!
It will be a good surprise
If you catch the Nobel prize!

2010

Author Index

- Abdeddaim, R.*, 115
Adelson, V. Y., 161
Agladze, K. I., 134
Ahokas, J., 68
Akulov, A. E., 105
Alakshin, E. M., 118, 142
Aldoshin, S. M., 194
Aleksandrov, E. B., 32
Andreev, N. K., 33
Anisimov, N. V., 95
Antonenko, A. O., 38, 163, 243
Artem'eva, M. N., 91
Asatryan, H. R., 165
Ayala, I., 53
Babicheva, E. S., 72, 134
Badalyan, A. G., 165
Baglasov, E. D., 93
Balevičius, V., 84
Baranov, P. G., 165
Batova, S. S., 95
Bayer, M., 55
Belov, P. A., 115, 139, 180
Bogachev, Yu. V., 75, 168, 207
Bogdan, A. A., 78, 99
Bogomyakov, A. S., 200
Borodkin, G. S., 194, 205
Brougham, D., 152
Bugaev, A. S., 149
Bunkov, Y., 36
Burghammer, M., 53
Burtseva, A. A., 194
Bystrov, S., 81
Chang, C.-F., 111
Charnaya, E. V., 38, 114, 149, 163, 243
Cherbunin, R. V., 55
Cheremisin, V. M., 91, 121, 137, 161
Cherkasskii, M. A., 237
Chernyshev, Yu. S., 232
Chizhik, V. I., 39, 81, 178, 232
Chudin, A. V., 83
Colletier, J.-P., 53
Coquelle, N., 53
Dagys, L., 84
Denisov, A. Yu., 93
Denisov, G. S., 66
Diachenko, S. V., 87
Dmitrenko, M. E., 217
Dmitriev, A., 171
Dolgushev, M., 89
Dorogan, I. V., 194
Drozdov, A. A., 91
Drozdovskii, A. V., 175
Dubovskii, P. V., 227
Edinach, E. V., 165
Efimov, S. V., 155
Eichhoff, U., 40
Elyashberg, M. E., 43
Enoch, S., 115
Eremina, R. M., 131, 224
Fazlizhanov, I. I., 131
Fedorov, A. L., 93
Fedunyak, I. P., 91
Fedunyak, O. I., 91
Fokin, A. V., 149, 243
Fomina, D. V., 95
Freude, D., 60
Frolov, V. V., 46, 108, 161, 178, 183
Frolova, S. R., 134
Gavrilova, T. P., 224
Georget, E., 115
Gerlovin, I. Ya., 55
Gippius, A., 235, 249
Glukhova, V. A., 95
Glybovski, S. B., 115, 180
Gromova, E. A., 99
Groves, A., 49, 126
Grunin, L. Y., 48
Gulyaev, M. V., 95
Gusakov, E. A., 194
Haase, J., 38, 60, 149
Hessel, A., 53
Huang, T.-H., 111
Hurshkainen, A. A., 115, 180
Ibragimova, M. I., 131
Ievlev, A. V., 83, 232
Ievleva, S. V., 108, 183
Ignatiev, I. V., 55
Il'ves, A. G., 78

- Illarionov, R. A., 186
 Ilyasova, T. M., 227
 Isaenko, L. I., 247
 Izmailov, S. A., 53, 98, 126, 127
 Järvinen, J., 68
 Kaempf, K., 49
 Kalinikos, B. A., 175
 Kamyshanskaya, I. G., 91, 121, 137
 Karpenko, M. N., 99
 Kataeva, G. V., 78, 99
 Katkova, M. A., 212
 Kavokin, K., 51
 Kazarinov, A. A., 189
 Kazarov, R. L., 121
 Khamzin, Aydar I., 192
 Khomenko, Yu. G., 78, 99
 Klimavičius, V., 84
 Klimovskikh, I. I., 200
 Klochkov, A. V., 102, 118, 128, 142
 Klochkov, V. V., 155, 197
 Kluev, E. A., 212
 Kodjikian, S., 118
 Koeppe, B., 66
 Kokh, K. A., 200
 Kolodina, A. A., 194
 Kolosova, O. A., 197
 Komissarova, O., 205, 214
 Komolkin, A. V., 52, 189, 244
 Kondrashov, A. V., 203, 210, 237
 Kondratyeva, E. I., 102, 118
 Koptug, I. V., 105
 Korableva, S. L., 118
 Koroleva, A. V., 200
 Koroleva, N. B., 212
 Koryukin, A. V., 203
 Kostina, A. A., 168
 Kotikov, D. A., 168
 Kozlenko, A., 205, 214
 Krestina, M. S., 105
 Krylova, E., 145
 Kumzerov, Yu. A., 38, 149, 243
 Kupriyanov, P. A., 107, 178
 Kurauskas, V., 53
 Kutovoi, S. A., 224
 Kuzmin, V. V., 142
 Kuzminova, A. I., 217
 Kuznetsova, M. S., 55
 Larrat, B., 115
 Lebedev, V. T., 232
 Lehtonen, L., 68
 Li, J., 152
 Limbach, H.-H., 66
 Litvinov, V., 152
 Lukyanov, B., 205, 214
 Lukyanova, M., 205, 214
 Luzhetckaia, N. V., 108, 183
 Luzik, D. A., 126
 Lyublinskaya, O. G., 148
 Malay, V., 205, 214
 Mamin, G. V., 165
 Mantsyzov, A. B., 111
 Marchenko, Ya. Yu., 186
 Marchenkov, V. V., 163
 Mariasina, S. S., 111
 Markelov, D. A., 89
 Mashkovtseva, L. S., 247
 Matveev, V. V., 58
 Maximychev, A. V., 72, 134
 Mazing, D. S., 207
 Mazur, A. S., 230
 Melchakova, I. V., 115, 139, 180
 Metelkina, K. K., 210
 Michel, D., 38, 60, 149
 Mikhailovskii, O., 53
 Mikushev, V. M., 114
 Milovidov, E. M., 93
 Milyukhina, I. V., 99
 Minkin, V. I., 194
 Moshnikov, V. A., 207
 Motygullin, I. G., 102, 128
 Mukhanov, E., 205, 214
 Mukhina, I. V., 212
 Muravyeva, M. S., 212
 Musatov, V. B., 91
 Narkhov, E. D., 93
 Natarov, V. O., 168
 Naumov, S. V., 163
 Nefedov, D. Yu., 38, 149, 243
 Negrimovsky, V. M., 72
 Nemrava, S., 247
 Neronov, Yu. I., 61
 Niewa, R., 247

- Nikiforova, A. V.*, 207
Nikitin, A. A., 240
Nikitina, A. V., 75, 168
Nikolaev, B. P., 186
Nikolaev, I. A., 48
Nikulin, A. V., 115
Nuzhina, D. S., 118
Okhotnikov, K., 235, 249
Orlinskii, S. B., 165
Osinin, A. S., 207
Osmolovskaya, O. M., 230
Osmolovsky, M. G., 230
Osterman, I. A., 111
Ozhogin, I., 205, 214
Pankov, V. V., 168
Parr, M. A., 186
Penkova, A. V., 217
Perepukhov, A. M., 72, 134
Perov, N. S., 247
Petrov, I. N., 121
Petrov, M. Yu., 55
Petrov, V. I., 218
Petrova, E. G., 168
Petrova, O. A., 111
Podkorytov, I. S., 49, 98, 126, 148
Podorozhkin, D. Yu., 38, 243
Polshakov, V. I., 111
Pomogailo D. A., 124
Popov, E. N., 218
Popov, V., 249
Prakhova, L. N., 78
Privalov, A. F., 145
Pugachev, A., 205, 214
Raaijmakers, A. J. E., 180
Rabdano, S. O., 49, 126, 223
Rogacheva, O. N., 53, 127
Romanov, N. G., 165
Romanova, I. V., 118
Rybkina, A. A., 200
Sabitova, V. A., 168
Safin, A., 221
Safin, T. R., 128, 142
Safiullin, K. R., 102, 128, 142
Sapunov, V. A., 93
Saveluev, D. V., 93
Sayapin, Yu. A., 194
Schanda, P., 53
Schekina, Yu., 214
Sedov, V. P., 232
Semenov, V. D., 230
Semisalova, A. S., 247
Sergeev, A. V., 93
Sergeyev, N. M., 64, 65
Sergiev, P. V., 111
Shaban, A., 223
Shchelokova, A. V., 139
Sheludiakov, S., 68
Shelyapina, M. G., 145
Shenderovich, I. G., 66
Shestakov, A. V., 131, 224
Shevelev, O. B., 105
Shevelkov, A., 235, 249
Shevtsov, M. A., 186
Shikin, A. M., 200
Shilova, A., 53
Shogina, A. A., 232
Shubina, N. S., 72, 134
Shumsky, A. N., 227
Shustov, V. A., 131
Shutova, T. G., 168
Shvets, N. A., 230
Simeschenko, P. I., 137
Skrynnikov, N. R., 49, 53, 98, 126, 127, 148
Slobozhanyuk, A. P., 139
Sokratilin, S. V., 232
Speranskiy, R. K., 218
Stanislavovas, A. A., 142
Sukhanov, A. A., 224
Sukharzhevskii, S. M., 75, 207
Surova, L., 145
Susin, D. S., 99
Suyasova, M. V., 232
Tagirov, M. S., 102, 118, 128, 142
Tereshchenko, O. E., 200
Tian, M., 152
Tkachev, V. V., 194
Tolstoy, P. M., 66
Trofimenko, A., 235
Troshkin, D. E., 237
Tyuryaeva, I. I., 148
Tyutyukin, K. V., 108, 183

- Usachev, K. S.*, 197
Uskov, A. V., 38, 149
Uspenskaya, Yu. A., 165
Ustinov, A. B., 175, 203, 210, 221, 237, 240
Ustinova, I. A., 240
Vainio, O., 68
Van den Berg, C. A. T., 180
Varzer, E. V., 243
Vasiliev, S., 68
Verbin, S. Yu., 55
Verchenko, V., 235, 249
Vershovskii, A., 171
Vinnik, D. A., 247
Vinogradova, T. I., 230
Voogt, I. J., 180
Vorobiev, A. Kh., 124
Voronin, A. S., 244
Woodhouse, J., 53
Wu, B., 152
Xu, J., 152
Xue, Yi, 53
Yakovlev, A. A., 91
Yakovlev, D. R., 55
Yakovleva, L. Yu., 186
Yatsyk, I. V., 131, 224
Yuwen, T., 53
Zagumennyi, A. I., 224
Zapasskii, V. S., 69
Zavartsev, Y. D., 224
Zaynullin, R. R., 192
Zgadzay, Yu. O., 155
Zherebtsov, D. A., 247
Zhernovoy, A. I., 87
Zhurenko, S., 235, 249

Magnetic Resonance and its Applications

Abstracts book

Saint Petersburg State University
November 20-26, 2016